Acoustic Concentration of Bioparticles

Povilas Dumčius

A Thesis Submitted for the Degree of Doctor of Philosophy

Cardiff University

Jan 2024

MUSL
Medical Ultrasound and Sensors Laboratory

TMEG
TISSUE MICROENVIRONMENT GROUP

ABSTRACT

This dissertation delivers substantial contributions to the domain of acoustofluidics, with a distinct emphasis on formulating innovative fabrication procedures, studying wave modes, and advancing particle manipulation techniques. The research presents the Dynamic Acoustofluidic System (DAS), constructed by exploiting Flexible Printed Circuit Board (FPCB) Interdigitated Electrodes (IDEs). This approach revolutionizes the fabrication of Surface Acoustic Wave (SAW)-based acoustofluidic systems, enhancing cost efficiency, accessibility, and the potential for rapid prototyping.

The Dynamic Acoustofluidic System (DAS) displays exceptional versatility by permitting the positioning of the IDT transducer at any desired angle relative to the piezoelectric substrate. This capability reveals wave modes beyond the recognized Rayleigh surface acoustic waves (SAWs). By strategically manipulating frequencies and exercising precise control over the positioning of the IDT, unprecedented control over streaming patterns has been accomplished, pushing past the limitations of nanoparticle manipulation as delineated in the existing literature.

Rigorous experimental investigations into liquid acoustic interactions form the core of this thesis, providing a detailed understanding of these complex processes. The use of FEM (Finite Element Method) simulations is primarily to hypothesize and visualize the underlying phenomena observed experimentally. These experimental insights have led to the development of the Acoustic Concentration of Extracellular Vesicles (ACEV) device, representing a significant advancement in rapid nanoparticle concentration techniques. The ACEV device, utilizing dual-wave mode, can efficiently concentrate nanoparticles as small as 20 nm from sample volumes of 50 µL within minutes. Importantly, this method maintains the integrity of extracellular vesicles (EVs) during the concentration process, ensuring the safe extraction of enriched particles while minimizing unwanted protein aggregates. Further refinement and automation of this concentration process hold great potential for enhanced performance and increased throughput.

Contents

Acknowledgements

Completing this PhD thesis has been a challenging yet rewarding journey, and I would like to take this opportunity to express my gratitude to the following people who have supported and encouraged me along the way.

Firstly, I would like to thank my supervisor, Dr Xin (Chris) Yang, for his unwavering guidance, support, and patience throughout my PhD. Dr Yang has created an excellent research environment for me, providing me with the necessary resources and creative freedom to express myself. His constant availability for discussions and his support beyond the lab has been greatly appreciated.

I would like to extend my deepest gratitude to my parents and family members, Linas Dumčius, Kristina Dumčiene, and Marijus Dumčius, for their unending support and encouragement. Their financial and emotional support enabled me to focus on my studies and excel in my research.

I am also grateful for the constant support and friendship of my dear friend, Tomas Krukovski, who stood by me during the most challenging times of my PhD journey. His belief in me and tolerance of my questionable behaviour is something I will always cherish.

I would like to express my gratitude to my lab colleagues, Roman Mikhaylov, Mercedes Martin, and Xiaoyan Zhang, who have provided invaluable support in the writing and brainstorming of my thesis and publications. Their suggestions and constructive feedback have been instrumental in shaping the presented work.

Finally, I am grateful for the people who have come and gone throughout my PhD journey, allowing me to learn from their experiences and contributing to my growth as a researcher.

Thank you all for your support, encouragement, and belief in me. This thesis would not have been possible without your help.

List of Publications

- **Povilas Dumčius**, Mikhaylov R, Zhang X, et al. Dual-Wave Acoustofluidic Centrifuge for Ultrafast Concentration of Nanoparticles and Extracellular Vesicles. Small (Weinheim an der Bergstrasse, Germany). 2023 Apr:e2300390. DOI: 10.1002/smll.202300390. PMID: 37118859.
- **Povilas Dumčius*,** Chao Sun*, Ke Wang, et al. High Throughput Acoustic Vibration Based Concentration of Cells. In preparation.
- Wang K, Sun C, **Povilas Dumčius**, et al. Open-Source Board Based Acoustofluidic Transwells for Reversible Disruption of the Blood-Brain Barrier for Therapeutic Delivery. Research Square; 2022. DOI: 10.21203/rs.3.rs-2323098/v1.
- Zhang X, **Povilas Dumčius**, et al. Multi-View Acoustofluidic Rotation Cytometry (MARC) for Pre-Cytopathological Screening. Advanced Science.
- Mercedes Stringer, **Povilas Dumčius**, Xiaoyan Zhang, et al. Flexible Printed Circuit Board Based Hexagonal Interdigital Transducer 2023. In preparation.
- Roman Mikhaylov, Mercedes Stringer, **Povilas Dumčius**, et al. A reconfigurable and portable acoustofluidic system based on flexible printed circuit board for the manipulation of microspheres. J. Micromech. Microeng. 2021 DOI 10.1088/1361-6439/ac0515.
- Mercedes Stringer, **Povilas Dumčius**, Xiaoyan Zhang, et al. Multidirectionally Patterned Interdigital Transducers for Enhancing Acoustofluidic Streaming with Flexible Printed Circuit Board. 2024, In preparation.

Conference Participations

- **Povilas Dumčius**, Mikhaylov R, Zhang X, et al. Extracellular Vesicle Enrichment via Rayleigh and Shear Surface Acoustic Waves. Acoustofluidics 2023.
- **Povilas Dumčius**. Conference speech. Dual-Wave Acoustofluidic Centrifuge for Ultrafast Concentration of Nanoparticles and Extracellular Vesicles
- **Povilas Dumčius**, Mikhaylov R, Zhang X, et al. A Flexible Printed Circuit Board Based SAW Device for Effective Concentration of Micro-particles. Acoustofluidics 2022.
- Roman Mikhaylov, Mercedes Stringer, **Povilas Dumčius**, et al. An Easy and Accessible Manufacturing Method for Reconfigurable SAW Devices. Acoustofluidics 2021.

*Mutual Co-Authors

"Quit. Don’t quit. Noodles. Don’t noodles…”

- Oogway

Chapter 1
Concentration of Bioparticles in Biomedicine

1.1. Introduction

Concentration, a fundamental aspect of scientific research and technological advancements, lies at the heart of transformative innovations in fields like gene therapy, proteomics, and human genome studies [1]. With its profound impact on diverse areas of research, concentration holds immense promise for unlocking a future filled with remarkable possibilities. Often overlooked, concentration plays a crucial role in enabling modern scientific breakthroughs. Dating back to the 1400s, the earliest documented use of centrifugal forces appeared in the form of hand-powered milk separators. This rudimentary technology paved the way for Antonin Prandtl's revolutionary approach to commercial milk processing using centrifugal separators in 1864 [2]. However, it was not until 1869 that centrifugation found its place in the laboratory setting. Swiss biologist Friedrich Miescher utilized this technique to isolate nucleic acids from white blood cells [3]. Gustaf de Laval subsequently introduced the first continuous centrifugal separator, thus enabling large-scale commercialization [3]. By the 1940s, centrifugation had become a staple in laboratories worldwide. Protocols from this era [4] detailing steps for collecting supernatant or sediment set the stage for many future scientific discoveries. From its humble beginnings, often demonstrated in school science experiments, centrifugation has evolved to play a vital role in contemporary research. Today's more sophisticated and efficient centrifuges permit researchers to separate and analyse samples with unprecedented precision. Innovations in centrifugation technology, including ultracentrifugation and density gradient centrifugation, have opened new avenues for isolating and purifying cells, nucleic acids, and other biomolecules. Propelled by humanity's insatiable curiosity about the human body, ground-breaking discoveries have forced us to delve into realms even smaller than cells [5]. However, conventionally induced forces often falter when applied to the small materials required for efficient analysis and disease discovery [6]. The burgeoning knowledge about nanomaterials has fuelled a growing demand for innovative separation and concentration technologies [7].

1.2. Cells

Embarking on a journey through the rich tapestry of the 17th century, we delve into the groundbreaking work of Robert Hooke, a pivotal figure whose microscopic observations

unveiled the cellular structure and laid the foundation for our understanding of bioparticles. Employing a newly developed scientific instrument—the microscope—Hooke meticulously examined a thin slice of cork, revealing a honeycomb-like structure filled with small compartments he termed "pores" or "cells" (See **Fig 1.1**). His groundbreaking observations, detailed in his 1665 book "Micrographia" [8], not only explained the buoyancy and springiness of cork but also hinted at a broader significance. His identification of the cellular structure laid the foundation for the subsequent exploration of cells as the basic units of life. Hooke's identification of the cellular structure inspired further inquiries into the microscopic world. Dutch scientist Antonie van Leeuwenhoek, a master microscope architect, expanded the horizon by detecting previously unseen organisms—bacteria and protozoa. Van Leeuwenhoek's meticulous observations, facilitated by his perfected simple microscope design, unveiled the existence of these tiny creatures, which he aptly named "animalcules." His insatiable curiosity led him to explore various specimens, including spermatozoa and dental plaque, documenting his findings in letters to the Royal Society

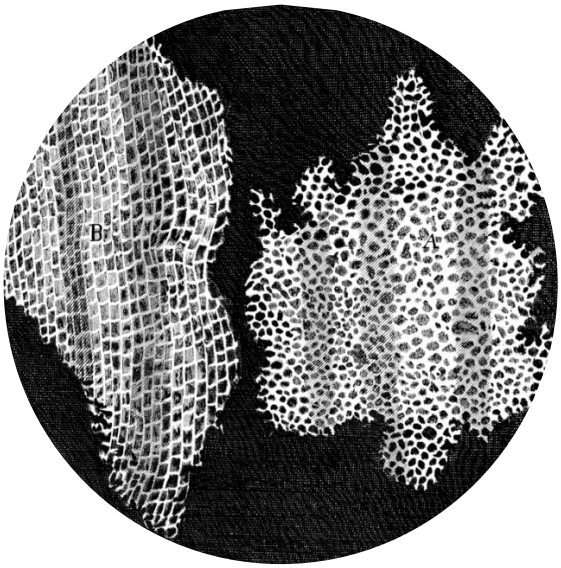

Figure 1.1. Robert Hooke's drawing of cells in a cork, 1665 [8].

The human body comprises approximately 37 trillion cells, as elucidated in earlier studies [9]. However, more recent investigations have refined this figure, indicating approximately 36 trillion cells in males and around 28 trillion cells in females [10]. Each cell's role and function are determined by its structure and specific purpose within the body. Just as musicians in an orchestra collaborate to create a captivating symphony, bioparticles within the human body communicate to orchestrate the intricate mechanisms that keep us alive. Individually, bioparticles have limited capabilities, but through communication and

cooperation, they form an efficient system capable of managing the human body's complexities.

Cells, the fundamental units of life, fall into two primary categories: prokaryotic and eukaryotic [11]. Prokaryotic cells are characterized by their simplicity. Unlike their eukaryotic counterparts, prokaryotic cells lack a true nucleus and membrane-bound organelles. Instead, the genetic material is found in a region called the nucleoid, floating freely within the cytoplasm.

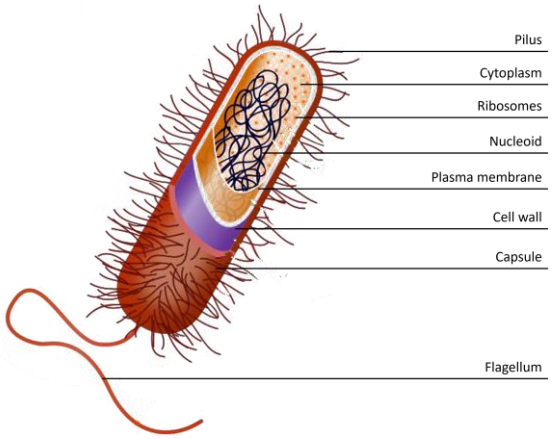

Figure 1.2. Procaryotic cell structure [12], [13].

Prokaryotes, which include bacteria such as Escherichia coli (*E. coli*), are generally smaller and structurally less complex (**Fig 1.2**) [13]. Despite this simplicity, they are incredibly diverse and have played a crucial role in shaping the Earth's ecosystems. Cells, whether prokaryotic or eukaryotic, are enclosed by a membrane dictating selective permeability and maintaining electric potential. The plasma membrane in animals is the outer limit, while plants and prokaryotes have a cell wall. The plasma membrane, a phospholipid bilayer, is crucial for maintaining cellular homeostasis and allows controlled substance passage. Within the membrane, the cytoplasm, dominating the cell's volume, is a semi-fluid material with a cytoskeleton (only in eukaryotic cells) supporting cellular structure. Microtubules, intermediate filaments, and microfilaments work together, contributing to cell shape, intracellular transport, and cellular motility.

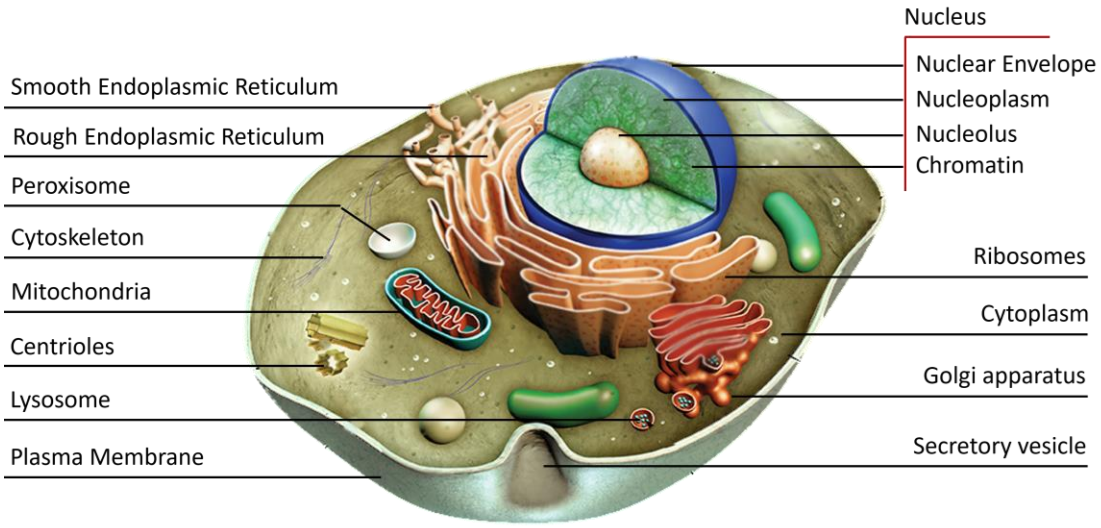

Figure 1.3. Eucaryotic cell structure [14], [15].

Eukaryotic cells (**Fig 1.3**) distinguish (**Table 1.1**) themselves through complexity and compartmentalization [14]. These cells possess a true nucleus, where genetic material is enclosed within a membrane. Additionally, eukaryotic cells feature a variety of membrane-bound organelles, each specializing in distinct functions [16]. For example, the Golgi apparatus processes and transports biomolecular materials, while mitochondria serve as the primary hub for cellular energy production. Peroxisomes specialize in detoxification processes, lysosomes function as centres for cellular waste disposal, and the endoplasmic reticulum intricately engages in synthetic activities. Ribosomes, integral cellular components, orchestrate the complex process of protein synthesis. Moreover, the centrosome plays a pivotal role in microtubule organization, particularly during specific phases of cell division.

Table 1.1 Differences between prokaryotic and eukaryotic cells [13], [14].

Characteristic	Prokaryote	Eukaryote
Nucleus	Absent	Present
Average Diameter	~1 µm	~10-100 µm
Cytoskeleton	Absent	Present
Cytoplasmic Organelles	Absent	Present
DNA Content	1×10^{6} - 5×10^{6}	1.5×10^{7} - 5×10^{9}
Chromosomes	Single Circular DNA	Multiple Linear DNA

1.3. Intercellular Communication

In the intricate tapestry of multicellular life, the orchestration of cellular activities relies fundamentally on the phenomenon of intercellular communication. As if part of an elaborate conversation, cells navigate a complex network of signalling pathways to exchange information, coordinate responses, and maintain the delicate balance of physiological processes. There are multiple ways that the cells communicate. For example neuronal communication [17] (shown in **Fig 1.4 a**) encompasses synaptic signalling, where neurons release neurotransmitters into the synaptic cleft, transmitting signals to target cells such as other neurons, muscle cells, or glands. This chemical communication is complemented by electrical signalling, where changes in membrane potential create electrical impulses, facilitating rapid and precise communication within the nervous system. Further phenomena, such as, direct communication [18] (shown in **Fig 1.4 b**) through gap junctions is exemplified in cardiac muscle cells. In the heart, gap junctions allow for rapid and synchronized contractions among adjacent cardiac muscle cells. This ensures the coordinated pumping of blood and is crucial for the overall efficiency of the heart's function. In contrast to direct communication, indirect communication relies on the release of signalling molecules into the extracellular environment. These molecules, often travel through the bloodstream or extracellular fluid to reach target cells, initiating a cascade of intracellular events. This mode of communication allows for the coordination of cellular activities over larger distances. Indirect communication can manifest in multiple forms of signalling, and it is not always beneficial. For example, autocrine signalling [19] (shown in in **Fig 1.4 c**) is characterized by cells producing signalling molecules that exert their effects on receptors located on the cell's own surface, thereby influencing the cell's activities. A notable example of this phenomenon is observed in cancer cells, where autocrine signalling is evident. In such cases, cancer cells produce growth factors that bind to receptors on their own surface, resulting in the stimulation of uncontrolled growth and proliferation. This self-stimulating mechanism contributes to the relentless expansion of cancer cells, eventually leading to tumours. Another noteworthy instance is endocrine signalling [20] (concept shown in in **Fig 1.4 d**), which involves the release of molecules, usually hormones, into the bloodstream by endocrine glands. An illustrative example is the pancreas, which releases insulin into the bloodstream. This insulin then travels to distant cells across the body, where it signals these cells to take up glucose. This process plays a crucial role in regulating blood sugar levels and maintaining proper energy balance within the organism.

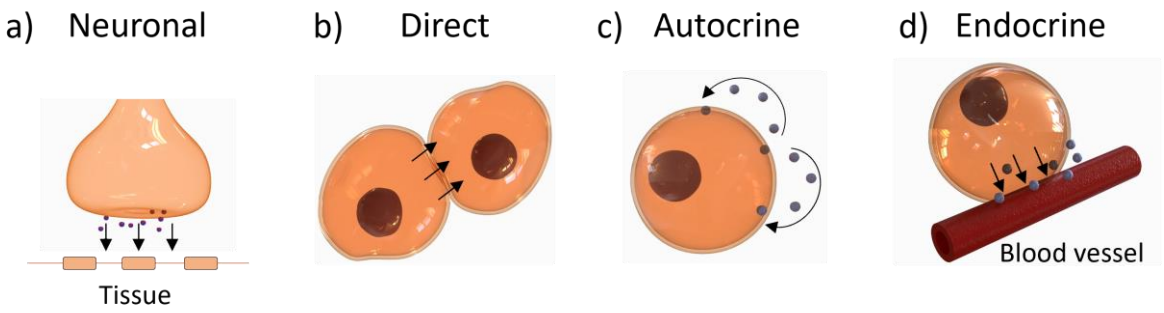

Figure 1.4. Intercellular communication. a) Neuronal, such as brain cells. b) Direct, such as cardiac muscle tissue. c) Autocrine signalling, such as cancerous tumour growths and d) Endocrine signalling found in themes such as, hormone release into the bloodstream. Dark brown is the nucleus, orange is the cell, and the small blue particles are vesicles [21].

Further, paracrine signalling shown in **Fig 1.5**, illustrates a pivotal mechanism in cellular life. In paracrine signalling, cells release signalling molecules into the local extracellular environment, and these molecules traverse the bloodstream or extracellular fluid to reach nearby target cells [22]. This method initiates a cascade of intracellular events, allowing for the coordination of cellular activities over larger distances. Examples of this intricate mode of communication include immune responses, tissue repair, and other physiological processes where local signalling plays a crucial role [23]. In paracrine signalling, cells release Extracellular Vesicles (EVs) that contain the signalling molecules, allowing for the transfer of information to neighbouring cells. The vesicles can fuse with the plasma membrane of target cells, delivering their cargo and affecting the cellular response [24]. This mechanism enables the communication between cells in proximity and plays a role in various physiological and pathological processes, including immune responses, tissue repair, and cancer progression.

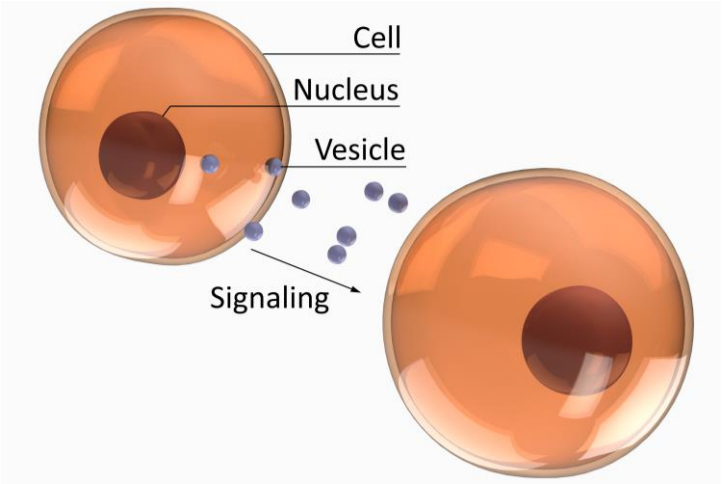

Figure 1.5. Paracrine communication, by cells secreting vesicles to transmit data [21].

In the subsequent discourse, due attention is accorded to the salient advent of EVs.

1.4. Extracellular Vesicles (EVs)

EVs, first discovered by Chargaff and West in 1946 [25], play a protagonist in immune regulation [26], [27] and the transfer of genetic material [28], [29], [30]. EVs carry a vast array of biomolecules such as proteins, RNAs, DNAs, lipids, and metabolites [24], [31], demonstrating considerable heterogeneity in size, content, and impact on recipient cells [23]. EVs have emerged as intriguing entities with significant clinical potential in various applications, including disease detection and drug delivery. EVs, small, membrane-bound structures released by cells (**Fig 1.6a-b**), are crucial in transmitting information between them. EVs play critical roles in transmitting signal-initiating elements and nucleic acids within the immediate pericellular space and over long distances [23] and are essential modalities for intercellular communication [32]. Such events contribute to homeostatic control of tissue environments [26] and orchestrate adaptive changes such as angiogenesis [33] and inflammation [34]. Body fluids, including blood, urine, saliva, and cerebral spinal fluid (CSF), contain EVs with important information about pathogenic processes, including metabolic and infectious diseases.

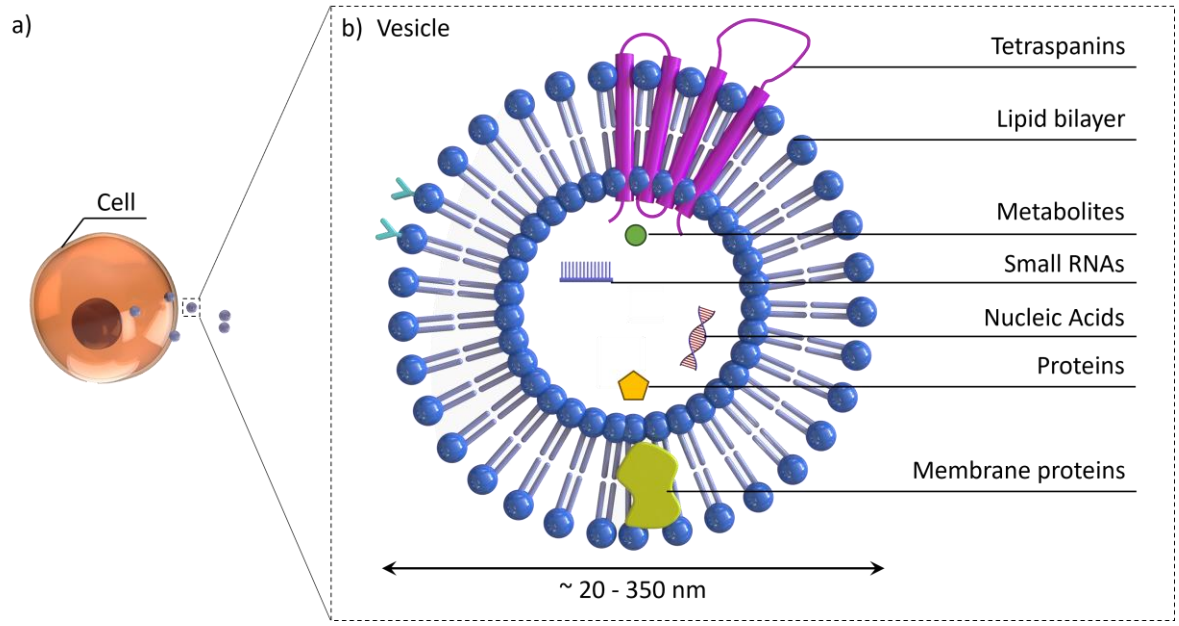

Figure 1.6. Simplified illustration of the EV structure, demonstrating a double phospholipid membrane equipped with specific EV proteins and containing DNA cargo [23].

EVs can be broadly classified into three main categories: apoptotic bodies, microvesicles, and exosomes [35].

Apoptotic bodies (500 nm - 2µm), the largest of the three, are released by cells undergoing apoptosis. Apoptosis progresses through several stages, first nuclear chromatin condensation, then nuclear splitting and the frequent appearance of micronuclei, then membrane blebbing and finally, splitting of the cellular content into distinct membrane-enclosed vesicles, termed apoptotic bodies or, more recently, apoptosome [35].

In contrast, healthy, live cells, showcase microvesicles that bud directly from the plasma membrane, have a 100–500 nm size and include cytoplasmic material [35]. Their biogenesis occurs via the direct outward budding and pinching of the plasma membrane releasing the nascent microvesicles into the extracellular space as shown in **Fig 1.7**.

Meanwhile exosomes, the smallest type, originate from endosomes within the cell. This typically involves three stages: biogenesis, intracellular trafficking, and fusion with the plasma membrane (See **Fig 1.7**). The formation of EVs starts with the inward budding of the plasma membrane, called endocytosis [36]. This early endosome then matures into a late endosome, which undergoes further endocytosis-like inward budding to create intraluminal vesicles (ILVs) (**Fig 1.7**) [37]. This results in the formation of a multivesicular body (MVB) within the cell. The MVB then transitions through the cytoplasm until it reaches the cell membrane. The outermost layer of the MVB fuses with the cell membrane, releasing its contents (ILVs) as membrane-enclosed vesicles, namely exosomes, into the extracellular space. [24]. It is worth mentioning that the formed MVBs are not limited by the secretion of vesicular components but can also be degraded by fusing with lysosomes [38] (**Fig 1.7**, yellow circle).

Once the EVs are released into the extracellular space, their fate is quite diverse. EVs can reach recipient cells and deliver their contents to elicit functional responses and promote phenotypic changes that will affect their physiological or pathological status.

For example, once the EV reaches a recipient cell, it will bind to the cell surface and can undergo various fates. Depending on the cell type, they can remain bound to the surface and can initiate intracellular signalling pathways (for example, antigen presentation) [38], also shown in **Fig 1.7**, (Surface Binding). Nonetheless, endocytosis or direct membrane fusion is one of the most commonly discussed mechanisms for a neighbouring cell to receive information [39], [40]. After the uptake, the process within the recipient cell begins with the formation of an early endosome and, subsequently, an MVB. This MVB is then transported near the nucleus, where the ILVs release their cargo, effectively completing the

communication process. The MVB in the recipient cell can also develop its own ILVs, and even fuse with its own membrane for re-secretion, finally the MVB within the recipient cell can also be degraded by fusing with the nearby lysosomes (See **Fig 1.7,** yellow circle). In essence, EVs act as dynamic messengers, orchestrating intricate chemical conversations by delivering precisely packaged cargo to recipient cells. They play a vital role in cellular communication, ensuring the targeted transmission of essential biochemical information.

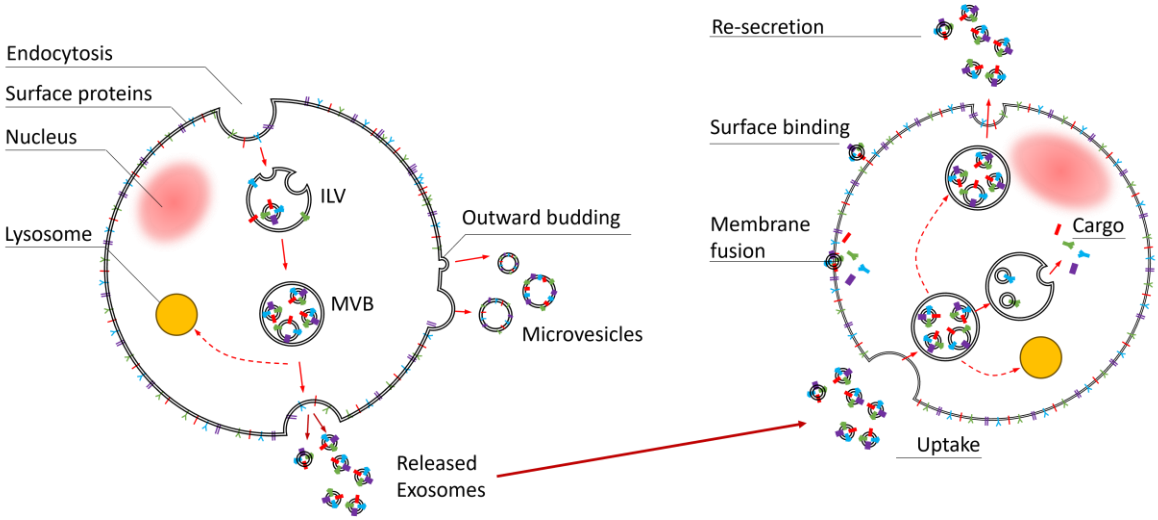

Figure 1.7. Simplified diagram illustrating extracellular vesicle (EV) (left) formation and uptake through endosomes, which progresses into a multivesicular body (MVB) containing intraluminal vesicles (ILVs). The MVB then moves towards the cell membrane, fuses, and releases exosomes into the extracellular space. Neighbouring cells absorb EVs through endocytosis, and the ILVs are further processed into proteins that reach the cell nucleus [23].

1.5. Importance of cell concentration & separation

The field of biology and biomedicine is built upon a deep understanding of cellular foundations, briefly introduced in the prior sections. It is evident, that biological sample preparation is a crucial step in various fields of biological research and diagnostics, including molecular biology, genomics, proteomics, and clinical diagnostics. Post-classical Latin employed the term *concentratio*, which means activity or an act of gathering at one location and bringing to a common centre, as early as 1550 [41]. Biological concentration refers to the abundance or density of specific molecules, cells, or substances within a biological system. The biological sample preparation process typically begins with the collection of the sample from its source, such as tissues, cells, bodily fluids, or environmental samples [42]. The procedure of bioparticle concentration varies in multiple degrees of freedom, such as time, equipment, complexity, morphology of the bioparticle and much more.

Accurate cell concentrations are paramount in clinical settings, influencing the precision of diagnostic tests and therapeutic interventions. Blood, a remarkable and intricate fluid, encompasses cellular components and plasma, each fulfilling unique functions, with Red Blood Cells (RBCs) being central to oxygen transport. Techniques like centrifugation (more in section 1.7) aid in separating RBCs for diagnostic purposes, enabling the assessment of their concentration and characteristics. [43]. This separation is particularly valuable in conditions like anaemia, where RBC concentration may be abnormal, providing essential diagnostic insights [44]. In addition, separating whole blood allows healthcare providers to administer specific blood components to patients in need. For example, a patient might need red blood cells to treat anaemia or platelets to assist with clotting disorders [45], [46]. In diseases like leukaemia, where abnormal, White Blood Cells (WBC) concentrations are typical, precise measurements are crucial for diagnosis and monitoring treatment effectiveness [47]. Furthermore, WBCs, integral to immune defence, demonstrate their importance in infection management. Monitoring the concentration and types of WBCs through diagnostic methods allows healthcare professionals to identify and assess immune responses [48]. By understanding the concentration and behaviour of WBCs, clinicians can gain valuable insights into the body's ability to combat infections and other immune-related challenges.

The significance of whole blood and its processing as a pivotal conduit for disease monitoring is hereby emphasized. The intricate separation of blood components in healthcare holds essential merit for diverse medical and research applications, facilitating in-depth study, precise diagnosis, and targeted treatment. [49].

Platelets, critical for clot formation, have concentrations that directly impact homeostasis. Analysing platelet concentration is vital in diagnosing clotting disorders. Furthermore, platelets contain high quantities of key growth factors, which can promote angiogenesis, matrix remodelling, and cell proliferation [50] therefore, the use of platelet concentrates to improve healing [51], [50], has been widely studied.

An additional noteworthy application pertains to the utilization of blood plasma, its composition and concentration of proteins, electrolytes, and hormones contribute significantly to overall health [52]. Serum, derived from plasma, is a key medium for diagnostic tests. Understanding the concentration of substances in serum, such as glucose or electrolytes, provides essential information about the body's metabolic state.

For example, miRNAs, a class of naturally occurring small noncoding RNAs, have recently been linked to cancer development [53]. It has been found that, that both serum and plasma harbour a substantial quantity of stable miRNAs originating from diverse tissues and organs

and that the expression profile of these miRNAs shows great promise as a novel non-invasive biomarker for diagnosis of cancer and other diseases [54].

Additionally, the concentration of waste products in plasma, such as urea and creatinine, reflects the efficiency of kidney function [55]. Their concentrations in the blood plasma are used for the screening of renal, kidney or cardiovascular disorders [56].

Another peripheral reason for concentrating cells is to maximize the signal-to-noise ratio in analytical techniques such as microscopy and molecular biology assays. The concentration of cellular constituents such as proteins, nucleic acids, or cellular organelles is raised by decreasing the sample's volume. This increased concentration makes it possible for scientists to identify and examine biomolecules and cellular structures more successfully, especially when working with rare or valuable samples [57].

In the realm of regenerative medicine, cell concentration is critical for optimizing cell densities. Achieving the desired cell density ensures the formation of functional tissues and improves the success of transplantation procedures. For example, it has been demonstrated that injection of the bone marrow-derived mesenchymal stromal cells (BMSCs) concentrates into the site of nerve transection in patients with facial nerve paralysis resulted in the improvement in eye closure and facial deviation in comparison with conventional surgical treatment [58].

Important to mention, cell washing is a fundamental procedure in biomedical and research contexts, involving the removal of unwanted substances from isolated cells to ensure the accuracy and reliability of subsequent analyses.

The concentration/separation applications of bioparticles are further extended, previously discussed organelles are essential biomarkers for diseases used by medical researchers and clinicians. Hence the concentration, purification and precise analysis is vital of such matter.

Previous reports informed that mitochondrial dysfunction was believed to be an important contributor to the pathogenesis of Alzheimer’s disease [59], [60]. Additionally, and interestingly, various conclusions have suggested that mid-life obesity is a risk factor for later-life dementia, Parkinson’s disease, and Alzheimer’s disease [61], [62], [63]. Specifically, obesity increases the risk of Alzheimer’s disease by 35% [64]. The mitochondrial organelles, therefore, are of high importance to be studied, which is rather unfeasible without the concentration, purification and preparator processes.

A deformed and enlarged nuclear morphology is a common characteristic of cancer cells, and the “roundness” of the nucleus is a good indicator to distinguish benign, low grade, and

malignant cells [65]. Therefore, abnormalities in nuclear structure or DNA content can indicate cancer or genetic disorders. In an exploratory case it has been found that certain nuclear lamina proteins are often absent (47%) in ovarian cancer cells and tissues [66]. It is evident that, the isolation of nuclei is indispensable in cancer research for studying genomic alterations, identifying genetic mutations, and assessing chromatin organization.

Dysfunction in lysosomal enzymes can lead to lysosomal storage disorders (LSDs) [67]. Concentrating lysosomes aids in studying enzyme activity and identifying lysosomal storage disorders, such as Tay-Sachs disease and Gaucher's disease [68]. Diagnostic tests often involve measuring enzyme levels or assessing lysosomal function.

Last, but not least, peroxisomes are self-replicating, single-membrane organelles harbouring enzymes that catalyse important cellular processes such as the detoxification of peroxides and fatty acids [69]. It has become clear that peroxisomes are involved in a variety of metabolic pathways, which implies the presence of many proteins in the peroxisomal matrix [70]. Dysfunction of these organelles can lead to peroxisomal disorders, including the Zellweger syndrome, with symptoms including, but not limited to craniofacial abnormalities, enlarged liver abnormal eyes, etc [71].

In essence, the concentration of cells and their organelles is essential in the existence and accuracy of diagnostics, the success of therapeutic interventions, and the advancement of scientific understanding. Relevance of Concentration & Separation not only ensures the reliability of medical procedures but also opens avenues research, diagnosis, and innovative treatments. In the vast landscape of healthcare and biological sciences, the significance of cell concentration resonates across disciplines, laying the foundation for precision medicine and transformative discoveries.

1.6. Importance of EV concentration & separation

EVs including exosomes can contain many types of biomolecules, including proteins, carbohydrates, lipids, and nucleic acids. This varies depending on the EVs origin, its physiological and pathological state, and even the precise cellular release site [24]. The protein composition within can also mark the existence of disease pathologies such as cancer or inflammatory diseases. The biogenesis of EVs offers a snapshot of a cell's life, reflecting the intracellular composition of the originating cell. Hence, the discovery of the role of EVs has led the researchers to explore their use as delivery vehicles of a variety of medicines. As exosomes are naturally formed and are involved in many biological and

pathological processes, they have garnered significant attention due to their potential clinical applications [72].

For example, a past study containing 27 patients diagnosed with lung adenocarcinoma and 9 control subjects were included [73]. The lung adenocarcinoma group exhibited a mean exosome concentration of 2.85 mg/mL, significantly surpassing the control group at 0.77 mg/mL ($P < 0.001$). The significant differences in total exosome levels between lung cancer patients and controls, alongside the similarity observed in circulating exosomal patterns and tumour-derived patterns, suggest the usefulness of circulating exosomes as a screening test for lung adenocarcinoma. Moreover, by examining the genetic material (RNA) of EVs) extracted from the serum, individuals with a specific brain tumour (glioblastoma) show notable changes in at least 121 genes [74]. This analysis enables the differentiation between healthy individuals and those with glioblastoma. EVs isolated from various bodily fluids have been found to contain specific mRNA, miRNA, and protein content related to the disease state for multiple cancer types, including pancreatic cancer [75]. Biomarkers carried by EVs have demonstrated the ability to differentiate between cancer patients and healthy individuals [61], through successful assays that quantified tumour derived EVs from as little as 1 µl of plasma, specifically pancreatic cancer EV biomarker that distinguished pancreatic cancer patients and healthy subjects. The molecular cargo within EVs, such as microRNAs, messenger RNAs, and proteins, reflect the disease status and serve as vital biosignatures for early disease diagnosis. For example, exosomes from liver cancer patients have a significantly higher tsRNA level than those from healthy controls, suggesting their potential as novel "liquid biopsy" biomarkers for cancer diagnosis [76]. Moreover, exosomes released from cancer cells are involved in cancer progression. Thus, data regarding the role of the exosomes in malignant cancer could lead to development of novel diagnostic and therapeutic methods [77]. In addition to their role in cancer detection, EVs can serve as biomarkers for mental disorders. Given their ability to cross the blood-brain barrier, exosomes might serve as indicators for neural dysfunctions [78],[79]. Not only the cargo EVs carry but also their numbers in plasma can be indicative of cancer and recurrence after therapy as demonstrated in patients with brain tumours such as Glioblastoma [80]. More specifically the mean concentration of EVs differs from 2×10^{10}, to 7×10^{10} EVs/mL in blood plasma in healthy and diagnosed patients respectively.

As exosomes are small and native to animals, they can avoid phagocytosis, fuse with the cell membrane, and bypass the engulfment by lysosomes. The fact that exosomes are a natural product of the body results in a low immune response [72]. Their natural ability to traverse biological barriers, such as the blood-brain barrier, and their inherent stability make

them attractive carriers for therapeutics. Researchers have explored various strategies to modify EVs, such as engineering their surface proteins or loading them with specific cargoes, including drugs, nucleic acids, or therapeutic peptides. An exosome-based delivery system has benefits such as specificity, safety, and stability. By their homing characteristic, exosomes can deliver their cargo to specific targets over a long distance. Exosomes can also be used to deliver interfering RNA or pharmaceutically active substances [81]. For instance, EVs derived from dendritic cells engineered to express rabies viral glycoprotein (RVG) have been successfully used to deliver siRNA across the blood brain barrier [82]. In more detail, the direct injection of siRNA without encapsulation led to noticeable, but not significant changes. In contrast, modified exosomes with encapsulated siRNA demonstrated a substantial (50.2% ± 9.1%) and targeted delivery to the brain [82]. The use of EVs as drug delivery vehicles holds immense potential in areas such as cancer therapy, regenerative medicine, and treatment of neurological disorders, offering a novel approach that may improve drug efficacy, reduce side effects, and overcome barriers associated with conventional drug delivery systems [83]. For example, high transfection efficiency has been shown, when utilizing targeting exosomes for effective siRNA delivery to both cancer and cancer stem cells [84]. This approach, particularly for lung cancer and cancer stem cells, shows potential as a versatile gene delivery platform in cancer therapy. Furthermore, the potential future of regenerative medicine is hinted at by studies utilizing exosomes for targeted delivery. Specifically, in rats suffering from osteoarthritis, enhanced results in improving cartilage regeneration have been shown [85]. The therapeutic potential of exosomes is also being explored for stroke, Traumatic Brain Injury (TBI), and other neurological disorders, with several preclinical studies showing promising results with both native and engineered exosomes [86], [87]. This list could encompass numerous additional applications, such as the treatment of glioma, tumour-targeted small RNA delivery, and selective brain tumour treatment, among others [88]. The importance of these applications, underscored by a substantial body of research conducted in the past decade, is expounded upon in this section. The field of targeted drug delivery is depicted as a relatively nascent area with considerable prospects. Nevertheless, at present, it is deemed sufficient.

EV significance whether in regenerative medicine, drug delivery or diagnosis, renders a crucial step which is their processing and how they are acquired or at what quantities administrated. Efficient and standardized exosome isolation methods are crucial for clinical use. However, challenges persist due to the complexity of biological fluids, the lack of specific exosomal markers, and the presence of similarly sized particles. Distinguishing pure exosomal fractions is difficult, hindering effective isolation [89].

In essence, EVs stand as biomedical keystones, unravelling crucial biomarkers for disease comprehension. Concentrating EVs proves pivotal for diagnostic strides, personalized healthcare, and groundbreaking therapies. However, challenges in isolation methods and biological fluid complexity necessitate advanced technologies for optimal purity. The crux of future research lies in refining EV processing, heralding a new era in precision medicine and transformative breakthroughs.

1.7. Concentration & Separation Technologies

Having emphasized the importance of the cellular constituents and EVs, with their respective functionalities, scholarly emphasis pivots toward the methodologies employed for the concentration and processing of these bioparticles. In its essence, four primary assets of bioparticles have been exploited for their separation and purification [90].

1.7.1. Centrifugation

A force experienced by an object due to gravity on Earth is often referred to as g [91]. This phenomenon is briefly illustrated in **Fig 1.8a**, where particles suspended in liquid are experiencing earth's gravity and sedimenting overtime. Subsequently, one of the first physical exploitations for separation and concentration of the bioparticle is directly related to its mass. Although there are a few instances of the use of the earth's gravitational field alone to effect for separation of biological particles (e.g., RBCs will separate into layers of erythrocytes and leukocytes after standing on the bench for 1-2 h [1]), for effective, streamlined, and smaller bioparticle manipulation (i.e., organelles) earths gravitational force is simply insufficient.

To achieve greater g forces, the medium with the suspended particles is rotated around a fixed axis (**Fig 1.8b)**, in a machine called centrifuge. The particles will experience radial centrifugal force, translating them further away from the rotating axis. Any object, whether it is a cell or an organelle, is subjected to a centrifugal force [1] when it is rotated at a certain speed. The centrifugal force (F_c) is expressed as:

$$F_c = m_p \omega^2 r \qquad 1.1$$

Where m_p, ω^2 and r, are the mass of the particle, angular velocity, and the distance of the particle from the axis of rotation.

Different centrifuges may have different rotor sizes, rotation speeds, and radii. Therefore as a standardization protocol, the magnitude of the force generated is normally expressed

relative to that of the earth's gravitational force and is known as the relative centrifugal field (RCF) or *g-force* [1]. Mathematically described as:

$$RCF = \frac{F_c}{g} = \frac{m_p \omega^2 r}{m_p g} = 11.18r\left(\frac{RPM}{1000}\right)^2 \quad 1.2$$

while the **Eq 1.1** grants the force exerted on an object in a rotating frame, the RCF provides a dimensionless measure that allows for standardization and comparison of centrifugal forces, making it easier to communicate and reproduce experimental conditions.

Although essentially two different types of centrifuges exist, swinging bucket (SB) and fixed angle (FA) [92], here the principles are briefly introduced using the SB centrifuge illustrated in **Fig 1.8.** The RCF at the r_{max} (**Fig 1.8b**) is quite often used by manufacturers to determine the maximum g forces in their products. However, in most experimental protocols the use centrifugal force in terms r_{av} (**Fig 1.8b**), provides a more practical and standardized way to communicate and replicate experimental conditions [92]. Full derivation, sedimentation rate & rotor length as well as the rotor angle importance are treated in better detail in [92]. Such classification of radii proves efficient when choosing the right rotor and speed for a particle is crucial. A k-factor (derived in Ref [92]) gauges the pelleting efficiency of a rotor at maximum speed, helping determine the time 't' (in hours) for EV sedimentation using various rotors.

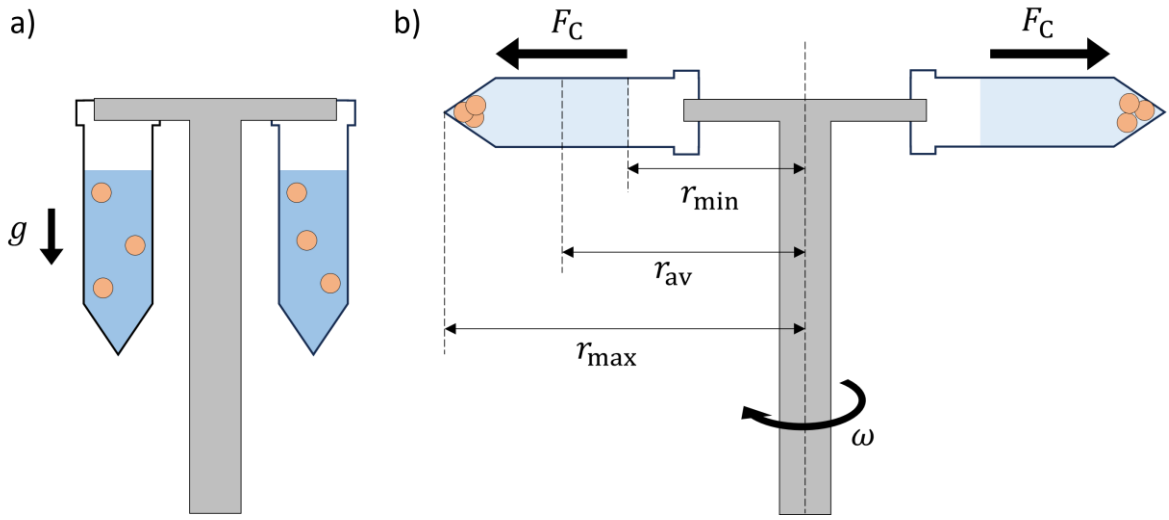

Figure 1.8. Principles of a centrifuge. a) A swinging bucket centrifuge with no angular force applied. The particles will sediment due to the forces of gravity. b) The swinging bucket centrifuge will apply a centrifugal force to the particles, decreasing the sedimentation time [93].

Centrifuges are not merely just rotating tubes, with additional functionalities existing such as acceleration and deceleration. Abrupt alterations in RPM can induce the formation of vortices

in the liquid due to the Coriolis effect, resulting in the mixing of the sample. This phenomenon is less pronounced in the straightforward pelleting of particles; however, its impact becomes noticeable when centrifuging whole blood to pellet erythrocytes. In such cases, if the rotor comes to a sudden halt, the erythrocytes are observed swirling up into the plasma supernatant [1].

Additionally, heat is generated by friction in the spinning rotor and produced by the motor, hence there is a tendency for the temperature of the rotor (and the sample) to rise with time. Some centrifuges (high-speed and ultra) requires refrigeration, because of the increased heat generation at the higher speeds of these machines and these are frequently used for prolonged periods in which the sample must be maintained at 0-4°C [1].

According to **Table 1.2** [1], centrifuges are traditionally classified into three groups giving to the maximum speed they can achieve (measured in rounds per minute or RPM)

Table 1.2. Classification of centrifuges based on their relative rotation speeds [1].

Class	max RCF (g)	RPM
Low-speed centrifuges	8000	7000
High-speed centrifuges	$40\,000 - 50\,000$	$21\,000$
Ultracentrifuges (UCs)	$+50\,000$	$+21\,000$

Low-speed centrifuges are used to harvest chemical precipitates, intact cells (animal, plant, and some microorganisms), nuclei, chloroplasts, large mitochondria, and the larger plasma-membrane fragments. High-speed centrifuges are used to harvest some microorganisms, viruses, mitochondria, lysosomes, and peroxisomes. Ultracentrifuges (UC) are used to harvest all membrane vesicles derived from the plasma membrane, endoplasmic reticulum and endosomes, ribosomes, ribosomal subunits, plasmids, DNA, RNA, and EVs. The exemplary SB centrifuge in **Fig 1.8a-b**, demonstrates a single particle affected by the earth gravity and RCF upon rotation respectively, which leads to the build-up of the pellet at the bottom as the suspended object are pushed away by F_c. However, laboratory sample processing commonly encompasses samples comprising multiple particles that vary in size, heterogeneity, density, and morphology. In addition, occasionally the bioparticles of interest such as organelles are inside the cell and must be released prior to their isolation. There exists a wide range of protocols for such practice and are extremely diverse and application based. To maintain a level of focus of the thesis, a brief introduction to the different procedures is offered. Differential centrifugation [94] is a straightforward method employed

to selectively separate, concentrate, and manipulate diverse bioparticles. It is also treated as the current golden standard for exosome isolation. In **Fig 1.9a**, a probing sample displays a variety of bioparticles with distinct morphologies. The underlying principle of differential centrifugation involves carefully selecting the right RCF to concentrate the objects into a pellet, whose mass 4is most affected by that specific centrifugal force. In this scenario, the desired particles are EVs which are the smallest in the sample. Although protocols, sample handling, resuspension medium, rotors size etc, do vary [95], most methods embrace four centrifugation steps [89]: initial steps involve two rounds of centrifugation: 10 minutes at 300 g, followed by another 10 minutes at 2000 g. This effectively precipitates cells, cell debris, and large vesicles (**Fig 1.9b-c**, yellow & red circles respectively). The subsequent step, a 30-minute spin at 10,000 g, separates exosomes from non-exosomal vesicles, typically larger than 100–150 nm (**Fig 1.9d**, green circles). Finally, exosomes are isolated in the last step through centrifugation at 100,000–150,000 g for 1–6 hours (**Fig 1.9e**, blue circles).

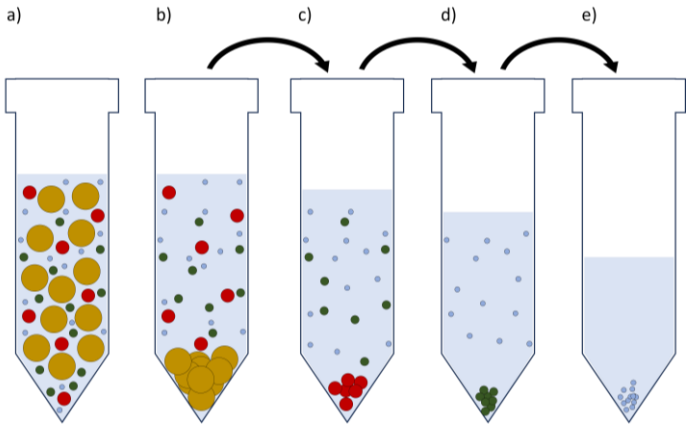

Example Particle	Size	Reference colour	References
Cells/Debris	4-12 µm	Yellow	[1], [86], [96]
Mitochondria	0.4-2.5 µm	Red	
Lysosomes	0.4-0.8 µm	Green	
EVs	0.05 – 0.4 µm	Blue	

Figure 1.9. Differential Centrifugation. a) The sample is first loaded into a test tube. b) The first phase of centrifugation removes cells, cell debris, and larger particles. c) The supernatant from the first phase is transferred into a new tube, and the d) process repeats until e) the particles of interest are separated. [89], [94].

Differential centrifugation presents advantages in effectiveness but faces limitations. It struggles with resolving particles of similar sizes and densities, risks contamination through

co-pelleting, and encounters challenges in separating particles with slight density variations [89]. Additionally, the high g forces applied during centrifugation can potentially damage EVs, altering their morphology and functional properties. The method proves unsuitable for extracting exosomes from small biomaterial amounts, and its drawbacks include labour intensity, cost and processing times that could take days to complete the process and hours if just considered the EV centrifugation step alone. Additionally, the efficiency is influenced by temperature and liquid viscosity, demanding individual adjustments to standard protocols. Density gradient centrifugation, in contrast to differential centrifugation, addresses the limitations posed by particle size and offers several advantages. This method efficiently separates particles of different sizes simultaneously in a single centrifugation step. The process involves loading the sample in a thin band atop a buffer solution with a preformed concentration gradient, gradually decreasing from the tube's bottom to the meniscus. The gradient itself could be formed from sucrose or more recently from iodixanol. The iodixanol gradient is isotonic at all concentrations used and, therefore, vesicles retain their shape and size when moving in the density gradient, which significantly increases separation efficiency. Subsequent high-speed centrifugation subjects the sample to approximately 210000 g for approximately 16 h, causing particles to move through the density gradient [89]. The particles sediment based on both their size and density. The critical point is reached when a particle's environmental fluid density matches its own, causing it to stop, and overtime form a distinct band or pellet. Careful collection of different fractions allows the isolation of particles based on their specific density. This method ensures higher purity in isolating specific fractions with minimal contamination, compared to differential centrifugation.

In essence, although centrifugation is effective for cells and microparticles, the recovery of extremely small bioparticles like EVs remains a complex and arduous task [95]. The manipulation of EVs (nano-sized materials) poses a considerable challenge, even with the highest RCFs applied through an ultracentrifuge. Furthermore, this difficulty in handling nano-sized materials raises concerns about the accuracy and completeness of isolating such particles using ultracentrifugation techniques [95]. The inherent challenge lies in the fact that enhanced gravitational field methods affect objects with varying masses and densities in distinct ways. Particularly, particles in the nanometre size range exhibit slower sedimentation, necessitating extended processing times of up to eight hours [94], [97]. The nanoparticle concentration process itself is intricate, labour intensive, involving multiple steps and despite their effectiveness, is time-consuming [94], [98], [99]. Specialized equipment, including gradient-forming and ultracentrifugation devices, is indispensable for successful implementation, contributing to the overall complexity of the method. Additionally,

the ultracentrifugation method institutes challenges such as compromised vesicle integrity and documented issues of sample impurity in some cases as low as 33%. [100], [101], [102]. In conclusion, ultracentrifugation does not meet the standards required for clinical applications, mainly due to the low achievable exosome purity, yield, integrity, expensive infrastructure and the lengthy processing time [103].

1.7.2. Ultrafiltration

Due to the strong cargo significance of nanoparticles, many methods are being developed, to address the current limitations regarding the centrifugation methods [103]. Another, example which also exploit the size physical properties is ultrafiltration. Ultrafiltration is often combined with UC, replacing a few of lower speed rounds of spinning in the UC method with filtration [104]. As shown in **Fig 1.10** a Nano-porous membrane with the typical pore size ranging between 0.8 and 0.1 µm is used to filter a suspension of bioparticles which are sorted out based on their sizes [104], [105], [106]. Following this step, the standard UC protocol continues. Compared to the standalone UC methods, ultrafiltration has shown a higher purity (5-folds higher compare to UC) of isolated exosomes as well as less time consumption (1–2 h) [107]. Nonetheless, trapping bioparticles in nanopores can cause clogging issues which result in low recovery rates [103]. Furthermore, due to the high forces applied to bioparticles as they pass through nanopores, high shear stresses can be generated which may change the morphology of EVs or even cause lysis. The disadvantages of this technique are the possibility of exosome deformation and contamination with fluid components smaller than the pore size of the filter. In addition, some exosomal vesicles can be absorbed on the membrane, resulting in the loss of some exosomes, which is significant for isolation from small volumes of fluids.

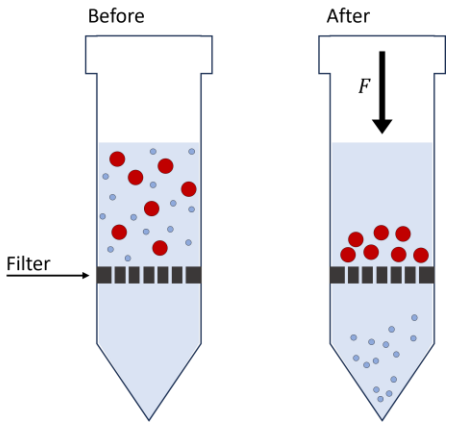

Figure 1.10. Ultrafiltration is demonstrated by first loading a sample into a test tube. Upon applying pressure force (F), the particles are forced downwards and through the filter. The smaller particles can penetrate, leaving larger ones behind [104].

1.7.3. Size Exclusion Chromatography

Size exclusion chromatography (SEC) is another size-based purification technique that is also known as “gel filtration [103]. SEC [108] (**Fig 1.11**) has attracted extensive attention as a more tractable approach for biomolecule separation, retaining structurally intact vesicles at relatively low concentrations and can efficiently isolate EVs with a diameter larger than 70 nm from platelet-free supernatant of platelet concentrates [109]. SEC separates biomolecules according to their hydrodynamic radius. The stationary phase consists of spherical porous particles (beads, dashed circles in **Fig 1.11**) with a carefully controlled pore size, through which the biomolecules diffuse based on their molecular size difference using an aqueous buffer as the mobile phase [110]. In other words, upon deposition of a sample into a medium containing bead, particles smaller than the pores of the beads gain entry and are temporarily trapped. Conversely, larger particles are excluded and readily flow through the medium. This trapping phenomenon results in a distinctive separation of particles during their descent. Consequently, smaller particles take a longer time to reach the bottom, causing larger particles to emerge first. SEC is shown to be a viable technique for obtaining purified exosomes free of albumin in a recent study comparing UC and SEC for exosome purification. However, it should be noted that this method is superior in the context of separation as it cannot provide highly concentrated samples due to the dilution of the sample which is critical in SEC operation. In addition, SEC is a time-consuming method, but capable of providing pure exosome isolations [111].

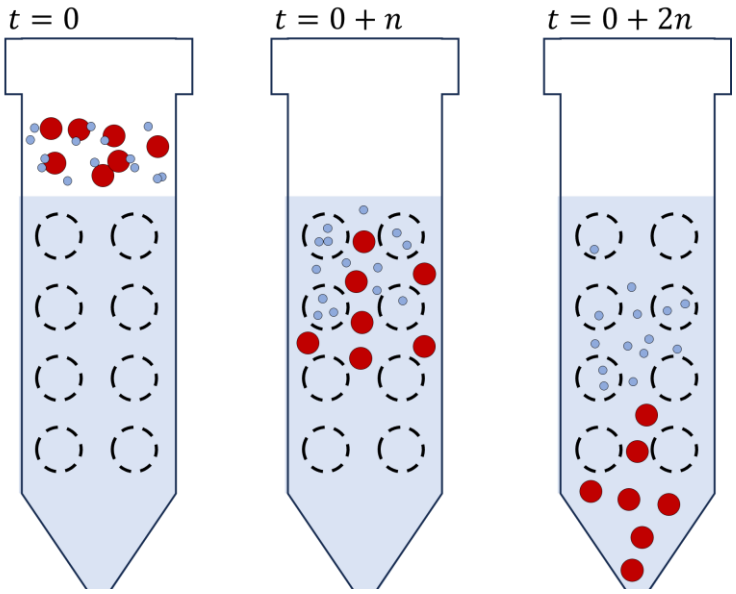

Figure 1.11. Size Exclusion Chromatography: At $t = 0$, the sample is loaded onto the column. As time progresses ($t = 0 + n$), particles sediment down, passing through porous beads. Smaller particles can enter and become temporarily trapped, taking a longer time to travel down. Finally, after ($t = 0 + 2n$), some more time elapses, and the larger particles exit first, followed by the smaller ones, essentially separating them [108].

1.7.4. Polymer-based precipitation

The separation and purification of bioparticles have been facilitated through the exploitation of four primary assets. Previously mentioned were density and size-based separation methods. Additionally, another crucial aspect of bioparticle exploitation lies in their functionality [105]. More specifically, the chemical characteristics of the surfaces of the bioparticles are crucial to the separation process in such methods. Polymer-based precipitation is an alternative method that uses a polymer to separate exosomes from other particles in the sample [103]. Polyethylene glycol (PEG) is one of the most often utilized polymers for this purpose. This polymer makes it possible to precipitate exosomes from a cell culture supernatant in an inexpensive, simple, and equipment-free manner, which facilitates the efficient isolation of exosomes. [112]. These polymers are added (shown in **Fig 1.12**) and saturate the solution by binding with water molecules, which causes less soluble substances like exosomes to precipitate. These target molecules can be precipitated and then sedimented using filtration or low-speed centrifugation (1500 g) to proceed with further steps. Commercial exosome precipitation kits are widely available in the market and are advertised to be compatible with various body fluids such as breast milk [95]. However, the main drawback of this method is the co-precipitation of non-exosomal components such

as proteins, which leads to a lower efficiency of exosome isolation and an extended processing time of up to 12 hours [113].

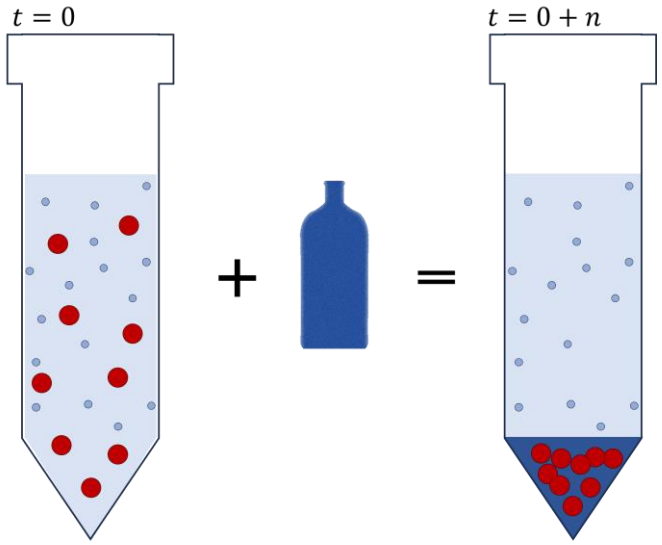

Figure 1.12. Polymer-based precipitation for exosome isolation. PEG is introduced into the solution at $t = 0$ and through passage of time, binding with water molecules and causing less soluble substances like exosomes to precipitate. Although it may co-precipitate non-exosomal components, impacting the isolation efficiency and extending processing time (up to 12 hours) [112].

1.7.5. Immunoaffinity-based.

Each type of EV has specific proteins on its surface which interact with their specific antibodies, peptides, or polysaccharides. More specifically, standard exosomal surface markers include CD9, CD41, CD63, and CD81 [114]. EVs can be isolated by immobilizing these antibodies on various surfaces such as magnetic beads, plates, chromatography matrices, and microfluidic platforms [103], [115]. Immunoaffinity chromatography is a process in which the binding affinity of an antigen to a parent antibody is utilized as a basis of separation [116]. The antibody specific to the protein of interest is immobilized onto a rigid solid support to yield an active immunosorbent **Fig 1.13a**. A complex mixture of proteins is then passed over the immunosorbent whereby the antibody captures the protein of interest, and the other not necessary proteins are washed away in the column fall through (**Fig 1.13b**). As shown in **Fig 1.13c**, the reversible interaction between the antigen and antibody can be disrupted (i.e., changes in medium pH) to yield a highly purified product in the column eluate [117].

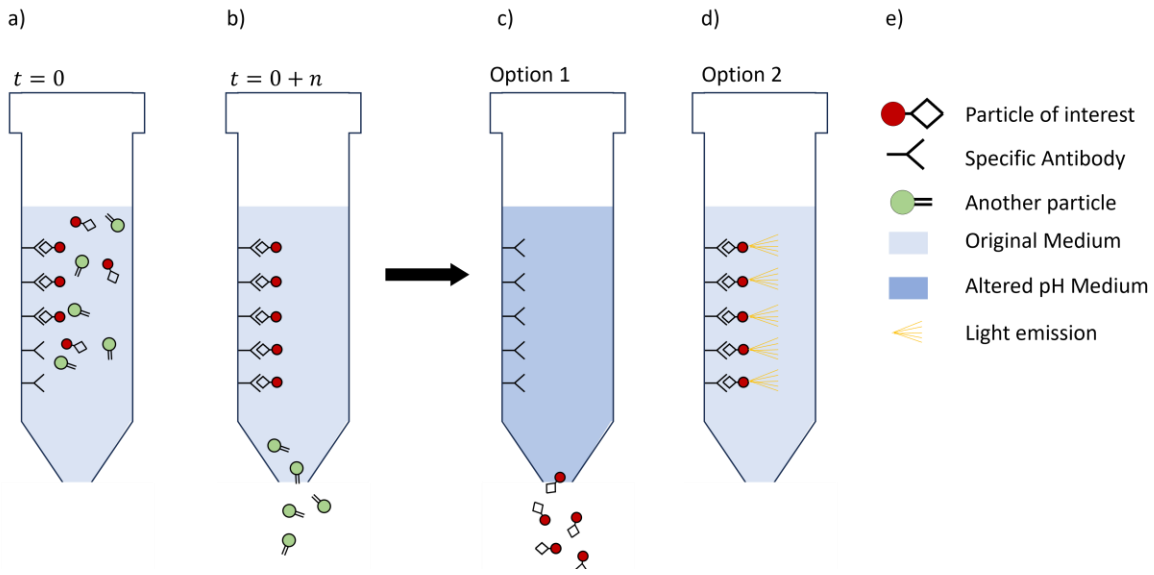

Figure 1.13. Immunoaffinity Chromatography method for EV isolation. (a) The active immunosorbent is created by immobilizing the specific antibody onto a solid support, in this case, the left side of the tube. (b) A complex protein mixture is passed over the immunosorbent, where the antibody captures the protein of interest (red), while unnecessary proteins (green) are washed away. After capture, there are a few options. The first is (c) by disrupting the reversible antigen-antibody interaction, the EVs can be released, or (d) captured particles can be further stained with a fluorescent dye for quantification [116].

In the pursuit of advancing analytical methods for EVs, SEC studies have demonstrated promising outcomes through the analysis of EVs directly on the chip without extraction. A device in this effort is called ExoChip, wherein a serum sample is introduced [118]. In the ExoChip, bioparticles within the sample traverse the chip, and during this transit, antibodies selectively capture EVs while permitting the uninterrupted flow of plasma with other types of bioparticles. An innovative departure in this method lies in the subsequent step, where EVs, still on the chip, undergo fluorescent staining and subsequent quantification [118]. Such and similar devices, however, suffer from low throughput due to the single-channel and limited lifespan of the microfluidic chips, which are typically shortened due to blocking or clogging [119]. Furthermore, large quantities of biological samples cannot be processed. And not so obvious fact, however, the cells herein aren't necessarily concentrated, rather highlighted.

1.7.6. Field Fractionation (FF)

Field fractionation (FF) techniques separate particles suspended in a fluid sample using what is called a "field," where under the action of the field, different particles move at different rates. The field used for the separation depends on the instrument; it can be a gravitational field, electric field, a centrifugal field, a thermal gradient, a magnetic force, and so on [120], [121]. While this method is not necessarily a pure concentration protocol, it is still very valid in terms of separation from the other bioparticles [122]. While it has a high separation resolution and can separate EV sub-populations, it requires multiple procedures and the processing time is up to 10 hours [122]. An example of fluid field is given in **Fig 1.14**. In short, particles within a fluid pass a long channel, bordered by semi-permeable membranes (dashed line, **Fig 1.14**). In a field such as fluid, a perpendicular flow is introduced across these membranes (cross flow, **Fig 1.14**), inducing a gradual drift in the particles traversing the channel. As particles flow along the chamber the crossflow separation field pushes the molecules towards the bottom of the channel. Once they reach the bottom, they diffuse back into the channel against the carrier flow. The magnitude B_{M} (indicated as arrows, **Fig 1.14**) to which the molecules can diffuse back into the channel is dictated by their natural Brownian motion, a characteristic based on size that is unique to each individual species. Smaller particles have a higher Brownian motion than larger ones and are able to diffuse higher into the channel against the cross flow [123]. This nuanced distinction in particle movement serves as a critical factor in the process, allowing for the selective manipulation and separation of particles based on size.

Flow field fractionation (FFF) method has been used for sorting subpopulations of EVs from culture media of cells and tumours with high resolution [105], but the tedious sample-preparation procedure compromises its throughput. One significant drawback is the complexity and high instrumentation cost associated with FFF systems. The initial investment and ongoing maintenance expenses can be substantial, potentially limiting its accessibility for smaller laboratories. In terms of resolution, FFF may face limitations in separating very small particles (nanoparticles) compared to alternative techniques like size exclusion chromatography (SEC). Finally, the sensitivity of FFF to operating conditions, such as flow rates and temperature, is another consideration. Maintaining consistent conditions is crucial for reproducible results [124].

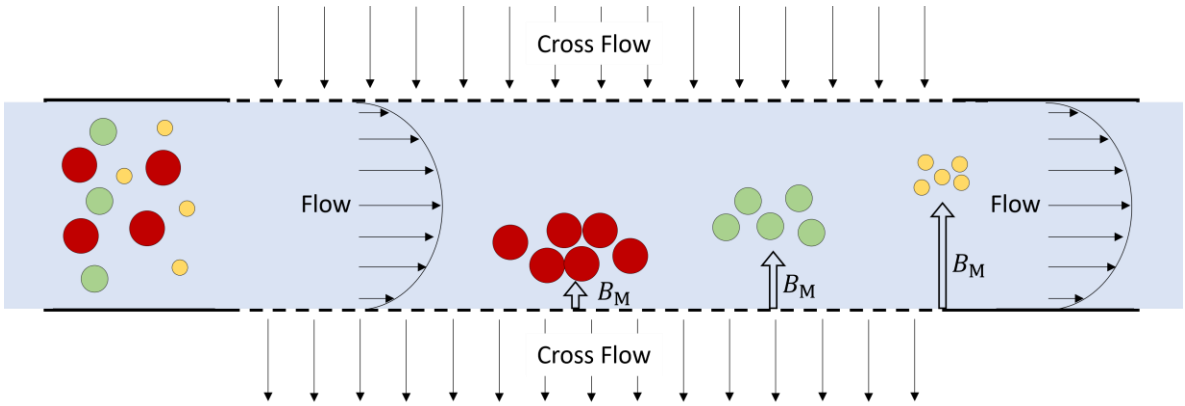

Figure 1.14. Field-Flow Fractionation method. Particles within a fluid pass through a long channel bordered by semi-permeable membrane (dashed line). A crossflow induces a gradual drift in particles, pushing them towards the bottom of the channel. The Brownian motion (B_M) allows particles to diffuse back into the channel against the carrier flow, with smaller particles exhibiting higher diffusion. As the time and flow passes the particles are separated [105].

1.7.7. Dielectrophoretic

Dielectrophoresis (DEP) is a phenomenon that manifests as a force acting on a dielectric particle exposed to a non-uniform electric field [125]. Despite not necessitating particle charge, dielectrophoretic activity is inherent to all particles in the presence of electric fields. The intensity of this force, however, is markedly influenced by factors such as the medium and electrical properties of particles, their shape and size, and the frequency of the applied electric field [125]. As a result, fields at a specific frequency can selectively manipulate particles. Dielectrophoresis has numerous medical applications as biological cells exhibit dielectric properties [126]. In biological applications dielectrophoretic technologies span across a wide field of applications, including, but not limited to trapping, detection, focusing and pairing [127]. However, the focus here is maintained to separation or concentration techniques. While DEP phenomena can be used in many ways for reference DEP integration in field fractionation is given. Here the field is applied in terms of electrodes with high voltage across them. In **Fig 1.15** the first section of the device has two interdigitated electrode arrays at top and bottom of the channel, which focus the particles into the centre of the channel by negative DEP. The second section contains a single electrode array, which differentially pulls the focused particles from the fluid flow by positive DEP, separating them into distinct bands [121]. The creators of the device claim a flow rate of 1 ml/hour, and empirical data showing that THP-1 cells were successfully captured on the electrode array [121].

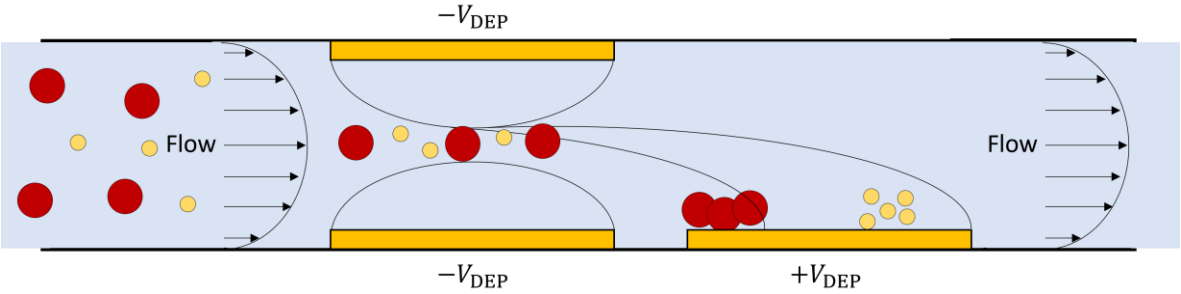

Figure 1.15. Dielectrophoretic Field-Flow Fractionation (DEP-FFF) system. The first section utilizes interdigitated electrode arrays to focus particles into the channel centre through negative $-V_{DEP}$ DEP, while the second section employs a single electrode array for positive $+V_{DEP}$ DEP, exposing the particles to a non-uniform electric field separating particles into distinct bands [121].

In another instance, integrated microfluidic-dielectrophoretic platform [128] utilizes DEP forces to trap SERS-active silver nanoparticles on-demand, enabling rapid detection of physiologically relevant methamphetamine concentrations in saliva. This robust, reusable assay provides label-free detection without requiring reagents or aggregation-inducing agents and are compatible with complex biological samples like saliva, with sensitivity down to 20 nm and results visible in under two minutes.

However, due to the drawback that dielectrophoretic mechanism is not compatible with high-ionic-strength biological fluids, in vivo applications based on current nanomaterials manipulation and assembly face significant challenges. Future research efforts might be looking into the possibility of solving this problem [129]. Nonetheless, the DEP technology should be used carefully for bioparticle manipulation, because the electric field and the Joule heating effect have a negative effect on bioparticle viability [130]. The bioparticle survival rate in the high electric field is very low, so DEP is only suitable to manipulate cells for a short period of time [127]. Therefore, a DEP chip that is more friendly to bioparticles is yet to be developed. In addition, the added complexity in parameters such as medium conductivity, and unpractical dilutions of the sample, yields these methods very application, particle and medium specific.

1.7.8. Acoustic

In recent years, acoustofluidic techniques, a fusion of acoustic and microfluidic principles, have emerged as a transformative solution in biomedical research, particularly in clinical diagnostics and therapeutics [131]. Operating on a label-free basis, these techniques leverage the differential effects of acoustic streaming and radiation forces on suspended particles, allowing precise separation based on size or physical properties. Notably,

acoustofluidic systems can handle particles, cells, and organisms with gentleness, ensuring the integrity of biological samples [131]. Additionally, manipulation of bioparticles through acoustophoresis [132],[133] has gained significant attention due to its biocompatibility, ease of use, high efficiency, and low cost [131], [134], [135]. As the field of acoustic separation techniques continues to develop, it may offer new and promising options for the isolation and analysis of EVs. Acoustic techniques offer a distinct advantage in manipulating small volumes, a critical aspect in sample processing for tasks like EV separation or concentration. This advantage becomes particularly pronounced when compared to conventional methods like differential centrifugation, which struggle when dealing with low-volume samples.

In essence, acoustic techniques leverage sound to manipulate particles. While this may seem straightforward, these methods can be categorized in various ways, with some of the most notable involving practices like droplet or microfluidic channel integration. In concentration processes, a droplet (**Fig 1.16 a, i**), when exposed to a specific sound wave, can be compelled into rotation, leading to the subsequent concentration of suspended particles (**Fig 1.16 a, ii**). For separation techniques, a sample can be guided through a precisely tuned microfluidic channel (refer to **Fig 1.16 b**). By selecting the appropriate power voltage and frequency, the sample can be separated from smaller suspended objects. This is primarily attributed to the fact that smaller objects are minimally affected by the sound wave, whereas larger ones experience a more significant influence.

The repeated emphasis on smaller objects being less affected by sound serves as a pivotal rationale for exploring acoustofluidic techniques further. Despite the relatively standardized nature of cell manipulation, the increasing benefits of acoustofluidic techniques are not fully realized by particles such as EVs. This discrepancy highlights an important avenue for research and underscores the unique challenges and opportunities within the field.

Furthermore, given acoustics' capacity for concentration, separation, and, in certain instances, particle differentiation, these phenomena hold the promise of eventual comprehensive integration, paving the way for the development of sophisticated bioparticle manipulation devices.

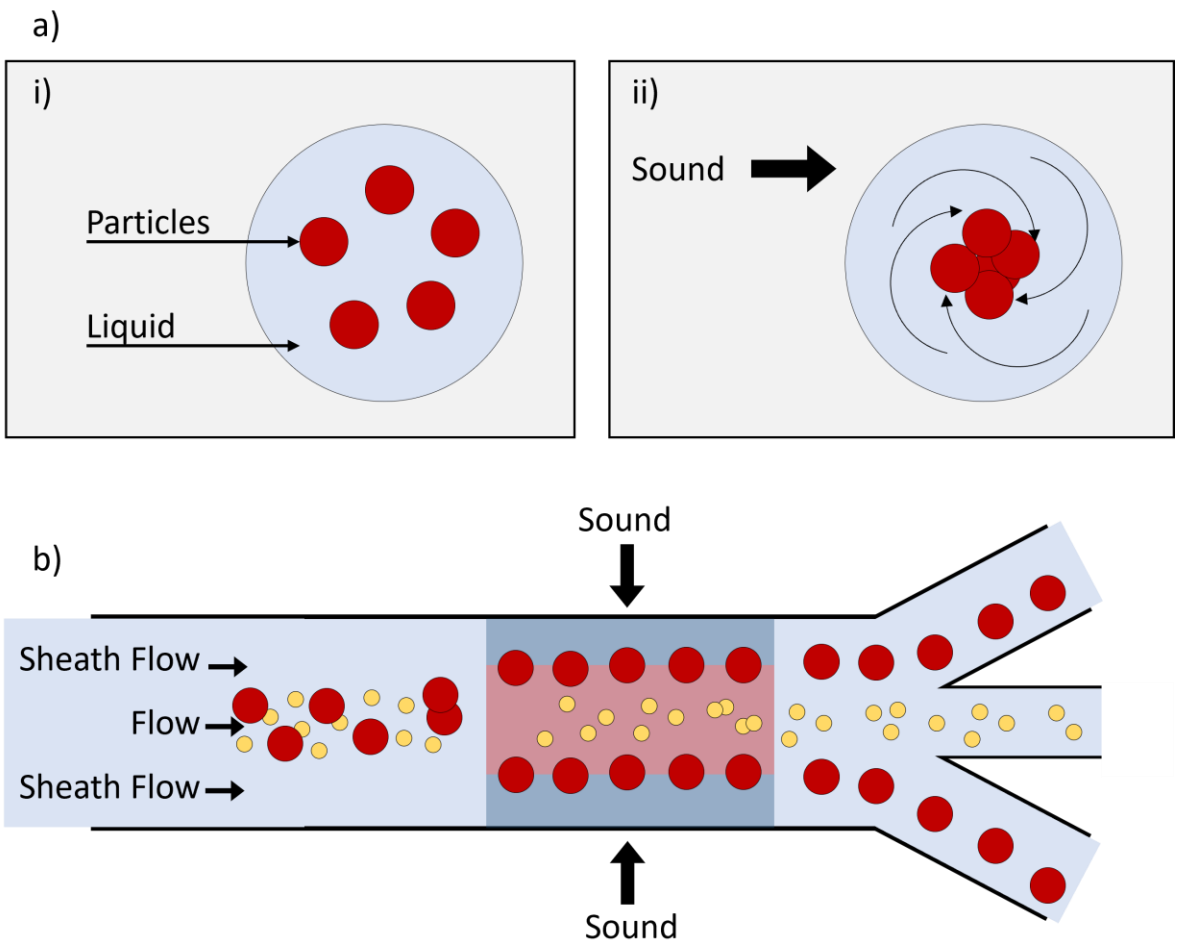

Figure 1.16. Simplified fundamental acoustofluidic techniques. For concentration processes (a, i), a droplet exposed to a specific sound wave can be compelled into rotation, leading to the concentration of suspended particles (a, ii). For separation techniques (b), a sample is guided through a microfluidic channel, enabling separation from smaller suspended objects by selecting the appropriate power voltage and frequency of the applied sound waves [131], [134], [135].

1.8. Conclusions

The evident importance of cells and EVs is highlighted through the exploration of their concentration and separation processes, revealing pivotal roles in diagnostics, therapeutics, and scientific advancements. However, challenges in isolation methods underscore the need for continued research and technological advancements to fully unlock the potential of these biomedical keystones. In the realm of EV concentration and separation, exosomes take centre stage as crucial biomarkers for diseases and potential drug delivery agents. The narrative, however, grapples with the current limitations of exosome isolation methods [136]. Ultracentrifugation, while dominant, falls short in efficient clinical applications due to issues

like low purity, yield, integrity, and lengthy processing time (4-12 h). Ultrafiltration, leveraging nanoporous membranes to filter bioparticles based on size, offers promising advantages such as higher purity and less time consumption (2-3 h) compared to standalone ultracentrifugation. However, challenges like clogging, shear stresses causing deformation or lysis, and the risk of exosome loss highlight the need for refinement. Size exclusion chromatography (SEC) emerges as a viable technique for purified exosomes but lacks the concentration ability and presents long processing times. Polymer-based precipitation kits, though widely available, suffer from co-precipitation of non-exosomal components, impacting efficiency and prolonging processing time. Immunoaffinity-based methods, while effective, encounter limitations in throughput and scalability. In addition, to the ~3 h processing times, it experiences limited availability of robust capture antibodies, additional washing and preparation steps needed, may lose the full functionality of exosomes after elusion. Flow field-flow fractionation (FFF) displays high resolution but compromises throughput due to a tedious sample preparation procedure, coupled with complexity and high instrumentation costs and processing times around 24 h. In the landscape of bioparticle manipulation, acoustofluidic techniques emerge as a revolutionary force for clinical diagnostics and therapeutics. Operating label-free, these methods utilize acoustic principles to precisely separate particles based on size or physical properties. With unmatched gentleness, biocompatibility, ease of use, and cost-effectiveness, acoustofluidic systems excel in comparison to traditional methods like differential centrifugation. Key strengths include the manipulation of small volumes, addressing critical aspects of tasks such as EV separation. By leveraging sound waves to selectively influence particles, acoustofluidics offer transformative potential, promising comprehensive integration and marking the future frontier in bioparticle manipulation for advanced biomedical applications.

1.9. Research Objectives

This PhD research aims to advance the field of nanoparticle manipulation by addressing key challenges in acoustic manipulation. The primary focus is to enhance the limits of sample volume, nanoparticle size, and processing time. The goal is to develop a practical and scalable manufacturing solution that is accessible and affordable. The research aims to design and prototype a compact device capable of efficiently manipulating nanoparticles, with the potential for future commercialization. Additionally, the study will explore strategies to improve the throughput of acoustic techniques and refine the size of manipulated nanoparticles. A significant aspect of the research involves the development of an ultrafast acoustofluidic centrifuge for extracellular vesicles (ACEV) as a proposed solution to

overcome existing limitations. The ACEV device will employ dual-wave modes to generate specific acoustic waves for precise manipulation within a liquid droplet. The desired outcome is to achieve efficient concentration of nanoparticles, contributing to potential advancements in rapid concentration of EVs. The research aims to demonstrate the ACEV's capability to induce visible aggregation and produce EV pellets within a minute’s timeframe. Ultimately, the goal is to make notable progress in the field of nanoparticle manipulation, with broad implications for various scientific and medical applications.

Chapter 2
The Science of Acoustofluidics

2.1 Introduction

Throughout history, waves have captivated the human imagination in various forms, from mesmerising water patterns to the harmonious melodies produced by musical instruments. The ancient Greeks and philosophers, recognising the significance of sound, constructed amphitheatres as early as 500 BC (**Fig 2.1**) to manipulate and experience the sound waves [137]. Pythagoras and his followers were among the first to conduct scientific investigations on the nature of sound, exploring the relationships between string vibrations and the resulting sound they produce [138]. After a considerable gap in sound research, Galileo Galilei revived the study of sound. In his final published book, he drew parallels between sound waves and the motion of water waves, rekindling scientific interest in the field [139]. Marin Mersenne defined a vital terminology concept of sound in his book *Harmonicorum Libri* [140] as follows:

"*All movements that occur in the air, in water, or elsewhere, can be called sounds, inasmuch as they lack only a sufficient delicate and subtle ear to hear them…*".

Mersenne also accurately predicted the speed of sound by measuring echoes [141]. In 1660, Robert Boyle conducted ground-breaking experiments on the effects of reducing air pressure, further advancing our understanding of sound [142]. Later in 1687, inspired by the work of the past, Isaac Newton published an extensive explanation of sound wave mechanics in his book "*The Principia*" [143].

In modern times, advancements in physics have deepened our understanding of wave phenomena, enabling us to harness their power for various practical applications and enhance our comprehension of the natural world. Waves can be observed not only in sound but also in other realms. They can be identified in the propagation trajectories of celestial bodies, ocean waves, wind patterns, and even the tiny ripples on the surface of a pond. Notably, light and electricity are also waves that constantly surround us. Fundamentally, a wave is a vibration, disturbance, or change in a medium. Sound waves were among the first waves recognised by humans to possess these properties. In this chapter, we explore the applications of sound waves in the field of acoustofluidics. Acoustofluidics involves the interaction between mechanical waves, such as sound, the liquids encountered, and any

objects immersed within the liquids. This field delves into the fascinating interplay between mechanical vibrations and the fluids they propagate through, enabling the manipulation of particles, cells, and fluids in a precise or chaotic fashion, a process known as acoustophoresis. To fully grasp the principles underlying acoustofluidics, it is essential to understand the fundamentals of wave propagation and the characteristics of different types of sound waves. As sound waves propagate through a fluid medium, they create pressure points that can be harnessed to manipulate particles, cells, and fluids with precision or in a more chaotic manner. This process is known as acoustophoresis. To fully comprehend the principles underlying acoustofluidics, it is essential first to establish a solid understanding of the basic concepts of waves.

Figure 2.1. The great theatre of Ephesus is a splendidly preserved and imposing building built around 50-100 AD. It is located in Ephesus, an ancient city in modern-day Selçuk, Turkey Fiel. This structure, made of marble, has a width of 145 meters, and its audience once reached up to 30 meters. In its heyday, it could accommodate up to 24,000 spectators [137].

2.2 Vibrations and Waves

Vibrations, the oscillations or movements of objects or particles, play a fundamental role in numerous scientific and technological domains. Understanding the behaviour and characteristics of vibrations is paramount for various applications, including manipulating and controlling fluids, cells and EVs.

There are two major types of vibrations: whole medium and surface. Whole medium refers to the transmission of waves through the entirety of the medium, as illustrated in **Fig 2.2**. When a sound wave source is applied along the x-axis (red arrow) in a solid medium (**Fig 2.2a**), it generates a longitudinal wave (**Fig 2.2b**). Longitudinal waves are characterised by

the parallel vibration of the medium in the same direction as the travelling wave. In these waves, the medium's contents (molecules/particles) move back and forth along the same axis as the wave. This motion creates compressions, where contents are close together, and rarefactions, where contents are spread out. Longitudinal waves can propagate through both solids and fluids, and they are also referred to as compressional or compression waves due to the compression and rarefaction effects they produce. In acoustofluidics, longitudinal wave vibrations are better known as bulk acoustic waves or BAWs [144].

In transverse waves, the crests and troughs result from the alternating displacements of particles in the medium perpendicular to the wave's direction of propagation. As the wave travels, the particles move upwards and reach their maximum displacement, forming the crest. Subsequently, the particles move downwards and achieve their maximum negative displacement, forming the trough. This continuous oscillation of particles perpendicular to the wave's direction creates a distinctive pattern of crests and troughs in a transverse wave. Transverse waves can occur in either the horizontal **Fig 2.2c** or vertical **Fig 2.2d** direction, depending on the orientation of the wave and the medium in which it propagates.

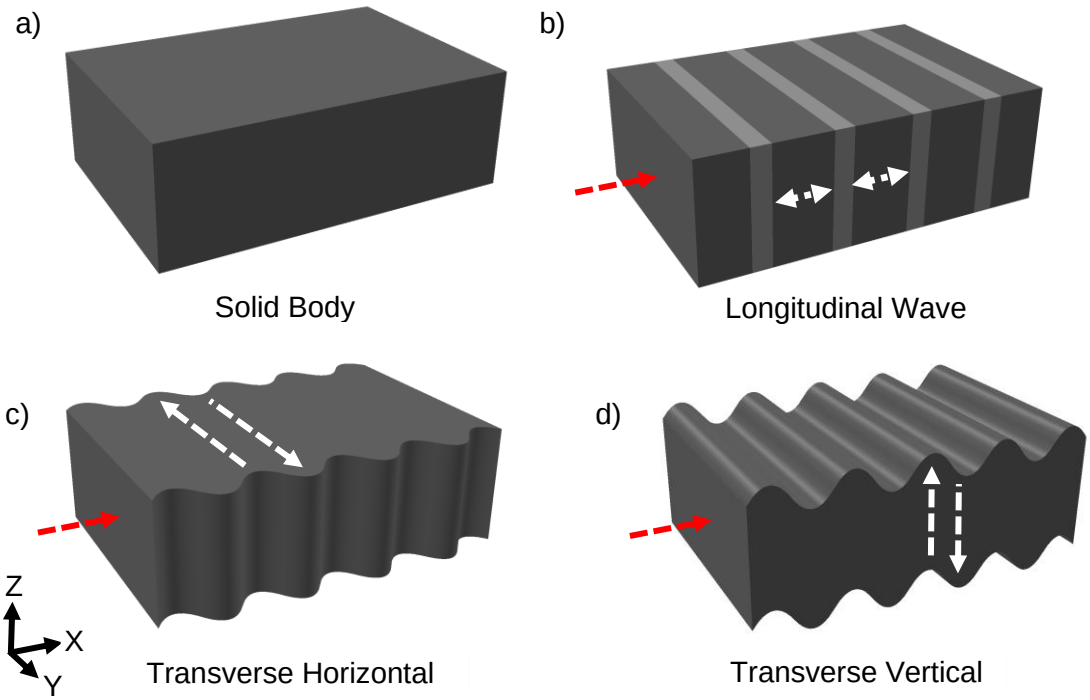

Figure 2.2. Various types of propagating body waves. a) Steady-state solid body without any force external force exposure, b) External force is introduced along the X-axis (red arrow), generating longitudinal waves that contract and expand in the X direction (white arrow). c) Horizontal

transverse waves with amplitude in the Y direction (white arrow) d) Vertical transverse waves with amplitude in the Z direction (white arrow) [144].

The second type of wave propagation was first proposed by Lord Rayleigh in 1885, namely the surface acoustic waves (SAW) [145]. These waves are split into Rayleigh (R-SAW) and shear (SH-SAW).

Rayleigh waves exhibit a distinct behaviour characterised by vertical oscillations in the z-axis while propagating along the x-axis, as depicted by white arrows in **Fig 2.3a**. The propagation of Rayleigh waves induces a vertical displacement of particles or molecules in the medium near the surface. This displacement leads to a wave pattern concentrated in the surface's vicinity. Due to the circular displacement pattern, Rayleigh waves are often described as having a "rolling" or "wave-like" motion. As the wave propagates along the surface, the particles, or molecules in the medium move in elliptical orbits (**Fig 2.3a**, green orbit), with the ellipse's major axis aligned perpendicular to the wave's direction of propagation. This circular motion gives the impression of a rolling wave, similar to the activity observed in ocean waves.

Unlike Rayleigh, shear waves (SH-SAWs) propagate along the x-axis and induce deformation in the y-axis, as depicted by white arrows in **Fig 2.3b.** SH-SAWs involve horizontal displacements of particles or molecules in the medium, occurring parallel to the surface. These waves are characterised by tangential or shear displacement and do not exhibit a vertical displacement component like the Rayleigh waves [146].

Lamb waves, named after the British mathematician Horace Lamb [147], are a type of surface acoustic wave that exhibit unique characteristics. They are generated when the amplitude of a wave is larger than the thickness of the material through which it propagates, resulting in a wave that extends throughout the entire thickness of the material. Lamb waves can propagate in both isotropic and anisotropic materials, and they have two modes of propagation: symmetric and asymmetric.

In the asymmetric mode (**Fig 2.3c**), the displacements of particles or molecules in the medium are non-uniform and have both vertical and horizontal components. This mode of Lamb wave propagation creates an asymmetrical wave pattern that exhibits displacements above and below the surface.

In the symmetric mode (**Fig 2.3d**), the particles or molecules in the medium undergo uniform displacements in the vertical direction, perpendicular to the material's surface, similar to Rayleigh. This mode of Lamb wave propagation creates a symmetrical wave pattern that oscillates above and below the surface [148].

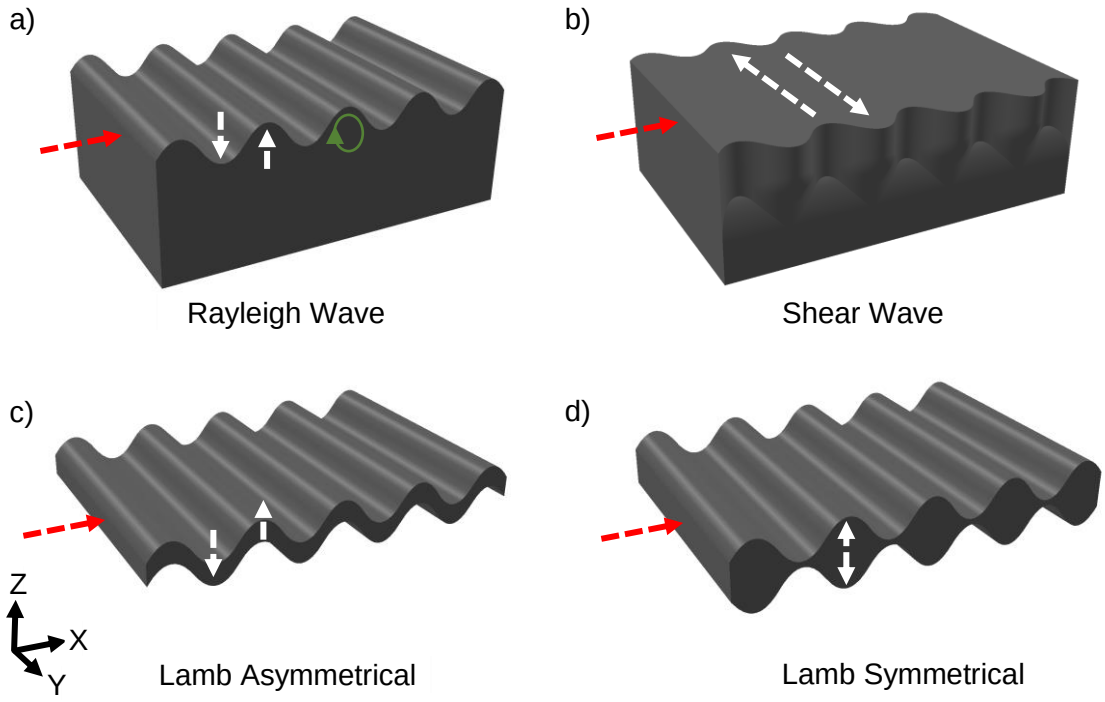

Figure 2.3. Various types of surface acoustic waves a) Rayleigh waves featuring amplitude in the Z direction (white arrow) and b) shear horizontal (SH) waves with amplitude in the Y direction (white arrow). Both Lamb waves exhibit amplitude in the Z direction, with one expanding c) asymmetrically and the other d) symmetrically [146], [147], [148].

2.3 Wave Properties

Waves and vibrations are ubiquitous and come in diverse forms and sizes, permeating all matter in our surroundings. Some waves can be seen, some can be sensed, and some heard. Despite their varying classifications, whether by wave mode or shape, all waves share fundamental characteristics, including amplitude, frequency, phase, velocity, and wavelength. Furthermore, all waves exhibit the ability to reflect, diffract, interfere, and transfer energy. In essence, a wave can be described [149] as:

$$y(x,t) = A\sin(k_{\mathrm{w}}x \pm \omega t \pm \theta_{\mathrm{w}}) \tag{2.1}$$

$$k_{\mathrm{w}} = \frac{\omega}{c} = \frac{2\pi f}{c} = \frac{2\pi}{\lambda} \tag{2.2}$$

$$\lambda = \frac{c}{f} \tag{2.3}$$

where A, k_{w}, x, ω, t, θ_{w}, λ, c and f represent amplitude (Pa), the wavenumber (rad/m), position (m), angular frequency (rad / s), time (s), phase (radians), wavelength (m), speed

of sound (m/s) and frequency (Hz). The displacement over time of a wave is described by **Eq 2.1**, where the amplitude determines the strength of wave propagation, and the medium's conductive ability (density) affects wave velocity. **Eq 2.2** reveals the relationship between wavelength (λ) and the medium's properties governed by parameter c, which is critical in designing sound wave actuators for acoustofluidics. **Fig 2.4a-b** demonstrates how a travelling wave changes in space over time, with constant wavelength and amplitude, when the wave encounters no obstacles or experiences diffraction into a different medium. The sinusoidal motion of a wave represents low and high acoustic pressure regions, as shown in **Fig 2.4c**, where longitudinal wave propagation of sound in air is present. When the wave reaches its highest amplitude $A+$, the air particles compress, and when the amplitude is $A-$, the particles disperse. This oscillation of air particles causes sound waves to travel. Wave propagation velocity can vary depending on medium density. For example, in water, the medium is denser; thus, the sound speed is around four times faster than air.

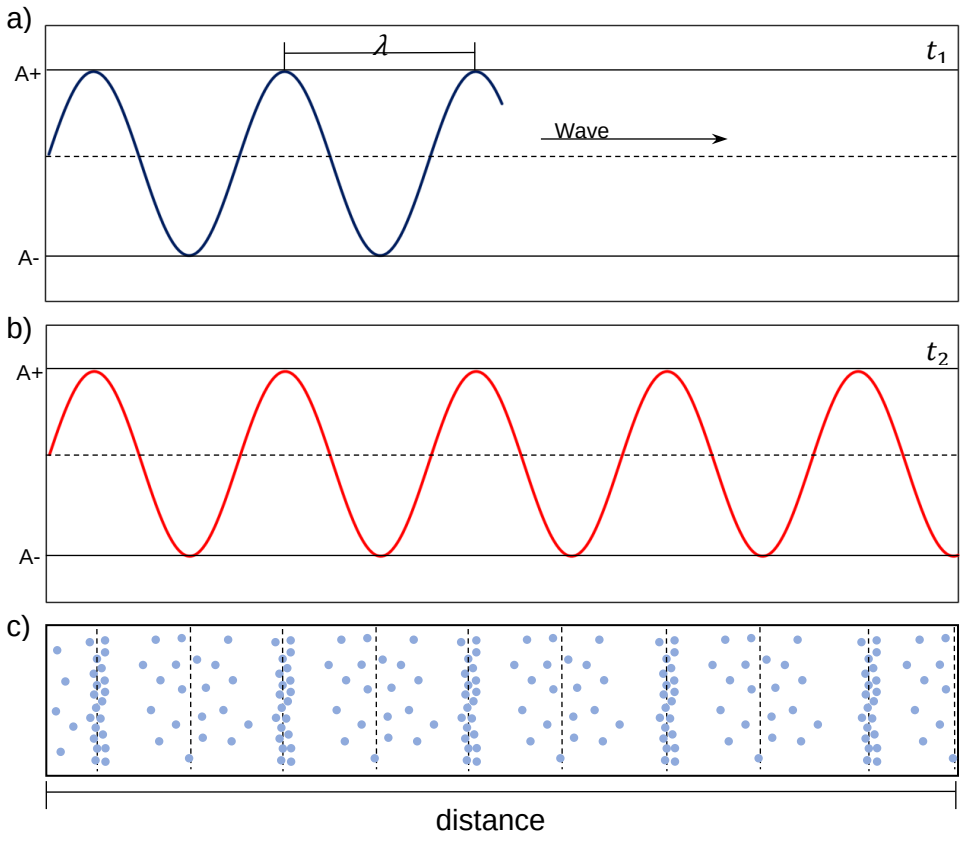

Figure 2.4. a) Sound wave depicted in the spatial domain at a specific time, t_1. b) Representation of the same wave after some time passes at t_2. c) representation of air molecules compressions and rarefactions resulting from a travelling wave.

2.4 Superposition

Wave superposition is a fundamental principle in wave theory that holds great significance in the field of acoustofluidics. When multiple waves intersect, their combined effect is determined by the alignment of their peaks and troughs. This concept of wave superposition becomes especially relevant in acoustofluidic systems, where identical counterpropagating waves interact. At time stamp t_1 (**Fig 2.5a**), two travelling waves before they intersect are shown. Each wave exhibits its distinct shape and amplitude. As these waves approach each other, their interaction becomes significant.

At time stamp t_2, the two waves are misaligned (**Fig 2.5b** top), leading to destructive interference where the peaks and troughs of one wave do not align with those of the other. As a result, the waves tend to cancel each other out, resulting in a weakened wave (**Fig 2.5b** bottom). Complete destructive interference occurs when the amplitudes of the two waves are equal, causing them to interfere destructively and eliminate the wave entirely. However, even if the amplitudes are not equal, destruction still occurs to some extent. This phenomenon highlights the intricate nature of wave interactions and emphasises the importance of amplitude alignment in determining the degree of wave cancellation.

Now, let us examine the scenario at the time stamp t_3. Here, the two waves are perfectly aligned (**Fig 2.5c** top), meaning that the peaks of one wave align with the peaks of the other, and the troughs align as well. If the amplitudes are exact, constructive interference occurs, doubling the intensity of the wave (**Fig 2.5c** bottom). This phenomenon illustrates the concept of wave reinforcement.

Over time, nodes and antinodes emerge counterpropagating waves of the same frequency continue to overlap. Nodes represent points along the wave where the amplitude reaches zero, while antinodes correspond to points of maximum amplitude. The formation of nodes and antinodes arises due to the time-averaged effects of the overlapping waves. Remarkably, despite the ongoing collision and interference between the counterpropagating waves, the resulting wave pattern appears to remain stationary, giving rise to standing wave phenomena. This observation underscores the fascinating nature of wave superposition and its ability to create intricate patterns and stationary regions within a dynamic wave system.

Understanding wave superposition, interference, and the formation of nodes and antinodes is vital for designing and operating acoustofluidic systems. By controlling the alignment of waves and utilising constructive or destructive interference, manipulation of particle motion, fluid flow, and other essential processes can be achieved.

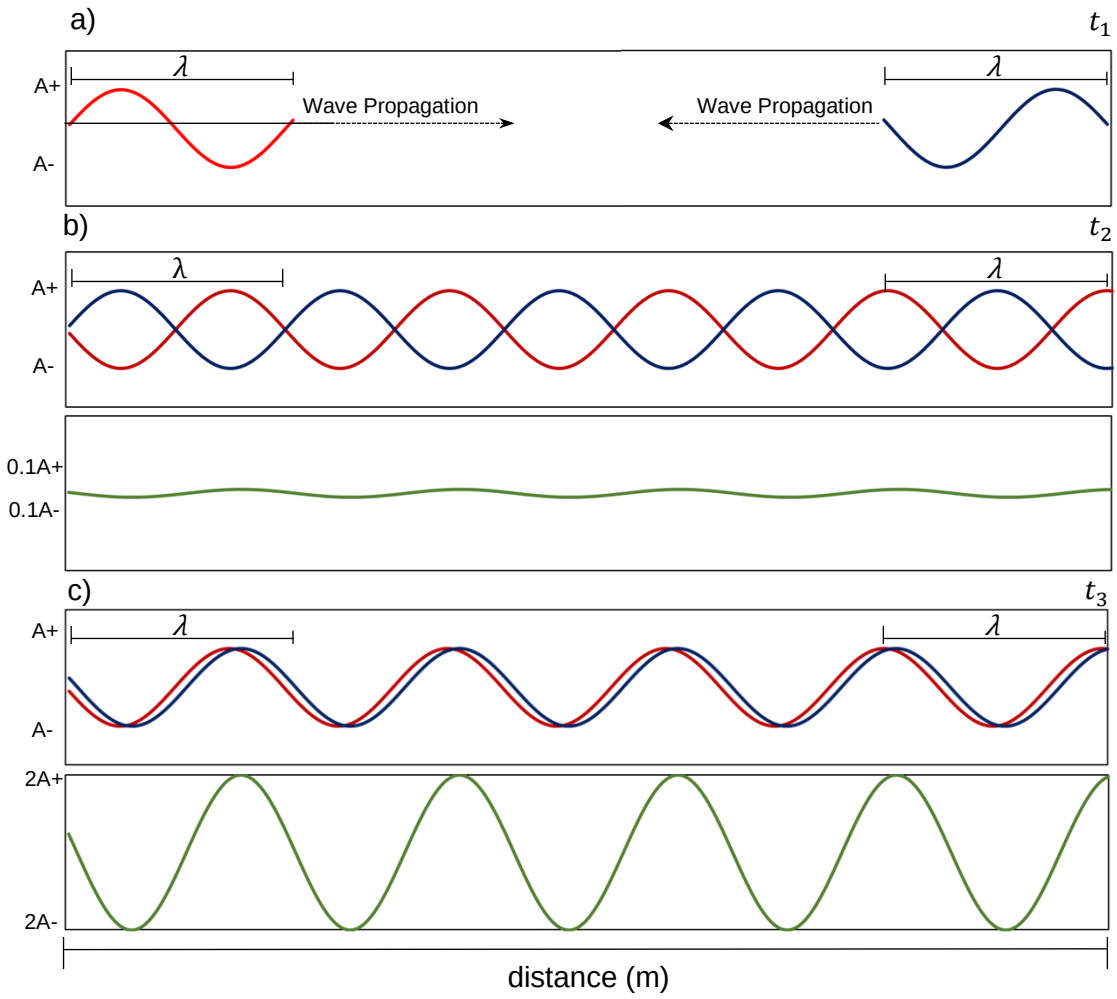

Figure 2.5. Illustration of two counterpropagating travelling waves (red and blue): a) not yet intersecting at a time t_1, b) peaks of the waves are out of phase at a time t_2, resulting in wave destructive interference (green), and c) peaks of the two waves align, leading to constructive interference (green) at time t_3.

2.5 Piezoelectricity

In the realm of wave dynamics, it is essential to explore the materials that possess unique properties suitable for harnessing and manipulating waves. One such class of materials is piezoelectrics, which exhibits a remarkable phenomenon discovered by Jacques and Pierre Curie in 1880 [150]. The term "piezoelectric" itself derives from the Greek words "piezo", meaning pressure or stress and "electricity," reflecting the characteristic of these materials to generate an electric potential in response to applied mechanical stress or pressure. Piezoelectricity is a reversible effect, meaning that when a voltage is applied to a piezoelectric material, it undergoes mechanical deformation or stress [151]. The extent and

nature of this deformation depend on various factors, including the specific material composition, electrode positioning, and shape. In nature, certain materials exhibit piezoelectric behaviours due to their non-centrosymmetric molecular crystal arrangement [152]. To be piezoelectric, a material typically possesses a periodic molecular structure (**Fig 2.6a**) and behaves as a dielectric [153]. It is worth noting that not all dielectric materials are piezoelectric. For example, glass, despite being a dielectric, has a disordered molecular arrangement that cannot accumulate a net charge and, therefore, does not exhibit piezoelectric properties. Piezoelectric materials like quartz, conversely, are composed of atoms arranged in an ordered hexagonal structure (**Fig 2.6b**) [154]. When such a hexagonal lattice is subjected to mechanical pressure or stress, its constituent atoms undergo displacements (**Fig 2.6c-d**). These displacements result in the accumulation of positive and negative charges on opposite sides of the lattice, creating a net charge difference and, consequently, a voltage drop across the material. Conversely, when an external voltage is applied to the piezoelectric material, the hexagonal structure deforms in response to the electric field.

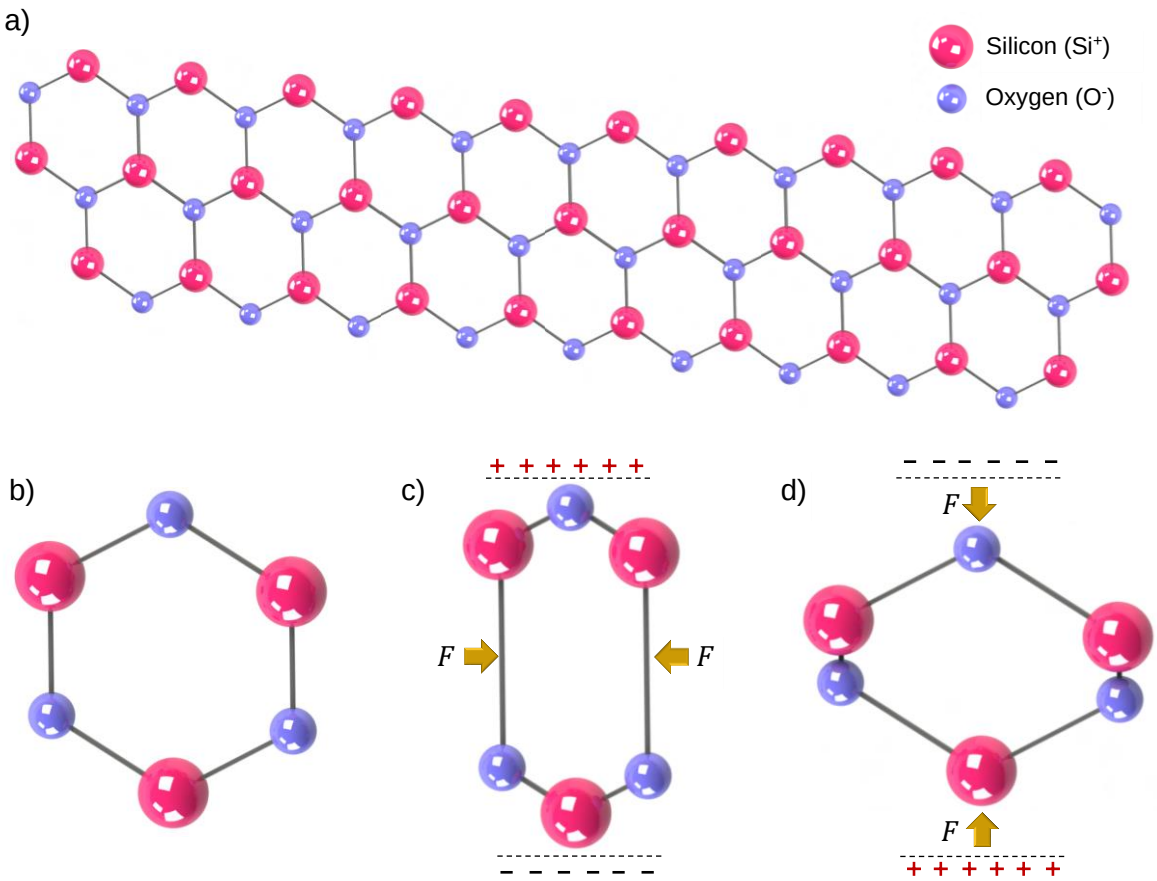

Figure 2.6. Molecular structure of a) of a Quartz crystal in an ordered hexagon shape, b) the hexagonal unit cell under no stress, c) force is applied causing net positive charge at the top and d) force is reversed causing negative net force at the top [154].

Acoustofluidics, the field that harnesses the power of sound waves to manipulate fluids and particles, heavily relies on the use of piezoelectric materials. These materials play a crucial role in acoustofluidic devices by converting electrical energy into mechanical deformation, thus generating sound waves for various applications. While natural piezoelectric materials do exist, such as quartz, laboratory-grown and processed materials are often preferred in acoustofluidic systems due to their higher effectiveness and tailored properties. Several factors govern the effectiveness of piezoelectric materials in acoustofluidic devices. One such factor is the coupling coefficient, which measures the efficiency of converting electrical energy into mechanical deformation. A higher coupling coefficient indicates a more substantial conversion and, consequently, more robust sound wave generation. The speed of sound is another important consideration when designing acoustofluidic devices. By considering the speed of sound in the piezoelectric material, researchers can determine the appropriate wavelength and frequency of the generated waves, ensuring optimal performance and precise control over fluid and particle manipulation.

Furthermore, the crystal lattice structure of the piezoelectric material, particularly the cut or orientation, plays a significant role. The cut determines the direction the material expands under electrical stimulation and influences the types of waves it can generate. By carefully selecting the cut, researchers can tailor the properties of the piezoelectric material to meet specific acoustofluidic requirements. Quartz, for example, has a high speed of sound but a relatively small coupling coefficient, making it less effective for generating strong sound waves for liquid and object manipulation in acoustofluidic systems. However, quartz finds applications in other fields, such as digital communication systems, cellular phones, automotive applications, medical instruments, and even the jewellery industry.

In the pursuit of generating effective waves using piezoelectricity, materials with high coupling coefficients and speed of sound are preferred in acoustofluidic applications. One such material is zinc oxide (ZnO), capable of generating Lamb waves, surface acoustic waves propagating along thin plates or films [155].

Additionally, materials such as lithium tantalate ($LiTaO_3$) and gallium nitride (GaN) are known for their high coupling coefficients and speed of sound [156]. These properties make them particularly useful in various acoustic applications, including acoustofluidics. By leveraging these materials' exceptional coupling coefficients and speed of sound, researchers and engineers can design and optimise acoustofluidic devices to achieve precise and efficient manipulation of fluids and particles.

The coupling coefficient efficiency excels in materials such as Lead Zinc Tantalate (Pb (Zr, Ti)O_3) known as PZT [157]. It has a high coupling coefficient (20-35) and a high speed of

sound topping 3900 m/s. This combination makes the PZT highly attractive. The primary application of PZT is adopted in manufacturing ceramic substrates used in PZT transducers, which are frequently employed in BAW devices to produce L-BAWs or other types of bulk wave propagation.

Lithium Niobate ($LiNbO_3$) is also a highly attractive material for acoustofluidic applications due to its significant coupling coefficient (5.6-11.3) and high speed of sound (3680-3980 m/s) [158]. $LiNbO_3$ is grown as a large crystal and diced into wafers [159]. Each angle cut of $LiNbO_3$ possesses unique characteristics, including different coupling coefficients and sound speeds, making it a versatile material for generating different types of sound waves. For instance, 128° Y-cut wafers are very efficient in generating Rayleigh waves, while 64° or 36° YX-cut wafers are better options for generating SH-SAW (shear horizontal surface acoustic waves) [159]. In addition to its exceptional acoustic properties, $LiNbO_3$ is optically transparent, which enables the integration of optical observation systems such as microscopes. This feature is especially useful in acoustofluidic devices requiring visual monitoring and fluid and particle manipulation control. However, it is essential to note that piezoelectric materials are an extensive subject area, and there are many other materials and variations to explore. This thesis will focus on piezoelectric materials and transducers made using 128° Y-cut $LiNbO_3$ and later PZT. These materials have been extensively studied and have shown promising results in acoustofluidic applications [132].

To better understand the conduct of the piezoelectricity, we begin reviewing the electromechanical interaction [160], as it reveals how both electrical and mechanical worlds are combined into a single piezoelectric phenomenon. We first investigate the electrical behaviour by considering two conductive plates in free space separated by distance t.

$$\vec{D} = \varepsilon\vec{E} \tag{2.4}$$

$$D = (\varepsilon_0(1 + \chi_e)) * \left(\frac{U}{t}\right) \tag{2.5}$$

here the electric displacement $\vec{D}$ is essentially a relationship of charge and the surface area of the conducting plates. It is governed by the electric field $\vec{E}$, a ratio between the applied voltage and the distance t between the plates. The absolute permittivity ε will change depending on material factors such as susceptibility χ_e (ε_0 is the permittivity of free space). The mechanical behaviour of a material in a zero electric field is described similarly.

$$\vec{S} = s\vec{T} \tag{2.6}$$

$$S = \frac{\Delta l}{l} = s\left(\frac{F}{A}\right) \tag{2.7}$$

here the strain $\vec{S}$ (deformation Δl with respect to l) will be governed by the stress $\vec{T}$ in the material according to the compliance s (reciprocal of the Youngs modulus $s = c^{-1}$) of the material when subjected to force F per unit area A. The application of mechanical stress $\vec{T}$ in a piezoelectric will cause deformation $\vec{S}$ and in turn will induce electric potential $\vec{E}$, thus:

$$\vec{D} = \varepsilon^T \vec{E} + d\vec{T} \tag{2.8}$$

Where d and ε^T is a piezoelectric charge constant and mechanical boundary condition (permittivity under constant stress), respectively. Furthermore, the relationship between the applied stress and the resulting electric field can be reduced [160] to:

$$\vec{E} = -g\vec{T} \tag{2.9}$$

Where piezoelectric voltage constant (g) is equal to $(\varepsilon^T)^{-1}d$ [m^2/N]. The presented relation is a fundamental concept of the *direct* piezoelectric effect.

On the other hand, when a piezoelectric material is exposed to the electric field, an electric displacement will occur, causing associated mechanical stress and deformation.

$$\vec{S} = s^E \vec{T} + d^{tr}\vec{E} \tag{2.10}$$

Where s^E is electrical boundary condition (compliance under constant electric field) respectively. Looking back at **Eq. 2.8,** the same parameter d appears in **Eq. 2.10** when describing the *electromechanical* interaction, and it represents both the induced polarisation and induced strain, respectively. Therefore, the piezoelectric charge constant is sometimes expressed in either [N/m^2] or [V/m]. As the material deformation is anisotropic, the added notation in d^{tr} denotes the transpose of d, allowing the description of deformation in multiple directions. The presented relation is a fundamental concept of the *inverse* piezoelectric effect. The introduced set of equations can be expressed in matrix notation (**Eq. 2.11**):

$$\begin{pmatrix} \vec{S} \\ \vec{D} \end{pmatrix} = \begin{bmatrix} s^E & d^{tr} \\ d & \varepsilon^T \end{bmatrix} \begin{pmatrix} \vec{T} \\ \vec{E} \end{pmatrix} \tag{2.11}$$

As we deal with materials in three-dimensional space, the strain $\vec{S}$ and stress $\vec{T}$ vectors adopt six elements. There are three for normal axis translations and three for shear translation. Additionally, the electric displacement $\vec{D}$ and electric field $\vec{E}$ vectors consist of the three normal axis displacements along the *x-, y-* and *z*-axis, yielding a rather substantial but a complete description of the behaviour of piezoelectric materials:

$$\begin{pmatrix} S_1 \\ S_2 \\ S_3 \\ S_4 \\ S_5 \\ S_6 \\ D_1 \\ D_2 \\ D_3 \end{pmatrix} = \begin{bmatrix} s_{11}^E & s_{12}^E & s_{13}^E & s_{14}^E & s_{15}^E & s_{16}^E & d_{11} & d_{21} & d_{31} \\ s_{21}^E & s_{22}^E & s_{23}^E & s_{24}^E & s_{25}^E & s_{26}^E & d_{12} & d_{22} & d_{32} \\ s_{31}^E & s_{32}^E & s_{33}^E & s_{34}^E & s_{35}^E & s_{36}^E & d_{13} & d_{23} & d_{33} \\ s_{41}^E & s_{42}^E & s_{43}^E & s_{44}^E & s_{45}^E & s_{46}^E & d_{13} & d_{24} & d_{34} \\ s_{51}^E & s_{52}^E & s_{53}^E & s_{54}^E & s_{55}^E & s_{56}^E & d_{14} & d_{25} & d_{35} \\ s_{61}^E & s_{62}^E & s_{63}^E & s_{64}^E & s_{65}^E & s_{66}^E & d_{16} & d_{26} & d_{36} \\ d_{11} & d_{12} & d_{13} & d_{14} & d_{15} & d_{16} & \varepsilon_{11}^T & \varepsilon_{12}^T & \varepsilon_{13}^T \\ d_{21} & d_{22} & d_{23} & d_{24} & d_{25} & d_{26} & \varepsilon_{21}^T & \varepsilon_{22}^T & \varepsilon_{23}^T \\ d_{31} & d_{32} & d_{33} & d_{34} & d_{35} & d_{36} & \varepsilon_{31}^T & \varepsilon_{32}^T & \varepsilon_{33}^T \end{bmatrix} \begin{pmatrix} T_1 \\ T_2 \\ T_3 \\ T_4 \\ T_5 \\ T_6 \\ E_1 \\ E_2 \\ E_3 \end{pmatrix} \quad (2.12)$$

Quantifying and predicting the amount of energy translated from mechanical displacement to electric field (and vice-versa) is best described by the coupling coefficient k derived in [160] as shown:

$$k = \frac{d^2}{s^E \varepsilon^T} \quad (2.13)$$

$$k^2 = \frac{mechanical\ energy\ to\ electric}{input\ mechanical\ energy} = \frac{electric\ energy\ to\ mechanical}{input\ electric\ energy} \quad (2.14)$$

2.6 Piezoelectric transducers

Piezoelectric transducers play a vital role in acoustofluidic systems, enabling the conversion of electrical energy into mechanical vibrations and vice versa. While piezoelectric materials alone possess the inherent property of generating electric charges in response to mechanical stress, their integration with strategically positioned electrodes is essential to transform them into powerful piezoelectric transducers used in acoustofluidics.

As previously discussed, sound waves can propagate in the bulk or on the surface of the medium. For bulk propagation, a piezoelectric material such as PZT can be sandwiched between two electrodes, and by applying an alternating voltage, an L-BAW is formed (**Fig 2.7**) along the z-axis. An L-BAW can be useful for various applications, such as manipulating particles, separating cells, and mixing fluids [144]. PZT transducers come in two types: single disk and multilayer. Multilayer PZT disks are commonly used due to their high displacement, reliability, and low cost [161]. The manufacturing process for both types is similar. The process involves selecting high-purity oxide materials, calcination, milling, granulation, burnout, sintering, finishing machining, termination with metal layers, and electrical field poling [162]. The resonance frequency f of the PZT transducer is determined by the inductive and capacitive reactance components, which is an essential characteristic as described [163]:

$$f = \frac{1}{2\pi\sqrt{LC}} \tag{2.15}$$

Due to the difficulty in manufacturing thin PZT ceramics, which are crucial for high-frequency operation, thin film piezoelectric transducers are commonly used for high-frequency BAW devices, despite their higher cost than traditional PZT transducers.

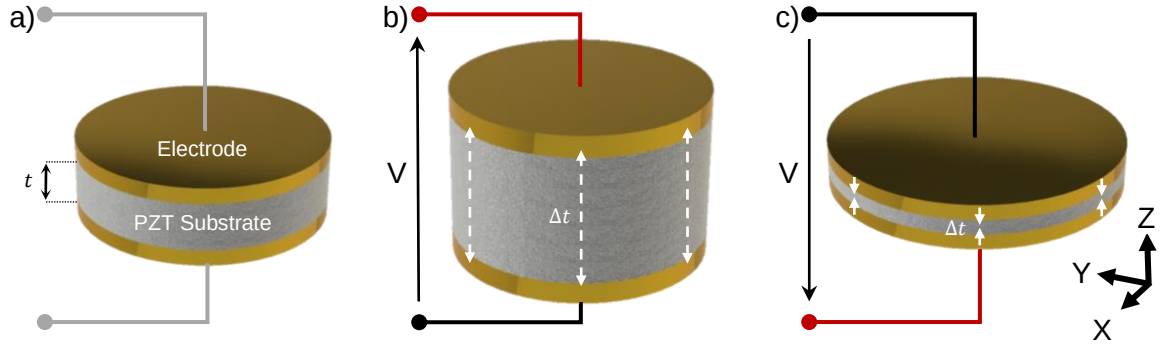

Figure 2.7. Functional principle of a BAW transducer and: a) BAW transducer in an undistorted state. When a b) positive potential voltage is applied, the piezoelectric substrate experiences expansion and c) contracts when the voltage is reversed [161].

On the other hand, to produce waves propagating across the solid surface, an interdigital transducer (IDT) is typically found [164]. The IDT is a device consisting of interlocking electrodes patterned on the surface of a piezoelectric substrate, such as $LiNbO_3$ (**Fig 2.8a**). When an AC voltage is applied to the IDT, it generates localised expansions and compressions on the surface of the substrate, resulting in the propagation of a surface wave (R-SAW) (**Fig 2.8b**). For a pure R-SAW, the spacing between the electrodes, or pitch, determines the wave's wavelength. The wavelength certainly depends on the speed of sound in the substrate, a property that must be carefully considered when designing an IDT.

IDTs are commonly manufactured in a cleanroom facility on a 128º Y-cut $LiNbO_3$ substrate. The process begins by spin coating photoresist on the wafer [165]. Then a mask with a predefined pattern is precisely aligned and placed above the substrate, followed by exposure to ultraviolet (UV) light from the top. After a thorough cleaning procedure, the wafer remains coated with a photoresist, but the areas corresponding to the mask design are removed or left (depending on the type of photoresist), thus forming the desired IDT pattern [166]. Next, chromium is deposited on the wafer to act as a conductive adhesion layer, and gold is subsequently deposited on top of the IDT electrodes. The process concludes by soaking the item in acetone to remove the remaining photoresist, leaving only the IDT pattern behind.

IDTs come in a variety of forms discussed later in the applications section; therefore, for simplicity, we now will consider the most conventional IDT design (**Fig. 2.8c**) and its design considerations, such as pitch size, IDE length, IDE width, Bus-IDE gap, and bus pad width. The desired operating frequency f of the IDT transducer is determined by the pitch size p_s responsible for the wavelength for a given speed of sound c_S in the material [167].

$$p_s = \frac{c_S}{f} \tag{2.16}$$

For example, a material with a speed of sound of 3980 m/s will adopt a pitch size of 200 µm, if 20 MHz is the desired operating frequency. The width of the IDT electrodes (IDE) on the other hand is widely accepted to be a quarter of a wavelength (a quarter of the pitch size). The Bus-IDE gap is also left the same width as a finger electrode.

Finally, the operating bandwidth of the IDT will be governed by the amount of IDT pairs on a single unit, described as:

$$BW = \frac{2f}{N} \tag{2.17}$$

where N is the number of fingers. An increase in N can minimise spurious responses, however, too many finger numbers will cause mass loading and scattering effects from the electrodes as well as occupy real estate [132]. The remaining parameter, bus-pad-width, does not necessarily impact the performance, nor is it usually considered in much detail; however, it is mainly designed to be sufficiently able to carry AC signals to the fingers and be large enough to accommodate wires connecting the signal and the IDT.

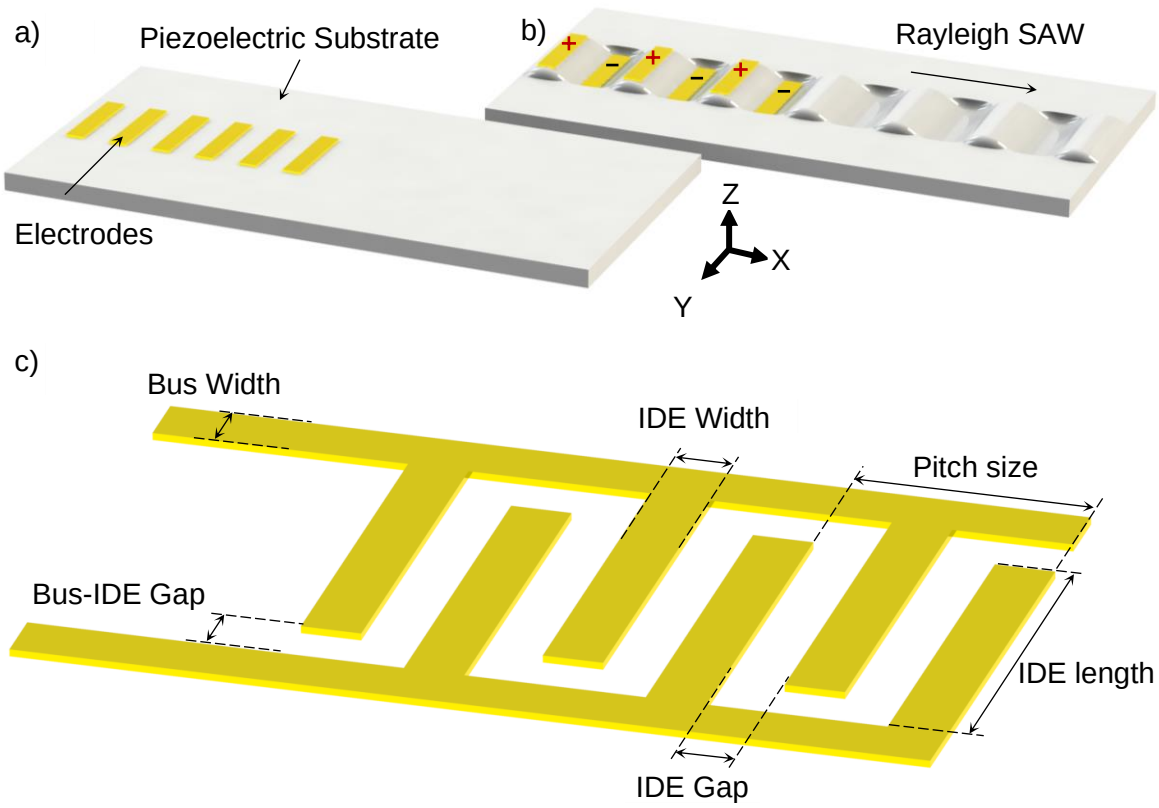

Figure 2.8. A traditional IDT is made up of consecutive sets of interdigital electrodes a) before the electric field is applied, and b) upon applying the electric field, the wave is launched towards the x-axis. c) Illustrates the fundamental dimensions of a conventional IDT [167].

2.7 Acoustophoresis

Acoustophoresis is the primary phenomenon in focus, where particles suspended in a fluid are influenced and manipulated using acoustic waves. These waves, travelling through the medium, create a pressure differential that directly affects the suspended particles. Subsequently, this pressure differential exerts what is known as an acoustic radiation force on the particles. The force generated by these acoustic waves moves the particles, which can then be effectively manipulated. Following this, as a consequence of the interaction between the acoustic field and the fluid medium, acoustic streaming develops. This is a secondary phenomenon characterized by a steady, directional fluid flow. Despite being a by-product of the main acoustophoretic process, acoustic streaming has significant effects on the system as a whole and can impact the precise manipulation of particles. Historically, similar phenomena have been observed for centuries. The ancient Chinese spouting bowl, or resonance bowl, is a notable example that demonstrates the principles of acoustic streaming. This fascinating instrument was used for entertainment and had spiritual and

healing connotations [168]. Acoustic streaming was first scientifically termed by Dvorak in 1876 through investigations of the Kundt's tube [169]. During the experiment, Dvorak noticed a distinct airflow pattern within the tube. He observed that the air near the nodes of the standing waves, where the amplitude of the vibrations is minimal, flowed from the nodes toward the antinodes along the axis of the tube.

Over the years, numerous scientists, including Schlichting, Westervelt, and Nyborg, delved deeper into the understanding of acoustic streaming. Their studies focused on elucidating the mechanisms of incompressible and compressible streaming, providing valuable insights into the intricate dynamics of fluid flow induced by acoustic waves [132]. Extensive investigations have been conducted to unravel the intricacies of acoustophoresis by pioneers like King back in 1934, who explored the behaviours of incompressible particles in acoustic fields [170]. Building upon this foundation, Yosioka and Kawasima further advanced the understanding in 1955 by analysing the forces acting on compressible particles in plane acoustic waves [171]. Gorkov later expanded upon these findings in a seminal paper published in 1962 [171]. It is upon this rich legacy of acoustophoresis that the present thesis is founded, aiming to harness this profound phenomenon for the development of novel devices capable of efficient cell and exosome separation.

2.7.1 Governing Equations

In the field of microfluidics, the flow of fluids and suspensions in channels with sub-millimetre-sized cross-sections is studied under the influence of external forces. Due to the dominance of viscosity over inertia, turbulent flow is typically absent, and instead, laminar flow with regular and predictable flow patterns is observed. This characteristic allows for precise control of solutes in terms of their spatial and temporal manipulation [172].

In microfluidics, the flow velocity is often significantly smaller than the speed of sound, leading to the assumption of fluid incompressibility. The first governing equation is the continuity equation, which describes the conservation of mass in a fluid. In the case of an incompressible fluid, where the density remains constant in both space and time, the continuity equation is simplified to,

$$\boldsymbol{\nabla} \cdot \boldsymbol{v} = 0 \tag{2.18}$$

The Navier-Stokes equation (the second governing equation), which describes the motion of fluids, is derived from the conservation of momentum and the momentum density. In the

case of Newtonian fluids at a given temperature, where viscosity is treated as a constant, the Navier-Stokes equation for incompressible fluids is as follows:

$$\rho\left[\frac{\delta \boldsymbol{v}}{\delta t} + (\boldsymbol{v}\cdot\boldsymbol{\nabla})\boldsymbol{v}\right] = -\boldsymbol{\nabla p} + \eta\boldsymbol{\nabla}^2\boldsymbol{v} + \rho\boldsymbol{g} \tag{2.19}$$

where $\boldsymbol{v}$ is the flow velocity, t is time, $\boldsymbol{p}$ is the pressure acting on a fluid. The bold character represents vectors, and the normal characters are the scalars. On the left-hand side of the equation, we have the inertial terms. The term $\frac{\delta \boldsymbol{v}}{\delta t}$ represents the time rate of change of velocity, and $(\boldsymbol{v}\cdot\boldsymbol{\nabla})\boldsymbol{v}$ represents the speed and direction of the fluid. These terms account for the inertia of the fluid and how it affects its motion. On the right-hand side of the equation, we have the forces acting on the fluid. The term $-\boldsymbol{\nabla p}$ represents the pressure gradient force responsible for fluid flow from higher to lower pressure regions. The term $\eta\boldsymbol{\nabla}^2\boldsymbol{v}$ represents the viscous force, where $\boldsymbol{\nabla}^2\boldsymbol{v}$ represents the Laplacian of the velocity field. This term accounts for the resistance to flow caused by internal friction within the fluid. The term $\rho\boldsymbol{g}$ represents any external forces or body forces acting on the fluid, such as gravity or electromagnetic forces. In short, The Navier-Stokes equation explains how fluids like water move. On one side, it describes the changes in fluid speed, while on the other side, it considers factors like pressure, viscosity, and other forces that affect the fluid's motion.

Provided equations can be constricted within the boundary conditions and the linear relationship between pressure p and mass density ρ to predict the motion of the fluid.

$$p = c_{\mathrm{L}}^2\rho \tag{2.20}$$

The governing equations are complex and challenging to solve analytically. Perturbation theory is a well-established concept that provides a solid foundation for analysing these equations but applies only in slow-streaming cases. Slow streaming refers to situations where the velocity of the fluid flow induced by acoustic waves is much smaller than the velocity of the acoustic waves. In this thesis, the emphasis is placed on studying slow streaming, where the streaming velocities are considered to be relatively small (10-80 mm/s) compared to the velocity of the acoustic waves (900 – 2000 m/s).

As the velocity of the streaming and liquid flow increases, turbulence becomes more prominent and needs to be considered when solving the Navier-Stokes equations. Turbulence significantly impacts fluid flow behaviour, introducing chaotic and unpredictable motion patterns that can greatly influence the overall flow dynamics. Therefore, considering turbulence is crucial for accurately modelling and understanding the behaviour of fluids in various systems. Turbulent flows involve chaotic and unpredictable motion patterns, which

can significantly impact the transport of particles, mixing, and overall fluid behaviour. Neglecting turbulence in the analysis can lead to inaccurate predictions and an incomplete understanding of the system's behaviour.

When viscous force is stronger than inertia, the fluid flow is laminar, with smooth and predictable motion. However, when the inertia force is stronger than the viscous force, the fluid flow becomes turbulent, leading to chaotic and unpredictable motion. This distinction is crucial in understanding acoustofluidic systems, as some systems have laminar flow that can be assumed to be zero, while others must take turbulence into account. As shown in **Eq. 2.21,** the dimensionless parameter R_{e}, the so-called Reynolds number, is introduced [173], providing a valuable means of classifying the turbulence of a liquid based on the ratio of inertia to viscous forces.

$$R_{\mathrm{e}} \equiv \frac{\rho_{\mathrm{f}}|\mathrm{U}|\mathcal{L}}{\eta} \tag{2.21}$$

where $|\mathrm{U}|$ and $\mathcal{L}$ are liquid velocity and characteristic length, respectively. The characteristic length $\mathcal{L}$ is dependent on the specific type of fluid movement present. Various modes of fluid movement, including Schlichting, Eckart, and Rayleigh, can be observed in acoustofluidic systems. These distinct modes are influenced by the boundary conditions, volume, and incident waves applied to the liquid. Understanding the nature of these fluid movements is crucial for designing and optimizing acoustofluidic devices and applications. In microfluidic devices, where the scale of the fluid channel is similar to the acoustic wavelength, boundary-driven streaming dominates. Boundary-driven streaming can be categorized into inner and outer streaming. Inner streaming, known as Schlichting streaming, is caused by the boundary layer effects between the solid and the fluid, resulting in steady vortices near the solid boundary. Outer streaming, known as Rayleigh streaming, generates counter-rotating vortices within the fluid. Another mechanism for acoustic streaming is bulk-driven streaming, also known as Eckart streaming or quartz wind, which occurs when acoustic energy dissipates into the bulk of the fluid. This type of streaming is more pronounced in larger microfluidic devices where the length of the chamber is comparable to or greater than the acoustic attenuation length. By exploring the behaviour of particles in response to the fluidic motion, we can bridge the gap between understanding particle-fluid interactions and the underlying principles described by the governing equations.

The Navier-Stokes equations are essential in microfluidics for understanding particle-fluid interactions and deriving the drag force experienced by particles. To understand the particle behaviour due to an external fluidic motion, first, it is imagined that a force that moves a

spherical particle of diameter d_p at velocity $\boldsymbol{v_p}$ through a fluid that itself moves with velocity $\boldsymbol{v}$ (See **Fig. 2.9**).

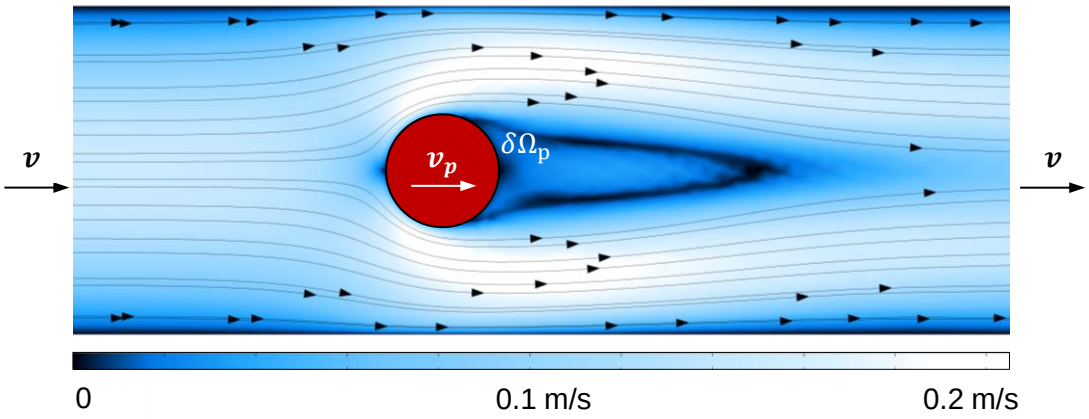

Figure 2.9. COMSOL simulation of a particle (red circle) experiencing stokes drag force due to the moving liquid from left to right at velocity $\boldsymbol{v}$. Over time the particle will be dragged along the streamline at the velocity $\boldsymbol{v_p}$

In microfluidic channels, the Reynolds number is typically small due to the low flow velocities, indicating that the effect of inertia on the fluid flow is relatively weak. All external fields such as gravity, buoyance, and electromagnetism are usually not considered for simplicity. Therefore, for microfluidic channel systems, neglecting the inertial terms and focusing on the dominant viscous forces described by the Stokes equations is justified. Consequently, this yields a linearised form of the Navier-Stokes equation,

$$0 = -\boldsymbol{\nabla} p + \eta \nabla^2 \boldsymbol{v} \tag{2.22}$$

Although the derivation of the drag force equation from the linear Navier-Stokes equation is a non-trivial task, the resulting equation for the viscous Stokes drag force ($\boldsymbol{F}^{DRAG}$) is provided. This equation is obtained by considering the no-slip boundary condition on the particle surface $\delta\Omega_p$ and studying the velocity and pressure field of the fluid.

$$\boldsymbol{F}^{\mathrm{DRAG}} = \int_{\delta\Omega} \mathrm{d}a(-p\boldsymbol{n} + \sigma' \cdot \boldsymbol{n}) = 6\pi\eta \left(\frac{d_{\mathrm{p}}}{2}\right)(\boldsymbol{v} - \boldsymbol{v}_{\mathbf{p}}) \tag{2.23}$$

The subtraction of velocities ($\boldsymbol{v} - \boldsymbol{v}_{\mathbf{p}}$) in the drag force equation, derivation accounts for the relative motion between the particle and the fluid, considering their different velocities. However, the effect of this relative velocity is combined to form the celebrated Stokes Drag Force, introduced in 1850 by George Gabriel Stokes, which renders the equation by not explicitly including the particle velocity as follows,

$$\boldsymbol{F}^{\mathrm{DRAG}} = 6\pi\eta\left(\frac{d_{\mathrm{p}}}{2}\right)\boldsymbol{v} \tag{2.24}$$

The viscosity term ($6\pi\eta\left(\frac{d_{\mathrm{p}}}{2}\right)$) directly relates to the fluid's resistance to flow. Higher viscosity results in increased frictional forces, leading to a greater drag force on the particle. Thus, the fluid's viscosity affects the drag force's magnitude. The velocity term ($\boldsymbol{v}$) governs and influences the particle speed in the surrounding fluid, as the higher velocity results in a larger drag force. Therefore, changes in viscosity and relative velocity both impact the drag force and form the fundamental theory of microfluidic devices.

The drag force in **Eq 2.24** is commonly notable and utilised for liquids in a microchannel since a laminar flow is developed due to the minuscule system nature, meaning a very low Reynolds number ($R_{\mathrm{e}} < 1$). Therefore, approximations made using **Eq 2.24** are valid as it only considers laminar flow [174]. However, in specific applications of acoustofluidics, larger liquid domains such as droplets are involved, which can rotate at higher velocities and turbulence. For instance, in droplet streaming applications, the volume of the liquid is considerably larger, and the velocity of the streaming motion is significantly greater. In addition, the lack of boundary condition in a sessile droplet system allows for more variables of freedom and more room to deform in unpredictable motions. This gives rise to more turbulence that cannot be ignored. Typically, a 30 µL droplet of volume will experience a streaming velocity of 40-80 mm/s, hence, $R_{\mathrm{e}} > 1$. To account for the additional disturbances introduced, the Schiller-Naumann drag force model (**Eq. 2.25**) further approximates the solution [174], [175].

$$\boldsymbol{F}^{\mathrm{DRAG}} = \left(\frac{3\eta C_{\mathrm{d}} R_{\mathrm{e}} m_{\mathrm{p}}}{4\rho_{\mathrm{p}} {d_{\mathrm{p}}}^2}\right)\boldsymbol{v} \tag{2.25}$$

$$C_{\mathrm{d}} = \frac{24}{R_{\mathrm{e}}}(1 + 0.15R_{\mathrm{e}}^{0.687}) \tag{2.26}$$

where m_p is the mass of the particle.

2.7.2 Perturbation theory

Perturbation theory in physics is a mathematical technique used to approximate solutions to complex equations by breaking them down into simpler, solvable parts. In the field of acoustics, perturbation theory is a well-established mathematical tool employed to elucidate the behaviour of acoustic waves in complex systems [176]. It assumes that a physical

system can be described by a known solution plus a perturbation term representing small deviations from this known solution. Perturbation theory is employed when the perturbation is small relative to the dominant term in the equation. By systematically expanding the equations in terms of the perturbation parameter, it becomes possible to derive approximate solutions and investigate the effects of the perturbation on the system's behaviour. In acoustics, perturbation theory is applied to solve the wave equation for small deviations from a known acoustic field, allowing for the analysis of acoustic wave propagation in heterogeneous media and the calculation of critical acoustic properties. The perturbations on a quiescent fluid are considered to the first and second order (subscript 1 and 2, respectively) in density ρ, acoustic pressure p, and velocity $\boldsymbol{v}$ as described [171],

$$\rho = \rho_0 + \varepsilon\rho_1 + \rho_2 \tag{2.27}$$

$$p = p_0 + \varepsilon p_1 + p_2 \tag{2.28}$$

$$\boldsymbol{v} = \boldsymbol{v}_0 + \varepsilon\boldsymbol{v}_1 + \boldsymbol{v}_2 \tag{2.29}$$

When there is no sound present, the fluid remains still, and $\boldsymbol{v}_0 = 0$. To analyse systems with slow streaming, the Mach number ($\varepsilon = \frac{v_1}{c_0}$) is introduced as a smallness parameter, representing the ratio of fluid velocity to the speed of sound. This method assumes the convergence of successive approximations, relying on the condition that ε is sufficiently small. However, the perturbation approach is not applicable for fast streaming scenarios where successive approximations fail to converge. The continuity and momentum equations (**Eq 2.18-19**) can be solved by employing perturbation expansions for each order component of the acoustic field. The first-order solution describes the oscillatory acoustic wave motions, with $\boldsymbol{v}_1$ representing the acoustic velocity and p_1 denoting the acoustic pressure field. Substituting the first-order solutions into second-order equations and time-averaging them yields the solution for acoustic streaming, which encompasses both harmonic and steady components. The second-order time-averaged velocity $\langle \boldsymbol{v}_2 \rangle$ corresponds to the acoustic streaming, while the second-order time-averaged pressure $\langle p_2 \rangle$ gives rise to the acoustic radiation force. This force occurs when acoustic waves interact with particles, causing their movement.

2.7.3 Acoustic Radiation Force

The Navier-Stokes equations are a fundamental concept in fluid dynamics, with their influence being ubiquitous across numerous fields. They are utilised to predict and analyse

a vast range of phenomena, from ocean currents and weather patterns to blood circulation and astrophysical events. Their applications extend into functional areas such as aerodynamics, critical for designing vehicles that move efficiently through air or water. Furthermore, the principles laid down by Navier and Stokes play a crucial role in understanding the movement of fluids under the influence of sound waves, namely the acoustophoretic effect. In this field, piezoelectric transducers are utilised in various forms to induce pressure on the fluids and the suspended particles. The particles suspended in the fluid are subjected to a variety of forces. Gravity pulls them downward, buoyancy might push them upward, Brownian motion (caused by thermal fluctuations) jostles them in all directions and drag forces resist the movement of the particles through the fluid.

Indeed, the acoustic radiation force commonly induced by the piezoelectric transducer applies a non-negligible impact on the particles, imparting momentum that can result in phenomena ranging from propulsion to spatial confinement or even aggregation under certain conditions. Acting as a principal mechanism for micro-particle manipulation within a fluid medium, the acoustic radiation force is a pivotal element in numerous applications across the field of acoustofluidics.

The perturbation expansions can be used to derive the acoustic radiation force equation. The primary acoustic radiation pressure ($\boldsymbol{F}^{\mathrm{RAD}}$) refers to the force experienced by an individual particle in a fluid due to the presence of a surface acoustic wave (SAW). In contrast, the secondary acoustic radiation pressure accounts for the forces resulting from the acoustic interactions among particles in the fluid [177]. The derivation of the acoustic radiation force is treated in detail by Bruss [171], but we summarise the main results. Acoustic radiation force $\boldsymbol{F}^{\mathrm{RAD}}$ is determined by the surface ($\delta\Omega$) integral of the time-averaged second-order pressure $\langle p_2 \rangle$ and momentum flux tensor $\rho_0 \langle \boldsymbol{v_1 v_1} \rangle$ at a fixed surface just beyond the oscillating sphere (**Fig 2.9,** $\delta\Omega_p$) [171]. Moreover, the generalised equation can be written as:

$$\boldsymbol{F}^{\mathrm{RAD}} = -\int_{\delta\Omega} \mathrm{d}a \, \{\langle p_2 \rangle \boldsymbol{n} + \rho_0 \langle (\boldsymbol{n} \cdot \boldsymbol{v_1}) \boldsymbol{v_1} \rangle\} \tag{2.30}$$

where $\boldsymbol{n}$ is the normal unit vector of the particle surface directed into the fluid.

This equation allows to quantitatively analyse the acoustic radiation force exerted on a single particle in a fluid. It provides valuable insight into the underlying physics of acoustophoretic systems and contributes to optimising and designing particle manipulation and separation techniques.

In general, the acoustic radiation force and its impact on the surrounding particles is also classified whether the waves are travelling or standing. The behaviour of Primary Acoustic Radiation Force (P-ARF) due to a travelling wave (i.e., L-BAW or T-SAW) has been derived by King [15]:

$$F_{\mathrm{TW_{RAD}}} = 2\pi\rho_{\mathrm{f}}|A|^2\left(k_w\left(\frac{d_{\mathrm{p}}}{2}\right)\right)^6\frac{9+2\left(1-\lambda_{\rho}\right)^2}{9\left(2+\lambda_{\rho}\right)^2} \tag{2.31}$$

$$\lambda_{\rho} = \frac{\rho_{\mathrm{f}}}{\rho_{\mathrm{p}}} \tag{2.32}$$

where A, d_{p}, ρ_{p} is the complex amplitude, diameter of the particle, density of the particle and particle, respectively. Travelling waves are commonly employed in droplet streaming applications and deflection techniques.

However, there is a key difference in the acoustic radiation force effect generated by the superposition of these two sources. When two waves counter-propagate and interfere constructively, they form a time-averaged effect of standing waves, where the attenuated wave into the fluid oscillates between high- and low-pressure points in one spatial location. These pressure points can be visualised as high-pressure regions (**Fig. 2.10b**, red region) and low-pressure (**Fig. 2.10b**, blue region). Dashed lines denote the regions of the highest amplitude, while solid black lines represent the areas that experience negligible acoustic forces. These area represent nodes and antinodes, where particles can be trapped [171]. The acoustic radiation force generated by the standing wave acting on a particle can be described as follows,

$$F_{\mathrm{SW_{RAD}}} = -\left(\frac{\pi p_0^2 V_{\mathrm{p}}\beta_{\mathrm{f}}}{2\lambda}\right)\varphi(\beta,\rho)\sin(2k_{\mathrm{w}}\mathrm{x}) \tag{2.33}$$

$$\varphi(\beta,\rho) = \frac{5\rho_{\mathrm{p}}-2\rho_{\mathrm{f}}}{2\rho_{\mathrm{p}}+\rho_{\mathrm{f}}} - \frac{\beta_{\mathrm{p}}}{\beta_{\mathrm{f}}} \tag{2.34}$$

where $V_{\mathrm{p}}, \beta_{\mathrm{f}}, \beta_{\mathrm{p}}, \lambda, \varphi, x,$ particle volume, fluid compressibility, particle compressibility, wavelength, acoustic contrast factor and particle distance from the node. The equation solving acoustic radiation force in a standing wave acoustic field is usually employed for applications such as separation and patterning in microchannels. One of the critical components of this equation is the acoustic contrast factor (φ), which encapsulates the difference in acoustic properties between the particle and the surrounding medium. Specifically, it measures the difference in density and compressibility between the two. As per the equation, when φ is positive, the acoustic radiation force (ARF) will push particles

towards the pressure nodes (areas of minimal pressure variation), whereas when φ is negative, the ARF directs particles towards the pressure antinodes (areas of maximum pressure fluctuation).

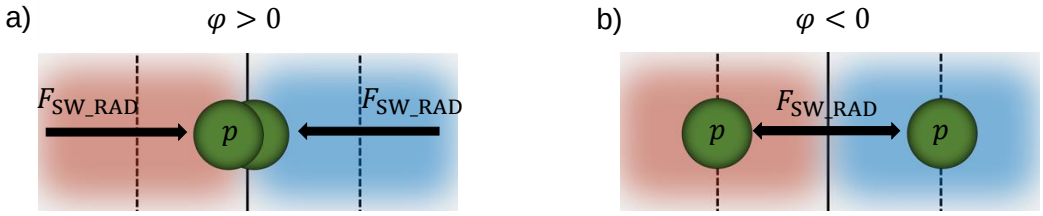

Figure 2.10. Directing particles towards nodes or antinodes, depending on whether the acoustic contrast factor is a) positive or b) negative, respectively.

2.8 Acoustic Interactions with liquids

Snell's Law [178], also known as the law of refraction, describes the behaviours of light as it passes through the boundary between two different media. It states that the ratio of the sine of the angle of incidence to the sine of the angle of refraction is equal to the ratio of the velocities (or indices of refraction) of the light in the two media. Mathematically, Snell's Law can be expressed as:

$$\theta_{\mathrm{R}} = \sin^{-1}\left(\frac{c_{\mathrm{L}}}{c_{\mathrm{S}}}\right) \tag{2.35}$$

While Snell's Law was originally derived for light waves, its principles can be extended to acoustic waves due to their analogous behaviours. When an acoustic wave encounters an interface between two media with different acoustic properties, such as different sound speeds or densities, Snell's Law can be used to determine the further behaviour of the wave. Such interaction between the wave and other medium causes energy diffraction at an angle. For instance, when a travelling surface acoustic wave, reaches a domain, the surface wave will diffract and in turn transmit the energy into as a longitudinal wave. In this particular case of droplet attenuation the dissipation follows the well-known Rayleigh angle θ_{R} (**Fig 2.11a**), which creates a pressure gradient inside the fluid [179]. Due to the occurred diffraction and energy transmission into the liquid, the propagating surface acoustic wave, progressively degrades in amplitude. This phenomenon is termed leaky SAW (L-SAW) noted in **Fig 2.11a**. Such damping of the L-SAW is predicted by the attenuation length [180] a^{-1} given by:

$$a^{-1} = \frac{\rho_{\mathrm{m}} c_{\mathrm{S}}^2}{f \rho_{\mathrm{f}} c_{\mathrm{L}}} \tag{2.36}$$

where ρ_f and ρ_m are the densities of the fluid and the material respectively (**Fig 2.11b**). In parallel the diffracted longitudinal wave will also decay [181] within the medium as given by:

$$\beta^{-1} = \frac{\rho_1 c_L^3}{4\pi^2 f^2 \left(\frac{4}{3}\eta + \eta'\right)} \tag{2.37}$$

where η and η' are the shear and bulk viscosities of the liquid.

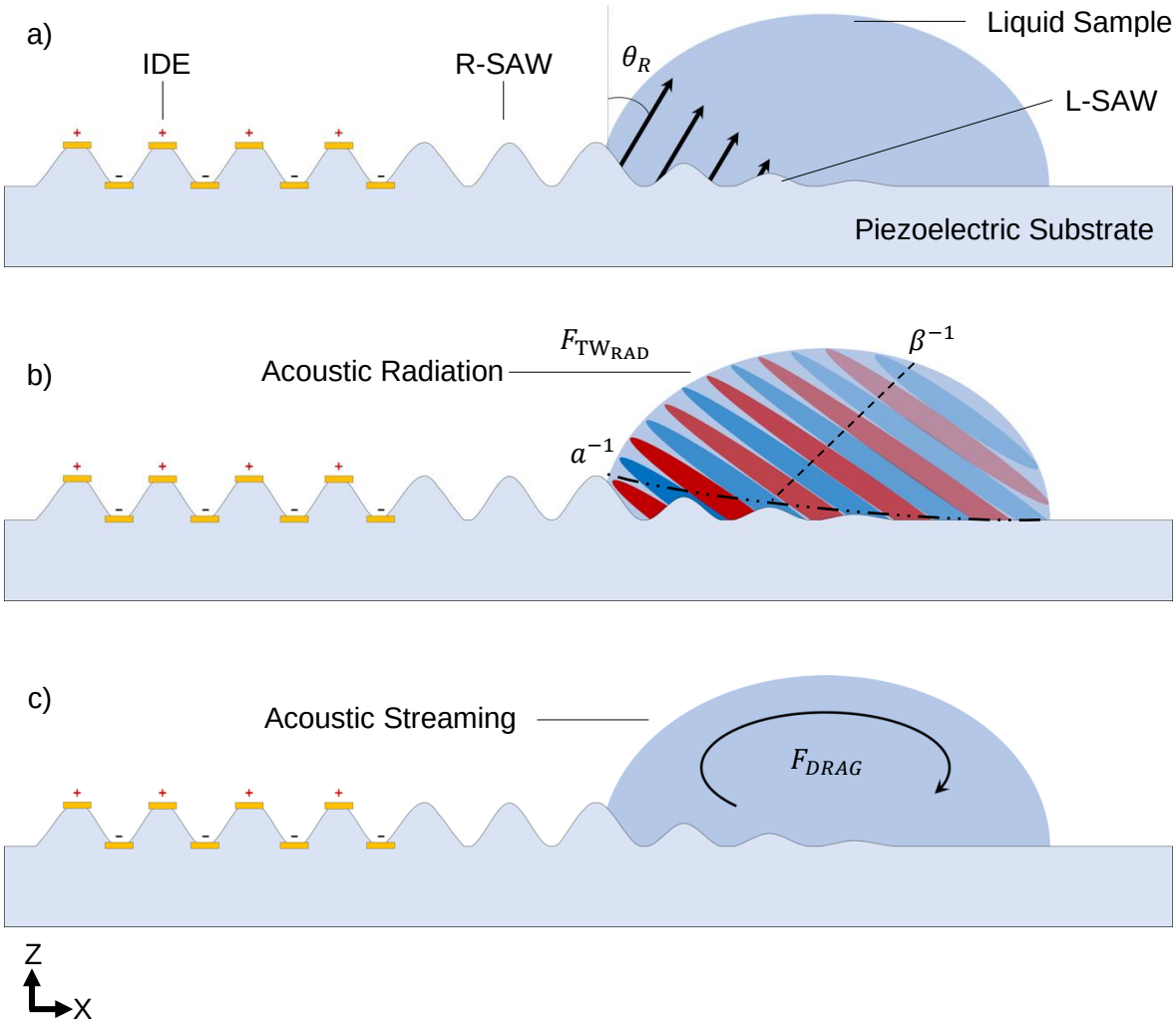

Figure 2.11. Liquid droplet interaction with a surface acoustic wave: a) initially, the wave diffracts into the droplet at a Rayleigh angle, which induces b) longitudinal wave propagation within the liquid domain that attenuates in tandem with the surface acoustic wave, generating a pressure gradient responsible for c) liquid streaming that exerts a drag force on the suspended particles.

The energy diffracted into the liquid droplet facilitates sound propagation through the fluid in the form of a longitudinal wave. This wave, now within the fluid domain, induces ARF that acts on both the fluid and the particles suspended within. The transmission of the ARF due

to the diffracted wave is visualized in **Fig 2.11b**, where a decaying longitudinal wave transmits substantial energy, thereby influencing the fluid and particles within. The resultant pressure gradient and the transmission of the ARF, characterized by an attenuation angle, induces a Stokes drag force (as shown in **Fig 2.11c**), instigating motion within the fluid domain. This phenomenon, with reference to the sessile liquid droplets, is utilized for acoustic streaming, concentration, mixing and separation applications.

There exist multiple strategies and techniques for positioning piezoelectric transducers, specifically interdigitated transducers (IDTs) relative to a circular droplet in acoustofluidic systems [132]. For instance, one conventional approach involves placing the IDT in front of the droplet, resulting in the formation of two vortex streams, which is a widely recognised configuration in acoustofluidics (**Fig 2.12a**). By introducing another IDT in front of the previous one, four streaming vortexes can be generated due to the interference of two counterpropagating waves (**Fig 2.12b**). When the droplet is asymmetrically positioned to the IDT (**Fig 2.12c**), a single vortex stream is developed as the passing wave continues to rotate the sample. This asymmetric IDT positioning technique is fundamental in acoustic concentration methods. Other methods of inducing a single vortex stream include the use of a slanted IDT (**Fig 2.12d**), which is essentially a variation of the asymmetric IDT positioning technique by frequency variation. This approach may be advantageous as it allows for improved manipulation of the IDT offset after sample placement. Additionally, a different method for inducing circular streaming (**Fig 2.12e**) can be utilised for particle concentration, although this configuration may be limited to a fixed droplet size. To accommodate the boundaries of the droplet that may not interact with surface acoustic waves (SAWs) in asymmetrical designs, a versatile interdigital transducer (IDT) design can be employed. This design ensures that the entire circumference of the droplet is exposed to an asymmetrical IDT wave, as depicted in **Fig 2.12f**.

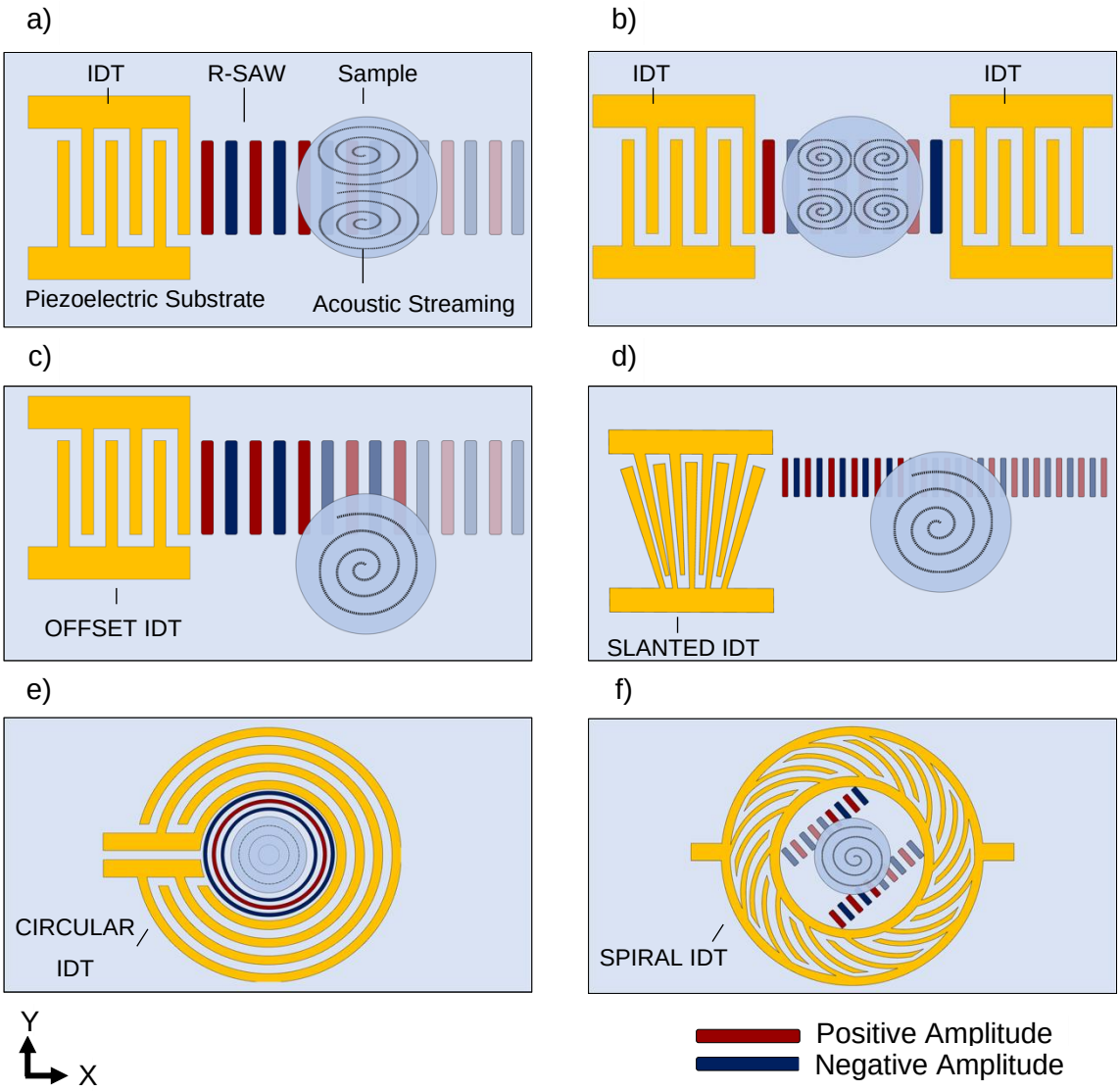

Figure 2.12. Various IDT configurations and designs relative to the liquid droplet for inducing different streaming patterns: a) Eckart streaming, b) four vortices created by two counterpropagating waves, c) single vortex streaming due to IDT offset, d) slanted IDT design generating a wave offset at a set frequency, e) circular IDT and f) an offset produced from all 360 degrees around the droplet, resulting in a more circular single vortex streaming pattern [132].

The fluid domain can be manipulated to adopt closed boundary conditions at a microscale, such as in the case of microchannels. An illustration of a surface acoustic wave attenuating into such a structure is provided (**Fig 2.13a**). Despite these boundary conditions, the attenuation of the wave is exclusively governed by the speed of sound in the mediums, maintaining Snell's law of wave attenuation at an angle. This principle remains applicable even under these unique circumstances.

The microchannel setup is particularly advantageous in particle separation applications, especially when coupled with the superposition of two counterpropagating waves in the channel. The transmission of the acoustic radiation force under these conditions leads to the establishment of a standing wave field within the fluid domain. This wave field consists of alternating high- and low-pressure areas (**Fig 2.13b**, red and blue regions respectively), forming antinodes and nodes respectively. The pressure antinodes correspond to areas of maximum pressure fluctuation, whereas the pressure nodes are points of minimal pressure variation. This alternating pressure landscape exerts differential forces on the suspended particles, effectively guiding their movement. Through the previously described acoustic radiation force, particles can be propelled towards either the pressure nodes or the pressure antinodes, depending on factors such as their acoustic contrast factor and size.

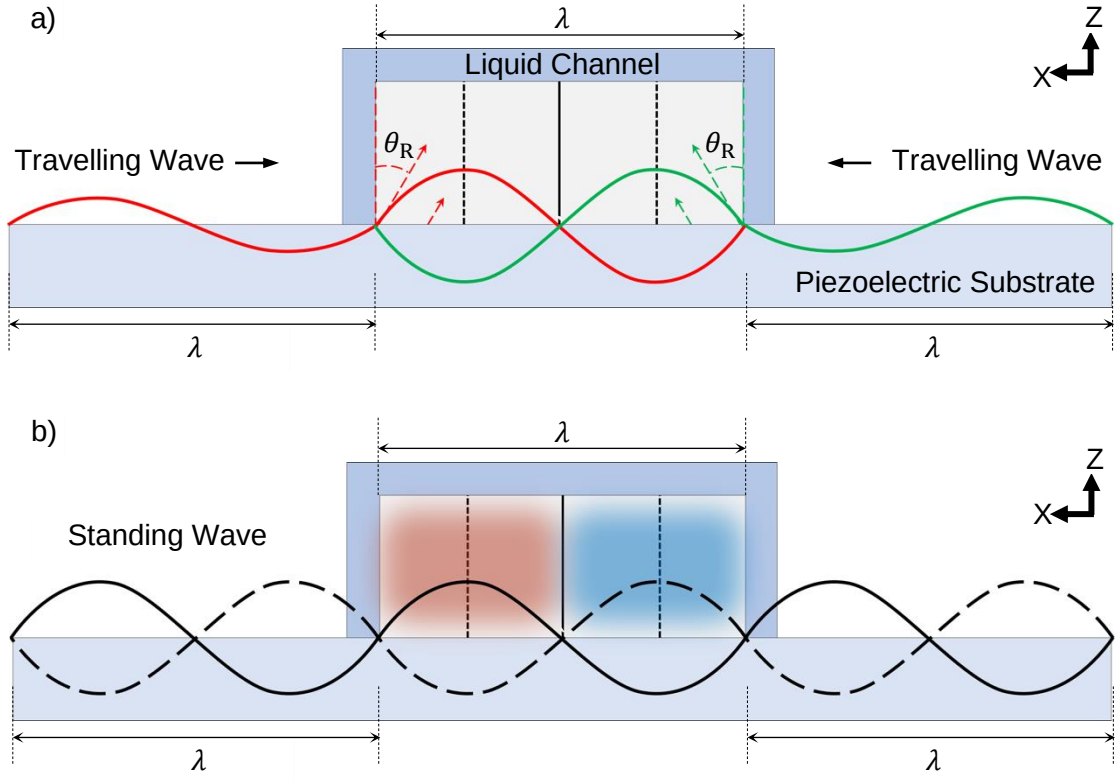

Figure 2.13. Microfluidic channel interaction with a surface acoustic wave: a) initially, the wave diffracts into the droplet at a Rayleigh angle, which superimposes with the identically counter propagating wave and induces b) nodes (solid line) and antinodes (dashed line).

There are various methods to generate standing waves and expose them to particles. Among these methods, the mentioned SAW or BAW transducers are commonly employed. To produce Standing Surface Acoustic Waves (SSAWs), two counterpropagating SAW

transducers are typically utilised at identical frequencies. On the other hand, for BAW (as illustrated in **Fig 2.14**), transducers can be coupled with a glass capillary [182] or in between silicon walls [183] to form a channel-like structure.

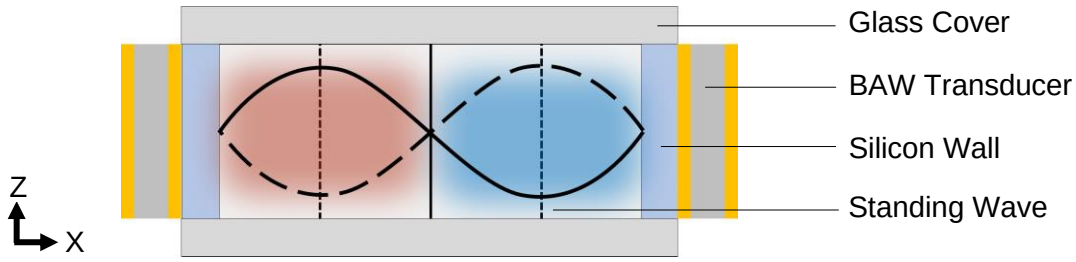

Figure 2.14. Induction of standing acoustic wave in a glass capillary due to the BAW transducer [183].

SAW devices are preferred due to their high precision and the ease with which they can be miniaturised, as well as their strong acoustic radiation force. However, their low throughput and high cost can be limiting factors. On the other hand, BAW devices are favoured for their simple device architectures and high throughputs. However, due to lower frequencies associated with BAW devices they are not ideal for handling particles >1 µm and require cooling due to excessive heat. Thus, the choice between SAW and BAW devices should be made depending on the specific application requirements, considering the advantages and limitations of each type of device.

The two major governing forces, drag force (or in this context acoustic streaming force; ASF) and Acoustic radiation force are both experienced by the particle and the fluid; however, one will dominate over another. For particles surpassing a certain size threshold, their motion becomes primarily governed by the acoustic radiation force. This size threshold isn't a constant value, but rather depends on a range of parameters. These include factors like the actuation frequency, the acoustic contrast factor (which represents the difference in acoustic properties between the particle and the surrounding fluid), and the kinematic viscosity (which is a measure of the fluid's resistance to flow). In the case of **Eqs. 2.25 & 2.33** particle size, mass, compressibility, and density will govern whether ASF or ARF are dominant. To illustrate this, we solve the equations and plot the results (**Fig 2.15a**) across a range of frequencies and particle sizes. The threshold line is indicated by a black dashed line. For enhanced understanding, **Fig 2.15b** presents a 3D map, demonstrating that even though the frequency increases, the force exerted on the particles remains predominantly influenced by their mass.

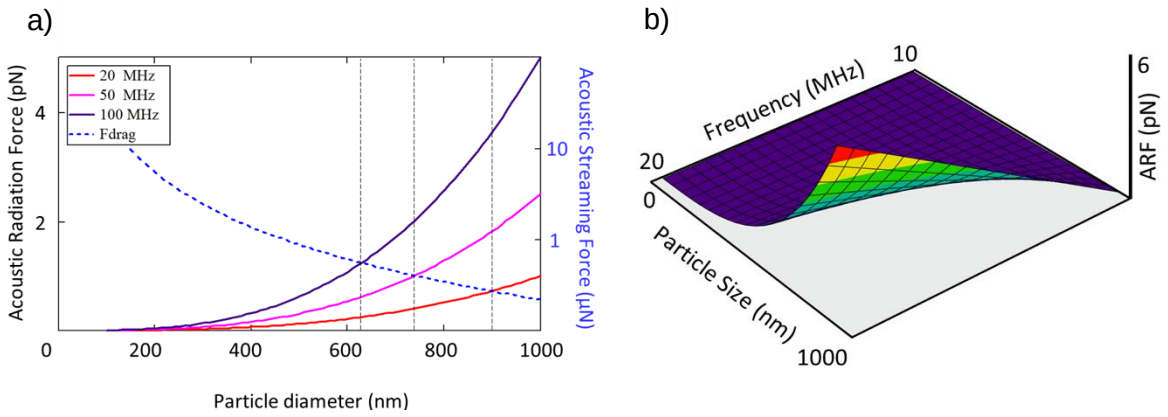

Figure 2.15. Numerical analysis of the effects of acoustic radiation and streaming forces: a) an increase in frequency leads to higher acoustic radiation forces, but these forces diminish for all frequencies as particle size decreases. The plotted acoustic streaming force for various particle sizes has a single point of intersection with the acoustic radiation force, indicating thresholds (dashed line) where one force becomes more dominant over the other. b) Illustrates a three-dimensional graph that emphasises the variations in particle size and frequency for modulating the acoustic radiation force.

2.9 Acoustofluidic Technologies

While acoustofluidic technologies find applications in diverse fields such as stimulation, patterning, and regenerative tissue applications [184], [185], [186], the following summary will focus on separation and concentration, outlining key concepts and limitations.

The phenomenon of ARF finds practical applications in size-based particle separation. By employing a microchannel configuration and introducing a heterogeneous sample into the system, subjected to a standing wave acoustic field, larger particles undergo a displacement due to the influence of ARF, ultimately translating them towards the pressure nodes of the standing wave. (see **Fig 2.16**). The acoustic waves can be excited either through a PZT or another ultrasonic source. In most scenarios, an IDT is present in technologies to form a SAW. As illustrated in **Fig 2.16**, the mixed sample is initially passed through a sample inlet, with one or two sheath flows. Upon SAW excitation, the smaller mass objects (depicted in green) remain unaffected by the radiation, while the larger ones (depicted in red) are compelled towards the acoustic nodes. Subsequently, three individual outlets facilitate the collection of the separated particles.

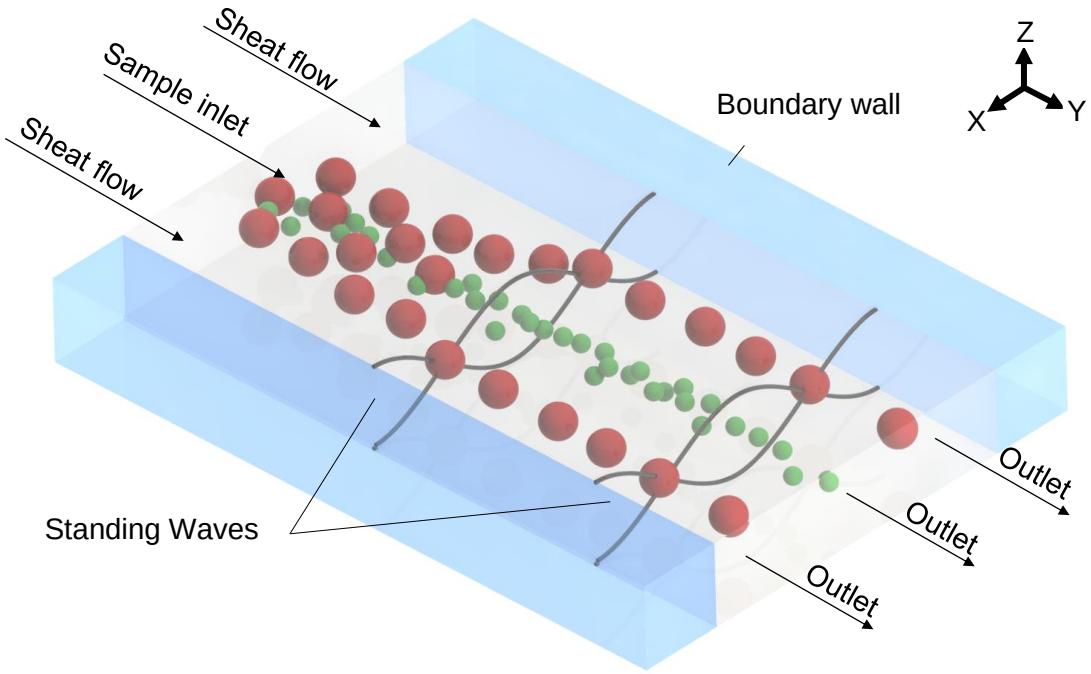

Figure 2.16. Size based particle separation due to the standing acoustic waves.

This technology has been applied numerous times, in instances such as, Escherichia bacteria separation from peripheral blood mononuclear cells (PBMC) with 91.5% efficiency [187]. The methodology can be seamlessly integrated with other approaches, such as imaging analysis. In a past study [188], a specific blood cell type was meticulously isolated from a pool of seven distinct blood cell types. Within the confines of this investigation, the image analysis software carefully activated the precise application of Surface Acoustic Wave (SSAW) to selectively actuate the targeted cells. One of the preeminent applications of Surface Acoustic Wave (SSAW) devices in contemporary research is the isolation of target cells, with a notable emphasis on circulating tumour cells (CTCs) [189]. CTCs, originating from tumour cells and distinguished by their larger size compared to normal cells, exhibit significant promise as valuable biomarkers, even in the early stages of cancer [190]. These cells possess a morphology that renders them ideal candidates for acoustofluidic separation based on their mechanical properties, utilizing a continuous Surface Acoustic Wave (SSAW). It's been demonstrated that the successful separation of various types of circulating tumour cells (CTCs) from white blood cells (WBCs) using a tilted angled SSAW (taSSAW) device is a promising avenue [191]. Through the continued application of SSAW, CTCs were selectively manipulated based on their distinct mechanical characteristics, resulting in an impressive recovery rate exceeding 83%. Subsequently, the integration of a PDMS-glass top hybrid channel into this device configuration significantly enhanced throughput [190].

Even though cells separation is interesting SAW devices have been constantly pushed to the nanoscale manipulation due to the vast potential biomedical applications, such as EV separation. A two-stage tilted angled Surface Acoustic Wave (taSSAW) method is perpetually employed for successful exosome separations in microchannels. This method was initially used to isolate exosomes from whole blood [192]. During the first phase, taSSAW separated whole blood cellular components from EVs at a frequency of 20 MHz. Microvesicles and exosomes were the two subpopulations of EVs that were further separated in the second stage, which occurred at a higher frequency of 40 MHz. The two EV subpopulations were analysed using western blotting and exosome-specific markers to confirm the effectiveness of exosome separation. Majority of exosomes were found to be concentrated in the former subpopulation, according to the results. Applications for this novel device included the early diagnosis of brain injury by isolating exosomes from plasma [193]. In order to determine whether cancer was present in several patients, it was also utilized to isolate exosomes from their saliva [193].

It is crucial to emphasize that the represented EV separation methodology is not a result of acoustic manipulation of the EVs but rather the inverse. The separation becomes feasible because acoustic forces lack the capacity to influence particles of such diminutive size. This limitation becomes apparent in applications such as concentration. Most acoustic techniques plateau at around 1 μm particle size, representing a regrettable constraint [132]. The inherent advantages of acoustic methods, unfortunately, do not seamlessly translate into the realm of EV processing. Regrettably, very few studies have successfully directly processed EV samples, underscoring the prevailing trend wherein most investigations impact everything around EVs rather than the EVs themselves.

For example, an acoustofluidic multi-well plate utilized circular stranding flexural waves to enrich micro/nanoparticles and cells [194] (**Fig 2.17d**). Upon excitation of the piezo ring, the acoustic waves move the particles in suspension to the middle. While this method can easily accumulate particles sized 30 μm, this method is limited to particles no smaller than 470 nm (carboxyl magnetic particles) and fall short of EV particle manipulation size. The size limitation threshold agrees with the ARF and ASF force comparison visualisation presented in **Fig 2.15.**

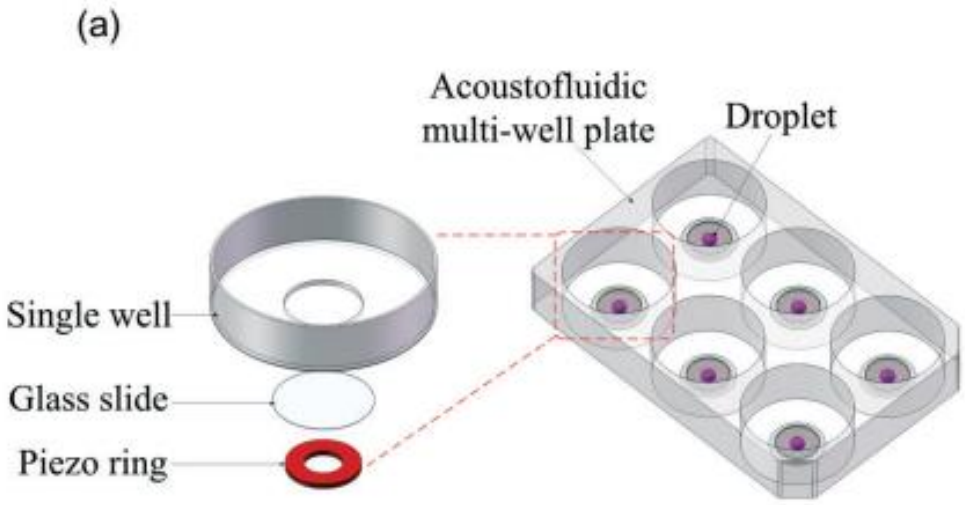

Figure 2.17. Acoustofluidic multi-well plate [194].

Alternatively, travelling surface acoustic wave (SAW) techniques (**Fig 2.18**) have been extensively researched over the years, aiming to address the limitations inherent in acoustic manipulation. By generating asymmetric SAW to cause azimuthal bulk liquid recirculation it is possible to generate an inward radial force that concentrated particles and yeast cells (5 - 10 µm) [195]. Subsequently, by carefully manipulating SAW frequency, streaming and radiation forces can be balanced for particle separation of 6 and 31 µm in a 2 µL sessile droplet [196], as well as 1 and 5 µm, 1 and 10 µm, 3 and 5 µm in the sample [197], [198].

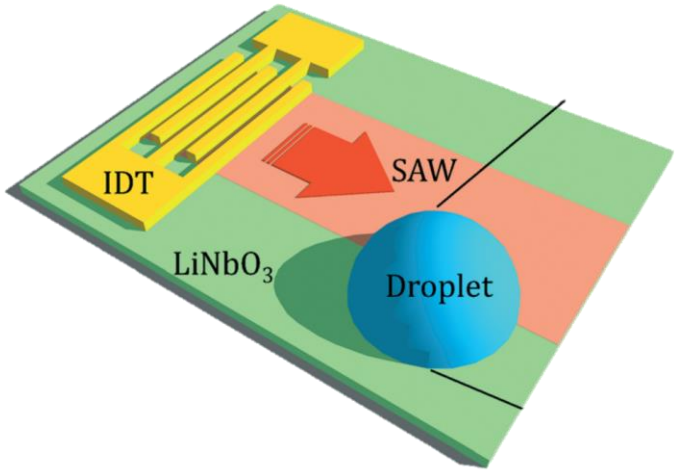

Figure 2.18. Sessile droplet, experiencing a travelling acoustic wave, emitted by the IDTs [195].

The notable limitation lies in the infrequent endeavour of the presented studies to influence particles smaller than 1 µm. Consequently, for applications such as drug delivery or detection, there is a clear imperative for focused investigations into direct manipulation

methods to attain concentration. Despite successful separation, concentration in these contexts remains underexplored and demands dedicated attention.

In pursuit to target these issues, effective concentration of nanoparticles was demonstrated by using chirped interdigital transducers (IDTs) producing SAWs in a glass capillary (**Fig 2.19**), in which nanomaterials ranging from 80 nm to 500 nm were enriched [199]. It is worth noting with due consideration that the volume throughput attained was modest, reaching only 0.5 µL. Given the sizes of EVs ranging way below 80 nm, particularly relevant in clinical applications, there is a need for an increase in throughput and continue enhancing the acoustic resolution to impact even smaller objects effectively.

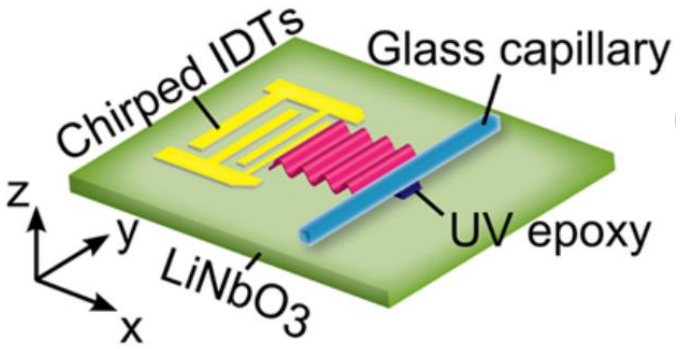

Figure 2.19. Scheme of the acoustofluidic-based nanoparticle-enrichment device [199].

One of the most notorious technologies, were the double-slanted IDTs (**Fig 2.20**) designed to yield a combination of acoustic streaming and droplet wobbling to break through the limitation of manipulating nanoparticles less than 100 nm. Rapid nanoparticle concentration and extracellular vesicle isolation/encapsulation were demonstrated, with the smallest size of 28 nm concentrated within 1 min in the samples up to 20 µL [200],[201].

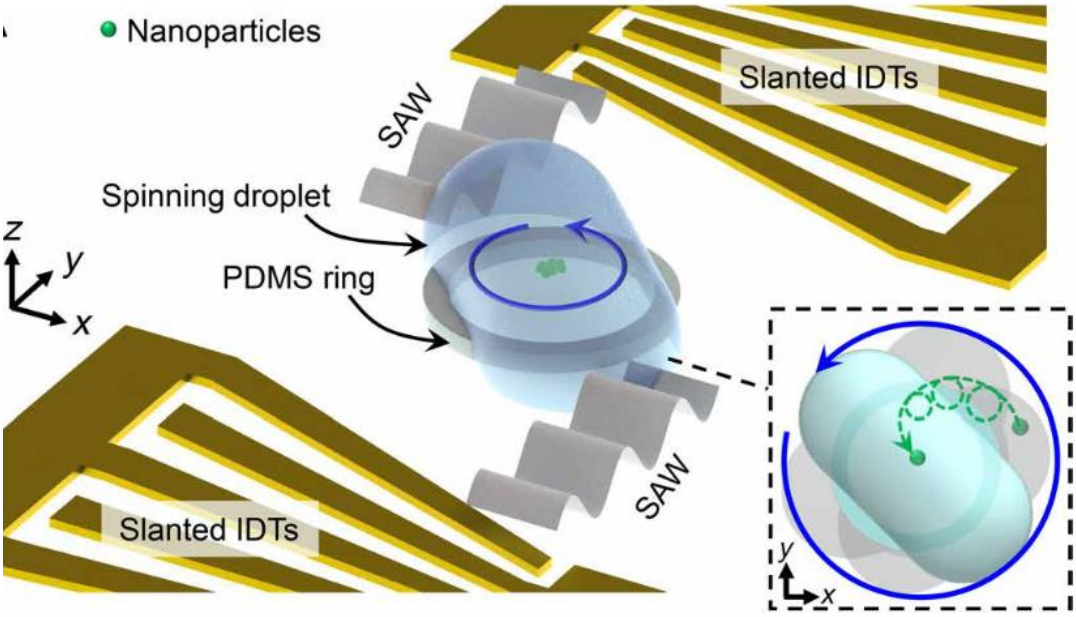

Figure 2.20. The acoustofluidic centrifuge system involves placing a droplet on a PDMS ring, which serves to confine the fluid boundary and is positioned between two slanted Interdigital Transducers (IDTs). As Surface Acoustic Waves (SAWs) propagate into the droplet, the liquid-air interface undergoes deformation due to the acoustic radiation pressure, initiating the rotation of the droplet. Particles within the droplet exhibit helical trajectories (inset) influenced by both induced vortex streaming and the spinning motion of the droplet [200].

While the wobbling technique proves challenging to control and replicate, the limited sample volume (below 20 µL) and the necessity for frequent recalibration due to the IDT design's adjustments of Surface Acoustic Wave (SAW) waves pose notable drawbacks. Furthermore, the absence of demonstrated retrieval capabilities, combined with the low sample volume, is attributed to the requirement for a robust spinning speed and internal streaming velocity. Notably, the open microfluidic design, while offering advantages, may still be susceptible to potential evaporation issues during extended processing times. Building upon the past advancements and evident fallbacks, the presented thesis investigates and extends the capabilities of acoustic manipulation for efficient nanoparticle concentration, aiming to address the critical challenges posed by the manipulation of particles smaller than 100 nm.

Chapter 3

Methods of the Dynamic Acoustofluidic System (DAS)

3.1 Introduction

In this chapter, we present a comprehensive methodology that introduces novel concepts and sets the stage for the experiments detailed in the following three chapters. Acoustofluidic devices, particularly those utilizing surface acoustic waves (SAWs), have shown significant potential in various biomedical applications, including cell separation, manipulation, and stimulation. One key advantage of SAW devices over bulk acoustic wave devices is their ease of fabrication for high-frequency applications and integration with microfluidic systems.

Traditionally, interdigital transducers (IDTs) are patterned on piezoelectric substrates using photolithography. However, this technique necessitates cleanroom facilities and results in permanently patterned IDTs, which limits their reusability. To address these limitations, this chapter introduces a novel development method for both the IDTs and microchannels, termed the Dynamic Acoustofluidic System (DAS). This innovative approach enables rapid prototyping and reconfigurability using off-the-shelf components and a portable control unit.

Additionally, we detail the methods for producing an acoustofluidic device for both microchannel and sessile droplet applications, incorporating 3D printable consumables. By introducing these novel concepts and methodologies, this chapter lays the foundation for the experimental work that follows in the next three chapters, showcasing the practical applications and advantages of the Dynamic Acoustofluidic System.

3.2 Thin film Printed Circuit Board Interdigital Transducer

One of the key components of an acoustofluidic system is the Interdigital Transducer (IDT). Traditionally, IDTs are fabricated using photolithography, a process that is not only expensive but also results in a fixed, non-modifiable system. To create a more versatile unit, we utilized detachable electrodes through the Thin-Film Circuit Board (TCB) technique. This approach allows for greater flexibility and cost efficiency, enabling rapid prototyping and reconfiguration of the acoustofluidic system. The TPCB patterned with interdigital electrodes was made by circuitfly.com, which consisted of dual metal bilayers (Au/Ni, 30 nm/2 μm) patterned on a 70 μm thick polyester laminate. The period of the interdigital electrode, electrode number, and aperture size were 200 μm, 40 pairs, and 13 mm, respectively. The

TPCB was linked with a coaxial wire soldered to its bus pads and terminated with an SMA connector.

3.3 TPCB and $LiNbO_3$ coupling.

To generate surface acoustic waves, the TPCB electrodes must be correctly coupled and positioned on the piezoelectric surface. During photolithography, electrodes are bonded to the wafer, ensuring good electrical contact. However, since the TPCB is detached, the electrodes need to be mechanically held in place to contact the wafer (**Fig 3.1**).

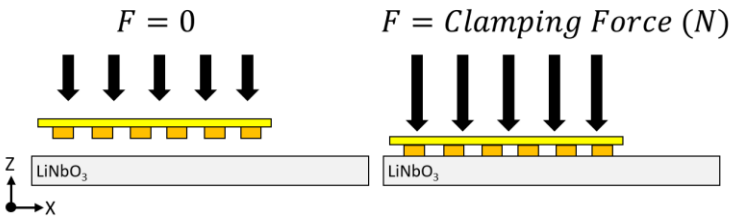

Figure 3.1. Concept illustrating the necessity of attaching TPCB to the lithium niobate, using some force.

If the mechanical pressure on the interdigitated transducers (IDTs) is too low, the contact will be poor; if it is too high, the waves will be suppressed. This relationship can be experimentally demonstrated by measuring the reflection coefficient (S_{11}) using a vector network analyser (VNA).

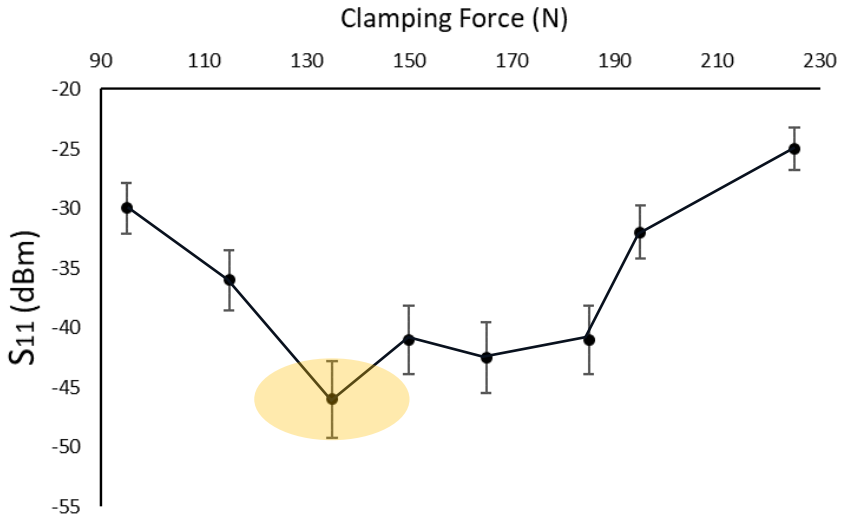

Figure 3.2. Relationship between the S_{11}/ at Rayleigh mode and the clamping force.

As observed (**Fig 3.2**), there exists a critical pressure point (**Fig 3.2, orange area**) where the electrodes achieve optimal contact, referred to as the "sweet spot." It is important to mention that VNAs are expensive. Therefore, when developing an accessible system, this chapter also discusses an alternative method to find this optimal contact point without using a VNA.

3.4 TPCB Housing (DAS-A)

The first step in developing the DAS involves the mechanical assembly of the Thin-Film Printed Circuit Boards (TPCBs), specifically focusing on the positioning of Interdigitated Transducers (IDTs) on the wafer. During this stage, both scenarios—particle alignment and sessile droplet manipulation—are carefully considered in the development process.

First, the DAS-A unit is developed to be configured for standing SAW applications with the incorporation of a microfluidic channel and presser (**Fig 3.3a**). Second, the DAS-A unit can be configured for travelling SAW applications such as sessile droplet manipulation (**Fig 3.3b**).

Nonetheless, both methods require a similar preliminary assembly process. A mechanical jig was utilised to mount the TPCB on the $LiNbO_3$ substrate and integrate the peripheral sensor components. As illustrated in **Fig 3.3c**, the DAS-A employs a straightforward clamping mechanism and is assembled in the following sequence, beginning from the bottom: a heatsink that supports the entire device and disperses heat, temperature sensors that measure the IDT temperature, $LiNbO_3$ that generates SAWs, TPCB IDTs that convert RF to SAWs, silicon pads that distribute clamping force evenly, localised pressers that apply the clamping force, force-sensitive resistors (FSRs) that measure the clamping force, FSR roofs that hold and press the FSRs, M5 screws that produce the clamping force, and main holders that hold the entire structure onto the heatsink. In this study, the experimental parts were produced using an Ender 3 Pro 3D printer (Creality, China). The printer was equipped with a 0.4 mm diameter nozzle and a heated print bed. The parts were designed using CAD software (Solidworks, USA) and saved in .STL file format. To prepare the parts for printing, slicing software (Cura) was used to generate the G-code files necessary for the printer. The parts were printed using PLA filament with a diameter of 1.75 mm, a layer height of 0.2 mm, and a print speed of 50 mm/s. The printing temperature was set to 200 °C, and the bed temperature was set to 60 °C. Following the printing process, the parts underwent a thorough cleaning and inspection to ensure there were no defects before being utilized in the experiments.

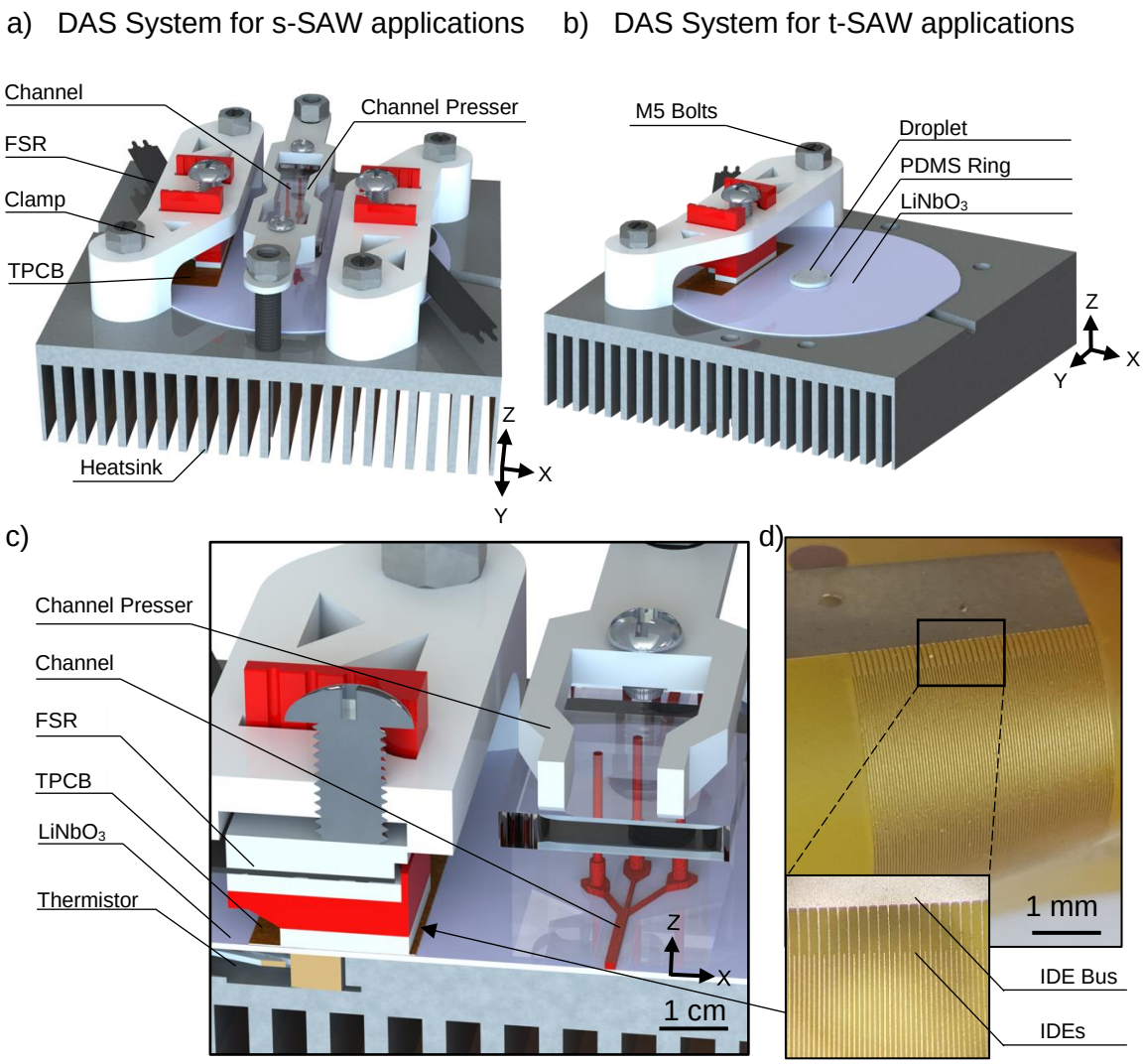

Figure 3.3. Design of the Dynamic Acoustofluidic System (mechanical components DAS-A) a) the DAS unit is configured to accommodate microfluidic flow for separation applications. b) the DAS unit is configured to accommodate a sessile droplet for streaming and concentration applications. c) shows a cross-section of the Z-X plane indicating critical components of the system. d) image of the TPCB IDT used in the experiments; the inset demonstrates the small nature of the IDT fingers.

3.5 Electrical System (DAS-B)

The second part of the DAS system comprises electrical components of the system. The electrical control unit was constructed using a microcontroller (ATMEGA328P) and integrated onto a proprietary PCB board, as depicted in **Fig 3.4c**. While most of the components on the PCB are relatively passive, the embedded system can be summarised as a block diagram, which highlights the system's key components, as shown in **Fig 3.4a**. The use of a microcontroller provided the system with the necessary computational capabilities to perform control and data acquisition tasks. The integrated design of the PCB board allowed for compact and efficient circuitry. The block diagram (**Fig 3.4b**) provides a clear overview of the system architecture, which is essential for understanding the system's functionality and performance. Essentially the re-chargeable portable unit is able to track its own IDT environment and take respective action based on the peripheral inputs. The design acts not only as a monitoring and IDT actuating system but as a guiding light for the user to assemble the device before operation.

a)

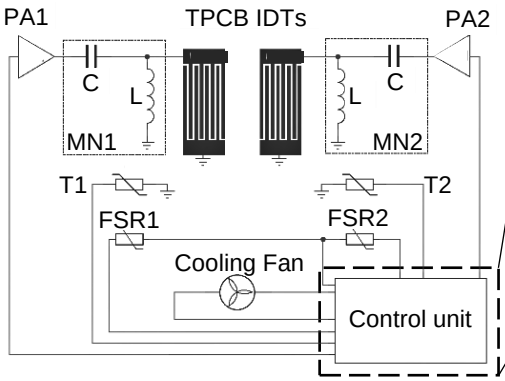

b)

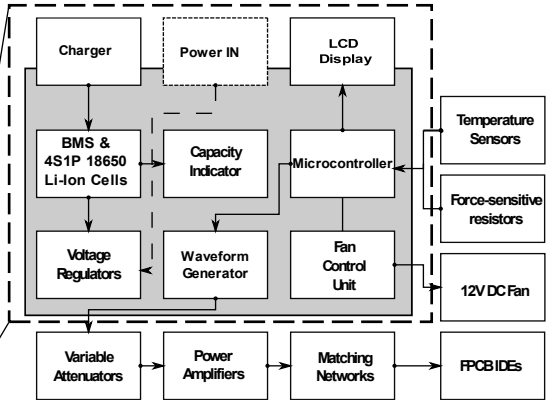

c)

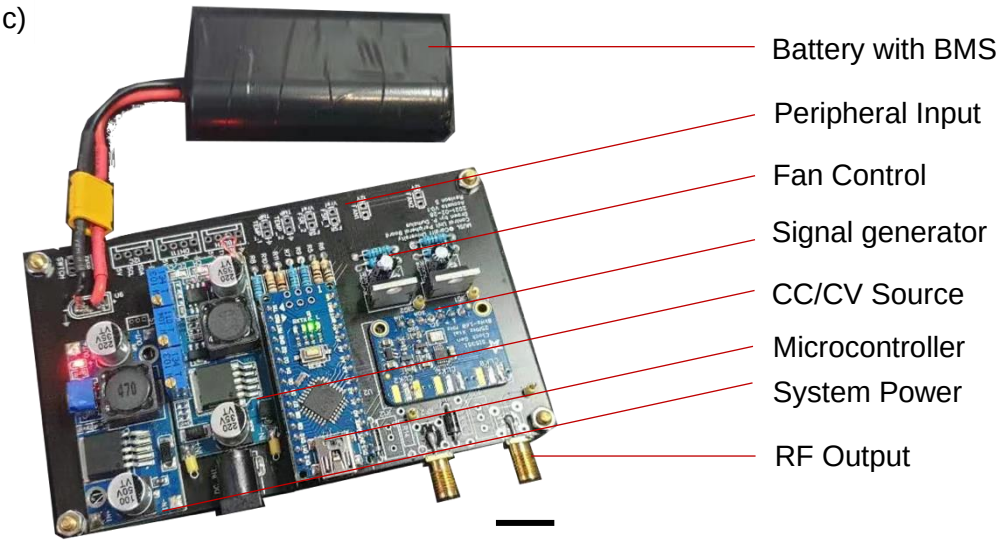

Figure 3.4. Design of the electronics system (electrical components DAS-B). a) shows a counter-facing arrangement of the IDTs and the peripherals tracking their performance, indicating a pair of thermistors, FSRs, matching networks, amplifiers and a single cooling fan controlled by the b) DAS-B system. c) shows an early model of the electronics PCB board accommodating key components. Scale bar 10 mm.

3.5.1 Power and Charging

The DAS-A module can be powered by either an internal battery or an external power supply. The battery, manufactured using 18650 Lithium-Ion cells, was designed to provide the required operating voltage and reasonable capacity. Specifically, four series cells in parallel (4S1P) were spot-welded together to achieve the desired specifications. At full power, the system using one IDT draws approximately 1-1.5 A, which allows for several hours of continuous use, making it suitable for portable experiments. To ensure optimal and safe battery charge and discharge cycles, a battery management system (BMS) was added. The BMS maintains the cells' voltage at similar levels to avoid discharging into neighbouring cells. In addition, a constant current/constant voltage (CC/CV) module based on LM2596 was used during charging, limiting the current to around 1A. Although this results in longer charging times, preventing Li-Ion cell damage is essential.

Furthermore, a battery capacity indicator was incorporated to inform the user of the current battery status. Although the integrated battery is a convenient feature, it is not a critical application component. Overall, the design and implementation of the battery management system ensure the safe and reliable operation of the DAS-A module.

3.5.2 Temperature

To monitor the temperature of the system, three temperature sensors were incorporated. The LM35 sensor was used to measure the internal temperature and humidity (DH11) of the device. In contrast, temperature sensors were placed beneath the IDTs (**Fig 3.4a**, T1 & T2) to prevent damage to the internal components and battery during charging. However, during experimentation, the significant amount of noise emitted by the IDTs hindered the collection of accurate data. To mitigate this issue, thermistors with a 10 kΩ voltage divider were employed, with supporting components placed further away (+10 cm) to prevent local voltage potential splits within the chip. A separate voltage reference node was established exclusively for the thermistors, and the noise was filtered out by employing coils and chokes. The effectiveness of this approach was validated by comparing the readings with those of

two industrial thermometers (**Fig 3.5a**). As the temperature of the IDTs increased, a cooling fan was activated once a certain threshold was reached. A closed-loop control system was established by utilising an off-the-shelf N-Channel MOSFET (**Fig 3.4a**, Fan Control Unit) and toggling a GPIO pin (active-high). To evaluate the efficacy of the cooling system, the device was heated on a heat plate and removed once it reached 40°C. The device's temperature was monitored until it returned to room temperature (~21°C), and it was found (**Fig 3.5b**) that the device reached room temperature 95% faster when the cooling fan was active.

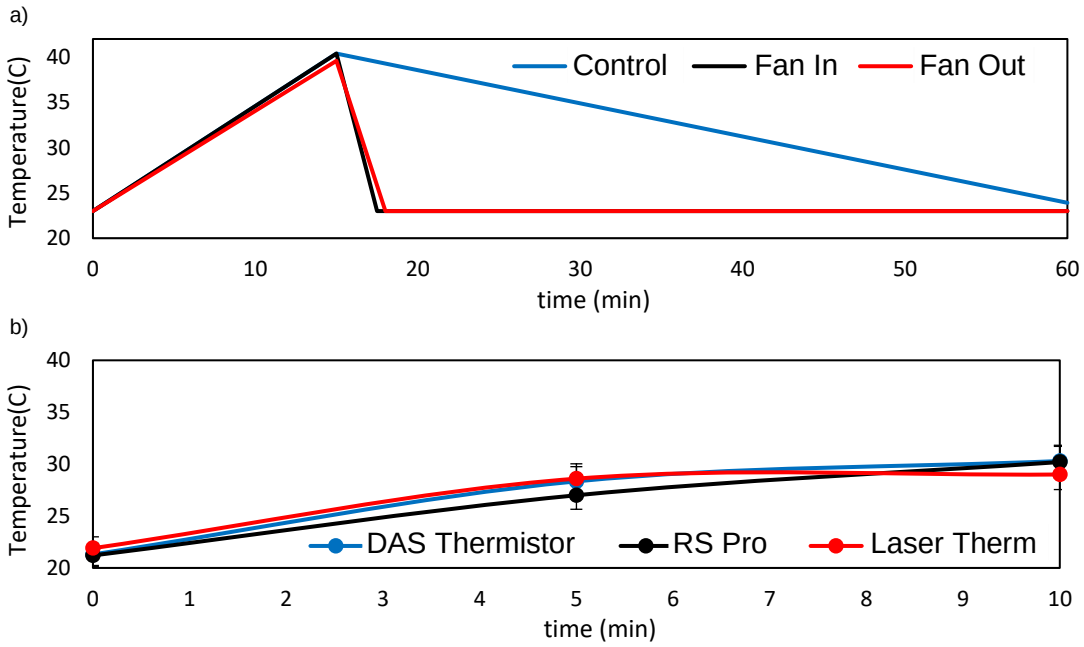

Figure 3.5. Characterisation of the fan performance and a) effects of the fan direction and presence. b) The thermistors' validity is in line with commercially available monitoring systems.

3.5.3 Signal Generation

If the DAS system was not utilized, radio frequency (RF) signals were generated using a signal generator (RS Pro RSDG 5162) and amplified with an RF power amplifier from Mini-Circuits (USA). However, to achieve a fully integrated device, it is essential to generate the signals required to drive the IDTs. To accomplish this, a silicon chip (Si5351) capable of three different RF frequency (8 kHz – 160 MHz) signal sources were integrated into the system and made accessible through a standard I2C protocol (**Fig 3.4b**, Waveform Generator). However, the signal generated by the Si5351 is only capable of reaching a maximum peak voltage of 5V, which is insufficient to drive the IDTs. To address this issue, an off-the-shelf amplifier was employed and mechanically integrated into the system (**Fig**

3.4b, Power Amplifiers), thereby allowing for an integrated heatsink as well. The selected 6W amplifiers were sufficient for all subsequent experiments, although it should be noted that this level of power may not always be required. To introduce power adjustment, a proof-of-concept series variable resistance was added. However, the author quickly discovered that reflection could damage the system and the amplifier was rapidly destroyed. To prevent such damage, a diode was initially introduced, but this approach was abandoned due to the significant forward voltage drop (~0.7V). Subsequently, an electrically controlled variable attenuator (ADC----) was added before the amplification block (**Fig 3.4b**, Variable Attenuators). There are several methods for adjusting the power of the amplifiers output, including manual adjustment by turning the feedback knob on the variable attenuator or replacing the knob with an I2C programmable variable resistance chip, which would enable output power to be adjusted via software.

3.5.4 Force Sensitive Resistors (FSR)

To achieve efficient propagation of surface acoustic waves (SAWs), it is critical to exert an appropriate clamping force on the TPCB-IDT mounted on the wafer using the mechanical setup described previously. Insufficient pressure will result in insufficient contact between the IDTs and the piezoelectric substrate, whereas excessive pressure will choke the IDTs and prevent efficient SAW propagation. Vector Network Analyzer is typically used to determine the reflection coefficient S_{11}, but it can be expensive and difficult to operate in the context of a flexible and accessible system. To address this concern, a force-sensitive resistor (FSR) was integrated between the IDT and the clamping bolt. The FSR undergoes deformation and changes its electrical resistance in response to the applied pressure, enabling measurement of the pressure using a microcontroller (ATMEGA328P). Under no stress, the FSR reports 0; under maximum stress, it reports 1024 due to the total ADC resolution of 10 bits. The corresponding FSR resistance can be linked to the pressure applied by bolts to determine whether the optimum pressure was applied for efficient SAW propagation. The value of the FSR is then finally co-related with the S_{11} and can indicate whether too much or too little force is exposed. **Fig 3.6** shows a decreasing reflection coefficient as more pressure is added until the reflection coefficient t picks back up. At around 200 (a.u), optimal S_{11} is achieved and can be used for assembly without the need to use expensive VNA equipment. This is very consistent with the sweet spot observed in **Fig 3.2**.

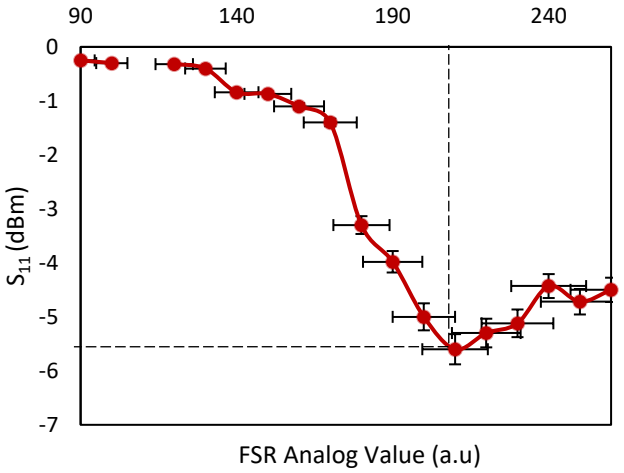

Figure 3.6. Force sensitive resistor and S_{11} relationship indicating an optimum pressure of the TPCB clamping force (dashed lines).

3.5.5 Matching Network

The TPCB technique employs mechanical clamping of the finger electrodes to the wafer, which introduces an impedance mismatch due to contact resistance between the two materials. To address this issue, matching networks (MN) based on lumped components were designed, with the specific components chosen depending on the IDT used. A proprietary PCB (**Fig 3.7d**) board was built to accommodate the calculated inductors and capacitors for all MNs. S_{11} was initially measured using a Vector Network Analyser (VNA) Smith chart, and calculations were performed to bring the impedance point to the middle (**Fig 3.7a**). During the design of a matching network, S_{11} is recorded by placing the matching network PCB in series with the same wires used in the experimental setup. The PCB is then short-circuited (**Fig 3.7d**, black arrow) to allow the signal to pass through, and this accounts for any impedance alterations introduced by PCB and wire imperfections when selecting the correct components. However, in most cases, the calculated values were not able to achieve the desired matching, and therefore the final matching network was designed by carefully tuning different components on the PCB over multiple attempts.

An example is shown in **Fig 3.7e-f** of two TPCB IDTs before and after, respectively. For the initial impedance (Z=23.3-18.5 jΩ), a CL network is built with 170 pF and 346 nH, respectively. A dramatic performance increase is observed as the S_{11} falls from -3 dBm to approximately -30 dBm.

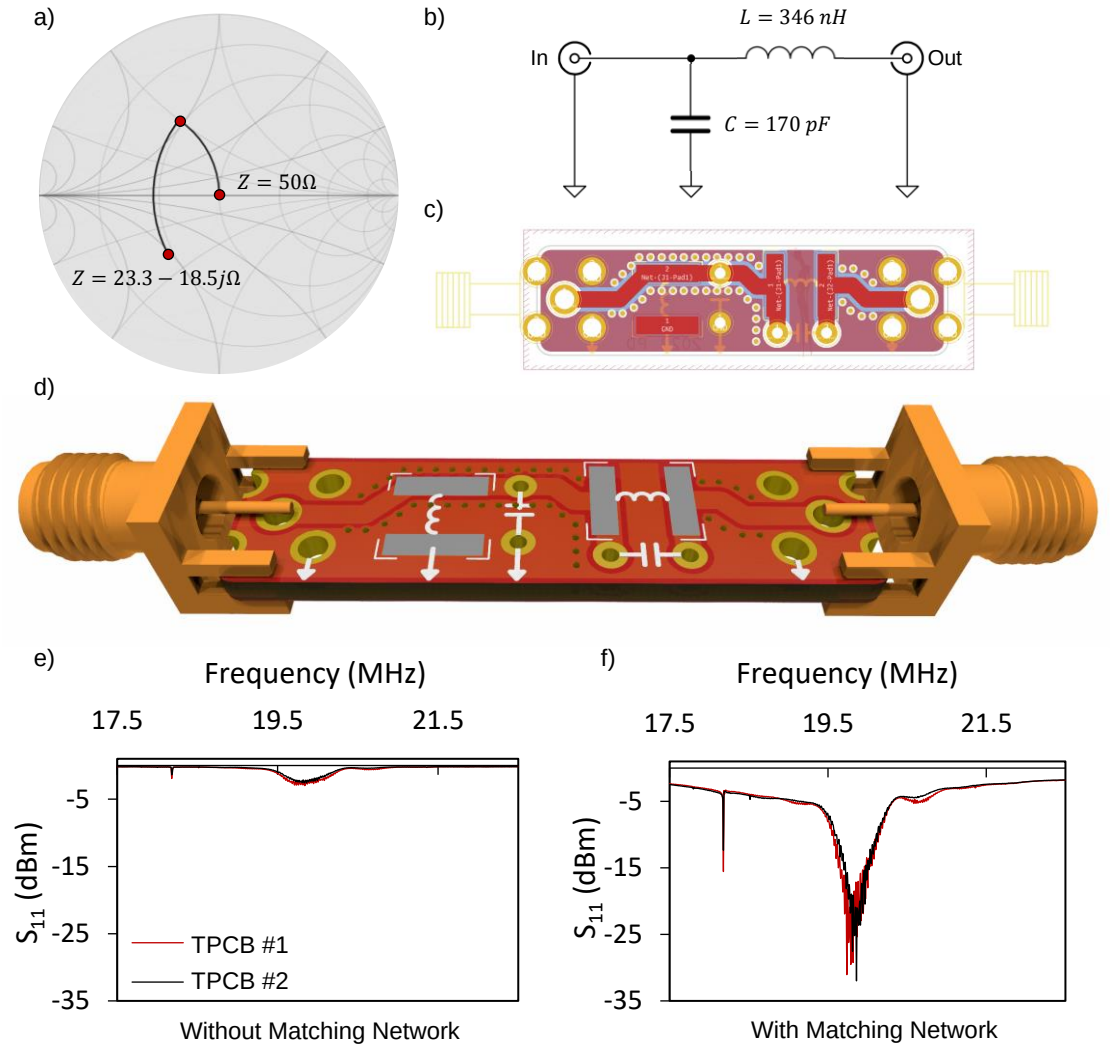

Figure 3.7. Design of the matching network for the DAS system a) Smith chart indicating impedances before and after matching network. b) high pass capacitor and inductor network with respective values, and c) the PCB designed to accommodate the circuit, followed by a d) 3D render of the PCB prior to manufacturing. Impedance matching of the TPCB is validated using S_{11} by two separate IDTs, e) before and f) after integrating the circuit.

3.5.6 Electronics Enclosure

The components previously discussed were integrated into a compact black box with an integrated interface, which underwent several iterations to improve its stability and execution. The device is powered by a rechargeable battery but can also be connected to an external power source. The internal amplifier can be bypassed to accommodate higher power requirements, and an external power amplifier can be used. The electrical box is equipped with an LCD screen for real-time monitoring of the system's parameters during

operation. The user is guided with feedback regarding the optimal pressure exerted on the IDTs and temperature limits. The frequency and power can be adjusted via two knobs and reprogrammed through a PC interface. The DAS-B unit is primarily intended for driving the TPCB-IDT (DAS-A unit) but can be applied in any acoustofluidic application that utilises two or fewer IDTs. Although there are several potential improvements for a more integrated version, such as an FPGA-based waveform generator module, an integrated coupler for monitoring delivered and reflected power, a more user-friendly interface, and support for higher IDTs and power, the current device has enabled exploration of the lithium niobate.

3.6 3D Printer Based Acoustofluidic Consumables

Microchannels are small, narrow channels with dimensions typically in the range of micrometres. Microchannels can be manufactured using techniques such as photolithography, soft lithography, and micro-milling. However, these techniques often require expensive equipment and can be time-consuming and labour-intensive. To maintain DAS as a dynamic and accessible method, consumables such as microchannels and rings must be manufactured with widely available equipment. Our team developed 3D-printed moulds using PLA to replace traditional silicon wafer-based ones, eliminating the need for clean room-based manufacturing. To create these molds, a 0.25 mm nozzle and 1 mm thick glass slides were used. The process of developing the moulds is shown in **Fig 3.8a**. The first step involved placing a glass slide (measuring 76 mm (W) × 26 mm (L)) onto the 3D printer table and securing it with masking tape (**Fig 3.8a-1**). To accommodate glass slides of varying thicknesses, we adjusted the "Z offset setting" plugin in the 3D printer software (Cura). Next, the 3D-printed mold was directly printed onto the glass slide using a 3D-printer. Once completed, the mould was removed (**Fig 3.8a-2**) from the printer and allowed to cool. We inspected the structure to ensure full contact between the 3D-printed mold and the glass slide. The glass-bottom 3D-printed mould was then placed into a plastic petri dish and filled with PDMS (**Fig 3.8a-3**) (Sylgard 184, Farnell UK) following the manufacturer's protocol. The mold was cured on a hot plate (SD160, Colepalmer) at 45 °C for 24 hours, which is below the PLA melting temperature of 60 °C. Once the PDMS had set, we removed (**Fig 3.8a-4**) it from the mold, cut the outer perimeter of the channel and punch holes for the microfluidic tubing. We then placed a premade acrylic presser (measuring 47 mm (L) × 15 mm (W) × 3 mm (H)) on top of the microchannel and bolted it onto the pre-assembled DAS using a microchannel presser (see **Fig 3.3a**). The M5 nuts on the far edges of the microchannel presser were fastened until resistance was felt. Then, the M3 screws were screwed in to ensure an even distribution of the pressing force. Examples of the glass-bottom 3D printed

moulds, including single inlet/outlet and 3-inlet-2-outlet structures, are shown in **Fig 3.8b left**. Overall, this process allowed us to create moulds without the need for a clean room, making the process more accessible and efficient. The repeatability of the channel dimensions is presented in **Fig 3.8b right.**

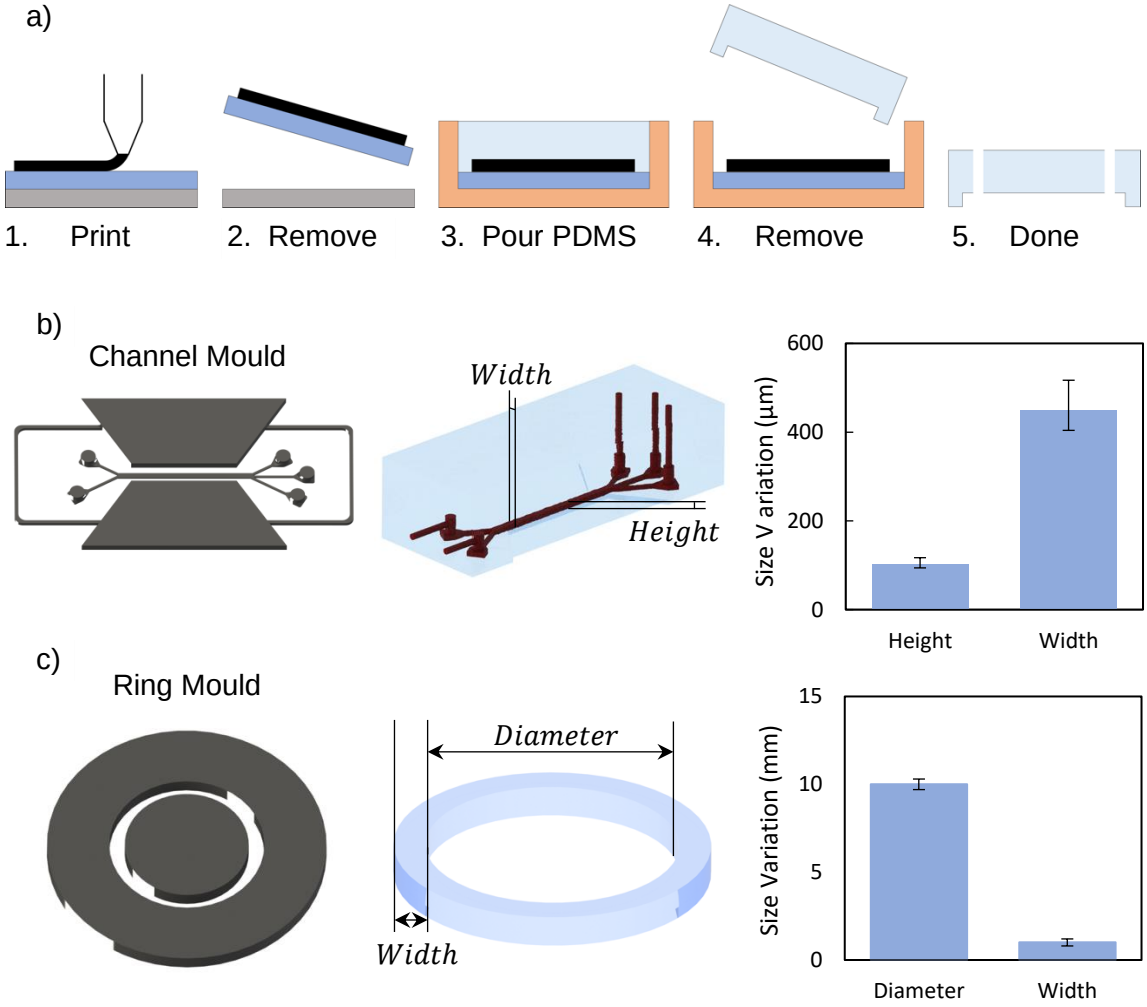

Figure 3.8. Microchannel manufacturing using a glass-bottom 3D printed mold: a) Progressive stages of developing the microchannel with the aid of the glass-bottom 3D printed mold. The process is versatile can produce b) microfluidic channels with high repeatability, as well as high precision c) PDMS rings for sessile droplet manipulation.

In addition to microchannel manufacturing, various moulds could be printed using the same technique, such as PDMS Rings (**Fig 3.8c left**), usually required for streaming applications, especially when DAS-A is assembled for tSAW applications. The scale of rings is usually much larger, therefore, the error (**Fig 3.8c right**) associated with 3D printing is much smaller, this provides a reliable way of producing round boundary conditions. In addition to manufacturing the PDMS rings using the 3D printing mould technique, another approach is

presented in **Fig 3.9.** First, a small amount of PDMS liquid is prepared. A pipette tip is inserted into the liquid **Fig 3.9-1**, and care is taken to ensure no air bubbles are trapped inside. The pipette tip is removed, as the PDMS around its neck remains **Fig 3.9-2**, and the combination is placed on a glass slide **Fig 3.9-3**. A vacuum pump can be used at this stage to ensure that all the air bubbles are removed from the PDMS. The glass slide, with the pipette tip and PDMS on top, is then cured for 24 hours at 45°C. During this time, the PDMS solidifies and takes the shape of the pipette tip. Once the curing is complete, the pipette tip is slowly removed, leaving behind PDMS rings with a diameter corresponding to the pipette's dimensions **Fig 3.9-4**. It is important to note that this method requires a high level of precision, and repeatability depends on the skill of the user. The insertion of the pipette tip into the PDMS requires careful attention to ensure that no air bubbles are trapped, and the process of removing the pipette tip must also be done carefully to avoid damaging the PDMS ring. As a result, this method is not suitable for high throughput manufacturing, but it can be useful for producing small quantities of PDMS rings with thinner walls, which can be beneficial in ensuring minimal SAW dampening the crossing over the boundary into the liquid.

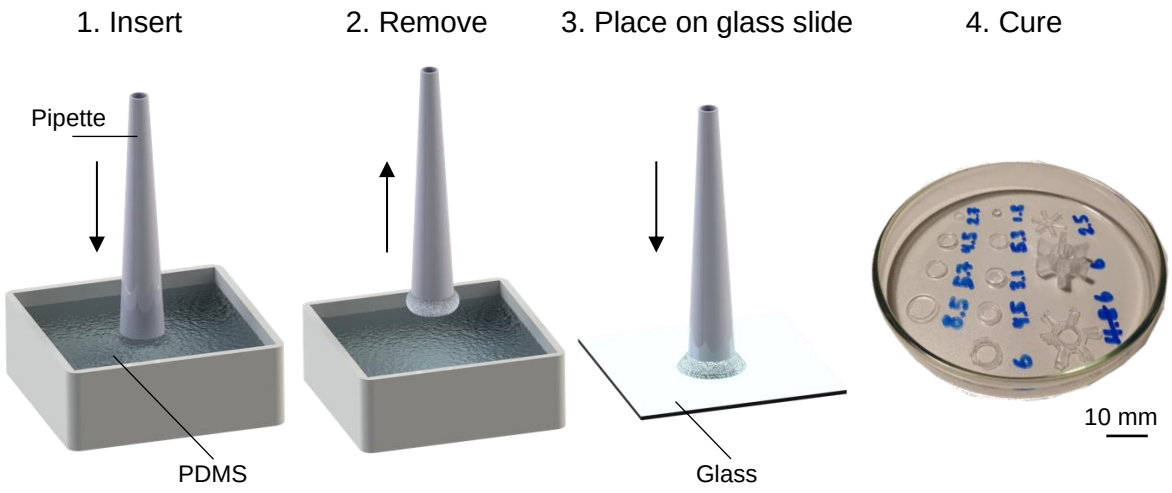

Figure 3.9. Alternative methodology to producing PDMS rings in a faster fashion. The process involves dipping a pipette into the PDMS and then curing it on a glass slide.

3.7 Assembly of the TPCB using a VNA

Before we benchmark assembly method and acoustofluidic capabilities of the DAS system, we assemble it using conventional methods such as VNA and treat it as a control group. To make sure the IDT is parallel to the edge of the reference flat minimum S_{11} value is used. During the preliminary assemblies of the DAS, an intriguing observation was made by

intentionally misaligning and not aligning the IDTs resulted in a decrease (or negative value increase) in the devices insertion loss (S_{21}). From this, we developed the theory that the S_{21} reading and a VNA could be used to align two IDTs chips with set locations to be parallel. To test this theory, we employed the procedure outlined in **Fig 3.10**, which involved connecting two IDTs to the VNA as a two-port network, with one IDT acting as the receiver and the other as the transmitter. One of the IDTs was kept unmoved, while the other was rotated as the transmitting IDT, and the S_{11} of the transmitting IDT was measured to monitor its changes during rotation. Overhead camera images of the transmitting IDT at different orientations were captured and analysed using a customised MATLAB code to determine the angle between the two IDTs.

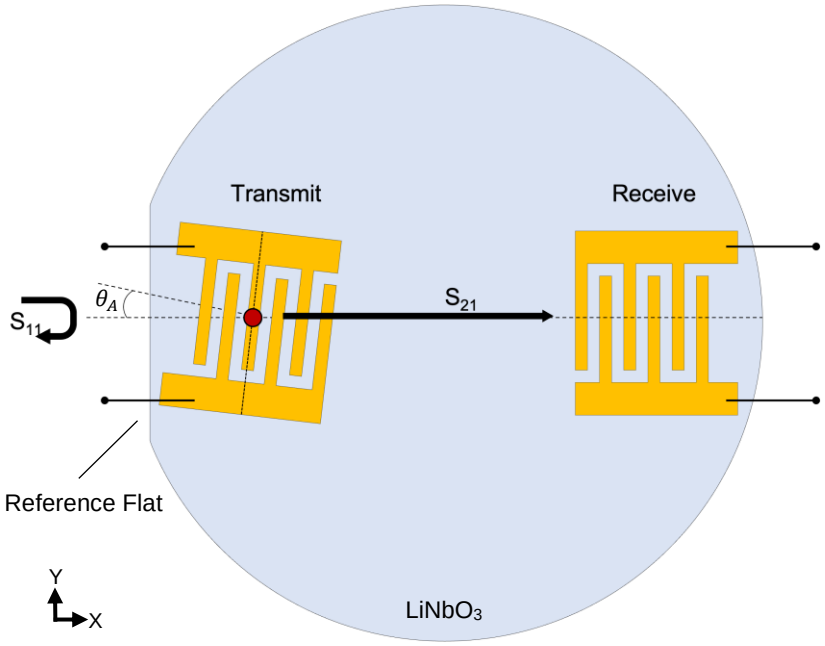

Figure 3.10. Schematic representing the setup used for S_{11} and S_{21} measurement. The received IDT is fixed while the transmitting IDT is twisted around the red point.

Five reference angles (17°, 11°, 6°, 2°, and 0°) were determined for the S_{21} readings, which were selected by identifying the most observable change in the S_{21}. The resulting S-parameters for the S_{11} and S_{21} readings at different orientations are shown in **Fig 3.11a** and **Fig 3.11b**, respectively. The S_{21} peak is maximised at the 0° angle, and this quickly declines as the parallelism of the IDTs is lost. This confirms that the S_{21} reading can be reliably used to establish the parallelism of the two IDTs, while the S_{11} reading is less sensitive to the change in angle.

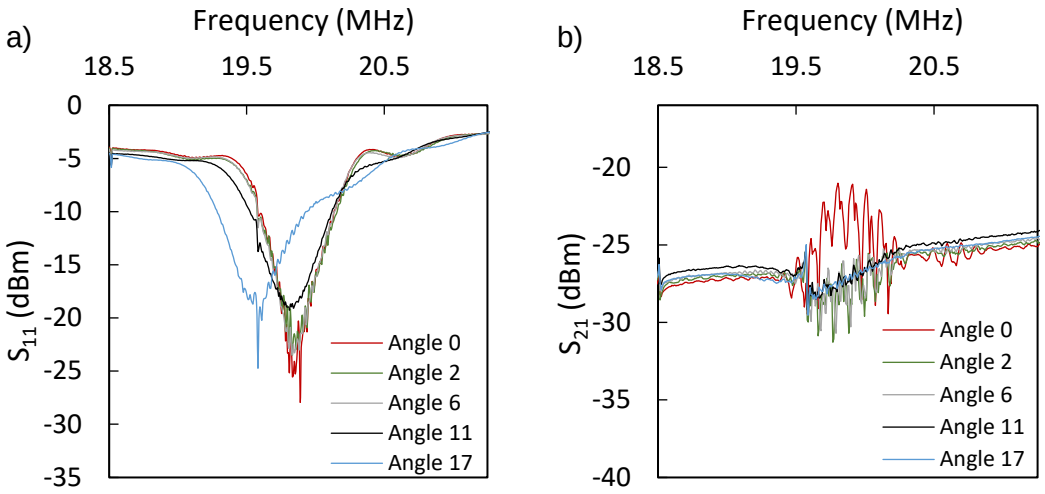

Figure 3.11. S-parameters of the DAS as an IDT rotates: a) Mean reflection coefficient (S_{11}) corresponding to different angles throughout the IDT's rotation. b) Mean insertion loss (S_{21}) at varying angles during the IDT's rotation.

3.8 Finite Element Model

To study the effects of TPCB misalignment and to address any arising hypotheses, a finite element model was constructed using COMSOL software (Multiphysics 5.4, COMSOL Inc) Piezoelectricity Multiphysics interface was used in the study. A trigonal crystal system with six elastic stiffness values, four piezoelectric tensors, and two dielectric coefficients was used to establish the piezoelectric characteristics. We utilized the piezoelectric coefficient values reported in Refs. [203] and [204] which yielded a complete definition of the Lithium Niobate as presented in Voigt notation:

$$[c_{ij}] = \begin{bmatrix} 199.5 & 55.27 & 67.67 & 8.7 & 0 & 0 \\ 55.27 & 199.5 & 67.67 & -8.7 & 0 & 0 \\ 67.67 & 67.67 & 235.2 & 0 & 0 & 0 \\ 8.7 & -8.7 & 0 & 59.48 & 0 & 0 \\ 0 & 0 & 0 & 0 & 59.48 & 8.7 \\ 0 & 0 & 0 & 0 & 8.7 & 72.2 \end{bmatrix} (GPa) \quad (5.1a)$$

$$[e_{ij}] = \begin{bmatrix} 0 & 0 & 0 & 0 & 3.65 & -2.39 \\ -2.39 & 2.39 & 0 & 3.65 & 0 & 0 \\ 0.31 & 0.31 & 1.72 & 0 & 0 & 0 \end{bmatrix} \left(\frac{C}{m^2}\right) \quad (5.1b)$$

$$[k_{ij}] = \begin{bmatrix} 45.05 & 0 & 0 \\ 0 & 45.05 & 0 \\ 0 & 0 & 26.2 \end{bmatrix} \quad (5.1c)$$

Firstly, the crystal and IDT coordinate systems were defined as (α, β, γ) and (x, y, z), respectively. Initially, the $LiNbO_3$ crystal and geometry coordinates were set to (0, 0, 0). Since the 128º Y-cut $LiNbO_3$ substrate was used in the experiment, a Euler angle coordinate transformation of (α + 0º, β + 38º, γ + 0º) was performed to describe the crystal cut angle. The rotation of the TPCB was simulated by rotating the substrate along α for different angles. The crystal rotation is illustrated in **Fig 3.12a** where the transparent geometry denotes the original position. To compute the acoustic pressure distribution inside the droplet, the "Thermoviscous Acoustics" module in the COMSOL software was utilized. Because the wafer used is x-axis propagating, we built our IDTs accordingly. The domain parameters and constants are presented in the Appendix 1 **Table 1**.

Fig 3.12b shows the meshed geometry used in the simulations. It is important to note that the IDTs are shown to scale with the size used in the experiments, while the droplet is significantly reduced in size (approximately 100 μm in diameter) due to computational power limitations.

The red area in **Fig 3.12**, denotes the slice made in COMSOL, to study the 2D plane of the model.

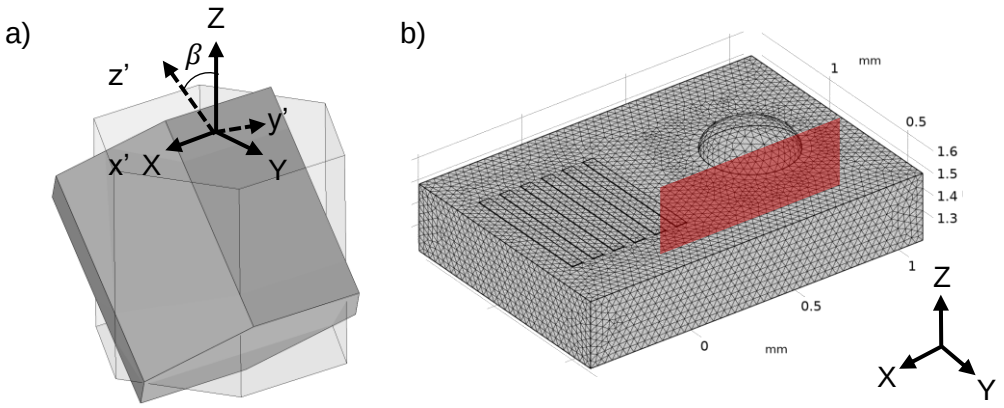

Figure 3.12. COMSOL Simulation of the 3D model a) rotation of the crystal for selection of the correct crystal orientation from original Z-axis. b) meshed geometry of the model with three pairs of IDTs and liquid droplet in front.

The liquid droplet domain the 3D model built in **Fig 3.12** does not allow for any interpretations regarding the acoustic attenuation from the piezoelectric domain, due to its small size which does not reflect the experimental setups and the nature of the lump models used for computing liquid interactions, based on Navier-Stokes equations which are notoriously hard to solve in 3 dimensions.

Therefore, to reduce the complexity, a 2D model is built with a real-sized droplet domain where the effects of mechanic-fluid interactions could be studied with higher confidence.

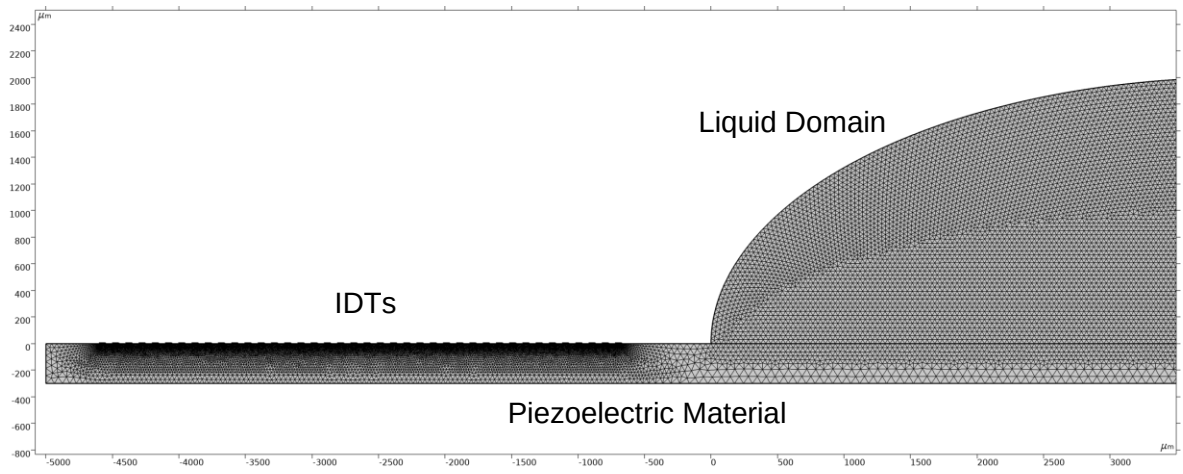

Figure 3.13. COMSOL Simulation of the 2D model including a real-size liquid droplet domain, and IDTs placed on $LiNbO_3$.

This model allows to better predict the acoustic attenuation into the droplet due to the deformation of the mechanical displacement on the piezoelectric surface.

The thesis does not compute the effects of acoustic waves on particles in the liquid due to the inherent limitations of the model and its scale. Coupling the small IDTs with the liquid boundary while maintaining a fine mesh is challenging. In real life, these effects occur in three dimensions, involving complex tasks and assumptions that may not yield significant benefits. The FEM must approximate the continuous and highly dynamic interactions between the acoustic waves and the particle surface. These interactions involve intricate pressure distributions and forces that vary significantly over time and space, which are challenging to capture accurately in a simulation environment.

The research presented in this thesis primarily focuses on experimental investigations to understand particle-fluid interactions. In instances where novel phenomena are observed, simulations are employed to hypothesize the nature of the waves and the deformation of the crystal material. To ensure the credibility of the simulations, experimental validations were conducted in parallel to maintain alignment with real-world conditions. These experiments provide a benchmark for the simulation results. However, due to the inherent simplifications and assumptions in the FEM, achieving perfect alignment between simulations and experimental data is challenging.

Despite, the integrated approach of combining experimental and simulation methods enhances the thought-provoking process, where complex phenomena is difficult to interpret.

3.9 Innovations and Contributions

The Dynamic Acoustofluidic System (DAS) method introduced in this chapter represents significant advancements over the current state-of-the-art in the field of acoustofluidics.

Table 3.1 provides a summary of the key innovations and contributions of the DAS compared to conventional methods. Each aspect is discussed in detail below.

Table 3.1. Summary of innovation and contribution with respect to the state-of-the-art.

Aspect	DAS	State of the art
Manufacturing Technology	PCB	Photolithography
Consumable Production	3D Printing Molds	Silicon Wafer Molds
Diversity	Reconfigurable	Fixed design
Commercialisation prospect	High	Low
Accessibility	Can be built by most labs, with a 3D printer	Limited due to cost and equipment
Equipment	Portable electronics	Laboratory equipment+
Cost	Hundreds	Thousands

Manufacturing Technology: The DAS leverages printed circuit board (PCB) technology for the fabrication of interdigital transducers (IDTs), contrasting with the photolithography techniques typically used in the state-of-the-art. PCB manufacturing is more accessible and cost-effective, eliminating the need for cleanroom facilities. This innovation not only reduces costs but also democratizes the fabrication process, allowing a wider range of laboratories to engage in acoustofluidics research and development. Additionally, the DAS does not require the use of a vector network analyser (VNA) to position the IDTs accurately, simplifying the setup and calibration process. The integration of electronics within the PCB also enhances the prospects for commercialization, as it streamlines the system and reduces the need for external equipment.

Consumable Production: Traditional acoustofluidic systems utilize silicon wafer molds, which are expensive and require specialized equipment. The DAS introduces 3D printed molds to produce consumables. This method is not only more affordable but also highly customizable and adaptable, facilitating rapid prototyping and iterative design improvements. This innovation greatly enhances the flexibility and scalability of acoustofluidic devices.

Diversity: One of the most notable innovations of the DAS is its reconfigurability. Unlike fixed design systems, the DAS allows for the easy reconfiguration of IDTs and microchannels. This flexibility enables a broader range of experiments and applications, from droplet manipulation to cell sorting, all within the same system. This adaptability significantly expands the potential use cases and operational parameters of acoustofluidic devices.

Commercialisation Prospect: The DAS shows a high potential for commercialization due to its reduced cost and complexity. By simplifying the manufacturing process and reducing dependency on specialized equipment, the DAS can be more easily adopted by commercial entities. This contrasts with the current state-of-the-art, which often remains confined to research settings due to high costs and technical barrier.

Accessibility: The DAS can be constructed in most laboratories equipped with a 3D printer, making it far more accessible than systems requiring expensive and specialized equipment. This accessibility is a crucial factor in promoting wider adoption and fostering innovation across various research fields. By lowering the entry barriers, the DAS enables more researchers to explore and contribute to the field of acoustofluidics.

Cost: The cost of implementing DAS is significantly lower than traditional methods. While conventional systems can cost thousands of dollars, the DAS can be built for a few hundred dollars. This drastic reduction in cost makes advanced acoustofluidic technology available to a broader audience, facilitating more widespread research and application.

3.10 Conclusions

In this chapter, we introduced the Dynamic Acoustofluidic System (DAS), highlighting its significant advancements over conventional acoustofluidic devices. The novel fabrication methods using Thin-Film Printed Circuit Board (TPCB) Interdigital Transducers (IDTs) and 3D-printed molds demonstrate the DAS's ability to be rapidly prototyped and reconfigured, thereby increasing its versatility and accessibility. The detailed descriptions of the mechanical and electrical components, along with the innovative use of force-sensitive resistors (FSRs), showcase the system's adaptability and precision.

The transition from traditional photolithography to PCB technology for IDT fabrication, coupled with the use of 3D printing for consumable production, significantly reduces the cost and complexity associated with creating and operating acoustofluidic devices. This democratization of technology allows more laboratories to engage in cutting-edge research without the need for expensive cleanroom facilities or specialized equipment.

Additionally, the DAS's reconfigurable nature opens a wide range of experimental possibilities, from droplet manipulation to cell sorting, all within a single system. This flexibility not only enhances the scope of research but also increases the commercial potential of the DAS, making it a viable option for both academic and industrial applications.

Overall, the DAS represents a leap forward in the field of acoustofluidics, offering a cost-effective, accessible, and versatile platform for a variety of biomedical applications.

Chapter 4

DAS for Particle Alignment and Separation

4.1 Introduction

Following the development of the DAS platform, it is essential to test its efficiency and compare it with existing methods, both in terms of assembly and its effectiveness in manipulating particles. One of the key acoustofluidic applications where DAS can effectively compete is particle manipulation within a PDMS channel. This application is crucial not only from the standpoint of its practical use but also as a critical step in characterizing the waves produced by the TPCB and determining their capability to affect particles in a conventional manner.

The experiments detailed in this chapter demonstrate that the DAS method can achieve results comparable to those of conventional methods, thereby building confidence in its use for the experiments described in the subsequent chapters. The DAS system demonstrates precise manipulation of micro-objects, such as droplets and cancer cells, and provides a low requirement for facilities and operation. The potential for the DAS system is significant, particularly in biomedical applications, and it has the potential to expand the use of acoustofluidic devices beyond specialised facilities. Our results showcase the promise of DAS and highlight the potential for further developments in the field of acoustofluidics.

4.2 Experimental Setup

After assembling the DAS unit for particle alignment using the techniques described in Chapter 3, the unit was tested for its capability to manipulate particles in microchannels. Additionally, the electronics developed in Chapter 3 were integrated into the system to enhance its functionality.

The DAS unit described here consists of two IDTs, labelled (**Fig 4.1a**) IDT-1 and IDT-2, which are positioned parallel to each other. A microchannel, featuring one inlet and one outlet, is situated between these transducers, and is held in place by a mechanical presser, as illustrated in **Fig 4.1a**. This entire setup, referred to as DAS-B, was placed under a microscope for detailed observation and connected to the DAS electronics unit (**Fig 4.1b,** DAS-A) to facilitate precise control and monitoring of the experiments.

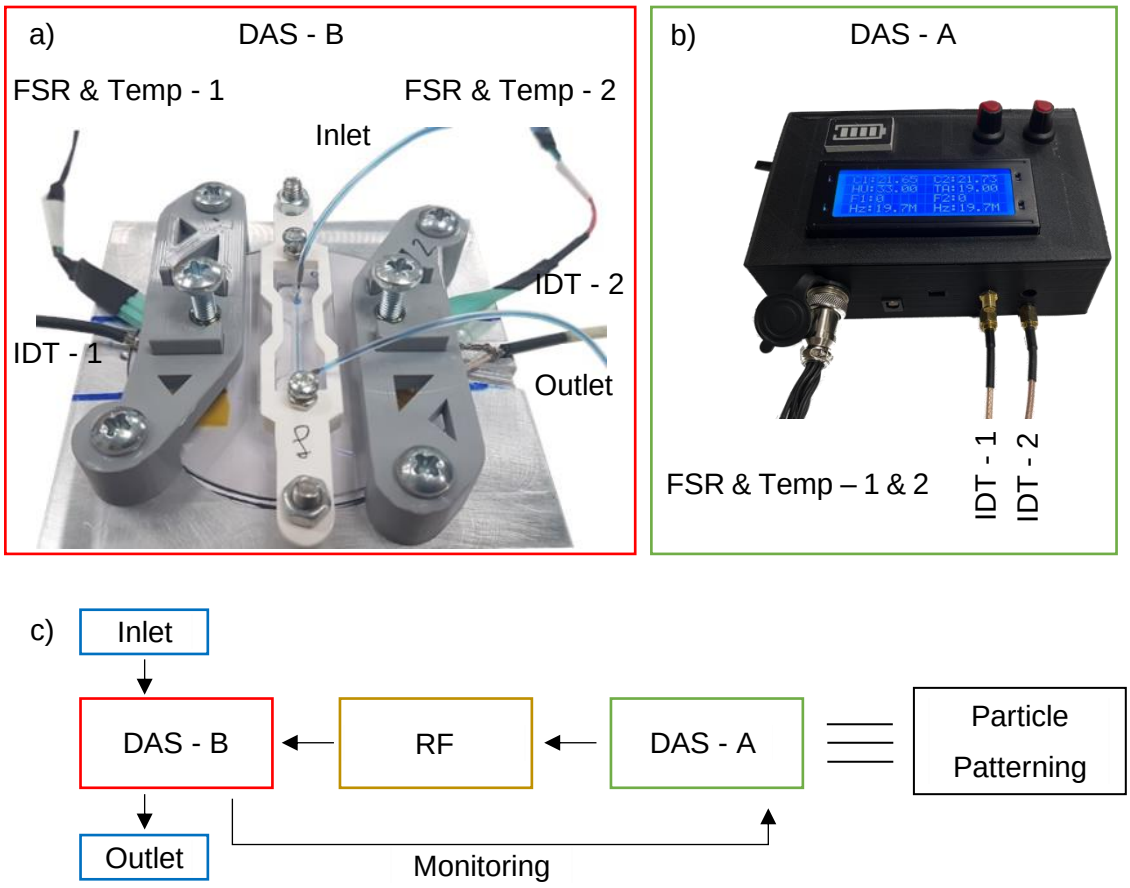

Figure 4.1 An experimental setup used for particle separation in a microfluidic channel. a) displays a DAS-B unit connected with the b) electronics system DAS-A. c) Operation flow reveals the key connections for successive particle separation/patterning.

All experiments were conducted following a structured methodology. Initially, DAS-A is employed to verify the coupling between the TPCB and the wafer. If the coupling is correct, DAS-A then generates a signal that is sent to the RF amplifier, which includes an internal matching network. This amplified signal is subsequently transmitted to the IDTs. In the event of any short circuit or overheating, DAS-A has the capability to disable the system to prevent damage. A brief overview of this setup is illustrated in **Fig 4.1c**.

4.3 Effects of IDT misalignment

Because the TPCB has varying degrees of freedom, they must not only be parallel to the edge of the wafer, but to each other, to ensure correct wave superposition. The lithium niobate is anisotropic, considering DAS method relies on mechanical assembly the errors introduced must be understood and ensured they can be minimised once the manual assembly takes place. This is important because if the IDTs are misaligned the waves

emerging might not produce correct wave superposition yielding a useless device. To make sure the statement above is true, the DAS was purposely setup at different angles to study and observe different particle alignment under different conditions.

First, the microchannels developed in Chapter 3 were all coated with 1% (w/w) bovine serum albumin solution for 10 min and then flushed with DI water. For the microsphere test, 10 µm polystyrene microspheres (Sigma Aldrich) were used and suspended in a 23% (v/v) glycerol and phosphate-buffered saline solution. The microsphere suspension was injected into the microchannels through a syringe in the same experimental setup as was shown in Chapter 3. Then, 10 µm microparticles were injected into the microchannel with IDTs actuated at 19 dBm while using the established S_{21} readings to align one of the IDTs at 0°, ~6°, and ~17° angles. The microparticles aligned into lines with angles of 0°, 2.5°, and 6° against the channel wall (As shown in **Fig 4.2a-c,** respectively). As can be observed the anisotropy of the material is apparent as the particles did not in fact align parallel to the IDTs, and this suggest that a wave offset is manifesting.

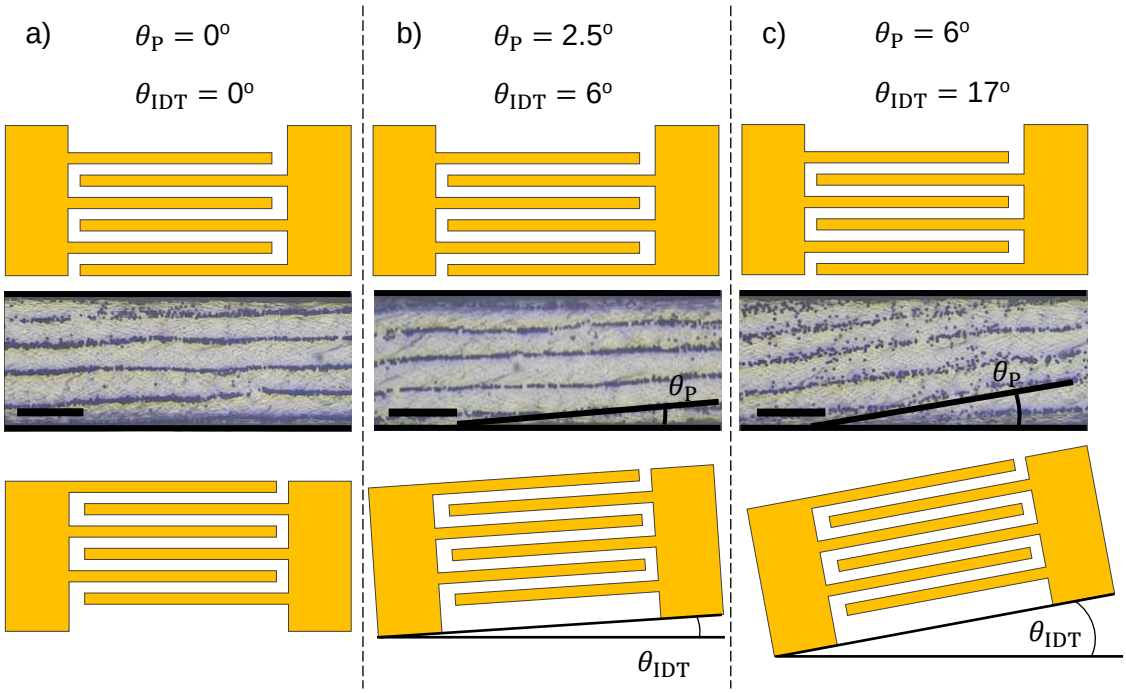

Figure 4.2. Microscope images displaying particle alignment of 10 µm particles as one of the IDTs is rotated based on S_{21} readings: a) 0°, b) ~6°, and c) ~17° angles. Microspheres aggregate along the PN lines at separate angle magnitudes noted as θ_P.

To attempt better explain the observed phenomena A COMSOL simulation was built in 2D top view, with a pair of IDTs situated on lithium niobate in front of each other. The meshed model can be seen in **Fig 4.3a**. When the IDTs are parallel (**Fig 4.3b**) the waves are also

parallel to the IDT edge and form noiseless superposition. Once the IDT tilted by 6° (**Fig 4.3c**), the wave superposition is still observed however, slightly curved, and less intensive. Similarly, when the IDT tilt is 17° (**Fig 4.3d**), the wave superposition is maintained, nonetheless also curved. At angle 17°, the wave is also much weaker, likely due to increase of reflection coefficient. The titled standing wave angle changes depending to which IDT it is closer. The wave propagating from the parallel IDT is more parallel whereas the waves near the titled IDT are more curved, producing a gradient. The finding observed in the simulation indicate that even though a dramatic angle change such as 17°, can still wave superposition, only few degrees of error might be present, this give sufficient confidence that the manual assembly is possible.

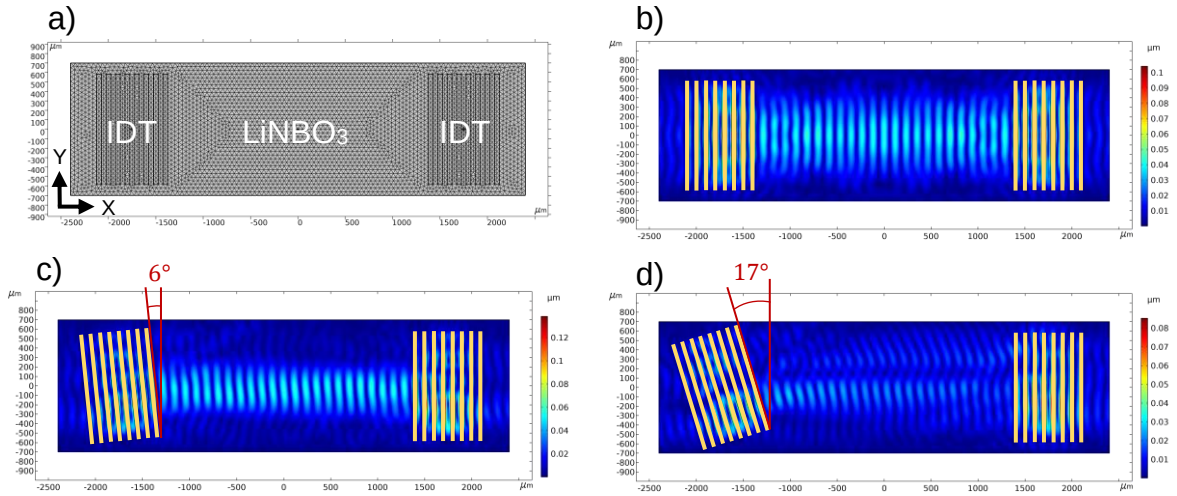

Figure 4.3. COMSOL Simulations of the TPCB misalignment. a) shows a meshed top view 2D model of the setup. Results demonstrate a change in wave angle due to the TPCB misalignment as b) perfect theoretical alignment, c) rotation of the TPCB is 6° and d) rotation of the TPCB is 17°.

4.4 DAS-B Performance using VNA.

We chose to measure the acoustic energy density to evaluate the performance of particle patterning when the VNA is used and using a MATLAB code (adopted from Ref. [202]) and treat the data as a control group for later comparison with DAS assembly method. This involved analysing microscope-captured videos of microsphere aggregation, extracting image frames, and analysing pixel intensity near the pressure node (PN) line. The acoustic energy density of the DAS was calculated at 0° with varying input power per IDT (15, 20, and 27 dBm), and the results are shown in **Fig 4.4a-c**. We observed that the time required for 99% of microspheres to aggregate on the PN line increased as input power increased, with values of ~1.9 s, ~0.6 s, and ~0.3 s observed for the respective input powers. To ensure

the reliability of these findings, tests were repeated three times, and an average acoustic energy density was obtained for each input power, as shown in **Fig 4.4d**. These results demonstrate that microspheres can be fully controlled through manipulation of input power and that the amplitude of the SAW changes with power. Therefore, this method provides an alternative means of characterising SAW-devices using only a microchannel and microparticles.

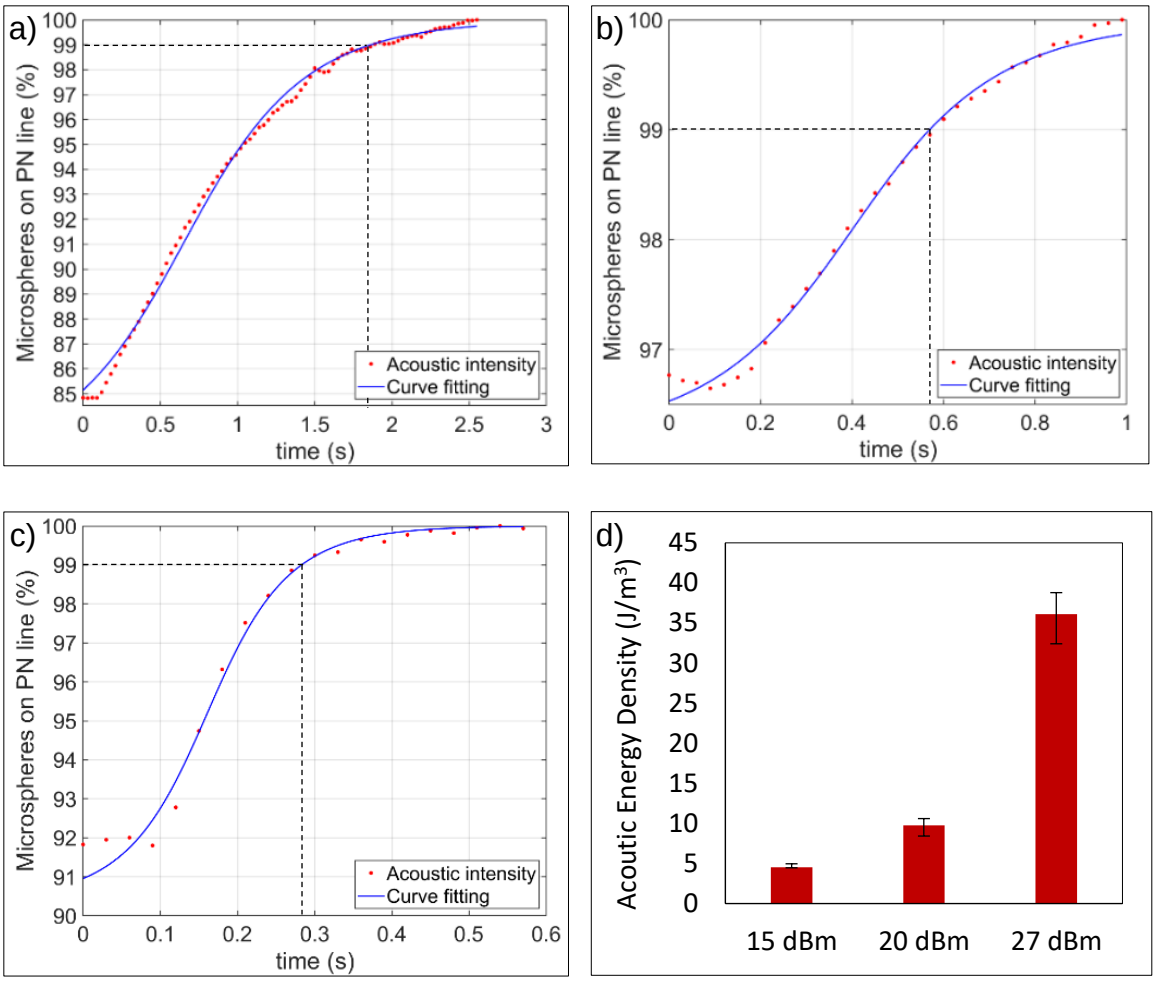

Figure 4.4. Acoustic energy density of the DAS with parallel IDTs: (A)-(C) Time required for 99% of microspheres to reach the PN line under input powers of 15 dBm (~1.9 sec), 20 dBm (~0.6 sec), and 27 dBm (~0.3 sec), respectively. d) Mean acoustic energy densities corresponding to the three input powers are 4.6 J/m³, 9.9 J/m³, and 36 J/m³, respectively (n = 3).

4.5 DAS-B Performance using DAS-A.

The confidence gained by characterising the DAS unit using conventional method, allowed to compare the DAS method effectively. One of the significant advantages of the DAS is its control unit, which includes FSRs that act as torque screwdrivers and provide a reliable

reference point in arbitrary units when applying optimal pressure to the IDTs. This allows the DAS device to be much simpler to use since it can provide both the required signal and a reference point for optimal pressure. However, one limitation of the control unit is that it cannot inform the user if the IDTs are aligned parallelly, which is essential for the proper functioning of the DAS. Therefore, we wanted to investigate whether the IDTs could be visually aligned by the user without compromising its effectiveness.

To align the IDTs visually, we utilised the fact that the localised presser offered a flat edge, and the FPCB IDEs chips had a front flat edge. These two edges can be used as visual guides to attempt to make the components locally parallel to each other. Additionally, the main holders were already parallel, making it possible to extend the parallelism to the two opposite IDTs. We aligned the FPCB IDEs chips visually five times to obtain an average S_{21} reading, which was then compared to the S_{21} achieved using the VNA. The results of this comparison are shown in **Fig 4.5b**, where it can be observed that the S_{21} peak achieved with VNA guided alignment (black curve) is slightly larger than the one achieved with visually guided alignments (red curve), but still remarkably close to it. In addition, the use of FSR over a course of twelve readings (**Fig 4.5a**), shows that the FSR can be trustworthy as efficient reflection coefficients are reached almost every time.

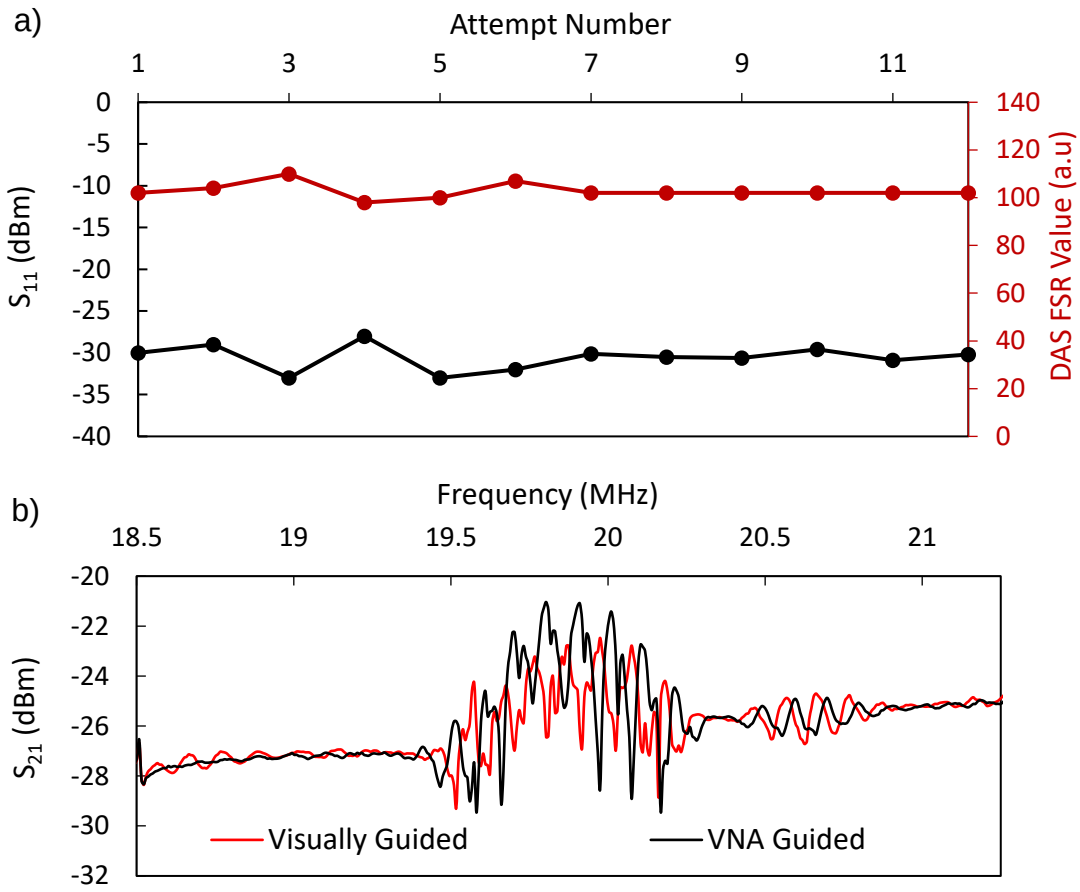

Figure 4.5. Assembly of the DAS using the electronics system DAS-B. a) demonstrates constant FSR value agreement with S_{11}, during full disassembly and assembly. b) Comparison of the S_{21} measurement obtained through VNA and visually guided assembly of the two IDTs (n = 5), showcasing the effectiveness of the assembled device in signal transmission.

The results from **Fig 4.4** led us to characterise the acoustic energy density of the visually guided assembly and compare it with the VNA guided alignment. The microsphere aggregation image for the visually guided assembly is shown in **Fig 4.6a**. We performed three tests of the assembly at 17 dBm of input power and obtained the average acoustic energy density shown in **Fig 4.6b**. Surprisingly, the visually guided assembly had slightly higher acoustic energy density than the VNA guided alignment. We speculated that this was due to the distance between the opposing IDTs being reduced during the visual experiments. To visually align the IDTs, the FPCB's edge must be exposed, which might have resulted in the FPCB IDEs chips being pushed further forward to expose more of the front edge. As a result, the distance between the IDTs was reduced, resulting in lesser wave attenuation and consequently, the acoustic energy density was increased. Overall, our findings confirm that the DAS can be assembled by visually aligning the two IDTs without the use of the VNA, making it a simpler and more accessible device to use.

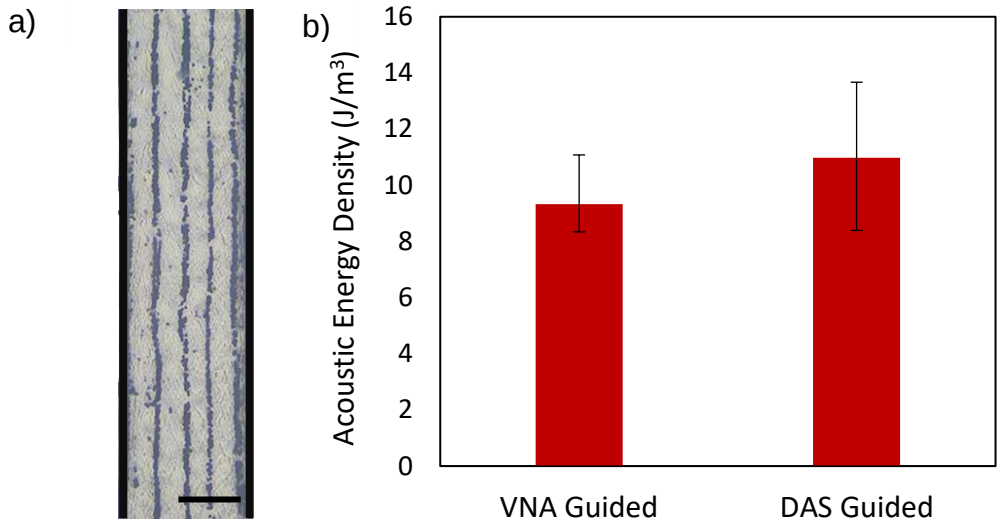

Figure 4.6. Assembly of the DAS using the electronics system DAS-B showcases a) microsphere aggregation on the PN lines of the VAD constructed by visually guided assembly (200 µm scale bar). The b) acoustic energy density of the DAS constructed by the two assembly methods, VNA and visually, with an acoustic energy of 9.3 ± 1.2 J/m^3 (Mean ± SD) and 10.9 ± 2.7 J/m^3 (Mean ± SD) at 17dBm, respectively (n = 3).

4.6 DAS with Rotated microchannels

While it has been shown that rotating one of the interdigital transducers (IDTs) can achieve tilt angle alignment, there is another method to accomplish this. The unique bonding mechanism used on the DAS makes it possible to adjust the tilted angle by rotating the microchannel that is clamped to the device. To test this method, two new microchannel pressers were used, designed to accommodate two different alignment angles of 15° and -5°, as shown in **Fig 4.7a-b**. In addition, a wider channel of 800 µm was used for these tests to clearly demonstrate the tilt angle phenomena. The pressers were used to clamp the microchannel and create the respective inclinations for aggregating the microspheres using 17 dBm input power. The results of these tests reveal that the tilted angles can be reconfigured by rotating either the microchannel or the IDTs. However, it is worth noting that rotating the microchannel would likely create a standard SSAW alignment, while tilting the IDTs could lead to more complex wave superposition. While static particle alignment may not be an issue, using this setup with flow for separation purposes could result in complications. In conclusion, tilting the IDTs may be an attractive alternative to rotating the microchannel, but further exploration is necessary to determine its stability and predictability.

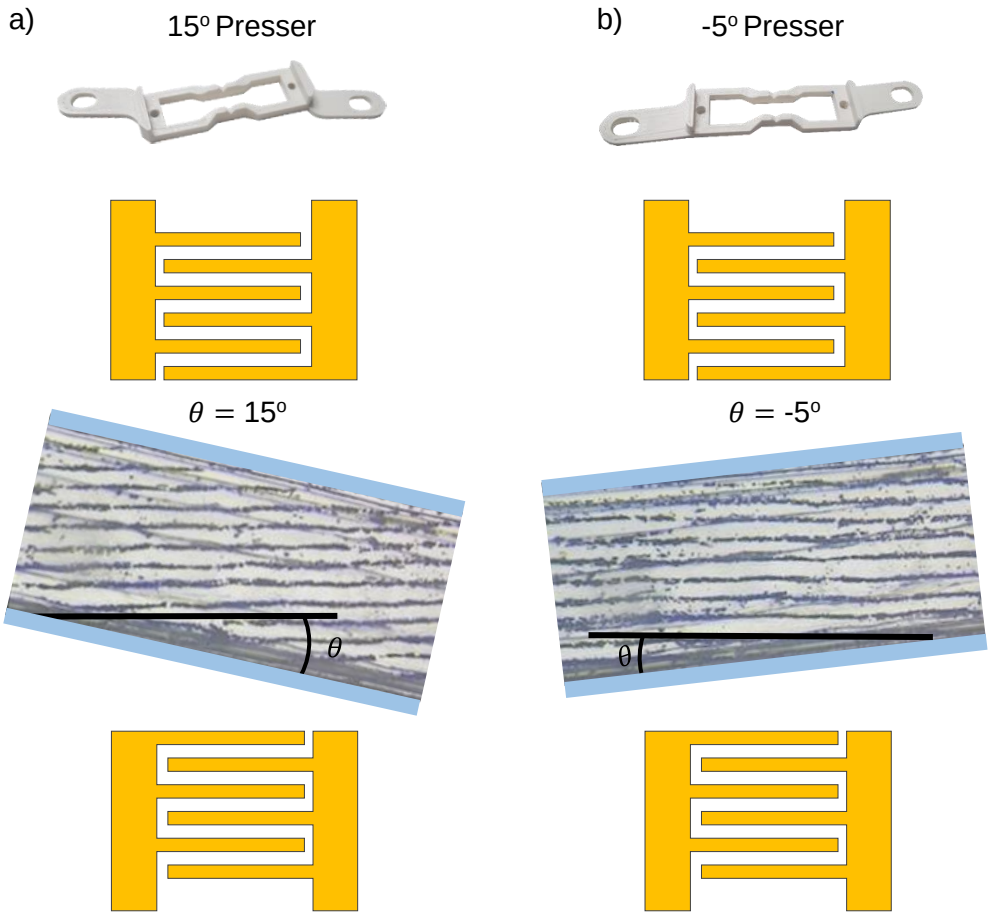

Figure 4.7. Adjusting the microchannel to a specific tilted angle: a) 3D printed microchannel pressers with a) 15° and b) -5° angles. Microspheres accumulating along the PN lines at 15° and -5° angles are relative to the microchannel wall. Scale bar is 450 µm.

4.7 Particle Separation using DAS.

The rotation of the microchannels forms the basis for particle separation in the Acoustofluidic system. However, it is essential to acknowledge that the initial plan to utilise 3D printed channels for the separation experiments faced a significant challenge. Due to sheet flow inlet constrictions, the 3D printed channels were deemed unsuitable for the intended application. Consequently, it was determined that a more precise 3D printer would be required to fabricate channels capable of handling the necessary separation tests. As a result, an alternative channel fabrication method (SU-8 Mould), was employed for the subsequent separation experiments. Nonetheless, the rest of the system remained unchanged.

Fig 4.8a left most side, illustrates the microfluidic inlets where the sample containing mixed particles is sandwiched between two focusing sheath flows. The right most side illustrates the post-SAW exposure region, where the mixed sample is separated into two outlets, and the particles are collected into separate containers. **Fig 4.8b-c** display the respective microscopic views of the green and blue zones in the channels, as noted in **Fig 4.8a**. Before the SAW is activated, the sample can be seen focused in the middle of the channel, with a heterogeneous distribution of particles (See **Fig 4.8b-c**, SAW OFF). The cloud-like structure and bright white dots represent the 1 µm and 5 µm particles, respectively.

Upon SAW actuation, the standing wave-induced pressure nodes align the larger particles and steer them into the sheath flow, away from the smaller particles. As the flow progresses, the steered and now separated larger and smaller particles drift into two separate outlets, as depicted in **Fig 4.8c**.

The successful separation of the 5 µm and 1 µm particles in the channel serves as a testament to the system's ability to perform complex tasks, such as particle separation. This achievement highlights the potential for the implementation of the dynamic Acoustofluidic system in a variety of applications and paves the way for future advancements in the field of Acoustofluidics.

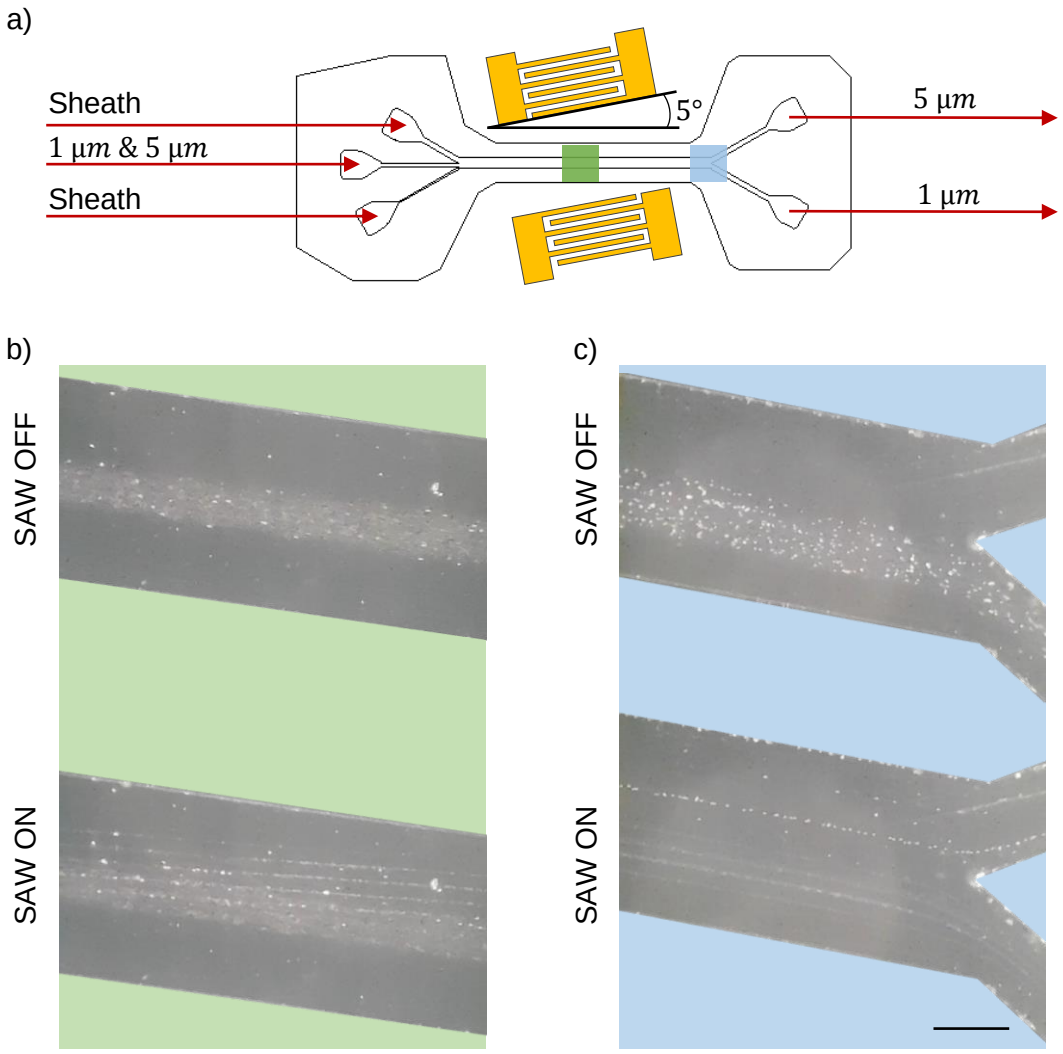

Figure 4.8. Demonstration of particle separation by using the DAS visually assembled system guided through the designed electronics DAS-B. The flow setup is shown a) two sheath and one sample inlet, followed by two outlets of separated particles. The particle separation effect is shown at two regions before and after applying the SAW a) middle of the channel b) near the outlets. Scale bar is 450 μm.

4.8 Innovations and Contributions

The application of the DAS (Dynamic Acoustofluidic System) platform represents a significant advancement in the field of acoustofluidics. Utilizing DAS method is proven, to offer a low-cost, flexible solution for rapid prototyping and particle manipulation. Unlike existing setups (comparison in **Table 4.1**) that are typically fixed and expensive, the DAS platform allows for effective particle manipulation in PDMS channels, including micro-objects like droplets and cancer cells, making it versatile and practical for various experiments.

Table 4.1. Summary of innovation and contribution with respect to the state-of-the-art.

Aspect	**DAS**	**State of the art** [131], [134], [135]
Platform Development	Flexible and low-cost DAS platform	Fixed and expensive setups
IDT Alignment and Superposition	Visual alignment for manual assembly	Requires precision instruments
Microchannel Rotation	Adjustable microchannel for alignment	Fixed microchannel positions
Simplicity and Accessibility	Simple and accessible setup	Complex and costly setups

4.9 Conclusions

In conclusion, this chapter successfully utilised a DAS method for the application of particle patterning and separation. The use of FPCB IDEs and DAS allowed for rapid prototyping without the need for a cleanroom facility. The DAS provided greater flexibility in resetting the angle between IDTs and the microchannel, which resulted in rotatable PN lines inside the device. Overall, this technology has great potential for the development and production of acoustofluidic devices and could potentially replace conventional cleanroom processes. The electronics system played a crucial role in driving the TPCB-IDEs to generate SSAWs and allowed for the characterisation of the SAW-based acoustofluidic system. The use of this system eliminated the need for other expensive configuration equipment, further increasing the affordability and accessibility of the acoustofluidic technology. In addition, 3D printable microchannels and PDMS rings were also developed for the acoustofluidic system. These components were fabricated using a low-cost 3D printer, continuing to make the manufacturing process more accessible and affordable. The combination of these advancements allows for rapid prototyping of SAW-based acoustofluidic devices. Overall, the use of this method can lead to more efficient and cost-effective manufacturing of SAW-based acoustofluidic systems, making it easier for researchers to explore their potential applications. In the next chapter, we will explore the application of this technology in the development of a novel platform for the isolation and analysis of extracellular vesicles.

Chapter 5

DAS for Sessile Droplet Manipulation.

5.1 Introduction

Following the successful presentation of DAS applied in particle patterning and separation, the same method is now applied to the field of sessile droplet manipulation. Previously, TPCB misalignments were identified as potential issues for patterning. However, in the context of droplet manipulation, these misalignments have turned out to be advantageous. The Dynamic Acoustofluidic System (DAS) offers a significant advantage with its capability to rapidly reposition IDTs at different angles. This flexibility is particularly beneficial as it overcomes the limitations typically associated with photolithography, which is both costly and rigid. Photolithography often lacks the practical justification for angled IDT placements due to the prohibitive expense and the discouraging results from traditional simulations, which show little promise in the field of acoustofluidics.

5.2 Using DAS for $LiNbO_3$ Characterisation

Using the DAS system, it was both cost-effective and efficient to position the IDT at various angles and test its effects. This approach allowed for rapid experimentation without incurring significant costs. The methodology employed in DAS facilitated the creation of an experimental setup, as illustrated in **Fig. 5.1**, aimed at exploring the reflection coefficients at these different angles.

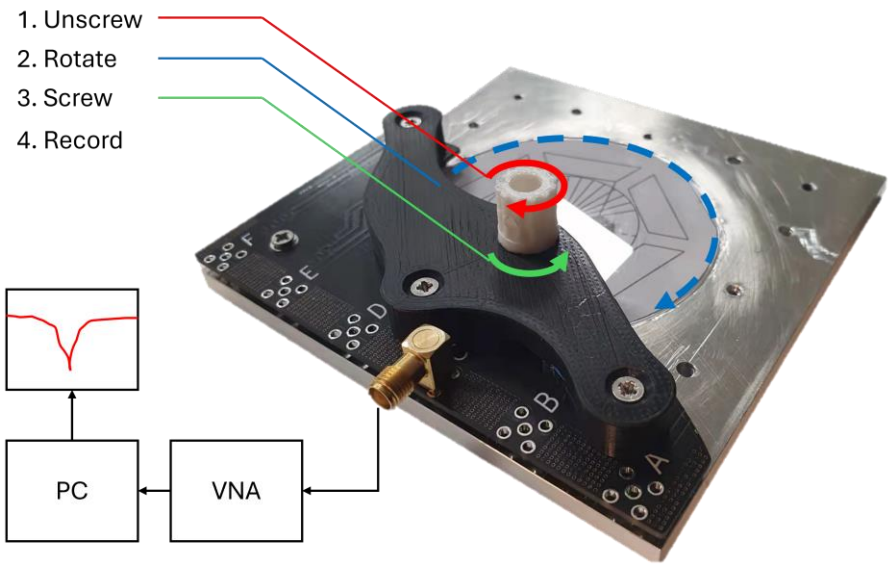

Figure 5.1. Experimental Setup of DAS used for VNA Analysis.

The process begins with the IDT in an unattached state, as shown in **Fig 5.1 (1)**, where the knob is unscrewed. Next, the Lithium Niobate wafer is rotated to the desired angle, as illustrated in **Fig 5.1 (2)**. Finally, the knob is tightened to secure the IDT to the wafer, completing the setup as depicted in **Fig 5.1 (3)**.

The reflection coefficient S_{11} was recorded using a vector network analyser (VNA, E5061B ENA, Keysight) during the rotation at an interval of 10°. At each angle, a sweep from 17 MHz to 40 MHz was performed. This method (**Fig 5.2**) generated a rather largely populated graph, as shown in **Fig 5.3,** indicating power absorptions allowing for a thorough investigation of the wafer.

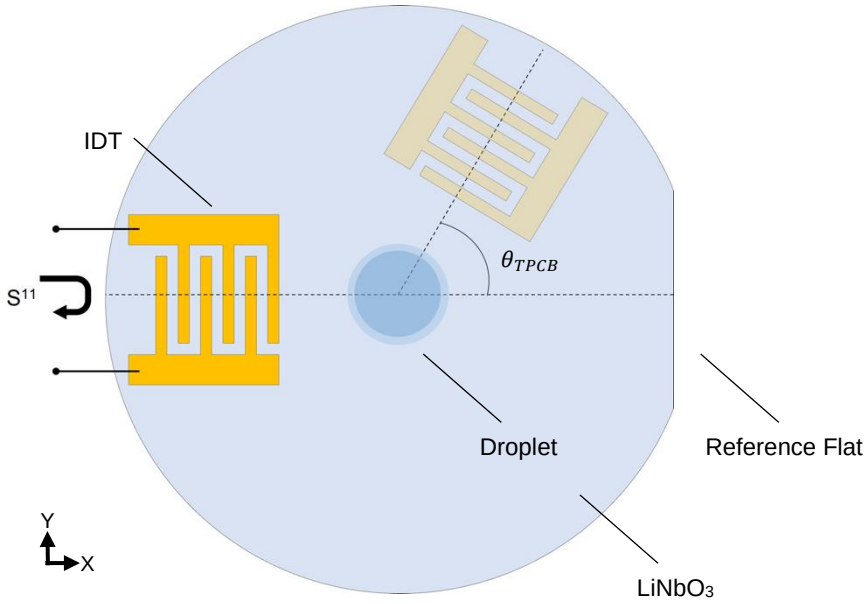

Figure 5.2. Experimental process used for the TPCB rotation experiments. The TPCB is rotated around the centre.

The placement of the conventional IDT at angle 0 (blue line) shows a significant dip at 20 MHz, which corresponds to the wavelength of the IDT and the speed of sound in the wafer. This dip indicates the presence of the Rayleigh SAW, which was shown in the previous section to pattern particles in a microchannel. As the TPCB IDT rotates, a frequency shift is observed, along with an increase in reflection coefficient (**Fig 5.4a**). The frequency shift results from changes in the speed of sound at different angles, while the increase in reflection corresponds to an increase in impedance and coupling coefficient in the material. These observations are consistent with previously observed phenomena shown in **Fig 4.2** & **Fig 4.3,** where a change in the IDT angle, maintained Rayleigh wave-like patterning. Therefore, the author refers to this region as the R-SAW Region. While the anisotropy in the material may eventually distort the wave, the dominance of the surface acoustic variable in

this region still enables manipulation and patterning, even with small distortions resulting from changes in angle.

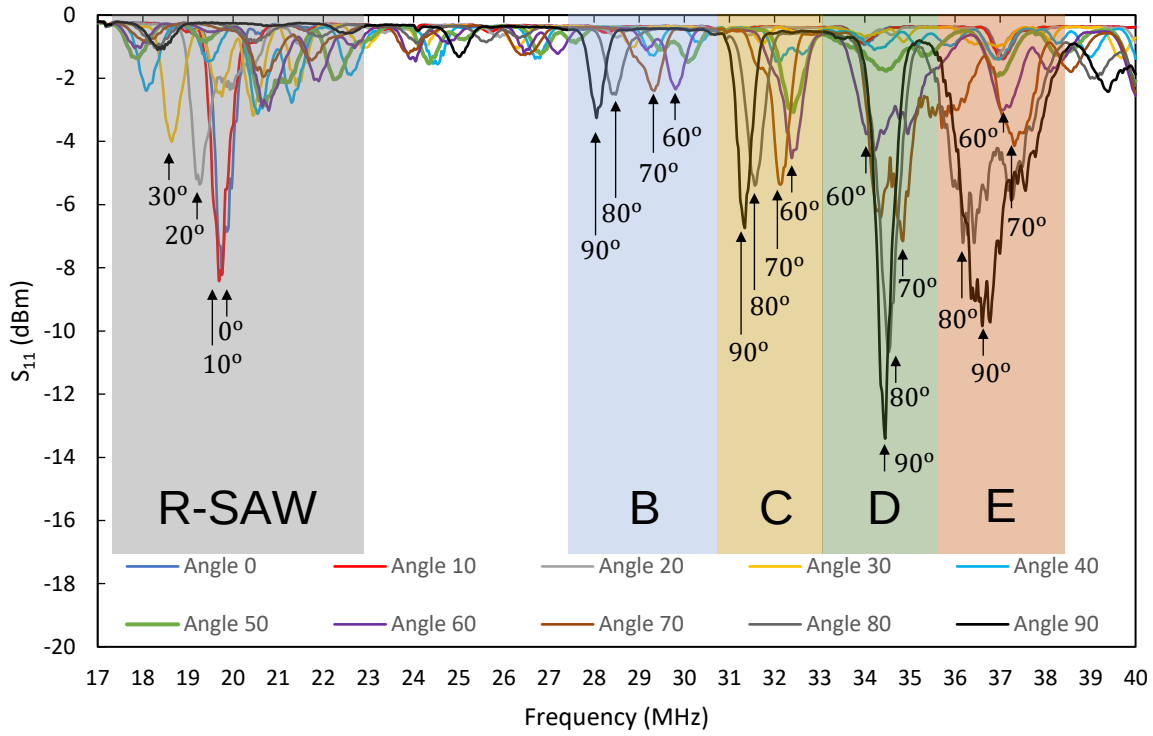

Figure 5.3. Scattering parameters analysis and respective region characterisation for a TPCB rotated at an interval of 10° around the $LiNbO_3$.

In contrast to the R-SAW Region, angles such as 90, 80, 70, and 60 exhibit multiple S_{11} dips. It is difficult to determine the exact waveform excited at each peak, as the dips only indicate the possibility of a waveform without specifying what that waveform may be. However, a trend between these angles is noticeable, particularly in regions B and C, whereas the angle changes from 90 to 60, the frequency begins to shift in a manner like a Rayleigh wave (**Fig 5.4b-c**). In regions D and E, while frequency shift is not as apparent, the reflection coefficient changes drastically (**Fig 5.4d-e).** To facilitate ease of reference to specific angles, the author will use terminology such as B-90 to denote the B harmonic at angle 90 throughout this section.

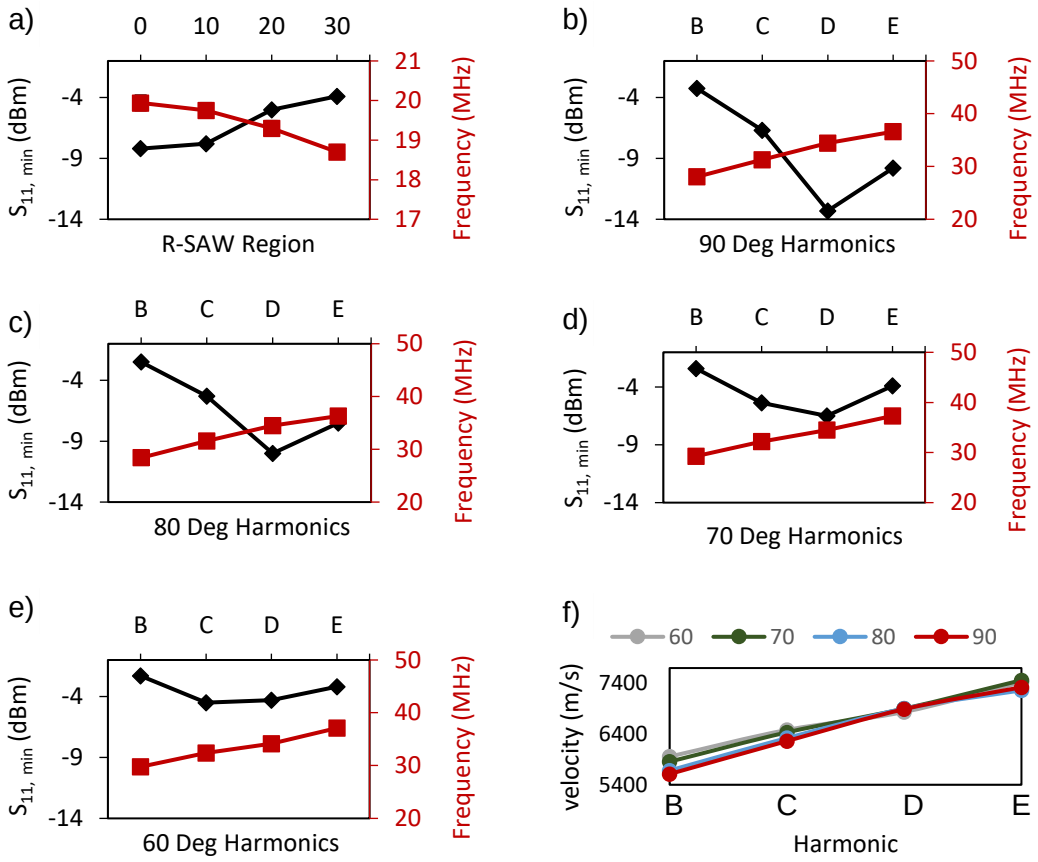

Figure 5.4. Identified region analysis from the S_{11} measurements highlighting changes in frequency and S_{11} magnitude for TPCB region a) R-SAW b) 90 Deg c) 80 Deg d) 70 Deg e) 60 Deg. f) Indication of the increasing wave velocity as the SAW frequency increases.

5.3 DAS Setup for sessile droplet manipulation

It is noteworthy that during our exploration of the wafer, numerous power absorption points were observed, suggesting the presence of waves. Considering the anisotropy of the wafer, these power dips can significantly impact the behaviour of droplets and the particles within them. To further investigate the waves generated, we set up our Dynamic Acoustofluidic System (DAS) with a PDMS droplet (**Fig. 5.5**), using the techniques described in Chapter 3. After filling the droplet with liquid and 10 µm particles, it was subjected to the wave modes determined using S_{11} parameters.

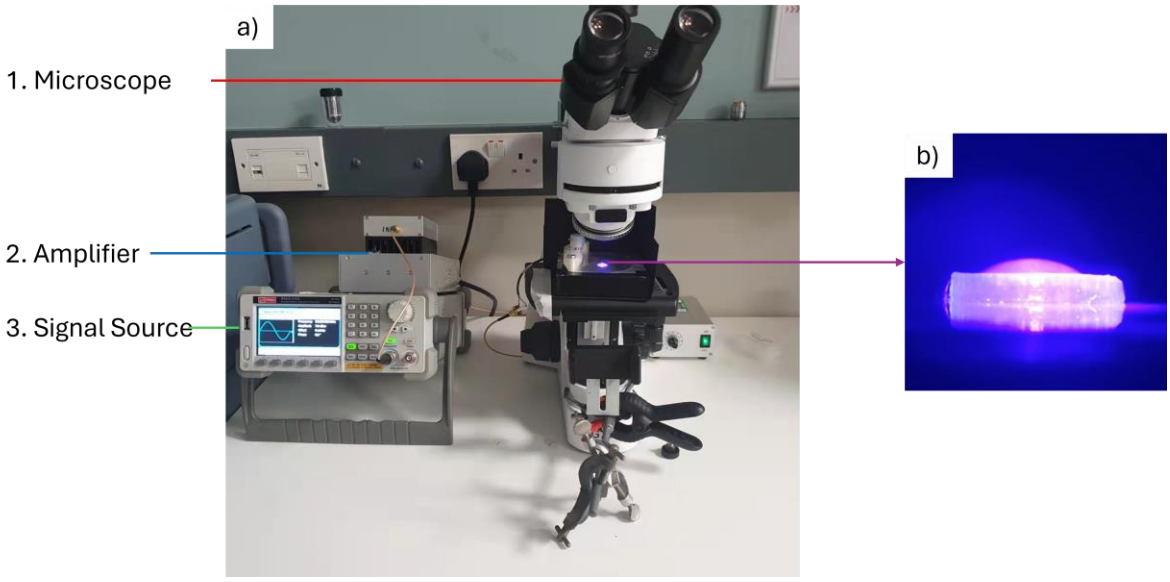

Figure 5.5. Experimental setup of DAS configured for sessile droplet experiments, with the flexibility to change angles.

The initial experiment was designed to observe and confirm known and expected phenomena in the field of acoustofluidics. For example, when a Rayleigh wave (in this case R-SAW-0, **Fig 5.3**) is introduced, it is expected to attenuate into the liquid, resulting in symmetric two-vortex streaming. As predicted, the system successfully demonstrated (**Fig 5.6**) this behaviour, thereby building confidence in the Dynamic Acoustofluidic System (DAS) as a reliable platform for conventional acoustofluidic phenomena.

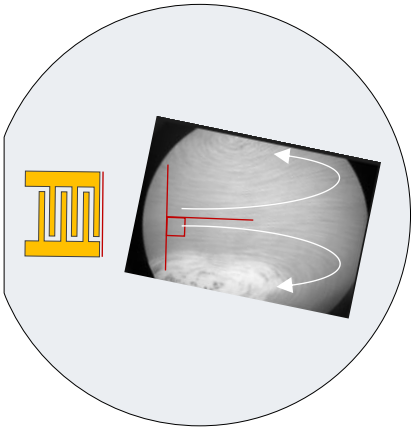

Figure 5.6. Sessile Droplet Streaming achieved using the DAS Method at a Rayleigh angle R-SAW-0.

Firstly, it is essential to note that the S_{11} minimum value has no direct relation to the droplet streaming pattern but is instead an indicator of the most efficient power absorption. Thus, operating outside the very minimum S_{11} does not render the system unusable, as there

remains a range where slight frequency adjustments result in different streaming patterns, only the streaming velocity is decreased as the reflection coefficient is now higher.

For the angle R-SAW-0, there is only one major dip observed, resulting in a single streaming showcase. In contrast, when the IDTs are positioned at angle 60, multiple dips are present, which allows for more comprehensive testing with droplets. By placing a droplet in front of the IDT, it is possible to apply the RF frequencies observed on the VNA and subsequently observe the liquid's translation as shown in **Fig 5.7**.

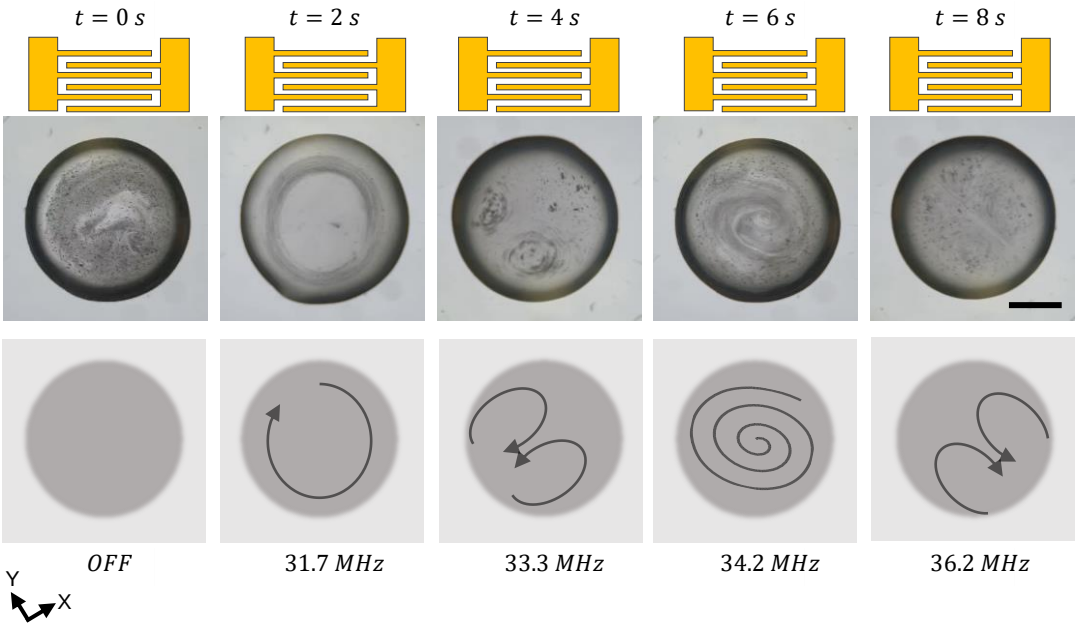

Figure 5.7. Identified droplet manipulation possibilities by adjusting the frequency at a set dual-wave harmonic.

The ring structure is particularly important in this context, as it represents a balance between acoustic ARF and centrifugal force, making it suitable for applications such as particle separation. Furthermore, by combining rotation and streaming, an effective mixing mechanism can be established. This technique shows promise in applications such as transfection when all effects are combined, paving the way for novel SAW-based microfluidic advancements.

Most interestingly, all of this is achieved with just a single interdigital transducer (IDT), eliminating the need to reposition the droplet. Instead, placing the droplet at the centre allows for versatile manipulation. It is expected that the wave steering, and complex wave superposition enables the achievement of a broader range of streaming patterns than those obtained with Eckart streaming alone.

At this point, it is known that different waves present in the wafer yield significantly different results in terms of particle manipulation within the droplet. Driven by a passion to explore these wave modes and their effects on liquid droplets, as well as to understand and characterize the wave modes measured using DAS and collected through S11 parameters, a series of experiments was conducted. These experiments involved exposing a single droplet to all the wave modes measured using the Vector Network Analyzer (VNA).

5.4 Sessile Droplet under different wave-modes

A PBS droplet sample with 10 µm particles in suspension was situated right in front the IDT and exposed to all the waves identified (in **Fig 5.3**). Firstly, the Rayleigh SAW region was exploited.

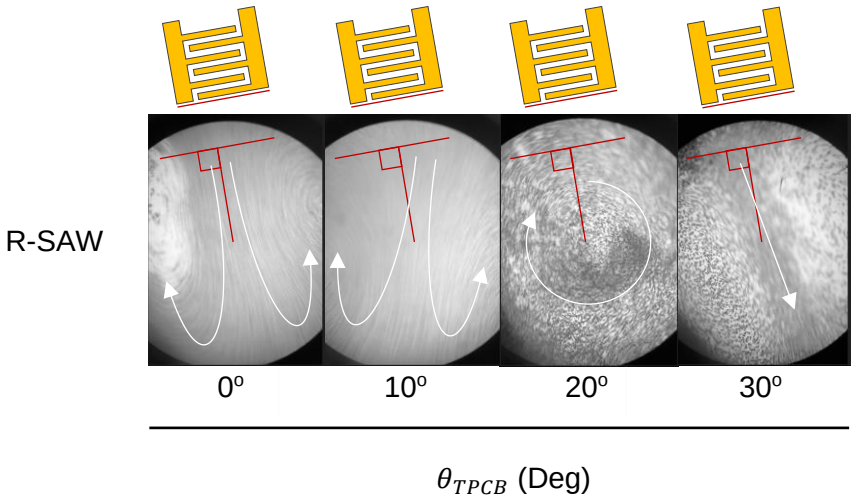

Figure 5.8. Behaviour of Sessile droplet as the IDT is rotated in the Rayleigh wave region.

The results are somewhat contradictory to what was initially expected. For instance, at an angle of R-SAW-0, the streaming patterns align with predictions. However, as the angle changes, despite the droplet remaining in front of the IDT, the streaming direction alters. The change itself is consistently observed at angles of 20 and 30 degrees. Predicting the streaming pattern proves challenging due to the influence of various factors such as viscosity, frequency, IDT shape, and the angle of wave propagation with respect to the droplet. In this study, since the only variable is the angle, it can be inferred that the anisotropy of the material produces waves that differ from the typical Rayleigh waves. Specifically, in this region, the waves are likely experiencing a phenomenon known as wave steering. This suggests that the material's anisotropic properties cause deviations in wave propagation, leading to the observed changes in streaming direction.

Further experiments were conducted to analyse the utilization of waves in the B, C, D, and E regions. Given that each of these regions exhibits multiple absorptions, as indicated by the VNA analysis, a grid of phenomena is presented in **Fig 5.9**.

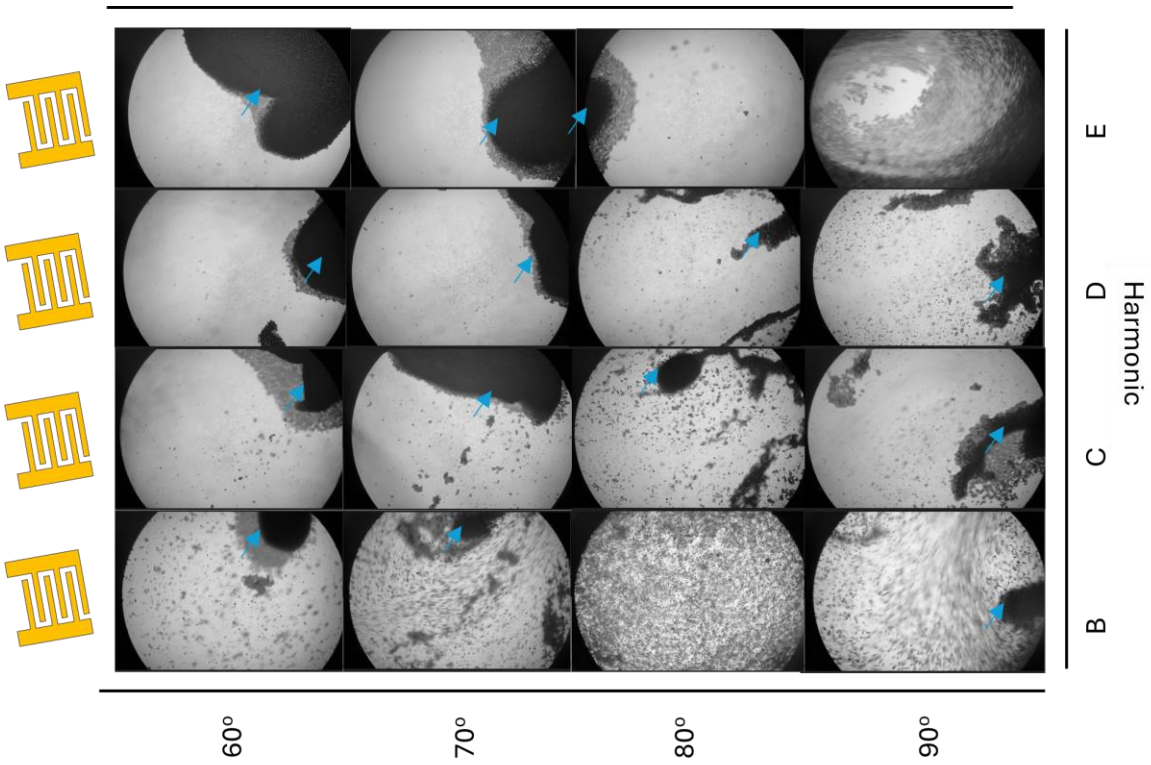

Figure 5.9. Microparticle streaming by positioning the liquid droplet in front of the IDT for a range of angle and frequency setups identified during S_{11} analysis. Scale bar 1 mm.

Surprisingly, the acoustic streaming and phenomena observed were unexpected. Some angles presented a stronger streaming velocity despite having lower reflection coefficients, which contradicts the theory that more power results in higher streaming velocity. While the streaming patterns remained diverse and unpredictable, the overall outcome of the experiment provided inspiring results.

In particular, **Fig. 5.9** (top left corner), for angles between 60 and 70 degrees at frequencies D and E, they exhibit a significant concentration phenomenon, much more pronounced than the Rayleigh SAW concentration. Conversely, angles between 80 and 90 degrees show prominent streaming phenomena but minimal concentration effects.

The ability to accumulate suspended particles (indicated by the blue arrow) in less than one second was notable. In other words, despite the presence of streaming at certain angles, when exposed to the right angle and frequencies particles experience a significant deflection

force away from the IDT. In this configuration, the particles are only deflected. However, by carefully positioning the Interdigital Transducer (IDT) to achieve single vortex streaming, the particle deflection phenomenon can be maintained. This adjustment results in a single vortex rotation, creating an ideal condition for particle concentration. But first, it was of interest to understand the underlying physics and phenomena behind the changes in streaming and particle deflection.

5.5 Simulations for waveform prediction.

When dealing with waves of this nature, where they are invisible to the naked eye and their amplitudes range from about 5 to 20 nm, physically observing and measuring them is a significant challenge. Describing and explaining their waveforms accurately is not trivial without the appropriate equipment. One such device that can assist in this task is a laser vibrometer. However, the process of using a laser vibrometer is slow, and its resolution field may be confined to a region of only a few hundred square micrometres.

In an effort to explain the phenomena observed in Fig 5.9 without the use of a laser vibrometer, alternative methods can be employed to visualize the waves.

In this section, the droplet domain is not used to determine streaming or particle effects within it. Instead, it serves to demonstrate that waves do attenuate from the piezoelectric substrate into a different medium, and that different wave propagation modes have varying effects. However, no predictions about its streaming patterns, nor nanoparticle translation, are made in this context.

5.5.1 COMSOL Model vs Experimental Data

As previously mentioned, (**Section 3.8**), COMSOL incorporates various material assumptions in its simulations. Consequently, relying solely on the developed model without validation could lead to questionable data. To build a degree of confidence in our model, we compared it with experimental measurements **Fig 5.10**. Specifically, we used a laser vibrometer to measure Rayleigh waves generated at R-SAW-0 on the wafer. These measurements were then compared with the results from our simulation model.

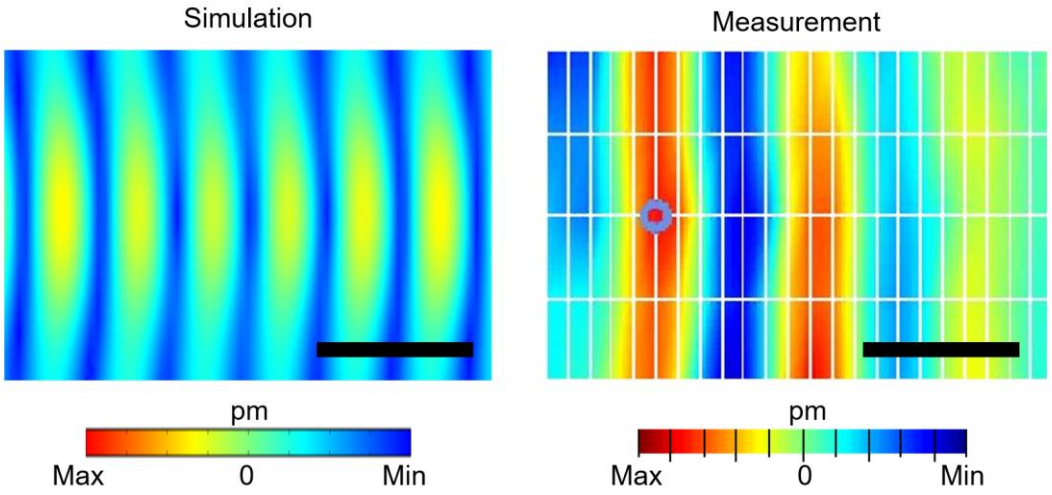

Figure 5.10. Surface deformation measurements on the $LiNbO_3$ for R-SAW-0 generated using an TPCB IDT, actuated at 1.5 V. The scale bar denotes 100 µm.

By closely examining the peaks and troughs and measuring the distance for each wavelength, we observed a notable similarity. COMSOL was able to predict the material displacement on the wafer's surface with some success. However, while this comparison provides some level of confidence, it is important to approach these results with caution. The assumption that our model accurately represents real-life measurements should be considered provisional and is carefully utilized in the upcoming sections.

5.5.2 Preliminary hypothesis

In **Fig 5.11**, the waveforms generated in the R-SAW region demonstrate the expected behaviour, as the surface acoustic wave is observed even as the angle rotates from 0 to 30 degrees. This phenomenon was also observed experimentally during sessile droplet streaming experiments (**Fig 5.8**). The streaming patterns were Rayleigh wave like, just changed drastically with the angle. Here, we can attempt to explain the previously observed phenomena by noting that the wave may have slightly steered and attenuated into the droplet at a different angle, resulting in varying streaming effects.

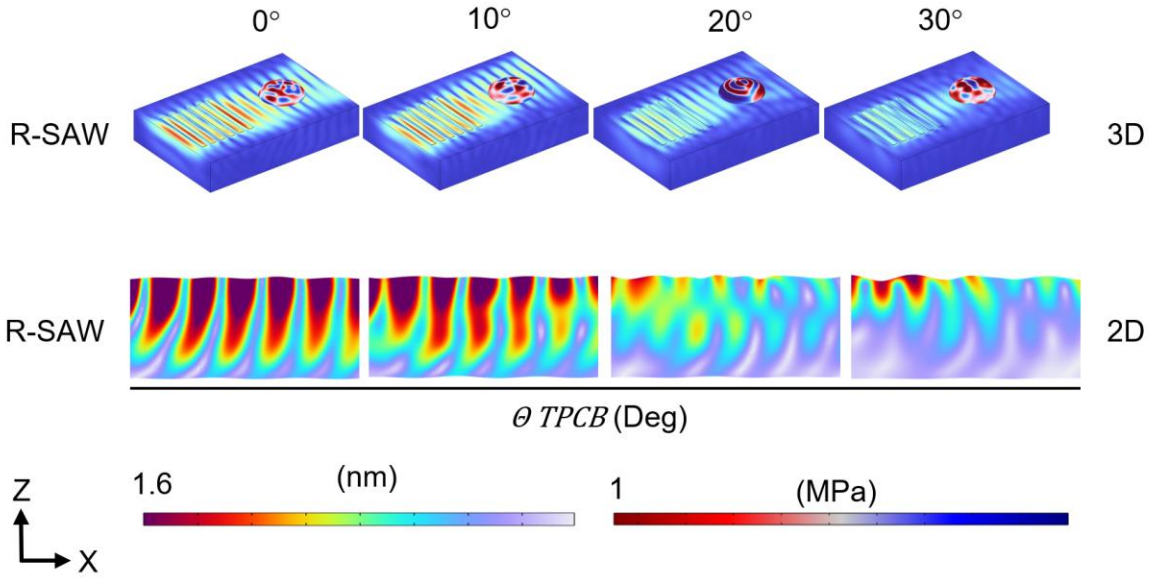

Figure 5.11. Results of the COMSOL simulations for a range of angle and frequency setups identified during S_{11} analysis.

By taking slicing the 3D (**Fig 3.12,** red area), a 2D view is revealed where the inside of the material can be studied. Rayleigh waves are surface-bound acoustic waves, and as demonstrated in the 2D simulations, surface deformations occur even when the IDT is tilted by a few degrees. This observation aligns with the particle patterning experiments (**Fig 4.2**), where particle patterns still formed despite the IDT tilt, albeit with less clarity. This finding does not contradict the simulation results, which showed highly irregular wave patterns at angles between 10 and 30 degrees.

Building on these foundations, we investigate the effects and formulate hypotheses regarding the observed concentration phenomena (**Fig 5.9**). It is known that angles around 60-70 degrees result in a high concentration effect, while angles around 80-90 degrees lead to significant streaming. Using COMSOL, we hypothesize which wave modes could exist at these angles to cause these effects.

The simulations for angles between 60 and 90 degrees at different harmonics (**Fig 5.12**) revealed surface displacement patterns that are quite similar. This consistency aligns with our experimental observations and confirms the existence of wave steering at various angles, thereby validating our experimental data. However, these simulations do not directly explain the concentration phenomenon we observed. Specifically, they do not elucidate why particles concentrate more at certain angles compared to others.

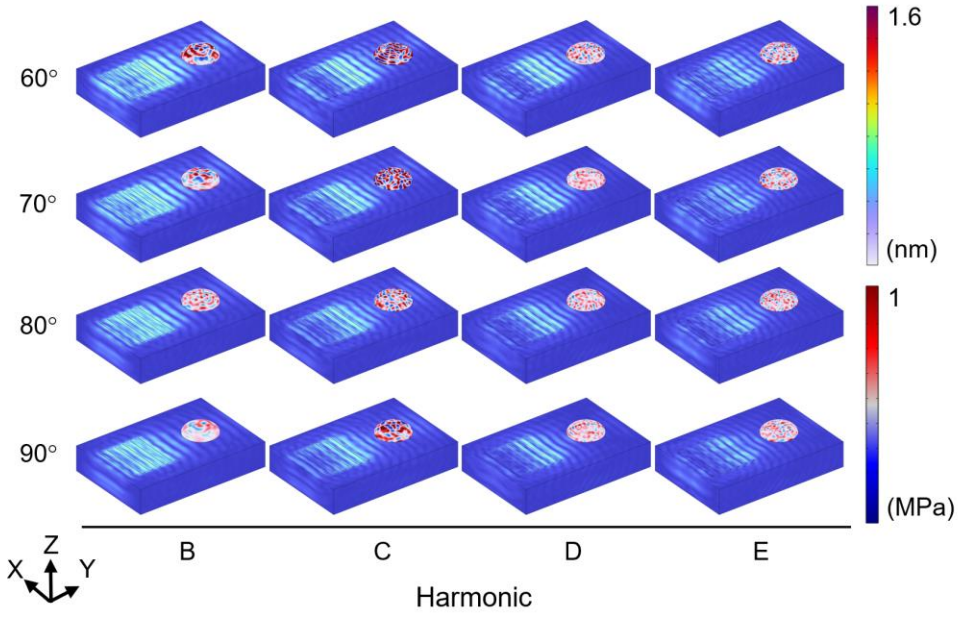

Figure 5.12. Results of the COMSOL simulations for a range of angle and frequency setups identified during S_{11} analysis.

To gain further insight, the study was similarly extended to include 2D models. One notable difference identified in the Rayleigh waves analysis is the increased internal displacement observed outside the Rayleigh region compared to angles between 60 and 90 degrees. Additionally, waves outside the Rayleigh region exhibit higher internal deformations and slight propagation at the top, which may contribute to the concentration effects observed experimentally.

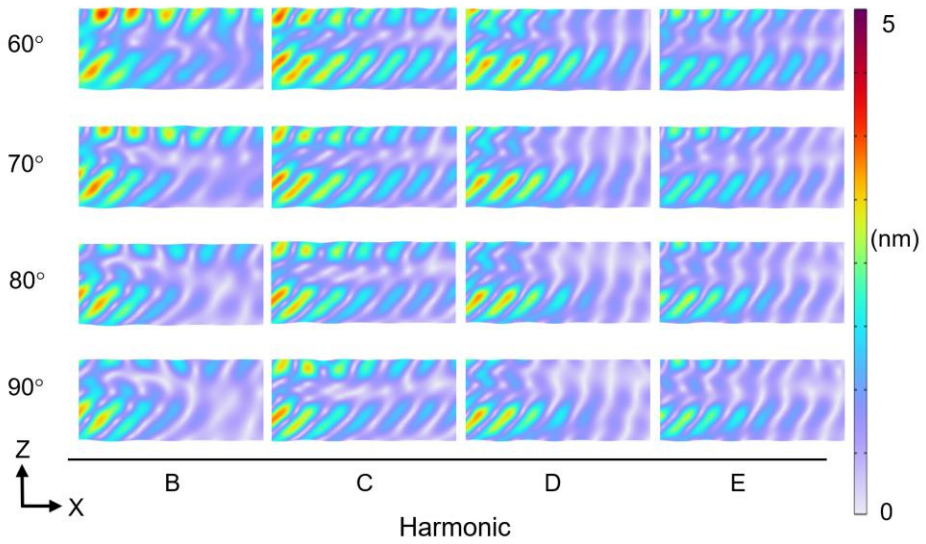

Figure 5.13. Cross section views of the 3D COMSOL simulation, revealing displacements amplitudes on the surface and within the bulk of the material for a range of angle and frequency setups identified during S_{11} analysis.

In conclusion, the simulations conducted thus far do not definitively explain why concentration phenomena is more pronounced at angles other than Rayleigh. However, by building slight confidence from measurements and matching them with simulations, as well as observing the steering effect in both practice and simulation, a notable hypothesis emerges. The waves at angles other than Rayleigh, and their respective harmonics, potentially possess more internal displacements along with surface deformations. This may cause more material to deform, leading to increased acoustic pressure in the droplet. This hypothesis should be approached with caution. The following section aims to reduce the model complexity and attempts to further explain the phenomena by utilizing a liquid domain the same size as the experiments but in two dimensions.

5.6 Dual-Wave Attenuation into a Liquid Droplet

Due to the inherent limitations of the simulation, the previous section provided minimal clarity about the exact cause of the concentration phenomena. However, it inspired a hypothesis that both shear and surface waves might coexist and contribute to these effects. This section aims to provide the background and reasoning behind this hypothesis by comparing the physics of Rayleigh and shear wave attenuation in a liquid droplet, as well as the acoustic propagation they exhibit in such environments. Three models were selected for this analysis. The Rayleigh model was used as a control group to validate some of the simulation data against known experimental practices. Additionally, two specific angles were chosen based on key observations: one angle where streaming was observed and another where a high concentration phenomenon was detected, R-SAW-0, D-90, and C-60 respectively. Simulations were conducted in a 2D side view with a liquid boundary domain coupled with lithium niobate, as shown in **Fig 5.14**. The results agree with commonly known Rayleigh SAW attenuation, governed by Snell's law, causing wave diffraction at 22°, as confirmed by the attenuation pattern shown in **Fig 5.14a**. On the other hand, SH-SAWs are in-plane propagating and tend to propagate upwards in the liquid droplet, as depicted in **Fig 5.14b**. The dual-waves mode demonstrated in **Fig 5.14c** exhibited both surface component attenuation and in-plane attenuation characteristics in the liquid droplet. The surface attenuation degree was slightly increased to 24°, which was due to the shift in wave velocity from 3980 m/s to 3580 m/s at this angle.

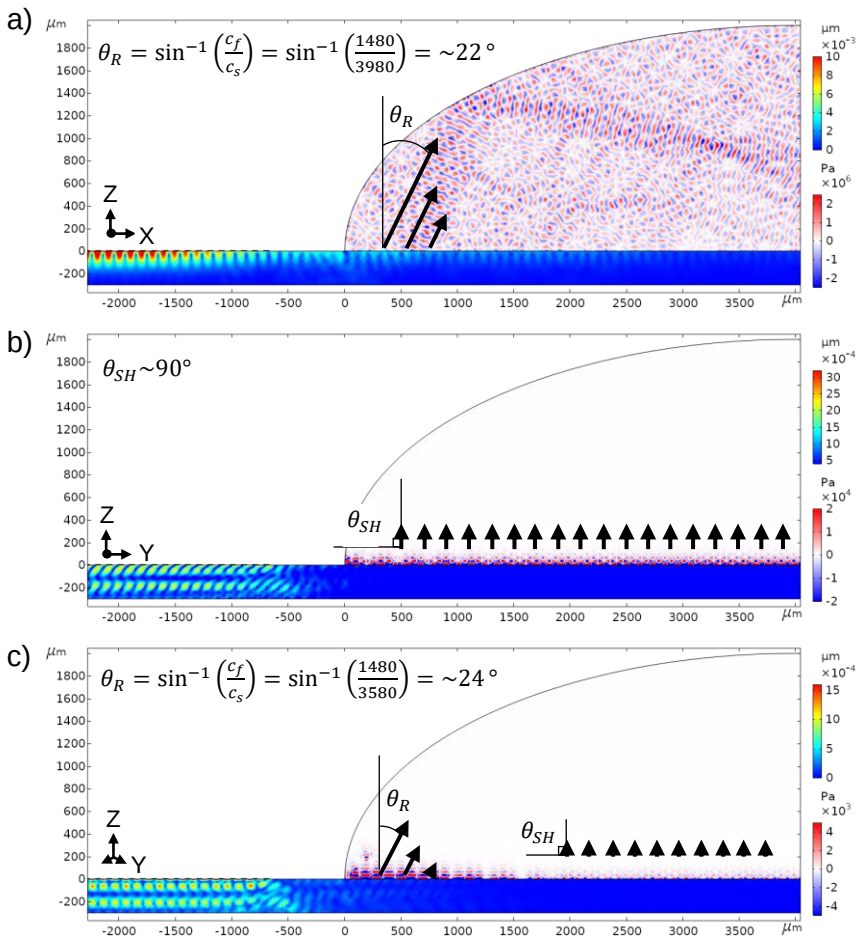

Figure 5.14. Two dimensional simulations reveal different diffraction angles for SAW attenuation into the liquid droplet at different harmonics a) R-SAW-0, b) D-90 c) C-60.

To establish a stronger connection between the simulation results and real-life data, we will analyse the generation of dual waves by comparing the S_{11} reflection coefficients. This analysis will be conducted as the TPCB progressively rotates around the centre of the wafer. By performing this comparison in parallel with our simulations, we aim to provide a comprehensive explanation of the dual-wave generation mechanism. In **Fig 5.15a-1**, we measure a dominant Rayleigh SAW frequency (green arrow) around 20 MHz, along with a minor harmonic (likely a SH-SAW) component (blue arrow) close to 35 MHz. This results in a sinusoidal wave being formed at the surface exclusively **Fig 5.15a-2**. At D-90 (**Fig 5.15b-1**), a dominant SH-SAW (blue arrow) is measured (~34.4 MHz) with a minor component of a Rayleigh SAW (green arrow). The wave simulation reveals internal stresses in the material (**Fig 5.15b-2**), with minimal surface displacement, commonly referred to as Quasi-SH-SAW. Furthermore, the SH-SAW frequency appears to be higher than the Rayleigh component, consistent with substrate studies [156].

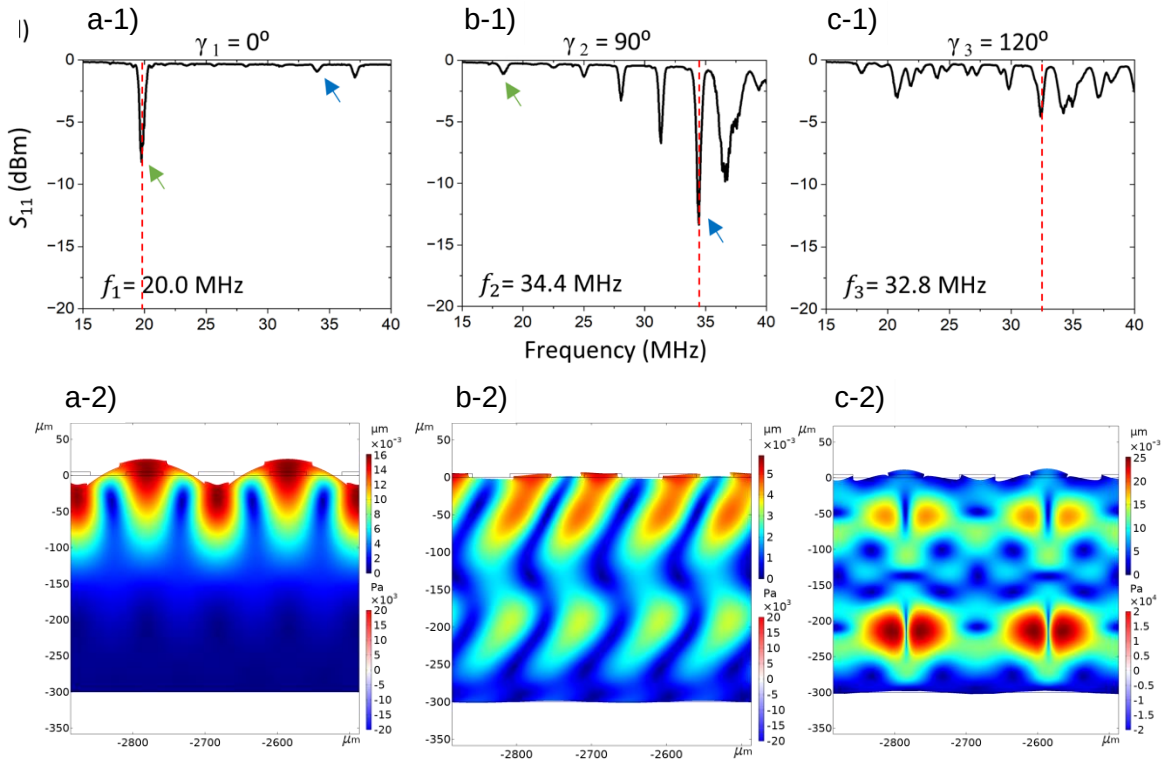

Figure 5.15. Two dimensional COMSOL simulations of the three key wave deformations and their scattering parameters. a-1 & 2) R-SAW-0, b-1 & 2) D-90, and c-1 & 2) C-60.

Essentially as the R-SAW-0 harmonic begins to reduce, the harmonic waves start to increase. A transition state (**Fig 5.15c-1**) between the Rayleigh (i.e., R-SAW-0) and SH-SAW (i.e., D-90) is identified as the dual-wave region, since both wave properties are manifested. This is demonstrated in **Fig 5.15c-2**, which shows that while the internal stresses are maintained, the surface displacement remains as well, resulting in a dual-wave.

The studies leading up to this point yield a rather map looking image of the lithium niobate (**Fig 5.15**). By extracting the data from a sweep of the simulation's areas were identified where each waves dominate. For example, Rayleigh SAW seems to mostly dominate at regions from 0°-40°. Whereas SH-SAWs are mostly identified at the range of 80°-90°. Combination of each is mostly manifested at angles 60°-70°. Lastly, a short comment about the waves generated in the white region (approx. 40°-50°.). Preliminary S_{11} analysis demonstrates very minimal absorption of any kind frequency. In an analogy the S_{11} curve seems to almost flatline, it becomes very difficult to identify or characterize any meaningful harmonics as its akin to digging through noise. It is does not necessarily mean that the waves generated in this region are neither Surface SH-SAW or Dual-waves, or that they will not actuate particles, they are disregarded due to being neither and difficult to predict.

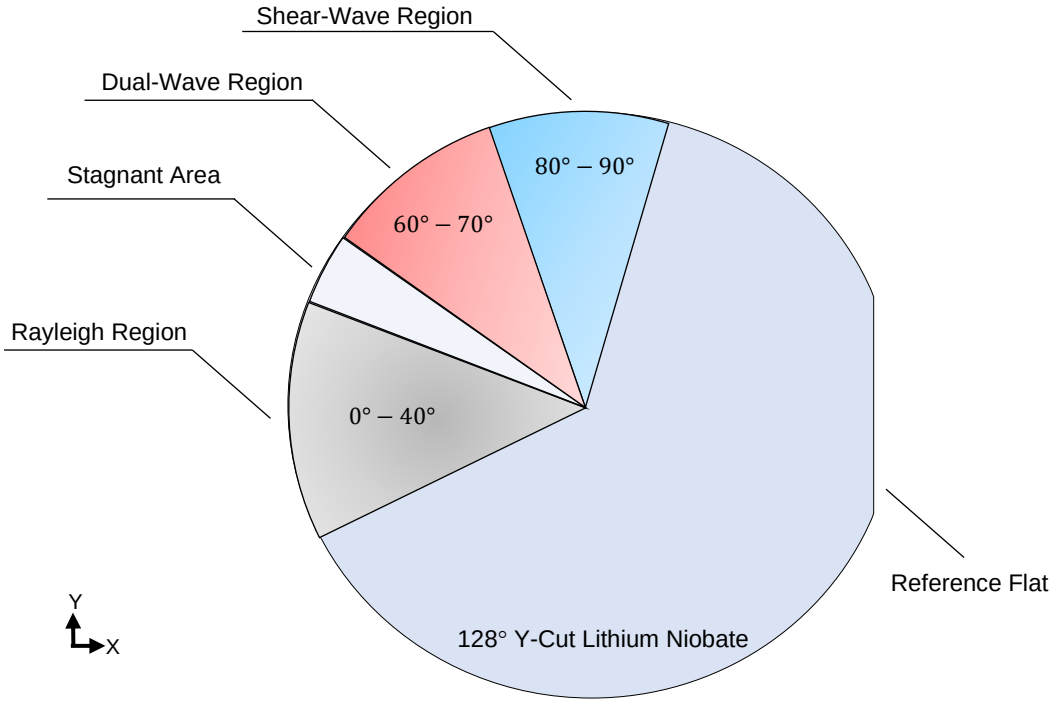

Figure 5.16. A rough representation of the wave types generated on a $LiNbO_3$ substrate.

5.7 Conclusions

This chapter explored the application of the Dynamic Acoustofluidic System (DAS) for manipulating sessile droplets, building on its successful use in particle patterning and separation. The DAS's ability to rapidly reposition Interdigital Transducers (IDTs) at various angles was leveraged to overcome the limitations of traditional photolithography, which is costly and inflexible.

Using DAS, notable changes were observed in the reflection coefficient (S_{11}) as the IDTs were rotated around the $LiNbO_3$ wafer. At 0°, a significant dip at 20 MHz indicated the presence of Rayleigh Surface Acoustic Waves (R-SAW). As the IDTs rotated, frequency shifts and variations in the reflection coefficient were noted, correlating with changes in the speed of sound and material coupling coefficients. Angles such as 60°, 70°, 80°, and 90° exhibited multiple S_{11} dips, suggesting the excitation of various waveforms.

The waves measured by the Vector Network Analyzer (VNA) were then exposed to the sessile droplet to study their acoustic translation phenomena. In the Rayleigh wave region, streaming was observed, with notable variations in streaming direction due to changes in angle. Particularly, at angles between 60° and 70°, a high concentration effect was observed, likely due to dual-wave interactions. It was hypothesized that dual-wave modes,

comprising both surface and bulk components, could explain the observed concentration effects in the droplet.

Overall, the DAS showed significant potential in manipulating sessile droplets by leveraging the anisotropic properties of $LiNbO_3$. The ability to reposition IDTs and observe the resulting acoustic phenomena provided valuable insights into wave behaviour and its applications in microfluidics. The hypothesis that dual-wave modes contribute to varying droplet manipulation effects was supported by experimental observations and simulations.

Future work should focus on validating these hypotheses through detailed simulations and experimental setups, incorporating advanced measurement techniques like laser vibrometer.

The following chapter applies the concentration phenomena observed for manipulation of nanoparticles.

Chapter 6

Concentration of Micro- & Nano- bioparticles

6.1 Introduction

The remarkable prominence of strong particle deflection, concentration ability and streaming pattern availability, as covered in the previous section (**Fig 5.9**), served as a source of inspiration for further research into advanced concentration techniques. This section presents an ultrafast acoustofluidic centrifuge for EVs (ACEV) [205]. To transcend the current limits of nanoparticle handling, the dual-wave mode hypothesized in Chapter 5, which simultaneously generates both Rayleigh and SH-SAWs is shown to effectively concentrate nanoparticles down to 20 nm within 105 s with a sample volume of 50 µL. In addition, the dual-wave mode maintains the capability of microparticle actuation and improves the throughput of cancer cell enrichment in a sessile droplet. The ACEV device demonstrates ultrafast concentration of EVs, where an EV aggregation is visible within seconds and by 30 s had produced EV pellets.

6.2 From DAS to ACEV

Originally, the Dynamic Acoustofluidic System (DAS) was developed for use in a laboratory setting, specifically designed to operate with the available microscopes. However, to perform the nanoparticle experiments discussed later in this chapter, the DAS device required modifications to adapt to smaller and more precise microscopes used for nanoparticle observations, in addition a blacked-out environment was required for most efficient fluorescent experiments, therefore a cover was designed (**Fig 6.1**). While the underlying methods and techniques remained identical, the physical configuration of the DAS had to be altered. This change was implemented rapidly, demonstrating the system's flexibility and adaptability to different experimental environments.

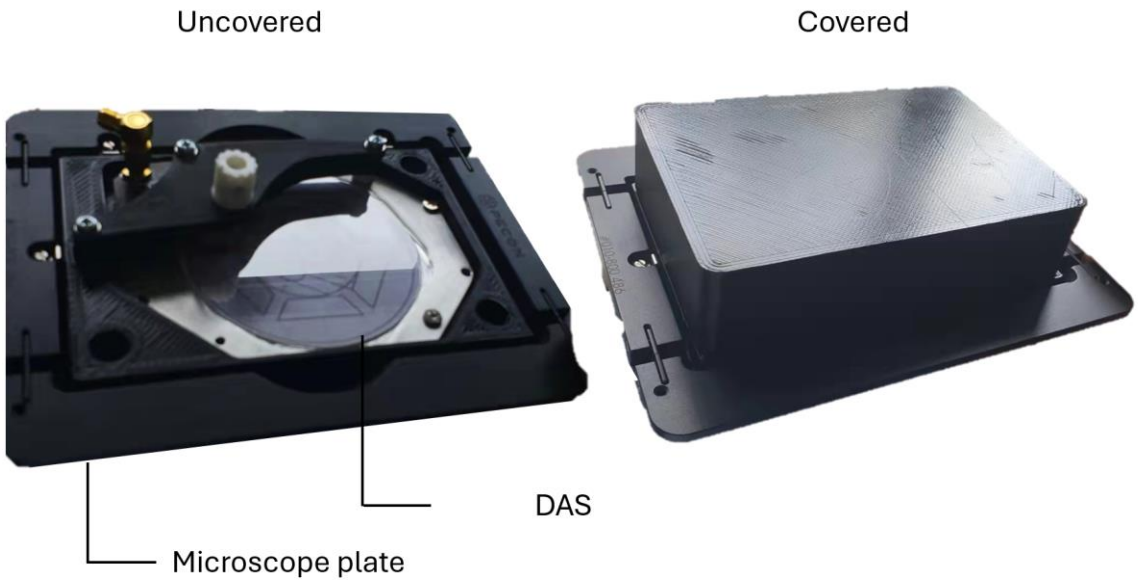

Figure 6.1. An experimental setup used for droplet manipulation. a) displays a DAS-B unit under the b) microscope linked to the c) electronics system DAS-A through a d) matching network system. Operation flow reveals the key connections for successive particle streaming.

Due to the nature of the experiments, some were conducted in an isolated laboratory while others were performed in a hospital setting, where the use of cells and EVs was necessary. As a result, the device depicted in **Fig. 6.1** was utilized under varying conditions. **Fig 6.2a-c** illustrates the experimental setup employed for synthetic particle experiments using a smaller microscope. However, for experiments involving cells and EVs, the device was positioned under a different microscope, resulting in the setup shown in **Fig. 6.2f**. This adjustment was necessary to accommodate the specific requirements of biological sample analysis.

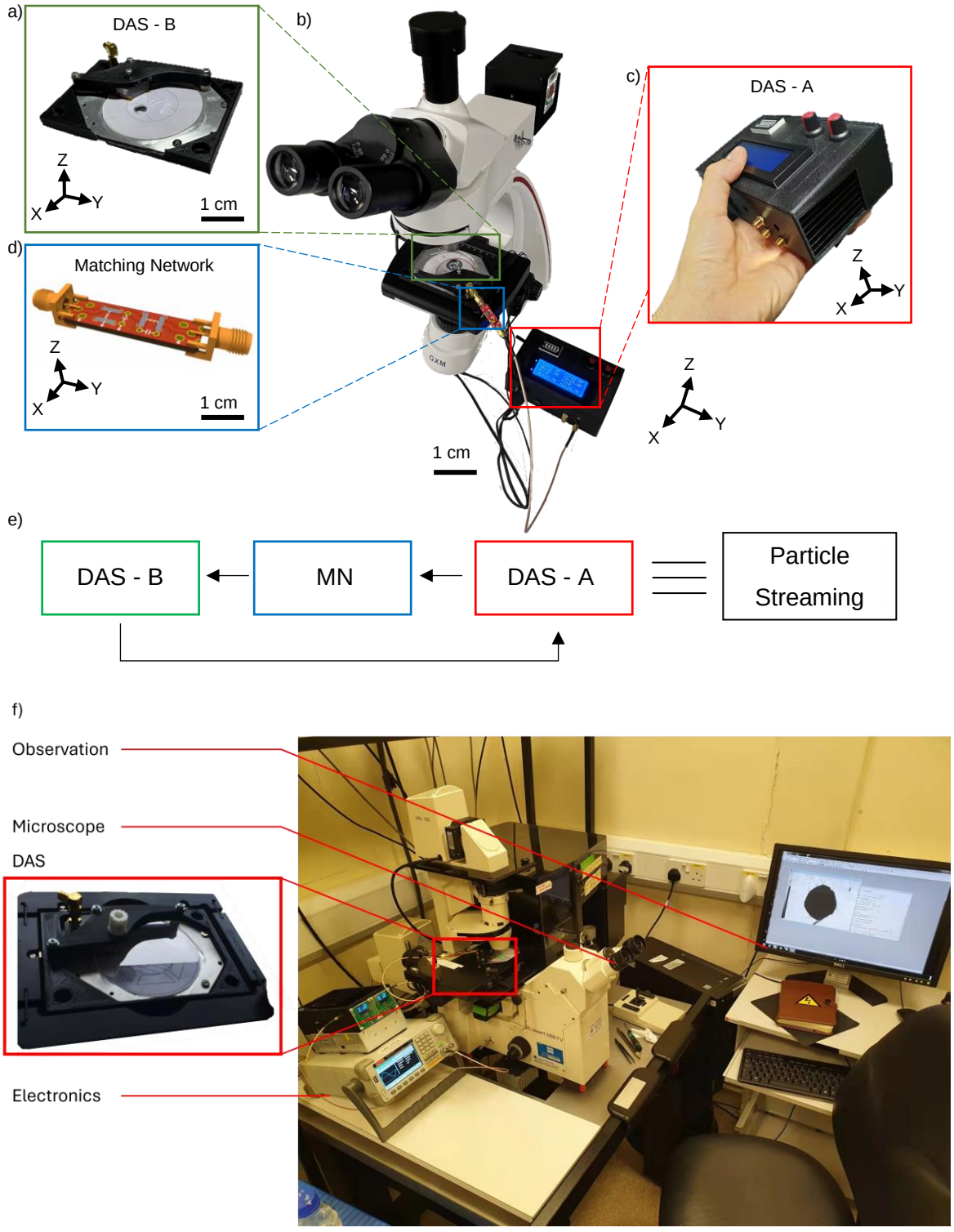

Figure 6.2. An experimental setup used for droplet manipulation. a) displays a DAS-B unit under the b) microscope linked to the c) electronics system DAS-A through a d) matching network system. Operation flow reveals the key connections for successive particle streaming. f) experimental setup used for biological sample concentration.

6.3 Operation of the Acoustofluidic Centrifuge for EV (ACEV)

Fig 6.1a shows the configuration of the ACEV device. A 128º Y-cut lithium niobate ($LiNbO_3$) substrate is bonded with a ring made from PDMS, which accommodates EV samples. An interdigital electrode patterned on a thin-film printed circuit board (TPCB) is mounted onto the $LiNbO_3$ substrate to produce SAWs travelling towards the EV sample loaded to the ring. By setting the angle between the electrode and the reference flat of the $LiNbO_3$ substrate to be 120º, a combination wave integrating Rayleigh and SH-SAWs is produced, which induces single vortex streaming and complex acoustic attenuation, effectively concentrating nanoparticles and EVs from the sample. The ACEV device offers a simple and accessible option to concentrate nanoparticles and EVs with ultrafast and low-volume fashions. The straightforward operation involves five steps, as shown in **Fig 6.3b**. (1) Cleaning and sterilising the PDMS ring inside-out. (2) Loading an EV culture supernatant of approximately 50 µL to the PDMS ring. (3) Starting the concentration process by switching on the SAW. (4) An EV pellet is formed at the centre of the sample within 35 s. (5) Extracting the EV pellet by using a pipette. The concentrated EVs are ready for downstream analysis. The ACEV device takes the advantage of the detachable electrodes when developing SAW devices [34], e.g., easy fabrication without accessing cleanroom facilities. The detachability feature allows rotation of the $LiNbO_3$ substrate to achieve arbitrary angles between the finger electrode and the reference flat of the substrate (**Fig 6.3a**).

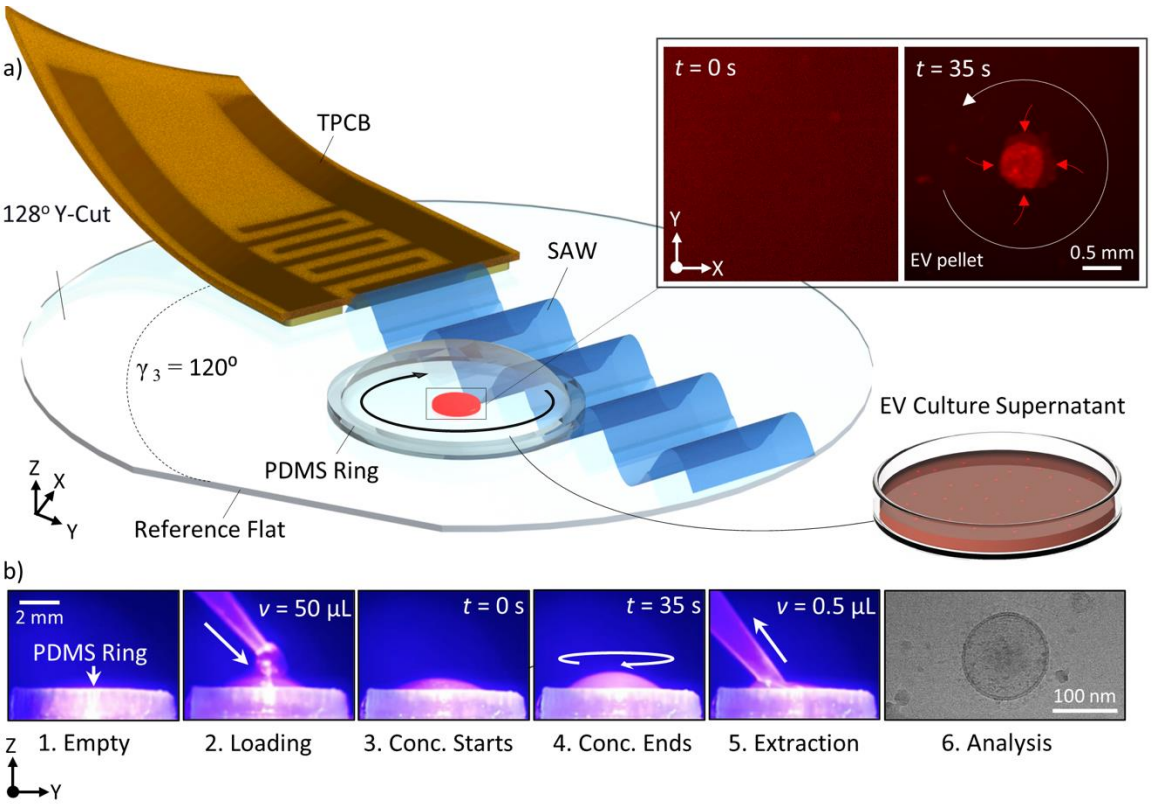

Figure 6.3. Acoustofluidic centrifuge for ultra-fast concentration of extracellular vesicles (ACEV). (a) The ACEV device is made by mounting a thin-film printed circuit board (TPCB) with interdigital electrodes to a 128º Y-cut LiNbO3 substrate. EV suspension is added to a PDMS ring as the sample reservoir. The concentration is achieved by the micro-streaming induced by surface acoustic wave (SAW), produced by the TPCB-based transducer. An inset shows the EV sample inside the PDMS ring before and after SAW concentration. (b) Process flow for using the ACEV device. 1. The PDMS ring is prepared for accommodating EV culture supernatant. 2. An EV suspension (50-µL) is loaded into the PDMS ring. 3. SAW is turned on to concentrate the EV supernatant. 4. Extensive microstreaming is noted in the EV sample, rising the sample higher. 5. The concentrated EVs form a pellet, which can be extracted using a pipette. 6. Harvested EVs are subjected to follow-up analysis, such as electron microscopy.

Such flexibility is essential in this chapter as it enabled the investigation of potential SAW modes apart from Rayleigh and SH-SAWs. Due to the contact impedance existing between the electrodes and the $LiNbO_3$ wafer, the TPCB-IDT yields less power efficiency than that made by the conventional photolithography process. This can be overcome by adding a matching network to the TPCB-IDT to improve impedance mismatching [206], [207]. Conventional SAW devices made using the photolithography process are often a one-off component, e.g., any modification to the IDT requires restarting the photolithography process, which limits the research throughput and increases the footprint of the device in this study. As the 128º Y-cut $LiNbO_3$ substrate is highly anisotropic, the generation of

Rayleigh SAW requires the interdigital electrodes to be positioned in parallel with the reference flat of the $LiNbO_3$ substrate, which is annotated as γ1 = 0º in **Fig 6.8a**. The diffraction of the acoustic wave causes the bulk fluid to translate along the direction of the SAW and exhibit Stokes Drag force on the suspended particles. The existence of the PDMS ring limits the forward translation and sample deformation, leading to circular streaming produced inside the boundary when positioning the TPCB-IDT asymmetrically with an offset to the droplet centre (**Fig 6.3a**) [196], [197], [208], [209]. The particles in the droplet experience slower circular streaming velocity in the centre resulting in a stagnation point established to accumulate the particle pellet.

6.4 Sample Volume, Size, Offset

By positioning the droplet in front of the IDT, only pushes the particles to the edge, however, to achieved concentration an offset Δd must be added. As the wave (**Fig 6.4,** red rectangle), passes through the droplet, acoustic radiation force will deflect particles as well as generated streaming and stokes drag force on the suspended particles. The added offset will generate a stagnation point where particles accumulate progressively. The value for the offset, must be carefully selected. If $\Delta d = 0$, the edge of the wave will cross past the concentrated material, disturbing the concentration. If Δd is too large the droplet will simply not experience enough wave exposure. In this thesis the offset used was determined experimentally, allowing for sufficient wave attenuation and area for the pellet to form, yielding a rule of thumb for authors experiments:

$$\Delta d = \frac{7 * d_{liquid}}{90} \tag{5.1}$$

where d_{liquid} is the diameter of the droplet.

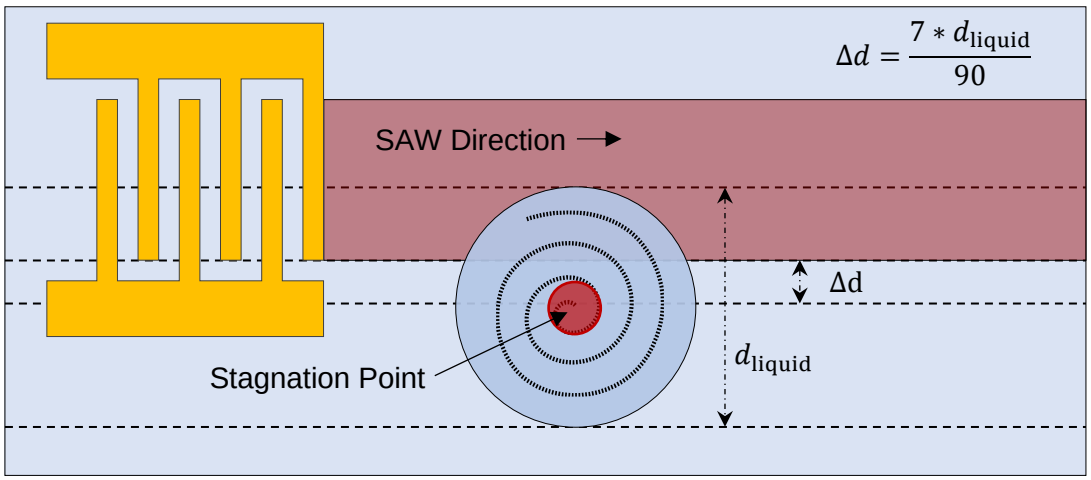

Figure 6.4. TPCB offset (Δd) configuration for a droplet of diameter d_{liquid} to produce an efficient stagnation point (red circle) required for concentration.

While determining the optimal offset value for the system, it became apparent that achieving single vortex rotation was not solely dependent on droplet diameter and offset. A critical factor was the liquid volume within the PDMS boundary. If the liquid volume fell below ~40 μL, double vortex streaming (see **Fig 6.5a**) was typically observed. This is not ideal for concentration applications. Conversely, adding liquid beyond the 60 μL range resulted in unpredictable liquid streaming motion, sometimes resulting in the observation of four or more vortices. Additionally, adding excessive liquid caused particles suspended near the top boundary of the liquid to not experience the acoustic radiation force due to wave attenuation. To define the range of volumes that generate single vortex streaming for an OD 10 mm droplet and an offset of $\Delta d = 0.78$ mm, we conducted experiments across a range of volumes. It is noteworthy that a value of 50 μL is precisely in the middle of the graph (see **Fig 6.5b**). Additionally, this volume showed the highest repeatability across multiple experiments. Therefore, we selected a liquid volume of 50 μL for subsequent experiments, as it provided a good balance between minimizing error and maintaining single vortex streaming.

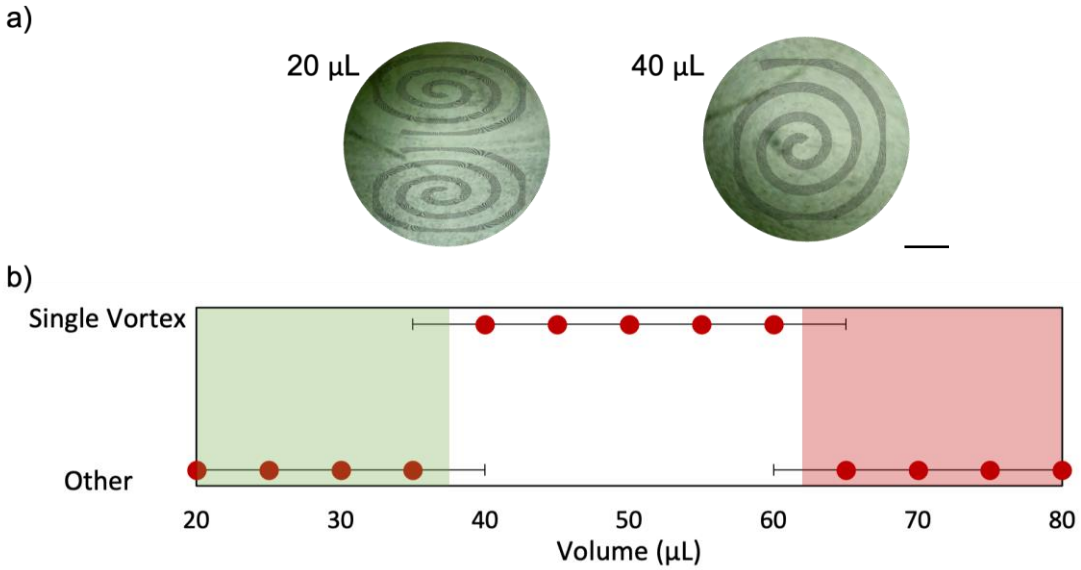

Figure 6.5. Effects of streaming patterns in a liquid due to changes in a) volume for a fixed offset and droplet diameter (10 mm). b) representative graph for which an efficient single streaming occurs promoting concentration. Scale bar 1 mm.

6.5 Angle Selection

Post determining the offset, volume and droplet diameter, the concentration efficiency of different harmonics introduced in Chapter 5 was tested. previous experimental data indicated that operating at harmonic angles resulted in a significantly enhanced deflection phenomenon, indicated by significant particle aggregation. As a result, it was determined that leveraging this phenomenon would be advantageous for smaller particles within the nanometre range. After conducting experiments with 100 nm particles (**Fig 6.6**) through all configurations, it became apparent that achieving tightly packed and round pellets (see **Fig 6.7** for circularity analysis) required correct selection of the appropriate harmonic for nanoparticle concentration. Round and tightly packed pellets are required for further extraction of post analysis.

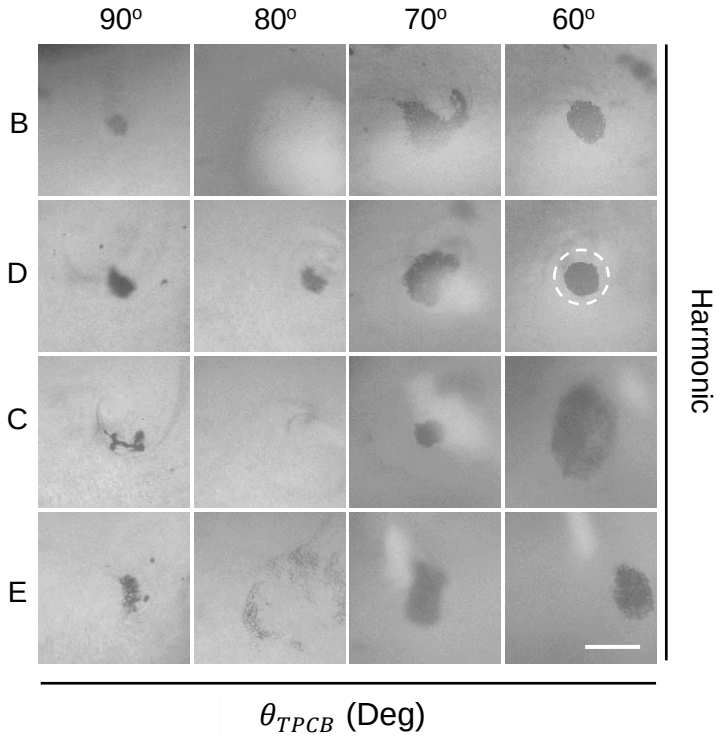

Figure 6.6. Nanoparticle concentration through a range of angle and frequency setups identified during S_{11} analysis. The dashed circle highlights the selected configuration for consequential experiments. Scale bar is 1 mm.

The formation of round and tightly packed pellets is critical in the nanoparticle concentration process, as they facilitate the extraction of the concentrated material for further analysis. If the pellets are dispersed or not tightly packed, it can make automation difficult and result in inefficient particle offloading. Additionally, if the pellets are not formed at the centre of the sample, it poses similar challenges for automated retrieval of the concentrated material. Therefore, it is important to ensure that the selected concentration configuration results in the formation of well-defined, tightly packed, and repeatable pellets at the centre of the sample, which can be easily retrieved using automated devices for further analysis.

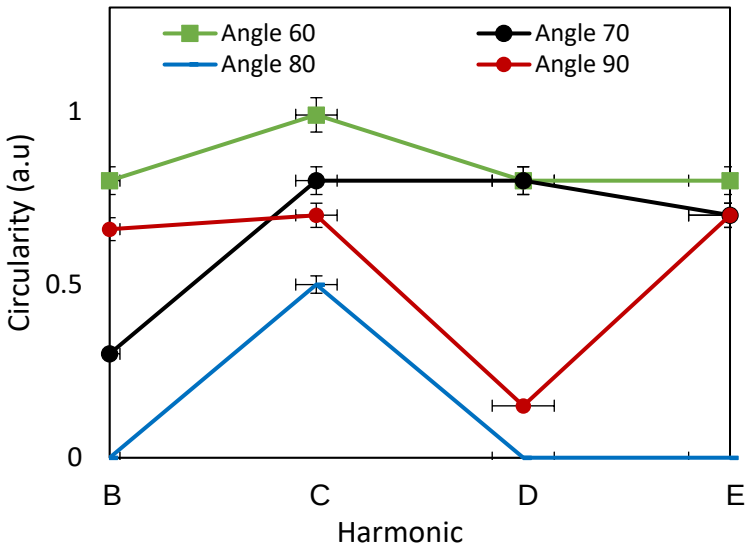

Figure 6.7. Concentrated pellet circularity analysis through a through a range of angle and frequency setups identified during S_{11} analysis.

At each angle tested (90, 80, 70, and 60), there was evidence that the harmonic had an impact on the nanomaterial, but the quality and efficiency of concentration varied significantly. At angle 90, the effect was present but minimal, and oval small, uneven pellets were observed with an average circularity of ~0.5. At angle 80, some aggregation occurred, but not in a pellet, and the effect was not as strong. At angle 70, the effect became much more apparent, but the pellets were not tightly packed, and the circularity was low (~0.65). At angle 60, the uppermost concentration efficiency was observed; however, different frequencies yielded different results. Ultimately, D-60 was selected as the harmonic for further concentration experiments because it had the highest circularity (~0.98) and the densest pellet packing. Although harmonic C-60 appears much larger it is not packed as effective spreading out material across higher area making it difficult for collection. To elaborate further, the experiments were conducted under carefully selected conditions, including the offset, volume, and droplet diameter discussed earlier. These parameters were determined to be the most suitable for achieving the single vortex streaming required for concentration. It is possible that by changing these experimental parameters, other angles might achieve good concentration efficiency (Full list for variables of influence **Table 6.1**). However, due to the wave steering effect, it can be challenging to position the droplet accurately for other modes. The wave steering effect refers to the fact that as the frequency and angles change the wave emitted by the IDT will change in its position and trajectory, which makes it difficult to control the droplet's position precisely. Therefore, the selection of D60 as the optimal harmonic for nanoparticle concentration was based on careful

experimentation and analysis of the results. While other angles and experimental parameters indicate the possibility of good concentration efficiency, the selected sample volume and positioning values were found to be the most effective and reliable for achieving optimal concentration efficiency when using D60 configuration. The D60 as discussed in earlier Chapter is a dual-wave mode SAW, encompassing both components of Rayleigh and Shear SAW.

Table 6.1 Variables that Influence Concentration.

Property	**120° Compatible**	**X° Compatible**
IDT Frequency	34.2 MHz	*x* MHz
IDT Angle	120°	*x*°
Liquid Volume	45 µL	*x* µL
Δ_{d}	~ 0.7 mm	*x* mm
d_{liquid}	9 mm	*x* mm
$PDMS_{\mathrm{wall\ thickness}}$	1 mm	*x* mm
Piezoelectric	$LiNbO^3$	*x*

6.6 Effects of the Dual-wave Mode

After the selection of D60 as the optimal concentration configuration for nanoparticle concentration, it was necessary to benchmark its performance against other configurations. In previous experiments, harmonics at angle 90 were found to be shear displacement dominating, while angle 0 was surface wave dominating. Hence, in this context, it was decided to test three different setups, including D60, shear-dominant harmonic at angle 90 (D90), and surface wave dominant harmonic at angle 0 (R-SAW-0), and compare their performance. Such analysis allows to draw a spectrum, from surface to shear and balanced displacement systems considering the three cases (**Fig 6.8a**).

First the trio, underwent additional simulation analysis as the results shown in **Fig 6.8b**. For the angle R-SAW-0 a typical out-of-plane surface displacement for generating Rayleigh SAW is achieved, in which the wave decays with a characteristic length approximately equal

to a wavelength below the surface. The wave mode for the D-90 reveals displacements in the plane of the surface and a compressional component, which highlights the presence of Quasi SH-SAWs [156]. The vibration pattern for D-60 demonstrates the out-of-plane surface displacement and internal compressional components. This scenario concludes a dual-wave mode existence and combines the advantage of the Rayleigh and SH-SAWs.

The deformation of the droplet surface (see arrows in **Fig 6.8b**) induced by the interaction with the acoustic waves at the centre (red curve) and the periphery (green and blue curves) is shown in **Fig 6.8e**. The Rayleigh SAW (R-SAW-0) slightly increases the height of the droplet at the three locations showing no nanoparticle concentration effect as no aggregation observed under the fluorescence microscope (**Fig 6.8e**, left). The SH-SAW (D-90) leads to a considerable rise at the droplet centre (up to 60%) and an intensive droplet jetting effect. Particle accumulation is vividly observed (white arrow, inset in **Fig 6.8e** middle). The concentration effect was observed for D-90 before but concluded to be inappropriate due to its poor pellet aggregation, low concentration circularity and performance.

The dual-wave mode taking place at D-60 shows considerable improvement. As shown in **Fig 6.8e right** the droplet surface denotes a notably increased height at the centre with an oscillation pattern on the periphery. The nanoparticles are successfully concentrated in the centre of the droplet (yellow arrow). It is predicted that a slight rise of the droplet height at the centre, while oscillation on the sides, might be supporting effective concentration of nanoparticles, however the author does not identify it as a leading cause.

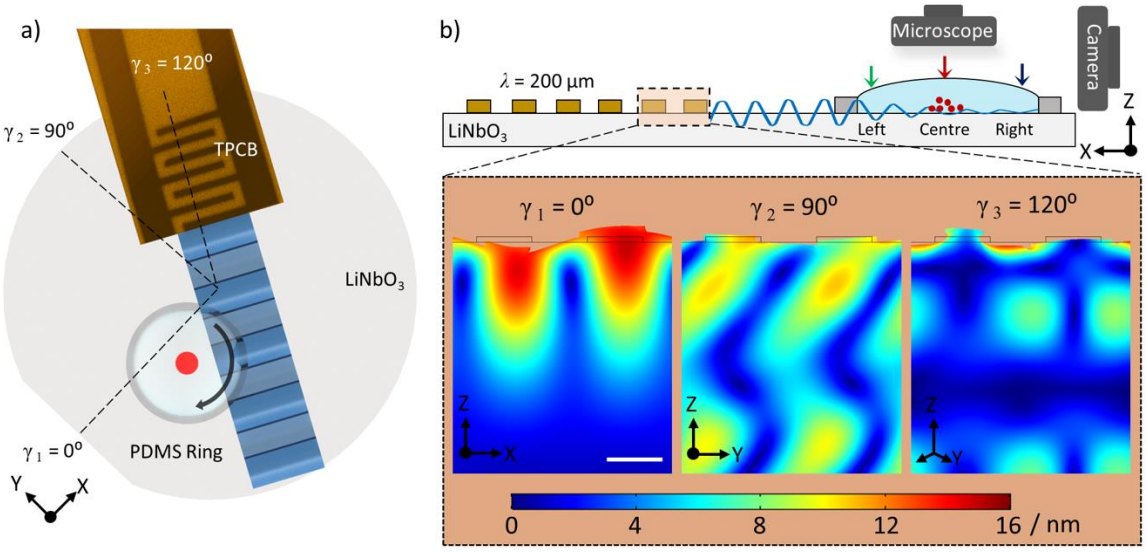

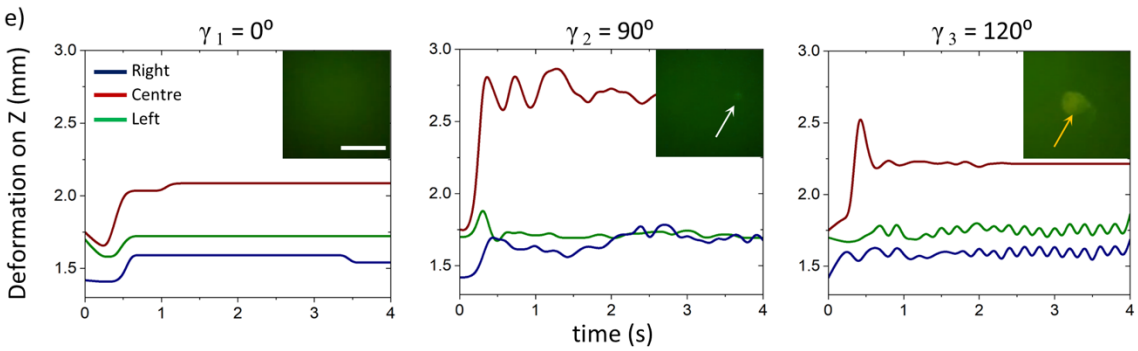

Figure 6.8. Characterization and optimization of the ACEV device. (a) The top view drawing shows the FPCB rotating on the 128º Y-cut LiNbO3 substrate. Three angles, γ1 = 0º, γ2 = 90º, and γ3 = 120º, with respect to the reference flat on the substrate, are selected for characterization. (b) Schematic diagram of the SAW interacted with the droplet in the PDMS ring. Three arrows indicate the regions for measuring the droplet deformation on the z-axis. An inset shows the numerical simulations of the interdigital transducer (IDT) vibration under the three different TPCB angles. The scale bar is 50 µm. (e) The droplet deformation on the z-axis is measured by three regions, as marked in Fig. 2b. Insets demonstrate the manipulation of 20 nm particles at different angles. Scale bars 0.5 mm.

In pursuit to mitigate issues existing at other angles, if more time is allowed for the D90 configuration to reach an acceptable pellet circularity, or more power is added, the droplet evaporated every time. When comparing to D60 (**Fig 6.9**), the droplet volume reduces only 8% when compared to D90 (43%). This solidifies the unsuitable condition for manipulating biological samples at shear dominating waves (for the droplet setup used). The findings also agree with previous results [156], where the Rayleigh SAW was compared directly with SH-SAW.

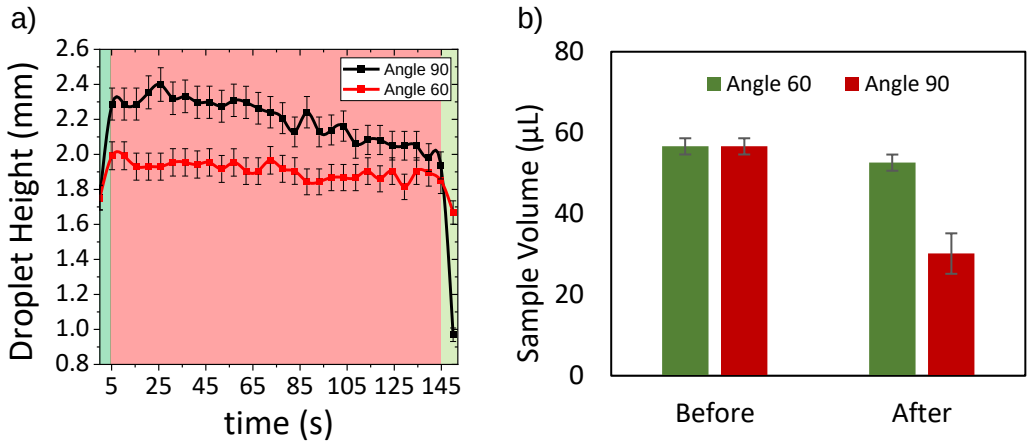

Figure 6.9. Droplet evaporation effects at setups D-90 and C-60. a) Upon SAW exposure the droplets experience slight jetting and vibration effects and gradually lose volume due to evaporation. b) Liquid volume before and after SAW exposure for angles D-90 and C-60.

6.7 Ultrafast Concentration of Microparticles

While the ACEV's remarkable ability to affect particles is noteworthy, what sets it apart from existing methods is the device's ability to handle relatively large sample volumes with high precision and efficiency. To assess the performance of the ACEV device in microparticle concentration, we used polystyrene microparticles of different sizes obtained from Sigma Aldrich, USA. The selected microparticle sizes were 1 µm, 5 µm, 8 µm, and 20 µm. Prior to testing, the particles were diluted in phosphate-buffered saline (PBS) to a concentration of ~0.01 g/mL. By using microparticles of varying sizes, the ACEV's concentration ability can be evaluated in the context of handling complex mixtures of microparticles, which is essential for cell manipulation applications.

In **Fig 6.10**, a sample volume of 50 µL was used, which is much larger than the typical volume used for sessile droplet concentration techniques [200]. Although the particle size in the micro scale is not ground-breaking, the ACEV device's ability to concentrate microparticles down to 1 µm within 18 s, represents a significant advance in the field of micro-particle manipulation. Concentrating such volume (50 µL) for a range (20 µm - 1 µm) of particle sizes with remarkable speed and precision is notoriously challenging with existing methods. Therefore, the ACEV device's ability to handle sample volumes with high efficiency and precision, while simultaneously concentrating particles of various sizes, makes it a highly promising tool for researchers and industrial applications. Its unique ability to concentrate particles of various sizes at unprecedented speeds can pave the way for new discoveries and innovations in the fields of medicine, biotechnology, and industrial manufacturing.

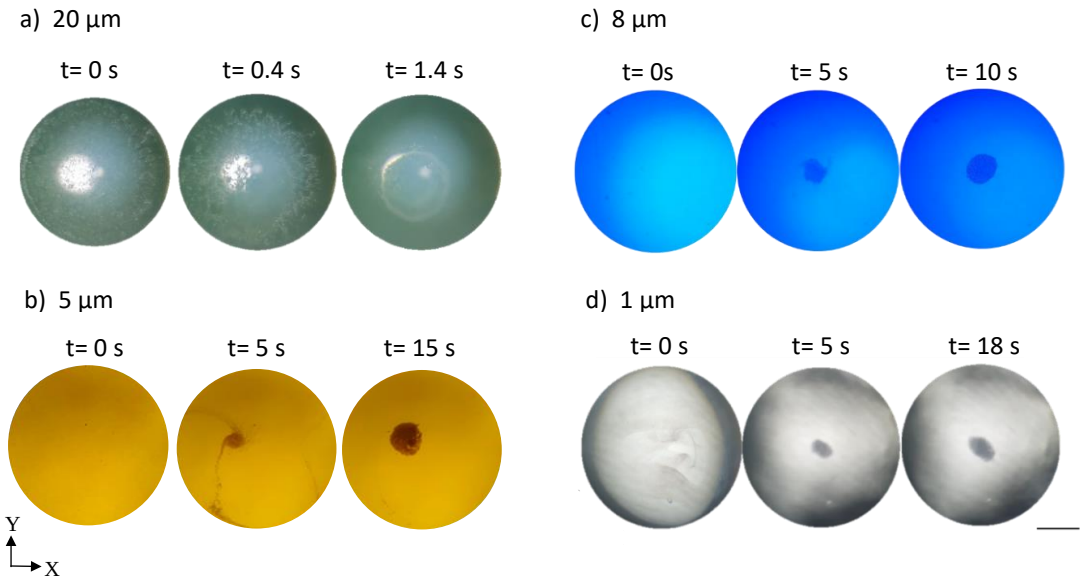

Figure 6.10. The concentration of micro particles with the size of 20 µm, 8 µm, 5 µm, and 1 µm, using the ACEV device. Timestamps for increasing pellet size over time are shown for respective microparticles. The scale bar is 1 mm.

6.8 Ultrafast Concentration of Nanoparticles

Polystyrene nanoparticles (Sigma Aldrich, USA) with sizes of 20 nm, 30 nm, 100 nm, and 500 nm were used to expand the concentration capability of the ACEV device, as these sizes cover a wide range of EV sub-populations [210]. These nanoparticles were prepared by diluting them into phosphate-buffered saline (PBS) at a ~ 0.01 g/mL concentration. As shown in **Fig 6.11**, fluorescence images with time scales provide a visual indication of the aggregation of the nanoparticles (white arrows in **Fig 6.11**). For all the particle sizes, concentration was observed as soon as the SAW was applied. The normalized fluorescence intensity (norm. Fluo int) across the sample (dashed line in **Fig 6.11**, left) was obtained to reveal the change in fluorescence intensity over time, as shown in **Fig 6.11**. Durations for concentrating the four particle sizes are 45 s, 50 s, 60 s, and 105 s, respectively. Nanoparticles were found to be aggregated at the bottom in the centre of the droplet (**Fig 6.8b**). These associated speeds represent a significant advance in the field of nanoparticle manipulation, enabling the concentration of a wide range of particle sizes with remarkable speed and precision. Achieving such precision and reproducibility in nanoparticle concentration is notoriously challenging with existing methods. Advances, brought by ACEV have important implications for nanoparticle research, enabling more accurate and efficient

analysis of sub-populations and potentially leading to new insights into their properties and applications.

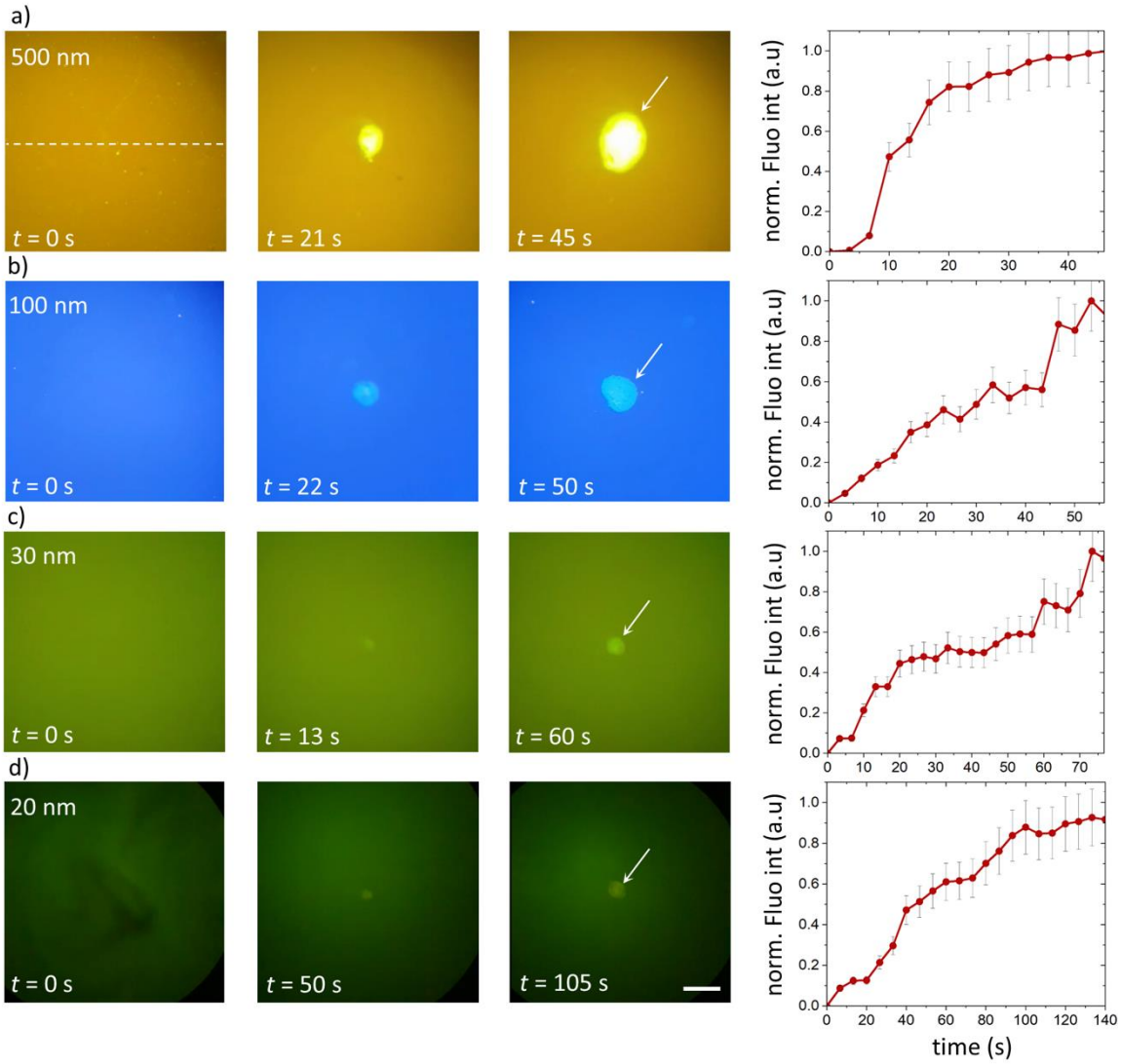

Figure 6.11. The concentration of nanoparticles with the size of 500 nm, 100 nm, 30 nm, and 20 nm, using the ACEV device. Fluorescence images of the sample with timestamps and the corresponding normalised fluorescence intensity (n = 5) are shown for (a) 500 nm, (b) 100 nm, (c) 30 nm, and (d) 20 nm nanoparticles. The dashed line highlights the measurement area. The scale bar is 0.5 mm.

6.9 Applied Power and Concentration Time

Attempts to improve the concentration time can be made by adjusting the power applied to the sample. However, while the process can be fast, it cannot be increased beyond a certain point due to applied power limitations. It is essential to apply the appropriate amount of

power to achieve the desired concentration rate without compromising the sample's integrity. Applying too little power (less than 0.12 W) will result in the sample only experiencing streaming, which will not produce the desired concentration (**Fig 6.12,** Streaming). Conversely, applying too much power (more than 0.2 W) will cause the sample to experience intensive wobbling, which can break the concentration. If the power continues to increase, the sample will eventually evaporate, resulting in a significant loss of the sample (**Fig 6.12,** Evaporation/Wobbling). Due to these limitations, the speed of the concentration process cannot be adjusted beyond the appropriate balance of power and time. It's crucial to find this balance to achieve optimal results without compromising the quality of the sample. **Fig 6.12** reveals an operating range where concentration was successful and improved by approaching the power limit. Based on these findings, the optimal power level appears to be located between the two extremes, around 0.15 W. However, to push the device's capabilities to their limits and obtain the most accurate results, the maximum power output was utilized without causing the sample to evaporate. This was done to achieve the most efficient concentration time. Nevertheless, it is advisable to operate the device within a moderate power range, striking a balance between streaming and evaporation extremes.

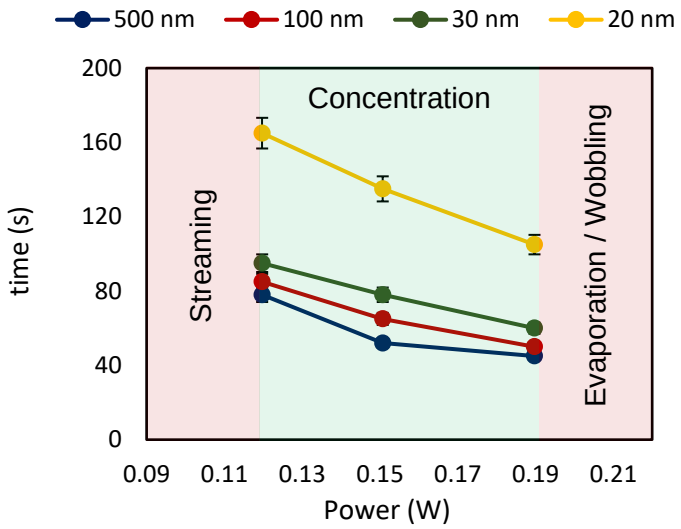

Figure 6.12. Applied power region of operation for particles sized 500 nm, 100 nm, 30 nm, and 20 nm, using the ACEV device.

6.10 Pellet Extraction and ACEV Performance

It is essential to have a simple extraction modality to collect the enriched EVs from the ACEV device for downstream applications, ideally using conveniently accessible tools such as

pipettes. As shown in **Fig 6.13a,** the nanoparticles are well concentrated in a pellet after ~50 s of SAW exposure. A pipette tip is placed near the pellet with guidance under the microscope. The plunger is then slowly released to extract a sample of 0.5 µL, resulting in the nanoparticle pellet being pulled up into the tip. To assess the concentration and extraction ability of the ACEV device, the fluorescence intensity of the original, concentrated, and depleted samples, was measured as shown in **Fig 6.13b**.

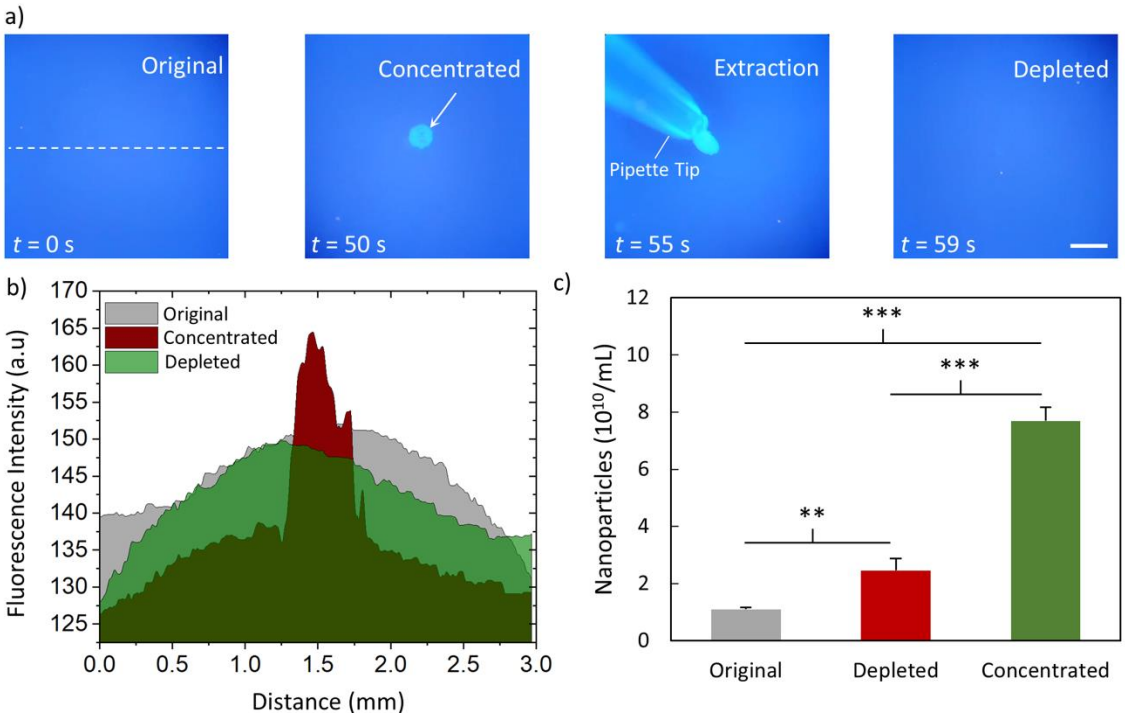

Figure 6.13. The concentration and extraction of nanoparticles in the ACEV device. (a) Fluorescence images of the original sample, concentration, during extraction, and depleted samples. The nanoparticle size is 100 nm. Scale bar 0.5 mm. (b) Fluorescence intensity of the sample upon the sequential steps. (c) Nanoparticle tracking analysis was performed to establish the nanoparticle density of the original sample, concentrated collection, and depleted sample. (n=3, ***p<0.001, one-way ANOVA with Tukey's post-test).

Before concentration, the fluorescence signal indicates the presence of randomly dispersed nanoparticles (grey area). After SAW concentration, a sharp spike in fluorescence intensity is observed at the centre of the droplet (red area), corresponding to the highly concentrated nanoparticles in the pellet. After pipette extraction, the intensity levels off, indicating a complete collection of the pellet. Nanoparticle tracking analysis (NTA) was used to further confirm the extraction completion. The size and concentration of particles present within Du145 cell line-derived samples were measured using a NanoSight™ NS300 system (Malvern Instruments, Malvern, UK) as described [41]. The instrument was calibrated with

80 nm silica beads, prior to each use (nanoComposix, San Diego, USA). Samples were diluted in particle-free water (Fresenius Kabi, Runcorn, UK), to concentrations up to 2×109 particles per ml. Data was collected at 25°C with a 488 nm laser and three videos of 60 s were taken in light scatter mode with the controlled fluid flow with a pump speed set to 50. Videos were processed using NTA 3.1 software (version 3.1 build 3.1.54), where minimum particle size, track length and blur were set at “automatic.” Background measurements of culture media, or water that had not been exposed to cells contained negligible particles.

As shown in **Fig 6.13c**, the nanoparticle density in the pellet increases to $7.69*10^{10}$, from the original sample of $1.11*10^{10}$, which describes the concentration capability of the ACEV device. The nanoparticle pellet’s integrity over time after the concentration is important to design the follow-up collection processes **Fig 6.14d** shows the pellet size of the four sizes of nanoparticles over 20 min after the ACEV concentration. In general, the pellet presents an average enlargement of ~50% after 20 min but only ~7% over 3 min. This should be sufficient to streamline most manual or automatic extraction processes. The whole processing time from the beginning of the ACEV concentration to pellet extraction takes less than one minute. This is a step change in nanoparticle concentration, in contrast to ultracentrifugation, or an assortment of other modalities that are well-known as a time-consuming and labour-intensive process [94].

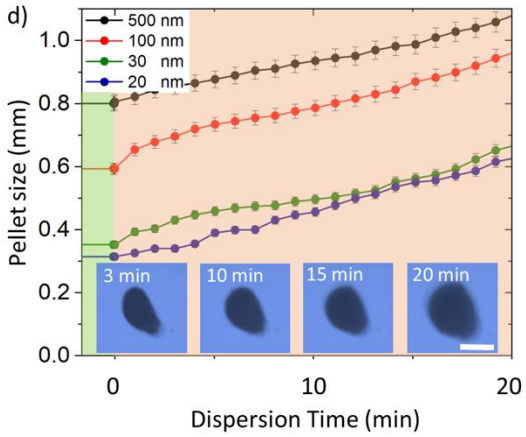

Figure 6.14. The pellet size changes over time; the inset is the dispersion of the 500-nm particle pellet over 20 min. Scale bar 1 mm.

6.11 Concentration of samples with varying viscosities

Testing the concentration capability of a particle manipulation device across a range of viscosities is crucial because it provides insight into the device's performance in diverse

fluidic environments. The viscosity of a fluid can significantly impacts particle motion and interaction, affecting the efficiency and precision of the concentration process. By testing the device's performance across a range of viscosities, researchers can assess its versatility and potential for real-world applications, where fluid viscosity can vary widely. Additionally, understanding how the device performs at different viscosities can help identify optimization opportunities and guide the design of future particle manipulation devices. To explore the concentration time for samples with various viscosities, the nanoparticle suspension was conditioned by adding glycerol to achieve a viscosity of 1 to 6 cP, which encompassed the range of several body fluids, including cerebrospinal fluid (~1 cP) and whole blood (4-5 cP) [211]. To achieve the viscosities required, six mixtures (1mL) of water and glycerol were prepared to simulate wide-ranging body fluids commonly rich with EVs for varied viscosity experiments (**Fig 6.15**). The viscosity ratios were determined analytically and then confirmed using a capillary viscometer. The ratios (water/glycerol) were 1 and 0, 0.787 and 0.212, 0.695 and 0.300, 0.637 and 0.362, 0.590 and 0.410, 0.557 and 0.442 mL for viscosities 1, 2, 3, 4, 5 and 6 cP respectively. Furthermore, 100 nm fluorescent polystyrene particles (Sigma Aldrich, USA) were mixed into the solution at a dilution of 670*10^6 particles/mL. Both the preparation and experiments were performed at a room temperature of 20ºC. The SAW concentration was processed on these samples with the result shown in **Fig 6.15**. The time required to concentrate the nanoparticles increased slightly from 30 s to 37 s when the sample became more viscous, which also impacted the efficacy of the concentration. For instance, at viscosities higher than 4 cP, similar to whole blood, it is struggled to observe nanoparticle pellets perceptibly. The sample used in most of the experiments in the study mimicked the viscosity of cell culture supernatant, i.e., 1.1 cP, which fell in the recommended viscosity range (0.5 – 3 cP) of the ACEV concentration.

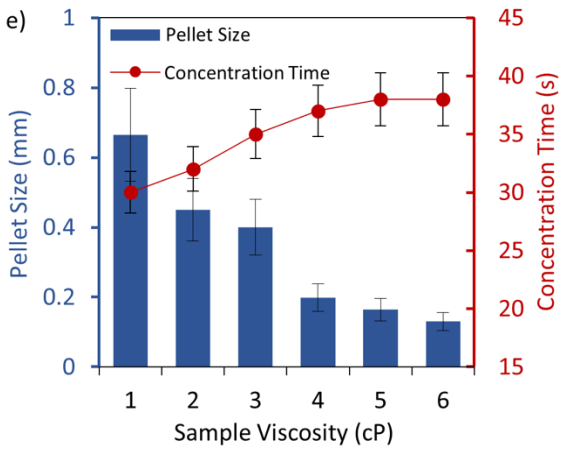

Figure 6.15. The concentration time for nanoparticles (100 nm) over various sample viscosities.

6.12 Cancer Cell Enrichment in ~10 seconds

The demonstrated ACEV capability affecting nanoparticles is not limited by it. It's worth noting that the concentration effect can also be applied to biological samples such as cancer cells. Cancer cells are difficult to detect and study due to their low abundance in biological samples. Concentrating these cells is crucial for effective detection, diagnosis, and treatment of cancer. For cancer cell concentration experiments, IHH Cells were cultured in Dulbecco's modified Eagle's medium supplemented with 10% fetal bovine serum and 1% penicillin-streptomycin. The cells were passaged every four to five days when reaching 65-80% confluency by trypsin incubation for 1-2 minutes, followed by phosphate-buffered saline (PBS) washing and resuspension. The cells were then fixed with 4% paraformaldehyde for 15 minutes and centrifuged at 1,500 rpm for 5 minutes to isolate the cells from the supernatant. Finally, the cells were washed again to remove the remaining paraformaldehyde.

The ACEV device shows promising results (See **Fig6.16a**), for concentrating cancer cells, offering an increase in the volume handled by acoustic state-of-the-art techniques. ACEV device can handle samples at varying dilutions and its effect is not limited by low or high cell densities. Furthermore, results in took only 40 s to achieve concentration of cancer cells, making it a highly efficient and practical tool for cancer research. It should be noted that the concentration speed could have been increased, however, to ensure the safety of the cells, a lower power setting was selected as the cells used were fixed and their viability could not be measured. This was done to mimic the safest possible conditions for live cells, in the unlikely event of acoustic pressure causing damage. Although studies have shown that acoustic pressure has minimal impact on cells, precautions were taken to minimize any potential damage due to handling. To quantify the concentration of cancer cells, the concentrated sample area was placed on a hemacytometer and examined using a microscope. The cells were observed, and the number of cells in a known area of the hemacytometer was counted. This cell count was then utilized to calculate the concentration of nanoparticles in the sample as illustrated in **Fig 6.16b**. The concentrated sample showed a significant increase of up to 250% in cancer cell density when compared to pre-acoustic treated samples.

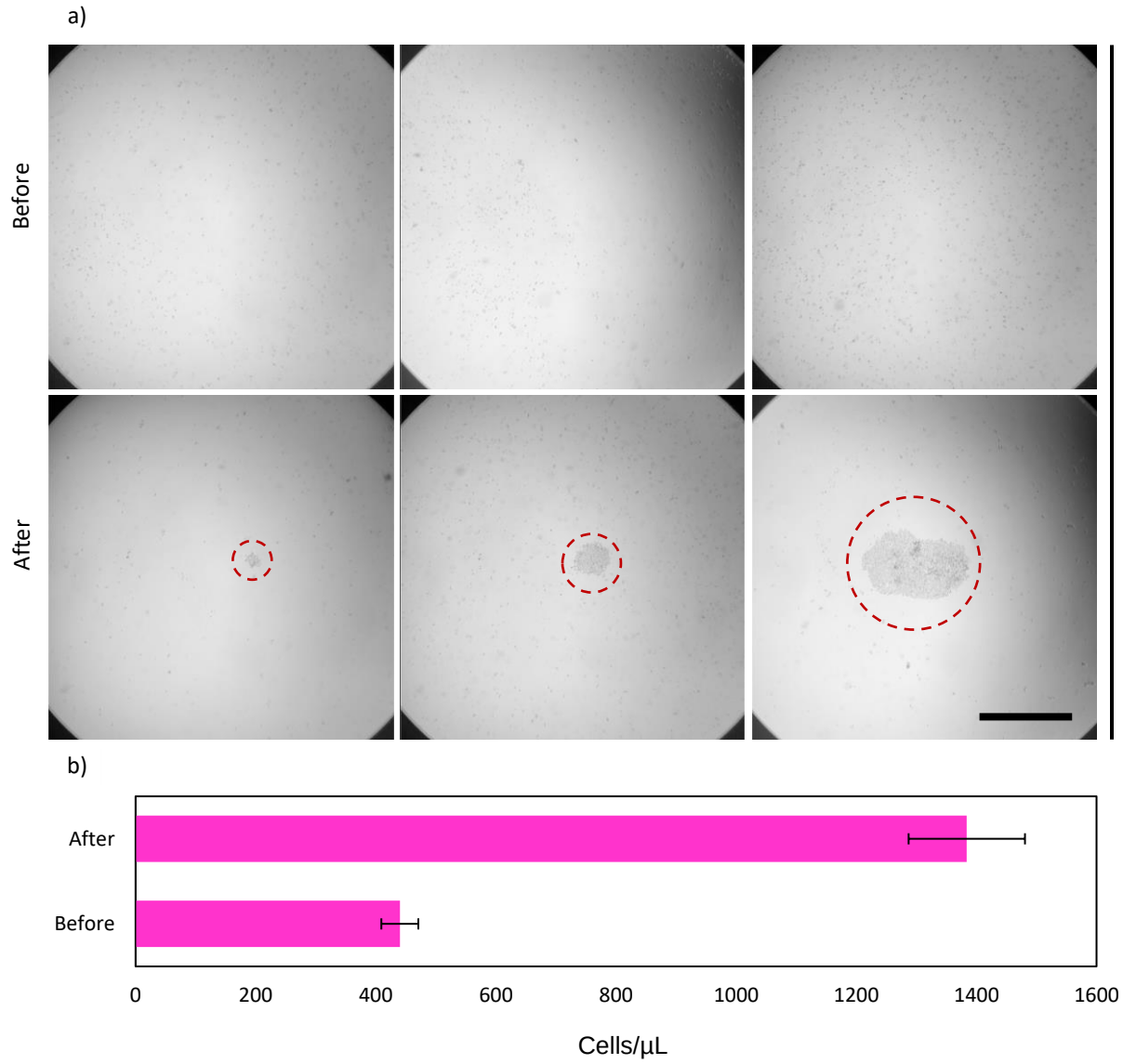

Figure 6.16. Concentration of a) Cancer cells in varying dilutions suspended in PBS. b) Haemocytometer measurements of cell density before and after concentration. Scale bar is 0.5 mm.

6.13 EV Enrichment in ~30 seconds

After systematic characterisation of the ACEV device, EV samples with four dilutions (160, 8, 0.4, 0.02 µg/mL) were applied to test the ACEV handling biological samples. It is notoriously difficult to estimate whether this concentration range is physiologically relevant, because as yet the EV field lacks definitive tools to specifically quantify vesicles, as opposed to other forms of particulates, present in body fluids [212]. This range would certainly serve

a variety of scenarios from cell culture soups and is likely appropriate for different forms of biofluids.

EVs were purified from Du145 prostate cancer cells, grown in bioreactors, by ultracentrifugation on a sucrose cushion as described [213]. Briefly, the bioreactors were seeded with an initial optimized concentration of 4 million cells and cultured in RPMI media with PS/LG and 10% FBS. Upon seeding, 15 mL RPMI with PS/LG and EV depleted FBS were added to the cell compartment, and the standard RPMI + PS/LG + 10% FBS was used in the upper compartment. The bioreactors were left to culture for two weeks. The media from the cell compartment was then removed, processed to remove any cell/debris which was not EV and then frozen at -80ºC until the ultracentrifugation step. The cell compartment was flushed and washed with RPMI media (no additives) before being replenished with 15 mL RPMI with PS/LG and EV-depleted FBS. The standard RPMI + PS/LG + 10% FBS used in the upper compartment was replaced afterwards. After the initial two weeks incubation period, this process was then repeated every week. Once enough samples were collected, EVs were purified using ultracentrifugation on a 30% sucrose/D2O [214]. Purified EVs were resuspended in PBS, aliquoted and stored at -80oC. Once defrosted, the EVs were used in experiments and not re-frozen to avoid frost damage. These aliquots were then measured using nanoparticle tracking analysis (NTA) and a micro-BCA protein assay to ascertain EV-particle concentration and protein concentrations respectively. Quantification of EV-particles and EV-protein was then repeated on the sample post-fluorescent labelling. To render these vesicles fluorescent for optical tracking, they were conjugated to Alexa-488 through a maleimide linker as described in [215]. The original EV sample (~50 µL) was then diluted and dispersed in 150 µL PBS. The sample concentration was further reduced to 1/40, then 1/400, and finally to 1/4000 to form a dilution range for testing. Control samples for cryo-electron microscope imaging and an immuno-assay to detect CD81 were prepared by adding 2 µL of EVs to 38 µL of PBS. Post-ACEV concentration pellets were collected using a pipette by manually extracting a fraction of the liquid (0.5 µL) near the concentration region, as depicted in **Fig 6.17a**. A sample of the equivalent volume was also taken from the peripheral, non-concentrated region. All these samples were stored immediately at -80ºC.

The wide-field fluorescence images shown in **Fig 6.17** present the concentration of EVs labelled with a fluorophore. The concentration process was somewhat similar to the nanoparticles, as an immediate EV aggregation occurred soon after applying the dual wave. Whatever dilutions, the ACEV device could concentrate the EVs within approximately 30 s with the sample volume of 50 µL, which is a tenfold increase in the volume handled by the state-of-the-art technique reported in Ref [200]. The formation of the EV pellet (0.4 µg/mL

sample) was recorded as shown in **Fig 6.17b**, EV aggregation becomes evident and visible in the droplet centre after only 20 s. The fluorescence intensity reaches the plateau at ~30 s (**Fig 6.17c**), denoting the completion of the pellet. The pipette was used to extract a 0.5-µL sample to collect the EV pellet for follow-up analysis. The total time from sample loading to EV pellet harvest was again less than 1 min. Observationally, the shape of the concentrated EVs was not uniformly round as for polystyrene nanoparticles, and certainly at higher concentrations present a shape that has a central bright core, surrounded by a more diffuse outer ring, akin to a "fried egg" (**Fig 6.17a**). We are uncertain why this is occurring but is likely due to the heterogeneity of EVs present in the sample, reflecting differences in size, densities, and molecular composition.

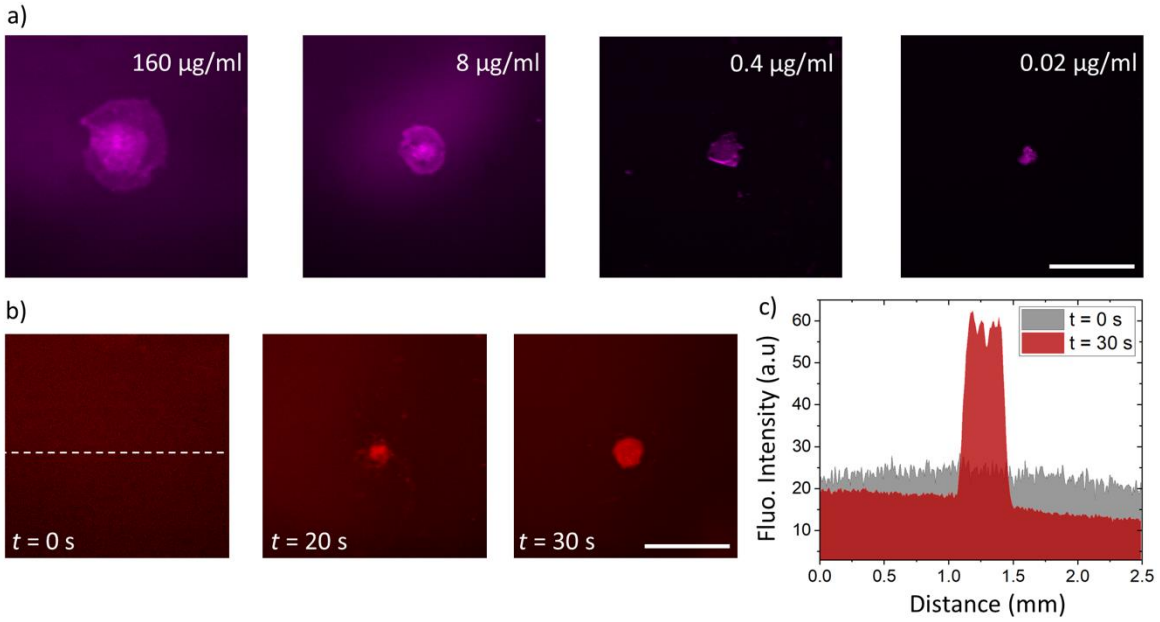

Figure 6.17. EV concentration using the ACEV device. (a) Four EV dilutions are concentrated by using the ACEV device. (b) The EV sample of 0.4 µg/mL is enriched within 30 s. (c) The normalized fluorescence intensity in the EV sample (0.4 µg/mL) before and after SAW concentration. Scale bars 1 mm.

6.14 EV Characterisation after ACEV Concentration

Maintaining EV integrity and function is critical when developing any EV manipulation technique or device. Apart from the EV concentration efficiency provided in **Fig 6.18a**, the following measurements were performed to systematically study the effects of the ACEV device on the EVs. Firstly, cryo-electron microscopy (cryo-EM) was used to check the existence of EVs and their structural features. EV samples were deposited onto glow-

discharging holey carbon 200-mesh copper grids (Quantifoil, Micro Tools GmbH, Germany) and subjected to vitrification using a Vitrobot (Maastricht Instruments BV, The Netherlands). Imaging of vitrified samples was conducted at the liquid nitrogen temperature using a transmission cryo-electron microscope (JEM-2200FS/CR, JEOL, USA) with a field emission gun operated at an acceleration voltage of 200 kV. More than 600 individual EVs were analyzed using ImageJ (National Institutes of Health).

The cryo-EM images of nanoparticles extracted from the control specimen (not subject to ACEV), post ACEV concentrated zone (pellet), and post ACEV depleted zone are shown in **Fig 6.18a-c**. The definition of the concentrated zone and the depleted zone is illustrated in **Fig 6.18d**. According to our observations, the nanoparticles in these collections are classified into: intact (green arrows), damaged (red arrows), and avesicular electron-dense particle (AEDP) (yellow arrows). We define “intact” as a rounded structure, in which the outer lipidic membrane is fully contiguous, with no evidence of gaps, disturbance or any perturbation hence the outside of the vesicle is truly separated from the inner luminal compartment by this integral membrane structure. For vesicles that appear to encapsulate other membrane-structures (vesicles within vesicles), our definition of “intact” focuses only on the outer membrane and does not consider possible perturbations of the encapsulated structures. For the term “damaged”, we observe examples where this outer lipidic membrane has indeed been compromised and is not contiguous. Often this reveals a possibility of a spill-out of content from the vesicle as further evidence of loss of integrity of the structure. Our definition of avesicular particles is based on the presence of dark nano-scale structures that lack evidence of a lipidic membrane, and although considered to be formed of protein and possibly other aggregated biomolecules their precise nature is not well known. Similar avesicular structures have, however, been reported elsewhere [49]. Representative images from the control group depict a variety of nanoscale yet heterogeneous vesicular structures with clearly delineated membrane boundaries that are circular and contiguous (green arrows), as intact vesicles. Some amorphous materials and rare AEDPs (yellow arrows) that lack membranes are occasionally observed. **Fig 6.18b** & **Fig 6.18c** show the representative images from the samples subjected to acoustic pressures from the concentrated and depleted zones.

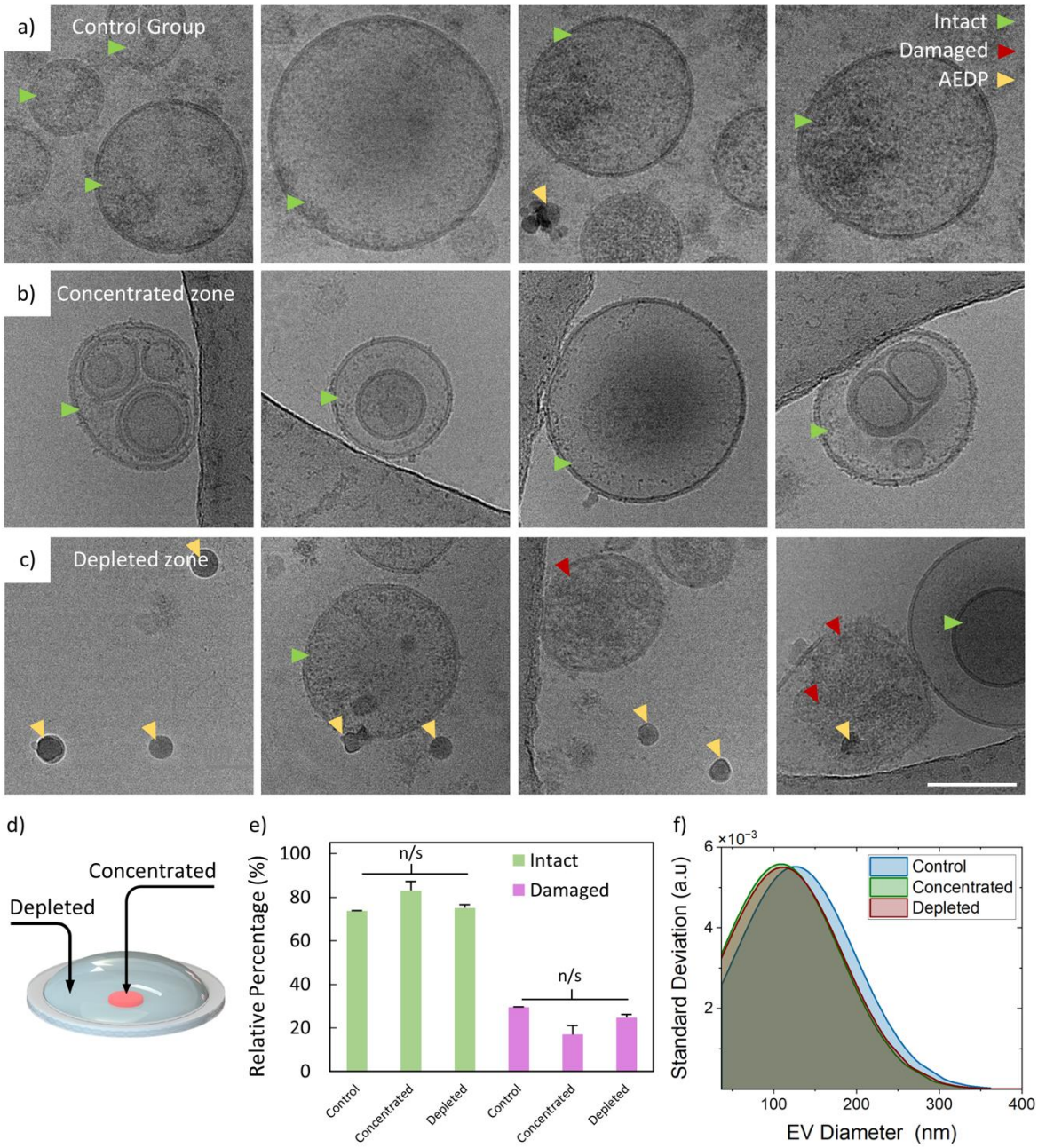

Figure 6.18. Analysis of the EV samples concentrated by using the ACEV device. (a) Gallery for cryo-electron microscopy (cryo-EM) imaging showing the nanoparticles in the (a) control group, (b) concentrated region, and (c) depleted region, scale bar 100 nm. (d) Indication of different sampling regions of the device. (e) Relative proportions of intact and damaged vesicles from a pool of cryo-EM images (>40 microscopic fields per condition), where there were no significant differences found. (f) Measurement of size variation taken from the cryo-EM images (n = 611). n/s means no significance.

A heterogeneous EV population within the concentrated zone with contiguous membranes can be observed (green arrows). Although the amorphous background material is still present, it is much less commonly observed than in the control group. The AEDPs, however, are not observed in this sample, and this was an unexpected yet highly desirable finding, as the ACEV appears therefore to remove these other types of particles from the EV concentrate. For the depleted zone, morphologically intact and damaged membranes (red arrows) were present together with a relative abundance of AEDP. Quantification of these images across over 40 regions of interest per specimen revealed that, on average, 75% of vesicles are classified as intact (**Fig 6.18e**). The proportions of damaged membranes in the Control and acoustic exposure groups are broadly comparable and hence this damage is most likely due to the processes in specimen handling before the ACEV concentration. These results reveal that the ACEV device has a minor impact on EV membrane integrity and does not, therefore, cause significant perturbation to the EV structure. The EV measurements (n = 611) revealed a comparable size distribution, indicating no vesicle size-based selectivity in the concentration process (**Fig 6.18f**). For many reasons, estimating a concentration effect by cryo-EM would be unreliable, and hence we used an orthogonal method to confirm that the ACEV device has indeed concentrated EVs, and not merely the fluorophore-related material. For this, we measured the vesicle-associated protein in the specified regions of the device. CD81 is a well-established EV biomarker highly abundant on the EV surface and is not a protein shed into the secretome of cells. Therefore, detecting the presence of CD81 would be a surrogate measure of the presence of vesicles. Purified EVs were immobilized on high-protein-binding ELISA plates (at doses of ≤10 µg per well) overnight in PBS. After immobilization, 1% (w/v) BSA/PBS blocking solution was added, and the wells were blocked for two hours. CD81 Primary antibodies (at 2 µg/mL) were added and incubated for two hours. After three washes, the detection was by incubating the solution with goat anti-mouse biotinylated secondary antibodies (PerkinElmer Life) for 1 hour. Following three washes, Europium conjugated to streptavidin was added, and after washing six times, the time-resolved fluorescence signal was measured via a BMG PHERAstar plate reader (BMG LATECH). The detailed procedure and methods were reported in the previous studies [215], [216].

Fig 6.19g shows that from an initial vesicle concentration of 129 µg/mL of CD81-positive vesicles, EVs are successfully concentrated by the ACEV device to 237 µg/mL in the concentration zone. In contrast, the depleted zone had a reduction of CD81-positive vesicles to <50 µg/mL, reflecting an 85% increase in CD81 (and hence EVs) between the concentrated and depleted zones. Lastly, looking closely at the cryo-EM images, we noticed

significant differences (**p<0.01) of 15-20 nm sized AEDPs present in the depleted region (see the yellow arrow in **Fig 6.18c** as an example). Such particle size is at the exact threshold of the ACEV current limitations (~20 nm). In fact, the vast majority of these structures were present, and arguably concentrated within the depleted zone (**Fig 6.19h**). It is not the first time that AEDPs have been identified from cryo-EM imaging, as these structures have been reported in many other studies [217], [218], [219]. Assuming AEDPs are undesirable from an EV-purification perspective, the ACEV device supplies the additional advantage of separating potentially detrimental aggregates while simultaneously concentrating intact EVs in less than a minute.

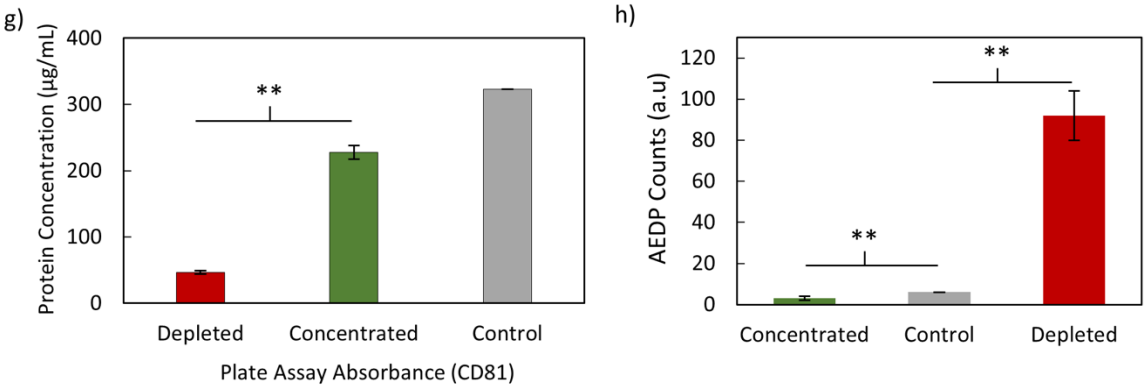

Figure 6.19. EV characterisation post concentration (a) Relative concentration of CD81-positive EV (n=2). (b) Numerical count of avesicular electron-dense particles (AEDP) in samples (n=2). Significance determined by 1-way Anova, with Tukey's post-test, where *p<0.05, **p<0.01, ***p<0.001.

Statistical analyses between experimental groups were performed using Prism-4 software V4.03 (Graph Pad, San Diego, CA). In experiments with more than two experimental groups, one-way ANOVA with Tukey's post-test was used. P-values less than 0.05 are considered significant (*p<0.05, **p<0.01, ***p<0.001). Bar graphs depict mean ± SD of n measures as detailed in figure legends.

6.15 Double Stage Concentration

The development of the dual wave mode is a prominent branch in the field of acoustofluidics. However, further advances can be made to extend the presented study. The waves generated using harmonics can manipulate particles in various directions. In Chapter 5, it was demonstrated (**Fig 5.7**) how a sessile droplet can experience different streaming modes by simply changing the applied frequency. This phenomenon can be utilized to our further

advantage in the concentration technique. It is possible that the 50 µL droplet is too large for the emerging wave to be handled effectively, leaving a considerable number of particles in the depleted zone. Nevertheless, expanding the throughput is an undeniable necessity, and as the droplet size increases, the identified issue will become more pronounced. To address this, instead of aiming to concentrate a single pellet in the centre, we can use different streaming modes to split the droplet into multiple parts and concentrate smaller pellets in various regions of the droplet. Then, by switching to a frequency that typically yields a central pellet, we can concentrate the small pellets rather than individual particles. **Fig 6.20a** shows a comparison of single-stage and double-stage concentrations. While single-stage concentration still performs well for nanoparticles, the double-stage concentration offers an optimized version of the phenomenon. The operation cycle for the double-stage concentration is similar, with only a single additional step. The particles are loaded as usual, and a frequency that generates two or more vortices is activated. Once the pellets reach a plateau, a frequency that produces a single vortex concentration is turned on, and the pellets aggregate in the middle. This approach ensures that particles initially closer to the edge are picked up by the smaller concentration regions and then conveniently placed for collection in the centre. The optimized version's improved performance is validated by the fluorescence intensity graphs shown in **Fig 6.20b**. The peak of the pellet is significantly sharper, and the depleted zone almost falls to zero when compared to the single-stage concentration. A small slope in the single stage concentration pellet indicates that more particles are dispersed.

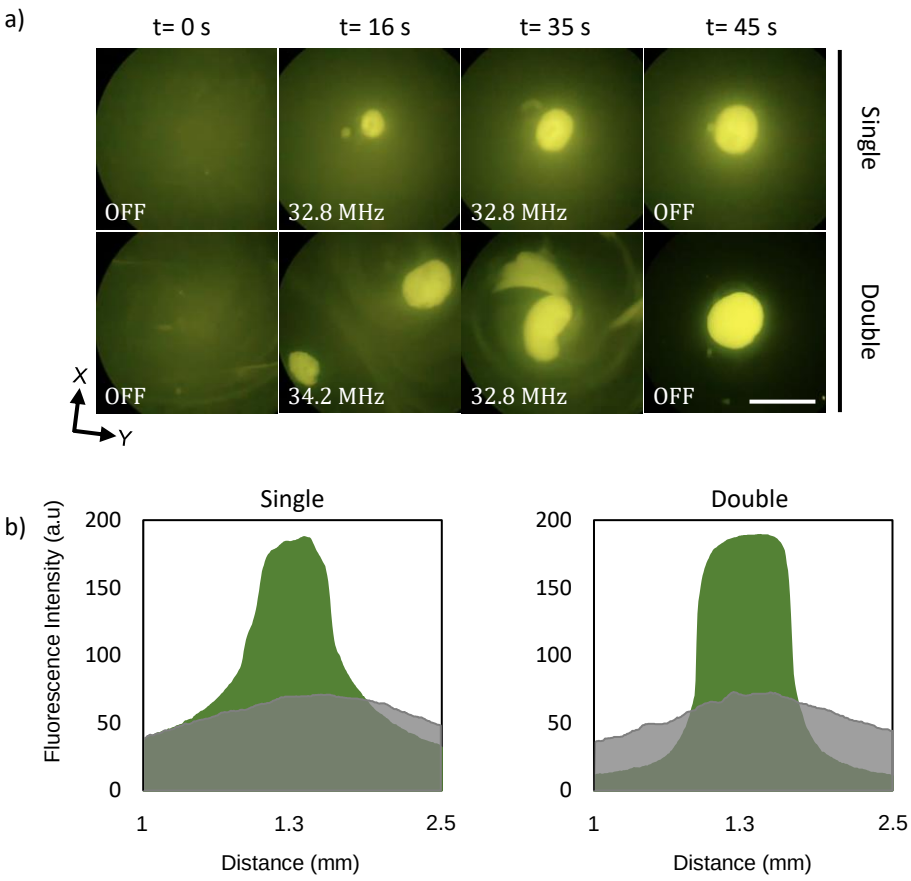

Figure 6.20. Comparison of a) single and double stage concentrations. b) fluorescence intensity analysis of single and double stage concentrations. Scale bar 1 mm.

6.16 Increasing Sample Throughput

Increasing throughput has been emphasized significantly throughout this thesis. Another straightforward technique for increasing throughput is to increase the droplet size. From the author's experience, the minimum handling volume practically useful is at least 0.5 mL. Therefore, further optimization is required to combine dual-waves with larger droplets. A proof-of-concept experiment is presented in **Fig 6.21a**, demonstrating that such a sample size is feasible to use and relatively easy to work with, most importantly maintaining the rapid speeds of under a minute. However, when the droplet size approaches 2.5 mL (**Fig 6.21b**), handling the fluid becomes more challenging, and extensive care must be taken to avoid breaking the surface tension.

Moreover, it becomes increasingly difficult to achieve single vortex streaming with a small IDT aperture as the droplet size increases. While it is possible to accomplish this, the IDT needs to be wider for the double-stage phenomenon to be implemented effectively. As a

result, with the current setup, multiple pellets develop, which can be easily collected using a pipette. Further research and development are needed to optimize the process for larger droplets, addressing the challenges in fluid handling and the requirements for the IDT aperture.

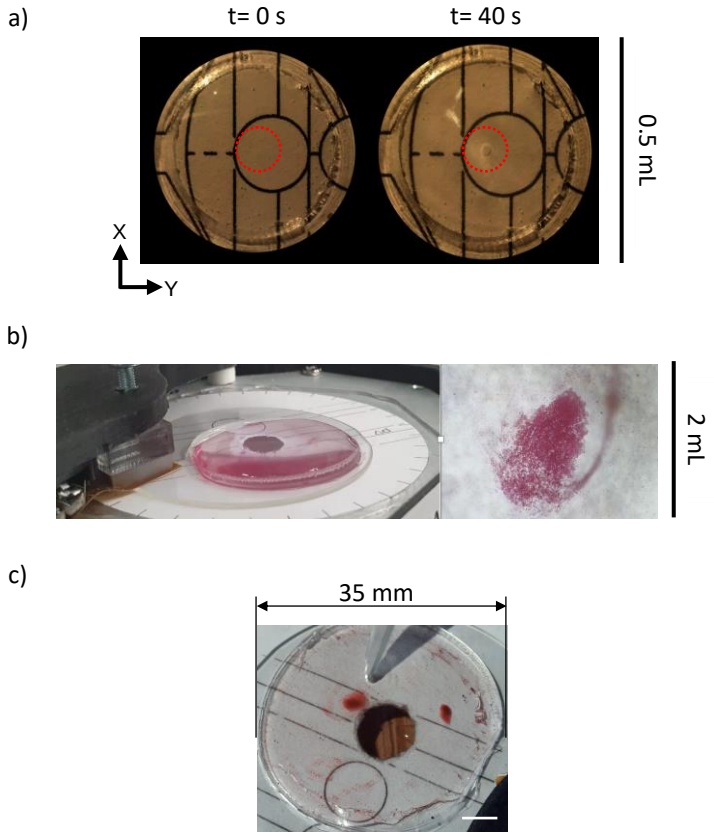

Figure 6.21. Possibilities of improving the sample throughput by increasing the PDMS ring diameter to accommodate a sample of a) 0.5 mL. Scale bar 5 mm. b) 2 mL. c) Multiple concentration pellets appearing due to the absence of the single vortex. Scale bar 5 mm.

6.17 Commercialisation

In conclusion, having identified the waves and standardized the pellet extraction techniques, it is now feasible to integrate all the results into a single, functional device. The DAS unit introduced in Chapter 4 can be further enhanced with technologies such as a camera, a screen, a robotic arm for automatic collection, and other features to provide a comprehensive benchtop device for use in the field.

In pursuit of this vision, **Fig 6.22** presents a developed benchtop prototype based on the original DAS. This updated version is equipped with a Raspberry Pi, a camera, and a display, further pushing the boundaries of EV concentration techniques in a portable and affordable

manner. Notably, the need for an expensive microscope has been eliminated. The combination of the camera and the Raspberry Pi allows for the integration of OpenCV's algorithms for colour and shape detection. Consequently, the device not only concentrates particles but also provides real-time information on attributes such as circularity, size, location, and concentration status.

Figure 6.22. Next generation DAS system equipped with a camera, screen, and real time pellet analysis (inset). Scale bar 5 cm.

Future work could involve refining the prototype to improve its reliability and user-friendliness, as well as exploring the integration of additional features. For example, incorporating a robotic arm is yet to be incorporated for automated pellet collection needed to streamline the process further, reducing the need for manual intervention. Ultimately, the development of this all-in-one benchtop device has the potential to significantly advance the field of acoustofluidics and make EV concentration techniques more accessible and efficient.

6.18 Innovations and Contributions

The Acoustofluidic Centrifuge for Extracellular Vesicles (ACEV) represents a significant advancement in the field of nanoparticle and microparticle concentration. Below is a detailed discussion about the key contributions from the ACEV platform.

Processing Time: ACEV dramatically reduces the processing time required to concentrate nanoparticles. The device can aggregate nanoparticles down to 20 nm within just 30 seconds. This ultrafast processing is a substantial improvement over conventional methods, which can only achieve similar results in 1 minute and with smaller sample volumes.

Volume: The ACEV device is capable of handling relatively large sample volumes efficiently. It processes volumes up to 50 µL with high precision, whereas the state-of-the-art methods are limited to very small droplets of around 5 µL for nanoparticles. This capability is crucial

for practical applications in biomedical and industrial fields where larger sample volumes are common.

Smallest Particle Size: ACEV excels at concentrating extremely small particles, capable of aggregating nanoparticles as small as 20 nm. This is a significant advancement over existing technologies, which typically handle particles no smaller than 28 nm and 500 nm on average. The ability to concentrate such small particles in larger volumes and shorter times marks a groundbreaking achievement in acoustofluidics. Prior to this research, it was thought to be impossible to concentrate particles of this size using acoustofluidic methods.

Commercialisation Prospect: The commercial potential of the ACEV device is high due to its simplicity and cost-effectiveness. The straightforward design and operation, combined with the use of commonly available materials like PDMS and lithium niobate, make it an attractive option for widespread adoption. This simplicity mirrors the innovations discussed in Chapter 3, emphasizing the low-cost manufacturing of interdigital transducers (IDTs) and the device. The device's ability to concentrate particles positions quickly and efficiently it well for commercial applications in research and industry.

Biocompatibility: The ACEV device maintains biocompatibility throughout the concentration process. It preserves the integrity of extracellular vesicles (EVs) and cells, ensuring that they remain viable for downstream applications. This is particularly important for biomedical research and therapeutic applications where maintaining the biological function of concentrated particles is critical.

Waves Utilised: ACEV utilises a combination of Rayleigh and SH-SAWs (shear horizontal surface acoustic waves), which significantly enhances its efficiency and effectiveness. This dual-wave mode creates a unique single vortex streaming pattern that allows for rapid and precise concentration of particles. The innovative use of these acoustic waves sets ACEV apart from other technologies that typically rely on a single wave mode, commonly Rayleigh.

Viscosity Handling: The ACEV device has demonstrated the ability to effectively handle different viscosities, showcasing its versatility in processing samples of varying physical properties. This adaptability is crucial for practical applications where sample viscosity can vary widely, such as in biological fluids.

Power and Frequency: ACEV operates at relatively low power and frequency levels compared to conventional methods, which typically require higher power inputs for similar results. This low power consumption not only reduces operational costs but also makes the device safer and more sustainable. The ability to affect particles of such small size at low

power and frequency is a remarkable achievement, highlighting the efficiency and effectiveness of the ACEV method.

Commercial Prospects: The ACEV method is just a step in a potentially new field of acoustofluidic particle concentration. Future research could continue exploring the double-stage concentration technique to further enhance the efficiency and capability of the device.

Overall ACEV stands as a highly competitive platform with regards to existing acoustic methods as summarized in **Table 6.2**.

Table 6.2. Comparison of different acoustic concentration techniques

Acoustic Techniques	Ref.	Volume Throughput	Particle size limit	Processing Time
Submicron Particle and Cell Concentration in a Closed Chamber	[220]	14 µL	200 nm	~ 30 s
Cell Agglomeration in the Wells of a 24-Well Plate Using Acoustic Streaming	[221]	1 mL	10 µm	~ 340 s
Acoustofluidic Centrifuge for Nanoparticle Enrichment	[200]	10 µL	100 nm	~ 60 s
Acoustofluidic Multi-Well Plates for Enrichment of Micro & nano Particles and Cells	[194]	30 µL	15 µL	~ 10 s
Acoustofluidic Particle Manipulation Inside a Sessile Droplet	[197]	5 µL	1 µm	~ 30 s
Manipulation of Cancer Cells in a Sessile Droplet	[208]	~ 6 µL	~ 5 µm	~ 25 s
Aggregation of a dense suspension of particles in a microwell using surface acoustic wave microcentrifugation	[209]	150 µL	5 µm	~ 30 s
Microliter ultrafast centrifuge platform for size-based particle and cell separation and extraction using novel omnidirectional spiral surface acoustic waves	[198]	1.5 µL	5 µm	~ 1 s
ACEV. (Dual-Wave Acoustofluidic Centrifuge for Ultrafast Concentration of Nanoparticles and Extracellular Vesicles)	**[205]**	**50 µL**	**20 nm**	**~ 30 s**

While ACEV stands as the leading platform in the acoustofluidics domain, it is essential to contextualize its performance within the broader landscape of available methodologies. Compared to other techniques involving different physical principles, ACEV demonstrates comparable efficacy in EV concentration. As shown in **Table 6.3**, ACEV achieves this within a significantly reduced timeframe, reducing the process from over 10 hours to just 30 seconds. However, it is important to acknowledge that this remarkable speed is somewhat offset by ACEV's relatively small processing volume, especially when compared to methods like ultracentrifugation. Addressing this limitation remains a key challenge for future

development. When comparing ACEV with other EV isolation techniques, several key factors emerge. Differential ultracentrifugation, for instance, is a widely used method due to its ability to handle large sample volumes. However, it requires expensive equipment and can damage EVs during the process, with a processing time of approximately 8 hours. Polymer-assisted precipitation offers unbiased separation but involves multiple procedures and a long processing time of around 12 hours. Immunoaffinity-based capture beads and microfluidic chips are notable for their ability to separate disease-related exosomes. Capture beads take about 18-24 hours and require additional washing steps, leading to a biased separation. Microfluidic chips reduce the processing time to about 2 hours but still face similar drawbacks in terms of additional washing and biased separation. Field flow fractionation (FFF) provides high separation resolution and can separate exosome sub-populations, but it involves multiple procedures and requires a specific membrane, with a processing time of about 10 hours. ACEV, on the other hand, stands out for its extremely rapid processing time of just 30 seconds and low cost. Despite its low processing volume, ACEV's speed and cost-efficiency make it a compelling choice for EV concentration, highlighting the need for further development to overcome its current limitations.

Table 6.3. Comparison of ACEV with respect to other EV isolation techniques

Other Techniques	References	Processing Time	Advantages	Disadvantages
Differential Ultracentrifugation	[93]	~8 h	Large processing sample volume	Expensive equipment, damage to EVs
Polymer-assisted precipitation	[222]	~12 h	Unbiased separation	Multiple procedures needed, long processing time
Immunoaffinity-based capture beads	[223]	~18-24 h	Ability to separate disease-related exosomes	Additional washing process needed, biased separation
Immunoaffinity-based microfluidic chips	[118]	~2 h	Ability to separate disease-related exosomes	Additional washing process needed, biased separation
Field flow fractionation (FFF)	[122]	~10 h	High separation resolution, ability to separate exosome sub-populations	Multiple procedures, Specific membrane required
ACEV	[205]	**~30 s**	**Extremely fast, and cheap**	**Low volume**

6.19 Conclusions

Chapter 6 highlights the advancements made by the Acoustofluidic Centrifuge for Extracellular Vesicles (ACEV) in the concentration and manipulation of micro- and nano-bioparticles. The dual-wave mode, which combines Rayleigh and Shear Horizontal Surface Acoustic Waves (SH-SAWs), has proven to be a significant leap forward in acoustofluidics, offering enhanced efficiency and precision over conventional methods. The ACEV device's ability to process a 50 µL sample within 30-35 seconds, and concentrate particles as small as 20 nm, underscores its superiority over existing technologies. Traditional methods often require lower sample volumes and longer processing times, making ACEV's performance particularly noteworthy. This rapid processing is facilitated by the unique dual-wave mode, which not only maintains the integrity of bioparticles but also enhances throughput for applications such as cancer cell enrichment and EV concentration. From a commercial perspective, ACEV's design, utilizing a single straight printed circuit board (PCB), presents a viable pathway to cost-effective and scalable production. In contrast, state-of-the-art methods rely on cleanroom-fabricated double slanted interdigital transducers (IDTs), which are more complex to operate and costly to produce. This difference in commercial viability is a crucial factor that positions ACEV as a more practical solution for widespread adoption in research and clinical settings. Biocompatibility is another critical aspect where ACEV excels. It maintains the integrity of bioparticles during the concentration process, a feature that is essential for downstream biological analyses and applications, something that ultracentrifuges are notorious in underscoring. Although biocompatibility is generally reported for current state-of-the-art technologies, the specific performance of ACEV in preserving particle integrity further enhances its applicability. The device's capability to handle viscosities up to 4-5 cP effectively is another advantage, as it broadens the range of samples that can be processed without compromising efficiency. This contrasts with the state-of-the-art methods, which, while effective, are less efficient in handling higher viscosities or even lacking reports in this category.

In terms of the technical specifics, ACEV operates at a frequency of 32.8 MHz, within the common MHz range of current technologies, but the dual-wave utilization presents a distinct advantage. The dual-wave approach not only enhances the manipulation and concentration capabilities but also simplifies the experimental setup, eliminating the need for repositioning droplets and enabling versatile streaming pattern control. The prospects for ACEV are highly promising, particularly in the field of extracellular vesicle research and clinical applications. Its innovative approach to nanoparticle concentration and the ability to handle small sample volumes with high precision set it apart from existing technologies. Future developments

could see the integration of additional features such as automated pellet collection and real-time analysis, further enhancing the device's usability and efficiency. In conclusion, the ACEV device represents a significant advancement in acoustofluidic technology, combining efficiency, precision, and commercial viability. Its potential to revolutionize nanoparticle concentration and bioparticle manipulation is substantial, making it a valuable tool for researchers and clinicians alike.

Chapter 7
Conclusions

7.1 Conclusions

The present work makes a significant contribution through the implementation of the DAS (Dynamic Acoustofluidic System) method, utilizing Flexible Printed Circuit Board (FPCB) Interdigitated Electrodes (IDEs), revolutionizes the fabrication process of SAW-based acoustofluidic systems. The DAS method can streamline manufacturing processes, making SAW technology more widely available for research and various applications. Incorporating 3D printable microchannels and PDMS rings further enhances the affordability and accessibility of this technology, enabling rapid prototyping of SAW-based acoustofluidic devices.

The DAS system facilitates positioning the IDT transducer at arbitrary angles relative to the piezoelectric substrate, thereby enabling the exploration of new wave modes. This unique approach provides the flexibility to investigate wave phenomena beyond the commonly used Rayleigh surface acoustic waves (SAWs) and address particle manipulation scales that have not been documented in the current literature.

Comprehensive studies were conducted involving analytical simulations and experimental investigations to enhance understanding of the intricate wave dynamics. These investigations revealed the improved manipulation of particles through the rotation of PCBs and led to the identification of dual-wave phenomena. The careful analysis of the interplay between surface and bulk components yielded valuable insights into the underlying mechanisms governing the observed enhancements in particle manipulation within our system.

Building upon these findings, the development of the Acoustic Concentration of Extracellular Vesicles (ACEV) device showcased a significant advancement in the ultrafast concentration of EVs. By utilizing dual-wave modes consisting of Rayleigh and Shear Horizontal Surface Acoustic Waves (SH-SAWs), nanoparticles as small as 20 nm were efficiently concentrated from sample volumes of 50 µL. The ACEV device demonstrated its ability to maintain EV integrity during concentration and facilitate the extraction of enriched particles, potentially excluding undesired protein aggregates. However, further improvements and automation of the concentration process are still warranted to enhance performance and throughput.

This thesis has uncovered the potential of dual-wave modes and highlighted the fusion of different modes to achieve superior concentration efficiency. The exploration into the generation of dual-wave modes represents a significant breakthrough in the field, with numerous other modes yet to be fully explored.

In summary, this work has successfully developed and validated an innovative and cost-effective fabrication methodology for SAW-based acoustofluidic systems, discovered the potential of dual surface acoustic waves for particle manipulation, and demonstrated the practical application of this technology in the ultrafast concentration of EVs. These findings make substantial contributions to the field of acoustofluidics, laying a solid foundation for further research and technological advancements in this exciting field.

7.2 Future Work

In future research, several avenues can be explored to advance the development of the nanoparticle concentration device proposed in this PhD thesis. Firstly, there is a need to investigate the scalability of the device, ensuring its compatibility with larger volumes of sample while maintaining efficient concentration capabilities. Furthermore, exploring the application of different types of nanoparticles and understanding their behaviour within the concentration device would provide valuable insights into the device's versatility and potential applications.

It is crucial to focus on enhancing the sample retrieval process in future research related to the development of the nanoparticle concentration device. Improving sample retrieval is essential to ensure efficient and reliable collection of the concentrated nanoparticles for downstream applications. One approach could involve exploring the use of innovative collection techniques such as microfluidic systems or robotic arm systems, which can selectively isolate and retrieve the concentrated nanoparticles from the device. Optimizing the design of the collection chamber or integrating automated systems for sample retrieval will minimize losses and improve the overall yield of the concentrated nanoparticles.

It is essential to explore alternative methods for detecting concentrated areas within the nanoparticle concentration device, particularly without relying solely on fluorescence-based techniques. While fluorescence is commonly used for nanoparticle detection and quantification, it may have limitations such as photobleaching, interference from background signals, or the need for specific fluorophores.

In addition, conducting a more comprehensive study of the mechanical waves generated within the nanoparticle concentration device is recommended. This can be accomplished by

employing advanced measurement tools such as a laser vibrometer. The laser vibrometer can provide high-resolution and non-contact measurements of the mechanical vibrations and wave propagation within the device. By analysing the characteristics of these waves, including their amplitude, frequency, and propagation patterns, a deeper understanding of the underlying physical phenomena driving the nanoparticle concentration process can be gained.

Future work should include testing the nanoparticle concentration device for its potential applications in separation and transfection techniques. The device's ability to concentrate nanoparticles could be evaluated in the context of separating different types of nanoparticles based on their size, charge, or other physical properties. By manipulating the operational parameters of the device, such as power levels and frequency, it may be possible to selectively concentrate specific nanoparticles, enabling efficient separation processes. Moreover, exploring the device's capabilities in transfection techniques, where nanoparticles are used to deliver genetic material into cells, could be highly valuable. By concentrating the nanoparticles, the device may enhance the transfection efficiency and provide a more precise control over the delivery process.

By addressing these future research directions, the development of the nanoparticle concentration device can be further advanced, opening new possibilities for nanoparticle manipulation and enabling breakthroughs in various fields such as nanomedicine, environmental science, and materials engineering.

Appendix 1: Values of constants

Table 1. Parameters for numerical and analytical analysis

Parameter	Symbol	Value
Fluid compressibility	β_f	$5 * 10^{-10}\ \frac{\mathrm{m}^2}{\mathrm{N}}$
Particle compressibility	β_p	$1.72 * 10^{-10}\ \frac{\mathrm{m}^2}{\mathrm{N}}$
Particle density	ρ_p	$1050\ \frac{\mathrm{kg}}{m^3}$
Fluid density	ρ_f	$997\ \frac{\mathrm{kg}}{m^3}$
Substrate density	ρ_s	$4650\ \frac{\mathrm{kg}}{m^3}$
Liquid sound velocity	c_L	$1500\ \frac{m}{s}$
Substrate sound velocity (x-axis)	c_S	$3980\ \frac{m}{s}$
Substrate sound velocity (x-axis + 60°)	c_{DW}	$3580\ \frac{m}{s}$
Liquid shear viscosity	η	$1\ cP$
Particle mass	m_p	$3.7 * 10^{-20} - 3.7 * 10^{-11}$ kg
Particle diameter	d_p	$20\ nm - 20 \mu m$

References

[1] J. Graham, *Biological Centrifugation*, 1st ed. Garland Science, 2020. doi: 10.1201/9781003076797.

[2] K. Cash, 'The History of the Centrifuge'. Accessed: 2024 June 1st [Online]. Available: https://www.marshallscientific.com/the_history_of_the_centrifuge_a/349.htm#:~:text=In%201864%2C%20Antonin%20Prandtl%20invented,apply%20centrifugation%20in%20the%20lab.

[3] 'Evolution of the Lab Centrifuge'. Accessed: 2024 June 1st [Online]. Available: https://www.labmanager.com/laboratory-technology/evolution-of-the-lab-centrifuge-19657

[4] A. Claude and J. Potter, 'Isolation of Chromatin Threads from the Resting Nucleus of Leukemic Cells', Dec. 1942.

[5] M. Tkach and C. Théry, 'Communication by Extracellular Vesicles: Where We Are and Where We Need to Go', *Cell*, vol. 164, no. 6, pp. 1226–1232, Mar. 2016, doi: 10.1016/j.cell.2016.01.043.

[6] K. Abhange *et al.*, 'Small extracellular vesicles in cancer', *Bioactive Materials*, vol. 6, no. 11, pp. 3705–3743, Nov. 2021, doi: 10.1016/j.bioactmat.2021.03.015.

[7] Y. Chen *et al.*, 'Exosome detection via the ultrafast-isolation system: EXODUS', *Nat Methods*, vol. 18, no. 2, pp. 212–218, Feb. 2021, doi: 10.1038/s41592-020-01034-x.

[8] H. Robert, *Micrographia*.

[9] E. Bianconi *et al.*, 'An estimation of the number of cells in the human body', *Annals of Human Biology*, vol. 40, no. 6, pp. 463–471, Nov. 2013, doi: 10.3109/03014460.2013.807878.

[10] I. A. Hatton, E. D. Galbraith, N. S. C. Merleau, T. P. Miettinen, B. M. Smith, and J. A. Shander, 'The human cell count and size distribution', *Proc. Natl. Acad. Sci. U.S.A.*, vol. 120, no. 39, p. e2303077120, Sep. 2023, doi: 10.1073/pnas.2303077120.

[11] M. Kozak, 'Initiation of translation in prokaryotes and eukaryotes', *Gene*, vol. 234, no. 2, pp. 187–208, Jul. 1999, doi: 10.1016/S0378-1119(99)00210-3.

[12] A. Zifan, *A prokaryotic cell*. Accessed: 2024 June 1st [Online]. Available: https://askabiologist.asu.edu/explore/cells-living-in-cells

[13] D. Gevers *et al.*, 'Re-evaluating prokaryotic species', *Nat Rev Microbiol*, vol. 3, no. 9, pp. 733–739, Sep. 2005, doi: 10.1038/nrmicro1236.

[14] T. M. Embley and W. Martin, 'Eukaryotic evolution, changes and challenges', *Nature*, vol. 440, no. 7084, pp. 623–630, Mar. 2006, doi: 10.1038/nature04546.

[15] *Cell Structure*. Accessed: 2024 June 1st [Online]. Available: https://www.aatbio.com/catalog/cell-structures-and-organelles

[16] C. P. Satori, M. M. Henderson, E. A. Krautkramer, V. Kostal, M. M. Distefano, and E. A. Arriaga, 'Bioanalysis of Eukaryotic Organelles', *Chem. Rev.*, vol. 113, no. 4, pp. 2733–2811, Apr. 2013, doi: 10.1021/cr300354g.

[17] E. Mayer, 'Neuronal Communication', *Biol Signals*, 1993, doi: 1993:2:57-76.

[18] H. P. Ehrlich, 'A Snapshot of Direct Cell–Cell Communications in Wound Healing and Scarring', *Advances in Wound Care*, vol. 2, no. 4, pp. 113–121, May 2013, doi: 10.1089/wound.2012.0414.

[19] M. B. Sporn and A. B. Roberts, 'Autocrine growth factors and cancer', *Nature*, vol. 313, no. 6005, pp. 745–747, Feb. 1985, doi: 10.1038/313745a0.

[20] J. Cantley, 'The control of insulin secretion by adipokines: current evidence for adipocyte-beta cell endocrine signalling in metabolic homeostasis', *Mamm Genome*, vol. 25, no. 9–10, pp. 442–454, Oct. 2014, doi: 10.1007/s00335-014-9538-7.

[21] M. Mittelbrunn and F. Sánchez-Madrid, 'Intercellular communication: diverse structures for exchange of genetic information', *Nat Rev Mol Cell Biol*, vol. 13, no. 5, pp. 328–335, May 2012, doi: 10.1038/nrm3335.

[22] M. Z. Ratajczak, Ed., *Stem Cells: Therapeutic Applications*, vol. 1201. in Advances in Experimental Medicine and Biology, vol. 1201. Cham: Springer International Publishing, 2019. doi: 10.1007/978-3-030-31206-0.
[23] R. Kalluri and V. S. LeBleu, 'The biology **,** function **,** and biomedical applications of exosomes', *Science*, vol. 367, no. 6478, p. eaau6977, Feb. 2020, doi: 10.1126/science.aau6977.
[24] F. Teng and M. Fussenegger, 'Shedding Light on Extracellular Vesicle Biogenesis and Bioengineering', *Adv. Sci.*, vol. 8, no. 1, p. 2003505, Jan. 2021, doi: 10.1002/advs.202003505.
[25] E. Chargaff and R. West, 'THE BIOLOGICAL SIGNIFICANCE OF THE THROMBOPLASTIC PROTEIN OF BLOOD', *Journal of Biological Chemistry*, vol. 166, no. 1, pp. 189–197, Nov. 1946, doi: 10.1016/S0021-9258(17)34997-9.
[26] P. D. Stahl and G. Raposo, 'Extracellular Vesicles: Exosomes and Microvesicles, Integrators of Homeostasis', *Physiology*, vol. 34, no. 3, pp. 169–177, May 2019, doi: 10.1152/physiol.00045.2018.
[27] L. Zitvogel *et al.*, 'Eradication of established murine tumors using a novel cell-free vaccine: dendritic cell derived exosomes', *Nat Med*, vol. 4, no. 5, pp. 594–600, May 1998, doi: 10.1038/nm0598-594.
[28] J. Ratajczak *et al.*, 'Embryonic stem cell-derived microvesicles reprogram hematopoietic progenitors: evidence for horizontal transfer of mRNA and protein delivery', *Leukemia*, vol. 20, no. 5, pp. 847–856, May 2006, doi: 10.1038/sj.leu.2404132.
[29] H. Valadi, K. Ekström, A. Bossios, M. Sjöstrand, J. J. Lee, and J. O. Lötvall, 'Exosome-mediated transfer of mRNAs and microRNAs is a novel mechanism of genetic exchange between cells', *Nat Cell Biol*, vol. 9, no. 6, pp. 654–659, Jun. 2007, doi: 10.1038/ncb1596.
[30] J. Skog *et al.*, 'Glioblastoma microvesicles transport RNA and proteins that promote tumour growth and provide diagnostic biomarkers', *Nat Cell Biol*, vol. 10, no. 12, pp. 1470–1476, Dec. 2008, doi: 10.1038/ncb1800.
[31] S. Keerthikumar *et al.*, 'ExoCarta: A Web-Based Compendium of Exosomal Cargo', *Journal of Molecular Biology*, vol. 428, no. 4, pp. 688–692, Feb. 2016, doi: 10.1016/j.jmb.2015.09.019.
[32] R. Isaac, F. C. G. Reis, W. Ying, and J. M. Olefsky, 'Exosomes as mediators of intercellular crosstalk in metabolism', *Cell Metabolism*, vol. 33, no. 9, pp. 1744–1762, Sep. 2021, doi: 10.1016/j.cmet.2021.08.006.
[33] L. Mashouri, H. Yousefi, A. R. Aref, A. M. Ahadi, F. Molaei, and S. K. Alahari, 'Exosomes: composition, biogenesis, and mechanisms in cancer metastasis and drug resistance', *Mol Cancer*, vol. 18, no. 1, p. 75, Dec. 2019, doi: 10.1186/s12943-019-0991-5.
[34] L. Bouchareychas *et al.*, 'Macrophage Exosomes Resolve Atherosclerosis by Regulating Hematopoiesis and Inflammation via MicroRNA Cargo', *Cell Reports*, vol. 32, no. 2, p. 107881, Jul. 2020, doi: 10.1016/j.celrep.2020.107881.
[35] M. Battistelli and E. Falcieri, 'Apoptotic Bodies: Particular Extracellular Vesicles Involved in Intercellular Communication', *Biology*, vol. 9, no. 1, p. 21, Jan. 2020, doi: 10.3390/biology9010021.
[36] Silverstein, 'ENDOCYTOSIS', 1977, doi: 46:669-722.
[37] S. Mathivanan, P. Fonseka, C. Nedeva, and I. Atukorala, Eds., *New Frontiers: Extracellular Vesicles*, vol. 97. in Subcellular Biochemistry, vol. 97. Cham: Springer International Publishing, 2021. doi: 10.1007/978-3-030-67171-6.
[38] G. van Niel, G. D'Angelo, and G. Raposo, 'Shedding light on the cell biology of extracellular vesicles', *Nat Rev Mol Cell Biol*, vol. 19, no. 4, Art. no. 4, Apr. 2018, doi: 10.1038/nrm.2017.125.
[39] E. R. Abels and X. O. Breakefield, 'Introduction to Extracellular Vesicles: Biogenesis, RNA Cargo Selection, Content, Release, and Uptake', *Cell Mol Neurobiol*, vol. 36, no. 3, pp. 301–312, Apr. 2016, doi: 10.1007/s10571-016-0366-z.

[40]L. A. Mulcahy, R. C. Pink, and D. R. F. Carter, ‘Routes and mechanisms of extracellular vesicle uptake’, *Journal of Extracellular Vesicles*, vol. 3, no. 1, p. 24641, Jan. 2014, doi: 10.3402/jev.v3.24641.
[41]O. Dictionary, ‘Concentration’. Accessed: Dec. 12, 2023. [Online]. Available: https://www.oed.com/dictionary/concentration_n?tab=etymology
[42]G. A. Williams, ‘Body fluid identification: A case for more research and innovation’, *Forensic Science International: Reports*, vol. 2, p. 100096, Dec. 2020, doi: 10.1016/j.fsir.2020.100096.
[43]Z. Pan *et al.*, ‘Field Determination of Phosphate in Environmental Water by Using a Hand-Powered Paper Centrifuge for Preconcentration and Digital Image Colorimetric Sensing’, *Journal of Analytical Methods in Chemistry*, vol. 2022, pp. 1–7, Jan. 2022, doi: 10.1155/2022/7359197.
[44]G. G. Joag, M. N. Karanjkar, D. B. Potdar, and J. M. Pawar, ‘Clinico - Hematological Profile of Nutritional Anaemia among Adolescent Girls in Rural Area’, *JPRI*, pp. 75–79, Nov. 2020, doi: 10.9734/jpri/2020/v32i3030906.
[45]A. Dewitte *et al.*, ‘Blood platelets and sepsis pathophysiology: A new therapeutic prospect in critical ill patients?’, *Ann. Intensive Care*, vol. 7, no. 1, p. 115, Dec. 2017, doi: 10.1186/s13613-017-0337-7.
[46]N. Islam *et al.*, ‘Frequency and Nature of Transfusion Related Adverse Reactions in Patients Admitted in A Tertiary Care Hospital’, *Bangla J Med*, vol. 33, no. 1, pp. 27–33, Dec. 2021, doi: 10.3329/bjm.v33i1.56786.
[47]M.-K. Song, B.-B. Park, and J.-E. Uhm, ‘Targeted Therapeutic Approach Based on Understanding of Aberrant Molecular Pathways Leading to Leukemic Proliferation in Patients with Acute Myeloid Leukemia’, *IJMS*, vol. 22, no. 11, p. 5789, May 2021, doi: 10.3390/ijms22115789.
[48]H. Fan *et al.*, ‘Validation of a Classification Model Using Complete Blood Count to Predict Severe Human Adenovirus Lower Respiratory Tract Infections in Pediatric Cases’, *Front. Pediatr.*, vol. 10, p. 896606, May 2022, doi: 10.3389/fped.2022.896606.
[49]R. Gorkin *et al.*, ‘Centrifugal microfluidics for biomedical applications’, *Lab Chip*, vol. 10, no. 14, p. 1758, 2010, doi: 10.1039/b924109d.
[50]D. M. Dohan Ehrenfest, L. Rasmusson, and T. Albrektsson, ‘Classification of platelet concentrates: from pure platelet-rich plasma (P-PRP) to leucocyte- and platelet-rich fibrin (L-PRF)’, *Trends in Biotechnology*, vol. 27, no. 3, pp. 158–167, Mar. 2009, doi: 10.1016/j.tibtech.2008.11.009.
[51]H. Whitman, L. Berry, and M. Green, ‘P/a telet Gel: An Autologous Alternative to Fibrin Glue With Applications in Oral and Maxillofacial Surgery’.
[52]L. Yin, N. He, C. Chen, N. Zhang, Y. Lin, and Q. Xia, ‘Identification of novel blood-based HCC-specific diagnostic biomarkers for human hepatocellular carcinoma’, *Artificial Cells, Nanomedicine, and Biotechnology*, vol. 47, no. 1, pp. 1908–1916, Dec. 2019, doi: 10.1080/21691401.2019.1613421.
[53]A. Esquela-Kerscher and F. J. Slack, ‘Oncomirs — microRNAs with a role in cancer’, *Nat Rev Cancer*, vol. 6, no. 4, pp. 259–269, Apr. 2006, doi: 10.1038/nrc1840.
[54]X. Chen *et al.*, ‘Characterization of microRNAs in serum: a novel class of biomarkers for diagnosis of cancer and other diseases’, *Cell Res*, vol. 18, no. 10, pp. 997–1006, Oct. 2008, doi: 10.1038/cr.2008.282.
[55]E. Olayinka, A. Ore, O. Ola, and O. Adeyemo, ‘Ameliorative Effect of Gallic Acid on Cyclophosphamide-Induced Oxidative Injury and Hepatic Dysfunction in Rats’, *Medical Sciences*, vol. 3, no. 3, pp. 78–92, Sep. 2015, doi: 10.3390/medsci3030078.
[56]M. A. Ferguson and S. S. Waikar, ‘Established and Emerging Markers of Kidney Function’, *Clinical Chemistry*, vol. 58, no. 4, pp. 680–689, Apr. 2012, doi: 10.1373/clinchem.2011.167494.

[57] G. Pegoraro, S. Bavari, and R. G. Panchal, ‘Shedding Light on Filovirus Infection with High-Content Imaging’, *Viruses*, vol. 4, no. 8, pp. 1354–1371, Aug. 2012, doi: 10.3390/v4081354.
[58] I. Szabłowska-Gadomska, S. Rudziński, and M. Dymowska, ‘Secretome of Mesenchymal Stromal Cells as a Possible Innovative Therapeutic Tool in Facial Nerve Injury Treatment’, *BioMed Research International*, vol. 2023, pp. 1–7, Jan. 2023, doi: 10.1155/2023/8427200.
[59] P. Picone, D. Nuzzo, L. Caruana, V. Scafidi, and M. Di Carlo, ‘Mitochondrial Dysfunction: Different Routes to Alzheimer’s Disease Therapy’, *Oxidative Medicine and Cellular Longevity*, vol. 2014, pp. 1–11, 2014, doi: 10.1155/2014/780179.
[60] T. Li, J. Qu, C. Xu, T. Fang, B. Sun, and L. Chen, ‘Exploring the common gene signatures and pathogeneses of obesity with Alzheimer’s disease via transcriptome data’, *Front. Endocrinol.*, vol. 13, p. 1072955, Dec. 2022, doi: 10.3389/fendo.2022.1072955.
[61] C. Procaccini *et al.*, ‘Role of metabolism in neurodegenerative disorders’, *Metabolism*, vol. 65, no. 9, pp. 1376–1390, Sep. 2016, doi: 10.1016/j.metabol.2016.05.018.
[62] L. B. Hassing *et al.*, ‘Overweight in midlife and risk of dementia: a 40-year follow-up study’, *Int J Obes*, vol. 33, no. 8, pp. 893–898, Aug. 2009, doi: 10.1038/ijo.2009.104.
[63] R. D. Abbott *et al.*, ‘Midlife adiposity and the future risk of Parkinson’s disease’, *Neurology*, vol. 59, no. 7, pp. 1051–1057, Oct. 2002, doi: 10.1212/WNL.59.7.1051.
[64] Anston, ‘Body mass index in midlife and late-life as a risk factor for dementia’.
[65] D. Zink, A. H. Fischer, and J. A. Nickerson, ‘Nuclear structure in cancer cells’, *Nat Rev Cancer*, vol. 4, no. 9, pp. 677–687, Sep. 2004, doi: 10.1038/nrc1430.
[66] C. D. Capo-chichi, K. Q. Cai, F. Simpkins, P. Ganjei-Azar, A. K. Godwin, and X.-X. Xu, ‘Nuclear envelope structural defects cause chromosomal numerical instability and aneuploidy in ovarian cancer’, *BMC Med*, vol. 9, no. 1, p. 28, Dec. 2011, doi: 10.1186/1741-7015-9-28.
[67] K. Kitatani *et al.*, ‘Activation of p38 Mitogen-Activated Protein Kinase in Gaucher’s Disease’, *PLoS ONE*, vol. 10, no. 8, p. e0136633, Aug. 2015, doi: 10.1371/journal.pone.0136633.
[68] D. Drążewski *et al.*, ‘Oral Health Status of Patients with Lysosomal Storage Diseases in Poland’, *IJERPH*, vol. 14, no. 3, p. 281, Mar. 2017, doi: 10.3390/ijerph14030281.
[69] S. Ciniawsky, I. Grimm, D. Saffian, W. Girzalsky, R. Erdmann, and P. Wendler, ‘Molecular snapshots of the Pex1/6 AAA+ complex in action’, *Nat Commun*, vol. 6, no. 1, p. 7331, Jun. 2015, doi: 10.1038/ncomms8331.
[70] M. Brownlee, ‘Biochemistry and molecular cell biology of diabetic complications’, *Nature*, vol. 414, no. 6865, Art. no. 6865, Dec. 2001, doi: 10.1038/414813a.
[71] S. J. Steinberg, G. Dodt, G. V. Raymond, N. E. Braverman, A. B. Moser, and H. W. Moser, ‘Peroxisome biogenesis disorders’, *Biochimica et Biophysica Acta (BBA) - Molecular Cell Research*, vol. 1763, no. 12, pp. 1733–1748, Dec. 2006, doi: 10.1016/j.bbamcr.2006.09.010.
[72] E. J. Bunggulawa *et al.*, ‘Recent advancements in the use of exosomes as drug delivery systems’, *J Nanobiotechnol*, vol. 16, no. 1, p. 81, Dec. 2018, doi: 10.1186/s12951-018-0403-9.
[73] G. Rabinowits, C. Gerçel-Taylor, J. M. Day, D. D. Taylor, and G. H. Kloecker, ‘Exosomal MicroRNA: A Diagnostic Marker for Lung Cancer’, *Clinical Lung Cancer*, vol. 10, no. 1, pp. 42–46, Jan. 2009, doi: 10.3816/CLC.2009.n.006.
[74] M. Noerholm *et al.*, ‘RNA expression patterns in serum microvesicles from patients with glioblastoma multiforme and controls’, *BMC Cancer*, vol. 12, no. 1, p. 22, Dec. 2012, doi: 10.1186/1471-2407-12-22.
[75] S. A. Melo *et al.*, ‘Glypican-1 identifies cancer exosomes and detects early pancreatic cancer’, *Nature*, vol. 523, no. 7559, pp. 177–182, Jul. 2015, doi: 10.1038/nature14581.

[76]L. Zhu *et al.*, ‘Exosomal tRNA-derived small RNA as a promising biomarker for cancer diagnosis’, *Mol Cancer*, vol. 18, no. 1, p. 74, Dec. 2019, doi: 10.1186/s12943-019-1000-8.
[77]M. Osaki and F. Okada, ‘Exosomes and Their Role in Cancer Progression’, *Yonago Acta Med.*, vol. 62, no. 2, Art. no. 2, 2019, doi: 10.33160/yam.2019.06.002.
[78]S. Saeedi, S. Israel, C. Nagy, and G. Turecki, ‘The emerging role of exosomes in mental disorders’, *Transl Psychiatry*, vol. 9, no. 1, p. 122, Mar. 2019, doi: 10.1038/s41398-019-0459-9.
[79]K. M. Kanninen, N. Bister, J. Koistinaho, and T. Malm, ‘Exosomes as new diagnostic tools in CNS diseases’, *Biochimica et Biophysica Acta (BBA) - Molecular Basis of Disease*, vol. 1862, no. 3, pp. 403–410, Mar. 2016, doi: 10.1016/j.bbadis.2015.09.020.
[80]D. Osti *et al.*, ‘Clinical Significance of Extracellular Vesicles in Plasma from Glioblastoma Patients’, *Clinical Cancer Research*, vol. 25, no. 1, pp. 266–276, Jan. 2019, doi: 10.1158/1078-0432.CCR-18-1941.
[81]A. Aryani and B. Denecke, ‘Exosomes as a Nanodelivery System: a Key to the Future of Neuromedicine?’, *Mol Neurobiol*, vol. 53, no. 2, pp. 818–834, Mar. 2016, doi: 10.1007/s12035-014-9054-5.
[82]L. Alvarez-Erviti, Y. Seow, H. Yin, C. Betts, S. Lakhal, and M. J. A. Wood, ‘Delivery of siRNA to the mouse brain by systemic injection of targeted exosomes’, *Nat Biotechnol*, vol. 29, no. 4, pp. 341–345, Apr. 2011, doi: 10.1038/nbt.1807.
[83]J. C. Akers, D. Gonda, R. Kim, B. S. Carter, and C. C. Chen, ‘Biogenesis of extracellular vesicles (EV): exosomes, microvesicles, retrovirus-like vesicles, and apoptotic bodies’, *J Neurooncol*, vol. 113, no. 1, pp. 1–11, May 2013, doi: 10.1007/s11060-013-1084-8.
[84]J. Bai *et al.*, ‘Engineered targeting tLyp-1 exosomes as gene therapy vectors for efficient delivery of siRNA into lung cancer cells’, *Asian Journal of Pharmaceutical Sciences*, vol. 15, no. 4, pp. 461–471, Jul. 2020, doi: 10.1016/j.ajps.2019.04.002.
[85]X. Liu, ‘Exosome-mediated delivery of kartogenin for chondrogenesis of synovial fluid-derived mesenchymal stem cells and cartilage regeneration’, *Biomaterials 269 (2021) 120539*, 2021.
[86]Z. G. Zhang, B. Buller, and M. Chopp, ‘Exosomes — beyond stem cells for restorative therapy in stroke and neurological injury’, *Nat Rev Neurol*, vol. 15, no. 4, pp. 193–203, Apr. 2019, doi: 10.1038/s41582-018-0126-4.
[87]Z. Wen *et al.*, ‘Mesenchymal stem cell-derived exosomes ameliorate cardiomyocyte apoptosis in hypoxic conditions through microRNA144 by targeting the PTEN/AKT pathway’, *Stem Cell Res Ther*, vol. 11, no. 1, p. 36, Dec. 2020, doi: 10.1186/s13287-020-1563-8.
[88]Y. Liang, L. Duan, J. Lu, and J. Xia, ‘Engineering exosomes for targeted drug delivery’, *Theranostics*, vol. 11, no. 7, pp. 3183–3195, 2021, doi: 10.7150/thno.52570.
[89]E. I. Yakubovich, A. G. Polischouk, and V. I. Evtushenko, ‘Principles and Problems of Exosome Isolation from Biological Fluids’, *Biochem. Moscow Suppl. Ser. A*, vol. 16, no. 2, pp. 115–126, Jun. 2022, doi: 10.1134/S1990747822030096.
[90]C. A. Price, *Centrifugation in Density Gradients*. 1982.
[91]I. Newton, *Philosophiae naturalis principia mathematica*. 1687. Accessed: 2024 June 1st [Online]. Available: https://archive.org/details/philosophiaenatu00newt_0
[92]M. A. Livshits *et al.*, ‘Isolation of exosomes by differential centrifugation: Theoretical analysis of a commonly used protocol’, *Sci Rep*, vol. 5, no. 1, p. 17319, Nov. 2015, doi: 10.1038/srep17319.
[93]K. Ohlendieck and S. E. Harding, ‘Centrifugation and Ultracentrifugation’, in *Wilson and Walker’s Principles and Techniques of Biochemistry and Molecular Biology*, 8th ed., A. Hofmann and S. Clokie, Eds., Cambridge University Press, 2018, pp. 424–453. doi: 10.1017/9781316677056.014.
[94]A. Bobrie, M. Colombo, S. Krumeich, G. Raposo, and C. Théry, ‘Diverse subpopulations of vesicles secreted by different intracellular mechanisms are present in exosome

preparations obtained by differential ultracentrifugation', *Journal of Extracellular Vesicles*, vol. 1, no. 1, p. 18397, Jan. 2012, doi: 10.3402/jev.v1i0.18397.
[95] W. P. Kuo and S. Jia, Eds., *Extracellular Vesicles: Methods and Protocols*, vol. 1660. in Methods in Molecular Biology, vol. 1660. New York, NY: Springer New York, 2017. doi: 10.1007/978-1-4939-7253-1.
[96] W.-P. Peng, S.-W. Chou, and A. A. Patil, 'Measuring masses of large biomolecules and bioparticles using mass spectrometric techniques', *Analyst*, vol. 139, no. 14, pp. 3507–3523, 2014, doi: 10.1039/C3AN02329J.
[97] R. J. Lobb *et al.*, 'Optimized exosome isolation protocol for cell culture supernatant and human plasma', *Journal of Extracellular Vesicles*, vol. 4, no. 1, Art. no. 1, Jan. 2015, doi: 10.3402/jev.v4.27031.
[98] J. Zhu *et al.*, 'Exosomes from nicotine-stimulated macrophages accelerate atherosclerosis through miR-21-3p/PTEN-mediated VSMC migration and proliferation', *Theranostics*, vol. 9, no. 23, pp. 6901–6919, 2019, doi: 10.7150/thno.37357.
[99] L. Zhu *et al.*, 'Exosomes Derived From Natural Killer Cells Exert Therapeutic Effect in Melanoma', *Theranostics*, vol. 7, no. 10, pp. 2732–2745, 2017, doi: 10.7150/thno.18752.
[100] Y. Lu *et al.*, 'The Emerging Role of Exosomes in Oral Squamous Cell Carcinoma', *Front. Cell Dev. Biol.*, vol. 9, p. 628103, Feb. 2021, doi: 10.3389/fcell.2021.628103.
[101] D. Lopes *et al.*, 'Bioengineered exosomal-membrane-camouflaged abiotic nanocarriers: neurodegenerative diseases, tissue engineering and regenerative medicine', *Military Med Res*, vol. 10, no. 1, p. 19, Apr. 2023, doi: 10.1186/s40779-023-00453-z.
[102] Q.-H. Xie *et al.*, 'Exosome-Mediated Immunosuppression in Tumor Microenvironments', *Cells*, vol. 11, no. 12, p. 1946, Jun. 2022, doi: 10.3390/cells11121946.
[103] X. Li *et al.*, 'Challenges and opportunities in exosome research—Perspectives from biology, engineering, and cancer therapy', *APL Bioengineering*, vol. 3, no. 1, Art. no. 1, Mar. 2019, doi: 10.1063/1.5087122.
[104] S. Gholizadeh *et al.*, 'Microfluidic approaches for isolation, detection, and characterization of extracellular vesicles: Current status and future directions', *Biosensors and Bioelectronics*, vol. 91, pp. 588–605, May 2017, doi: 10.1016/j.bios.2016.12.062.
[105] P. Li, M. Kaslan, S. H. Lee, J. Yao, and Z. Gao, 'Progress in Exosome Isolation Techniques', *Theranostics*, vol. 7, no. 3, pp. 789–804, 2017, doi: 10.7150/thno.18133.
[106] J. F. Quintana *et al.*, 'Extracellular Onchocerca-derived small RNAs in host nodules and blood', *Parasites Vectors*, vol. 8, no. 1, p. 58, Dec. 2015, doi: 10.1186/s13071-015-0656-1.
[107] L.-L. Yu *et al.*, 'A Comparison of Traditional and Novel Methods for the Separation of Exosomes from Human Samples', *BioMed Research International*, vol. 2018, pp. 1–9, Jul. 2018, doi: 10.1155/2018/3634563.
[108] H. G. Barth, 'Size Exclusion Chromatography'.
[109] A. N. Böing, E. van der Pol, A. E. Grootemaat, F. A. W. Coumans, A. Sturk, and R. Nieuwland, 'Single-step isolation of extracellular vesicles by size-exclusion chromatography', *Journal of Extracellular Vesicles*, vol. 3, no. 1, Art. no. 1, Jan. 2014, doi: 10.3402/jev.v3.23430.
[110] S. Fekete, A. Beck, J.-L. Veuthey, and D. Guillarme, 'Theory and practice of size exclusion chromatography for the analysis of protein aggregates', *Journal of Pharmaceutical and Biomedical Analysis*, vol. 101, pp. 161–173, Dec. 2014, doi: 10.1016/j.jpba.2014.04.011.
[111] T. S. Martins, 'A review on comparative studies addressing exosome isolation methods from body fluids'.

[112] Y. Weng *et al.*, 'Effective isolation of exosomes with polyethylene glycol from cell culture supernatant for in-depth proteome profiling', *Analyst*, vol. 141, no. 15, pp. 4640–4646, 2016, doi: 10.1039/C6AN00892E.
[113] N. Zarovni *et al.*, 'Integrated isolation and quantitative analysis of exosome shuttled proteins and nucleic acids using immunocapture approaches', *Methods*, vol. 87, pp. 46–58, Oct. 2015, doi: 10.1016/j.ymeth.2015.05.028.
[114] C. Théry, M. Ostrowski, and E. Segura, 'Membrane vesicles as conveyors of immune responses', *Nat Rev Immunol*, vol. 9, no. 8, pp. 581–593, Aug. 2009, doi: 10.1038/nri2567.
[115] B. J. Tauro, D. W. Greening, R. A. Mathias, S. Mathivanan, H. Ji, and R. J. Simpson, 'Two Distinct Populations of Exosomes Are Released from LIM1863 Colon Carcinoma Cell-derived Organoids', *Molecular & Cellular Proteomics*, vol. 12, no. 3, pp. 587–598, Mar. 2013, doi: 10.1074/mcp.M112.021303.
[116] C. Théry, S. Amigorena, G. Raposo, and A. Clayton, 'Isolation and Characterization of Exosomes from Cell Culture Supernatants and Biological Fluids', *CP Cell Biology*, vol. 30, no. 1, Art. no. 1, Mar. 2006, doi: 10.1002/0471143030.cb0322s30.
[117] A. Subramanian, 'Immunoaffinity chromatography', *MOLECULAR BIOTECHNOLOGY*, vol. 20, 2002.
[118] S. S. Kanwar, C. J. Dunlay, D. M. Simeone, and S. Nagrath, 'Microfluidic device (ExoChip) for on-chip isolation, quantification and characterization of circulating exosomes', *Lab Chip*, vol. 14, no. 11, pp. 1891–1900, 2014, doi: 10.1039/C4LC00136B.
[119] R. Bano, F. Ahmad, and M. Mohsin, 'A perspective on the isolation and characterization of extracellular vesicles from different biofluids', *RSC Adv.*, vol. 11, no. 32, pp. 19598–19615, 2021, doi: 10.1039/D1RA01576A.
[120] Spectradyne, 'Technology for particle size analysis'. Accessed: Nov. 27, 2023. [Online]. Available: https://nanoparticleanalyzer.com/technology.php
[121] D. Holmes, N. G. Green, and H. Morgan, 'Microdevices for dielectrophoretic flow-through cell separation', *IEEE Eng. Med. Biol. Mag.*, vol. 22, no. 6, pp. 85–90, Nov. 2003, doi: 10.1109/MEMB.2003.1266051.
[122] H. Zhang *et al.*, 'Identification of distinct nanoparticles and subsets of extracellular vesicles by asymmetric flow field-flow fractionation', *Nat Cell Biol*, vol. 20, no. 3, pp. 332–343, Mar. 2018, doi: 10.1038/s41556-018-0040-4.
[123] M. Chemist, 'Field Flow Fractionation application in MAB development'. Accessed: Nov. 27, 2023. [Online]. Available: https://www.manufacturingchemist.com/news/article_page/Field_Flow_Fractionation_application_in_MAB_development/88138
[124] K.-G. Wahlund, 'Flow field-flow fractionation: Critical overview', *Journal of Chromatography A*, vol. 1287, pp. 97–112, Apr. 2013, doi: 10.1016/j.chroma.2013.02.028.
[125] M. P. Hughes, 'Strategies for dielectrophoretic separation in laboratory-on-a-chip systems', *Electrophoresis*, vol. 23, no. 16, pp. 2569–2582, Aug. 2002, doi: 10.1002/1522-2683(200208)23:16<2569::AID-ELPS2569>3.0.CO;2-M.
[126] R. Pethig, 'Review Article—Dielectrophoresis: Status of the theory, technology, and applications', *Biomicrofluidics*, vol. 4, no. 2, p. 022811, Jun. 2010, doi: 10.1063/1.3456626.
[127] C. Qian *et al.*, 'Dielectrophoresis for Bioparticle Manipulation', *IJMS*, vol. 15, no. 10, pp. 18281–18309, Oct. 2014, doi: 10.3390/ijms151018281.
[128] R. Salemmilani, B. D. Piorek, R. Y. Mirsafavi, A. W. Fountain, M. Moskovits, and C. D. Meinhart, 'Dielectrophoretic Nanoparticle Aggregation for On-Demand Surface Enhanced Raman Spectroscopy Analysis', *Anal. Chem.*, vol. 90, no. 13, pp. 7930–7936, Jul. 2018, doi: 10.1021/acs.analchem.8b00510.

[129]L. Liu, K. Chen, N. Xiang, and Z. Ni, 'Dielectrophoretic manipulation of nanomaterials: A review', *Electrophoresis*, vol. 40, no. 6, pp. 873–889, Mar. 2019, doi: 10.1002/elps.201800342.
[130]N. Lewpiriyawong, C. Yang, and Y. C. Lam, 'Dielectrophoretic manipulation of particles in a modified microfluidic H filter with multi-insulating blocks', *Biomicrofluidics*, vol. 2, no. 3, p. 034105, Sep. 2008, doi: 10.1063/1.2973661.
[131]J. Rufo, F. Cai, J. Friend, M. Wiklund, and T. J. Huang, 'Acoustofluidics for biomedical applications', *Nature Reviews Methods Primers*, vol. 2, no. 1, Art. no. 1, Apr. 2022, doi: 10.1038/s43586-022-00109-7.
[132]M. Stringer *et al.*, 'Methodologies, technologies, and strategies for acoustic streaming-based acoustofluidics', *Applied Physics Reviews*, vol. 10, no. 1, p. 011315, Mar. 2023, doi: 10.1063/5.0134646.
[133]J.-C. Hsu and C.-L. Chao, 'Full-wave modeling of micro-acoustofluidic devices driven by standing surface acoustic waves for microparticle acoustophoresis', *Journal of Applied Physics*, vol. 128, no. 12, Art. no. 12, Sep. 2020, doi: 10.1063/5.0017933.
[134]Y. Xie *et al.*, 'Microfluidic Isolation and Enrichment of Nanoparticles', *ACS Nano*, vol. 14, no. 12, Art. no. 12, Dec. 2020, doi: 10.1021/acsnano.0c06336.
[135]Y. Gu *et al.*, 'Acoustofluidic Holography for Micro- to Nanoscale Particle Manipulation', *ACS Nano*, vol. 14, no. 11, Art. no. 11, Nov. 2020, doi: 10.1021/acsnano.0c03754.
[136]M. Wu, A. Ozcelik, J. Rufo, Z. Wang, R. Fang, and T. Jun Huang, 'Acoustofluidic separation of cells and particles', *Microsyst Nanoeng*, vol. 5, no. 1, p. 32, Jun. 2019, doi: 10.1038/s41378-019-0064-3.
[137]'Ephesus Theatre'. [Online]. Available: https://ephesus.us/ancient-ephesus/ephesus-theatre/
[138]I. Caleon and S. Ramanathan, 'From Music to Physics: The Undervalued Legacy of Pythagoras', *Sci & Educ*, vol. 17, no. 4, pp. 449–456, Apr. 2008, doi: 10.1007/s11191-007-9090-x.
[139]G. Galilei, *TWO NEW SCIENCES*. 1638.
[140]M. Mersenne, *Harmonicorum Libri*. 1636.
[141]I. S. Caleon and R. Subramaniam, 'From Pythagoras to Sauveur: tracing the history of ideas about the nature of sound', *Phys. Educ.*, vol. 42, no. 2, pp. 173–179, Mar. 2007, doi: 10.1088/0031-9120/42/2/007.
[142]J. B. West, 'Robert Boyle's landmark book of 1660 with the first experiments on rarified air', *J Appl Physiol*, vol. 98, 2005.
[143]I. Newton, *The Principia*. 1687.
[144]G. Zhang, *Bulk and Surface Acoustic Waves : Fundamentals, Devices, and Applications*. Jenny Stanford Publishing Pte. Ltd, 2022.
[145]Lord Rayleigh, 'On Waves Propagated along the Plane Surface of an Elastic Solid', *Proceedings of the London Mathematical Society*, vol. s1-17, no. 1, Art. no. 1, Nov. 1885, doi: 10.1112/plms/s1-17.1.4.
[146]C. Steinem and A. Janshoff, 'SENSORS | Piezoelectric Resonators', in *Encyclopedia of Analytical Science (Second Edition)*, P. Worsfold, A. Townshend, and C. Poole, Eds., Oxford: Elsevier, 2005, pp. 269–276. doi: 10.1016/B0-12-369397-7/00556-2.
[147]L. Horace, 'On waves in an elastic plate', Mar. 1917, doi: https://doi.org/10.1098/rspa.1917.0008.
[148]R. Tao *et al.*, 'Thin film flexible/bendable acoustic wave devices: Evolution, hybridization and decoupling of multiple acoustic wave modes', *Surface and Coatings Technology*, vol. 357, pp. 587–594, Jan. 2019, doi: 10.1016/j.surfcoat.2018.10.042.
[149]M. Long, '2 - Fundamentals of Acoustics', in *Architectural Acoustics (Second Edition)*, M. Long, Ed., Boston: Academic Press, 2014, pp. 39–79. doi: 10.1016/B978-0-12-398258-2.00002-7.
[150]'the-discovery-of-the-piezoelectric-effect.pdf'.

[151]K. Uchino, ‘1 - The development of piezoelectric materials and the new perspective’, in *Advanced Piezoelectric Materials*, K. Uchino, Ed., in Woodhead Publishing Series in Electronic and Optical Materials. , Woodhead Publishing, 2010, pp. 1–85. doi: 10.1533/9781845699758.1.
[152]K. M. Ok, E. O. Chi, and P. S. Halasyamani, ‘Bulk characterization methods for non-centrosymmetric materials: second-harmonic generation, piezoelectricity, pyroelectricity, and ferroelectricity’, *Chem. Soc. Rev.*, vol. 35, no. 8, p. 710, 2006, doi: 10.1039/b511119f.
[153]D. Damjanovic, ‘Ferroelectric, dielectric and piezoelectric properties of ferroelectric thin films and ceramics’, *Rep. Prog. Phys.*, vol. 61, no. 9, pp. 1267–1324, Sep. 1998, doi: 10.1088/0034-4885/61/9/002.
[154]G. A. Lager, J. D. Jorgensen, and F. J. Rotella, ‘Crystal structure and thermal expansion of α-quartz SiO_2 at low temperatures’, *Journal of Applied Physics*, vol. 53, no. 10, pp. 6751–6756, Oct. 1982, doi: 10.1063/1.330062.
[155]R. M. Moroney, R. M. White, and R. T. Howe, ‘Microtransport induced by ultrasonic Lamb waves’, *Appl. Phys. Lett.*, vol. 59, no. 7, pp. 774–776, Aug. 1991, doi: 10.1063/1.105339.
[156]C. Fu *et al.*, ‘Vertical jetting induced by shear horizontal leaky surface acoustic wave on 36° Y-X $LiTaO_3$’, *Appl. Phys. Lett.*, vol. 110, no. 17, Art. no. 17, Apr. 2017, doi: 10.1063/1.4982073.
[157]K. Uchino, ‘High-Power Piezoelectrics and Loss Mechanisms’, in *Advanced Piezoelectric Materials*, Elsevier, 2017, pp. 647–754. doi: 10.1016/B978-0-08-102135-4.00017-5.
[158]Y. Q. Fu *et al.*, ‘Advances in piezoelectric thin films for acoustic biosensors, acoustofluidics and lab-on-chip applications’, *Progress in Materials Science*, vol. 89, pp. 31–91, Aug. 2017, doi: 10.1016/j.pmatsci.2017.04.006.
[159]V. Ya. Shur, ‘6 - Lithium niobate and lithium tantalate-based piezoelectric materials’, in *Advanced Piezoelectric Materials*, K. Uchino, Ed., in Woodhead Publishing Series in Electronic and Optical Materials. , Woodhead Publishing, 2010, pp. 204–238. doi: 10.1533/9781845699758.1.204.
[160]J. Holterman and P. Groen, *An introduction to piezoelectric materials and applications*. Apeldoorn: Stichting Applied Piezo, 2013.
[161]K. Uchino, ‘Chapter 10 - Manufacturing Methods for Piezoelectric Ceramic Materials’, in *Advanced Piezoelectric Materials (Second Edition)*, K. Uchino, Ed., in Woodhead Publishing in Materials. , Woodhead Publishing, 2017, pp. 385–421. doi: 10.1016/B978-0-08-102135-4.00010-2.
[162]W. G. Nelson, *Piezoelectric Materials: Structure, Properties and Applications*. in Materials Science and Technologies. New York: Nova Science Publishers, Inc, 2010. [Online]. Available: https://search.ebscohost.com/login.aspx?direct=true&db=nlebk&AN=339712&site=ehost-live&scope=site
[163]‘The Tehcnology and Operation of Piezo Sounder’.
[164]G. Destgeer, B. H. Ha, J. H. Jung, and H. J. Sung, ‘Submicron separation of microspheres via travelling surface acoustic waves’, *Lab Chip*, vol. 14, no. 24, Art. no. 24, Nov. 2014, doi: 10.1039/C4LC00868E.
[165]Y. Vladimirsky, ‘10 - LITHOGRAPHY’, in *Vacuum Ultraviolet Spectroscopy*, J. A. R. Samson and D. L. Ederer, Eds., Burlington: Academic Press, 1999, pp. 205–223. doi: 10.1016/B978-012617560-8/50032-3.
[166]XiaoMing Hu, ‘Photolithography technology in electronic fabrication’, in *Proceedings of the 2015 International Power, Electronics and Materials Engineering Conference*, Atlantis Press, May 2015, pp. 843–850. doi: 10.2991/ipemec-15.2015.156.
[167]J. Kirschner, ‘Surface Acoustic Wave Sensors (SAWS): Design for Application’, *Microelectromechanical systems*, p. 11, Jun. 2010.

[168]J. A. Schufle, ‘Answer: Chinese Brass Water-Spouting Bowl’, doi: https://doi.org/10.1086/352653.
[169]V. Dvorak and Prof. A.M. Mayer, ‘On acoustic repulsion’, 1878, doi: DOI: 10.1080/14786447808639500.
[170]‘On the acoustic radiation pressure on spheres.pdf’.
[171]H. Bruus, ‘Acoustofluidics 7: The acoustic radiation force on small particles’, *Lab Chip*, vol. 12, no. 6, p. 1014, 2012, doi: 10.1039/c2lc21068a.
[172]N. Riley, ‘STEADY STREAMING’, 2000.
[173]H. Bruus, ‘Acoustofluidics 1: Governing equations in microfluidics’, *Lab Chip*, vol. 11, no. 22, p. 3742, 2011, doi: 10.1039/c1lc20658c.
[174]M. Karimi, G. Akdogan, K. H. Dellimore, and S. M. Bradshaw, ‘COMPARISON OF DIFFERENT DRAG COEFFICIENT CORRELATIONS IN THE CFD MODELLING OF A LABORATORY-SCALE RUSHTON-TURBINE FLOTATION TANK’, 2012.
[175]‘Analysis of conventional drag and lift models for multiphase CFD modeling of blood flow.pdf’.
[176]H. Bruus, ‘Acoustofluidics 2: Perturbation theory and ultrasound resonance modes’, *Lab Chip*, vol. 12, no. 1, pp. 20–28, 2012, doi: 10.1039/C1LC20770A.
[177]Y. Fan, X. Wang, J. Ren, F. Lin, and J. Wu, ‘Recent advances in acoustofluidic separation technology in biology’, *Microsyst Nanoeng*, vol. 8, no. 1, p. 94, Sep. 2022, doi: 10.1038/s41378-022-00435-6.
[178]J. Qian, Y. Wang, S. Yuan, H. Sun, and X. Liu, ‘Reflected acoustic wavefront manipulation by an ultrathin metasurface based on three-dimensional generalized Snell’s law’, *Appl. Phys. Express*, vol. 12, no. 9, p. 094001, Sep. 2019, doi: 10.7567/1882-0786/ab3492.
[179]A. Wixforth, C. Strobl, Ch. Gauer, A. Toegl, J. Scriba, and Z. v. Guttenberg, ‘Acoustic manipulation of small droplets’, *Anal Bioanal Chem*, vol. 379, no. 7–8, Art. no. 7–8, Aug. 2004, doi: 10.1007/s00216-004-2693-z.
[180]R. M. Arzt, E. Salzmann, and K. Dransfeld, ‘ELASTIC SURFACE WAVES IN QUARTZ AT 316 MHz’, *APPLIED PHYSICS LETTERS*, vol. 10, no. 5, 1967.
[181]‘lighthill1978.pdf’.
[182]I. Iranmanesh, R. Barnkob, H. Bruus, and M. Wiklund, ‘Tunable-angle wedge transducer for improved acoustophoretic control in a microfluidic chip’, *J. Micromech. Microeng.*, vol. 23, no. 10, Art. no. 10, Sep. 2013, doi: 10.1088/0960-1317/23/10/105002.
[183]K. Xu *et al.*, ‘Isolation of a Low Number of Sperm Cells from Female DNA in a Glass–PDMS–Glass Microchip via Bead-Assisted Acoustic Differential Extraction’, *Anal. Chem.*, vol. 91, no. 3, Art. no. 3, Feb. 2019, doi: 10.1021/acs.analchem.8b04752.
[184]J. Gai *et al.*, ‘High-Frequency Ultrasound Boosts Bull and Human Sperm Motility’, *Advanced Science*, vol. n/a, no. n/a, Art. no. n/a, Feb. 2022, doi: 10.1002/advs.202104362.
[185]S. Kim, H. Nam, B. Cha, J. Park, H. J. Sung, and J. S. Jeon, ‘Acoustofluidic Stimulation of Functional Immune Cells in a Microreactor’, *Advanced Science*, vol. 9, no. 16, Art. no. 16, 2022, doi: 10.1002/advs.202105809.
[186]D. V. Deshmukh *et al.*, ‘Continuous Production of Acoustically Patterned Cells Within Hydrogel Fibers for Musculoskeletal Tissue Engineering’, *Advanced Functional Materials*, vol. n/a, no. n/a, Art. no. n/a, May 2022, doi: 10.1002/adfm.202113038.
[187]Y. Ai, C. K. Sanders, and B. L. Marrone, ‘Separation of Escherichia coli Bacteria from Peripheral Blood Mononuclear Cells Using Standing Surface Acoustic Waves’, *Anal. Chem.*, vol. 85, no. 19, Art. no. 19, Oct. 2013, doi: 10.1021/ac4017715.
[188]A. A. Nawaz *et al.*, ‘Intelligent image-based deformation-assisted cell sorting with molecular specificity’, *Nat Methods*, vol. 17, no. 6, Art. no. 6, Jun. 2020, doi: 10.1038/s41592-020-0831-y.

[189] M. Wu *et al.*, 'Circulating Tumor Cell Phenotyping via High-Throughput Acoustic Separation', *Small*, vol. 14, no. 32, p. 1801131, Aug. 2018, doi: 10.1002/smll.201801131.
[190] M. Wu *et al.*, 'Circulating Tumor Cell Phenotyping via High-Throughput Acoustic Separation', *Small*, vol. 14, no. 32, Art. no. 32, Aug. 2018, doi: 10.1002/smll.201801131.
[191] P. Li *et al.*, 'Acoustic separation of circulating tumor cells', *PNAS*, vol. 112, no. 16, Art. no. 16, Apr. 2015, doi: 10.1073/pnas.1504484112.
[192] M. Wu *et al.*, 'Isolation of exosomes from whole blood by integrating acoustics and microfluidics', *Proc. Natl. Acad. Sci. U.S.A.*, vol. 114, no. 40, Art. no. 40, Oct. 2017, doi: 10.1073/pnas.1709210114.
[193] Z. Wang *et al.*, 'Acoustofluidic Salivary Exosome Isolation: A Liquid Biopsy Compatible Approach for Human Papillomavirus–Associated Oropharyngeal Cancer Detection', *The Journal of Molecular Diagnostics*, vol. 22, no. 1, Art. no. 1, Jan. 2020, doi: 10.1016/j.jmoldx.2019.08.004.
[194] P. Liu *et al.*, 'Acoustofluidic multi-well plates for enrichment of micro/nano particles and cells', *Lab Chip*, vol. 20, no. 18, pp. 3399–3409, 2020, doi: 10.1039/D0LC00378F.
[195] H. Li, J. R. Friend, and L. Y. Yeo, 'Surface acoustic wave concentration of particle and bioparticle suspensions', *Biomed Microdevices*, vol. 9, no. 5, pp. 647–656, Aug. 2007, doi: 10.1007/s10544-007-9058-2.
[196] P. R. Rogers, J. R. Friend, and L. Y. Yeo, 'Exploitation of surface acoustic waves to drive size-dependent microparticle concentration within a droplet', *Lab Chip*, vol. 10, no. 21, p. 2979, 2010, doi: 10.1039/c004822d.
[197] G. Destgeer, H. Cho, B. H. Ha, J. H. Jung, J. Park, and H. J. Sung, 'Acoustofluidic particle manipulation inside a sessile droplet: four distinct regimes of particle concentration', *Lab Chip*, vol. 16, no. 4, pp. 660–667, 2016, doi: 10.1039/C5LC01104C.
[198] N. Zhang *et al.*, 'Microliter ultrafast centrifuge platform for size-based particle and cell separation and extraction using novel omnidirectional spiral surface acoustic waves', *Lab Chip*, vol. 21, no. 5, pp. 904–915, 2021, doi: 10.1039/D0LC01012J.
[199] Z. Mao *et al.*, 'Enriching Nanoparticles via Acoustofluidics', *ACS Nano*, vol. 11, no. 1, Art. no. 1, Jan. 2017, doi: 10.1021/acsnano.6b06784.
[200] Y. Gu *et al.*, 'Acoustofluidic centrifuge for nanoparticle enrichment and separation', *Sci. Adv.*, vol. 7, no. 1, p. eabc0467, Jan. 2021, doi: 10.1126/sciadv.abc0467.
[201] Z. Wang *et al.*, 'Acoustofluidics for simultaneous nanoparticle-based drug loading and exosome encapsulation', *Microsyst Nanoeng*, vol. 8, no. 1, p. 45, Apr. 2022, doi: 10.1038/s41378-022-00374-2.
[202] R. Barnkob, P. Augustsson, T. Laurell, and H. Bruus, 'Acoustic radiation- and streaming-induced microparticle velocities determined by microparticle image velocimetry in an ultrasound symmetry plane', *Phys. Rev. E*, vol. 86, no. 5, Art. no. 5, Nov. 2012, doi: 10.1103/PhysRevE.86.056307.
[203] H. Ledbetter, H. Ogi, and N. Nakamura, 'Elastic, anelastic, piezoelectric coefficients of monocrystal lithium niobate', *Mechanics of Materials*, vol. 36, no. 10, pp. 941–947, Oct. 2004, doi: 10.1016/j.mechmat.2003.08.013.
[204] M. S. Namnabat, M. Moghimi Zand, and E. Houshfar, '3D numerical simulation of acoustophoretic motion induced by boundary-driven acoustic streaming in standing surface acoustic wave microfluidics', *Sci Rep*, vol. 11, no. 1, p. 13326, Jun. 2021, doi: 10.1038/s41598-021-90825-z.
[205] P. Dumčius *et al.*, 'Dual-Wave Acoustofluidic Centrifuge for Ultrafast Concentration of Nanoparticles and Extracellular Vesicles', 2023.
[206] R. Mikhaylov *et al.*, 'Development and characterisation of acoustofluidic devices using detachable electrodes made from PCB', *Lab Chip*, vol. 20, no. 10, pp. 1807–1814, 2020, doi: 10.1039/C9LC01192G.

[207] R. Mikhaylov *et al.*, 'A reconfigurable and portable acoustofluidic system based on flexible printed circuit board for the manipulation of microspheres', *J. Micromech. Microeng.*, vol. 31, no. 7, p. 074003, Jul. 2021, doi: 10.1088/1361-6439/ac0515.
[208] H. Nam, H. J. Sung, J. Park, and J. S. Jeon, 'Manipulation of cancer cells in a sessile droplet *via* travelling surface acoustic waves', *Lab Chip*, vol. 22, no. 1, pp. 47–56, 2022, doi: 10.1039/D1LC00801C.
[209] A. Sudeepthi, A. K. Sen, and L. Yeo, 'Aggregation of a dense suspension of particles in a microwell using surface acoustic wave microcentrifugation', *Microfluid Nanofluid*, vol. 23, no. 5, p. 76, May 2019, doi: 10.1007/s10404-019-2243-9.
[210] M. Yáñez-Mó *et al.*, 'Biological properties of extracellular vesicles and their physiological functions', *Journal of Extracellular Vesicles*, vol. 4, no. 1, p. 27066, Jan. 2015, doi: 10.3402/jev.v4.27066.
[211] R. S. Rosenson, A. McCormick, and E. F. Uretz, 'Distribution of blood viscosity values and biochemical correlates in healthy adults', *Clinical Chemistry*, vol. 42, no. 8, pp. 1189–1195, Aug. 1996, doi: 10.1093/clinchem/42.8.1189.
[212] A. Clayton *et al.*, 'Considerations towards a roadmap for collection, handling and storage of blood extracellular vesicles', *Journal of Extracellular Vesicles*, vol. 8, no. 1, p. 1647027, Dec. 2019, doi: 10.1080/20013078.2019.1647027.
[213] J. Webber, R. Steadman, M. D. Mason, Z. Tabi, and A. Clayton, 'Cancer Exosomes Trigger Fibroblast to Myofibroblast Differentiation', *Cancer Research*, vol. 70, no. 23, pp. 9621–9630, Dec. 2010, doi: 10.1158/0008-5472.CAN-10-1722.
[214] C. Théry, S. Amigorena, G. Raposo, and A. Clayton, 'Isolation and Characterization of Exosomes from Cell Culture Supernatants and Biological Fluids', *CP Cell Biology*, vol. 30, no. 1, Mar. 2006, doi: 10.1002/0471143030.cb0322s30.
[215] H. D. Roberts-Dalton *et al.*, 'Fluorescence labelling of extracellular vesicles using a novel thiol-based strategy for quantitative analysis of cellular delivery and intracellular traffic', *Nanoscale*, vol. 9, no. 36, pp. 13693–13706, 2017, doi: 10.1039/C7NR04128D.
[216] J. Webber *et al.*, 'Proteomics Analysis of Cancer Exosomes Using a Novel Modified Aptamer-based Array (SOMAscanTM) Platform', *Molecular & Cellular Proteomics*, vol. 13, no. 4, pp. 1050–1064, Apr. 2014, doi: 10.1074/mcp.M113.032136.
[217] G. Raposo and W. Stoorvogel, 'Extracellular vesicles: Exosomes, microvesicles, and friends', *The Journal of Cell Biology*, vol. 200, no. 4, Art. no. 4, Feb. 2013, doi: 10.1083/jcb.201211138.
[218] P. D'Acunzo *et al.*, 'Mitovesicles are a novel population of extracellular vesicles of mitochondrial origin altered in Down syndrome', *Sci. Adv.*, vol. 7, no. 7, p. eabe5085, Feb. 2021, doi: 10.1126/sciadv.abe5085.
[219] D. Zabeo, A. Cvjetkovic, C. Lässer, M. Schorb, J. Lötvall, and J. L. Höög, 'Exosomes purified from a single cell type have diverse morphology', *Journal of Extracellular Vesicles*, vol. 6, no. 1, p. 1329476, Dec. 2017, doi: 10.1080/20013078.2017.1329476.
[220] A. Akther, S. Marqus, A. R. Rezk, and L. Y. Yeo, 'Submicron Particle and Cell Concentration in a Closed Chamber Surface Acoustic Wave Microcentrifuge', *Anal. Chem.*, vol. 92, no. 14, Art. no. 14, Jul. 2020, doi: 10.1021/acs.analchem.0c01757.
[221] Y. Kurashina, K. Takemura, and J. Friend, 'Cell agglomeration in the wells of a 24-well plate using acoustic streaming', *Lab Chip*, vol. 17, no. 5, Art. no. 5, 2017, doi: 10.1039/C6LC01310D.
[222] T. Salafi, K. K. Zeming, and Y. Zhang, 'Advancements in microfluidics for nanoparticle separation', *Lab Chip*, vol. 17, no. 1, Art. no. 1, 2017, doi: 10.1039/C6LC01045H.
[223] S. Mathivanan, J. W. E. Lim, B. J. Tauro, H. Ji, R. L. Moritz, and R. J. Simpson, 'Proteomics Analysis of A33 Immunoaffinity- purified Exosomes Released from the Human Colon Tumor Cell Line LIM1215 Reveals a Tissue-specific Protein Signature*□S'.